Development of Novel Polyurethane Coatings for Protection of Leading-Edge of Wind Turbine Blades

by

Feras Zweiri

This dissertation submitted to the Faculty of Engineering, Computing, and the Environment in partial fulfilment of the requirements for the degree of Doctor of Philosophy in Mechanical Engineering.

Department of Mechanical engineering
Kingston University London

July 2024

Acknowledgements

I would like to express my sincere appreciation to my first supervisor, Associate Professor Homayoun Hadavinia, and my supervisory team members, Professor Neil Williams, and Dr Ali Heidari, for their invaluable support during my PhD. Their guidance and knowledge have been essential in producing the work presented in this thesis. I am particularly grateful to Dr Hadavinia for his unwavering support throughout the duration of my project and for imparting important life lessons that I will treasure in my future endeavour.

I extend my gratitude to Dr Francesco De Vanna, Mr Michael Carraro, and Professor Ernesto Benini from the Department of Industrial Engineering at the University of Padova, Italy, for their contribution to the three-dimensional aerodynamics modelling of the wind turbine blade.

I also wish to thank Dr Nadiim Domun for conducting the abrasion tests on the specimens we manufactured from six PU nanocomposites, and for providing the necessary data on wear resistance of these nanocomposites which was used in our assessments of the developed coatings.

My sincere appreciation goes to all the technical staff at Kingston University for their helpful support with the practical and experimental work. Special thanks to Dean Wells, our technician in the materials lab, for his friendly support and training on the various equipment necessary for my project; Simon Crust for his assistance with SEM and EDX analysis, and Abdi Ataei for his help with TGA and DSC testing.

Last but not least, I would like to thank my loving family, especially my mother and father, for their continuous emotional, financial, and spiritual support, and my dear sister and brother for their encouragement throughout the duration of my PhD.

Abstract

Wind turbine performance is often hindered by leading-edge erosion (LEE), caused by factors such as rain, hail, UV radiation, sand, dust, insects, and other airborne particulates. LEE can degrade blade aerodynamics, reduce annual energy production (AEP), increase repair costs, and compromise structural integrity, ultimately leading to higher electricity costs. As a result, enhancing erosion protection, particularly for blade leading edges, is a very active area of research.

Initially, computational fluid dynamics (CFD) analyses using ANSYS Fluent were carried out to evaluate the impact of erosion on lift, drag, and glide ratio. Damage to the leading edge was shown to reduce lift and increase drag, particularly at higher angles of attack. A 500k element 2D model using the 4-equation Transition Shear Stress Transport model (TSST) provided a good balance between computational efficiency and accuracy, while a five million element 3D model ensured grid independency. It was shown that the 2D model had 30 times lower computational cost than the 3D model, making it suitable for developing a digital twin to estimate turbine lifespan efficiently.

The CFD results highlighted the need for effective leading-edge protection. Currently, polyurethane (PU) is widely used for this purpose. This project aimed to enhance PU coatings by incorporating nanomaterial additives, specifically graphene nanoplatelets (GNP), carbon nanotubes (CNT), and fumed nanosilica (SiO_2). After extensive testing, the manufacturing process for the coatings was finalised, followed by physicochemical and mechanical characterizations, including differential scanning calorimetry (DSC), thermogravimetric analysis (TGA), Fourier transform infrared spectroscopy (FTIR), dynamic mechanical analysis (DMA), water contact angle (WCA), scanning electron microscopy (SEM), and energy-dispersive X-ray analysis (EDX).

Mechanical tests assessed properties like Young’s modulus, tensile strength, elongation, tearing resistance, and wear resistance. Accelerated water uptake tests at 22°C, 32°C, and 45°C showed that pure PU had the highest permeability and lowest WCA, while $PU+SiO_2+GNP$ had the lowest permeability.

Ultimately, the results from all the tests were compared, and the most efficient coating was identified. Among the options, $PU+SiO_2+CNT$ exhibited the best performance in terms of mechanical properties and water absorption.

List of Publications

[1] F Zweiri, N. A. Williams, H Hadavinia (2024), Performance of polyurethane and polyurethane nanocomposites modified by graphene, carbon nanotubes and fumed silica when exposed to wet environments, *Polymers and Polymer Composites* 32, 09673911241274092, 2024.

[2] M Carraro, F De Vanna, F Zweiri, E Benini, A Heidari, H Hadavinia (2022), CFD Modeling of Wind Turbine Blades with Eroded Leading Edge, *Fluids*, 7(9), 302.

[3] F Zweiri, F De Vanna, A Heidari, E Benini, N Williams, H Hadavinia (2022), The effect of leading edge erosion on wind turbine blade aerodynamic performance, 3rd International Symposium on Leading Edge Erosion of WT Blades, Technical University Denmark.

Table of Contents

Chapter 1: Introduction

Chapter 2: Literature review

Chapter 3: CFD modelling of undamaged and leading edge eroded blades

Chapter 4: Processing of polyurethane nanocomposites and their physicochemical analyses

Chapter 5: Mechanical testing of pure and nanomodified polyurethane

Chapter 6: Water absorption testing

Chapter 7: Conclusions and recommendations

List of Figures

List of Tables

Nomenclature

Roman letters

C_D	Drag Coefficient
C_f	Friction Coefficient
C_p	Pressure Coefficient
C_L	Lift Coefficient
c	Water Concentration
c_s	Saturation Moisture Content
D	Diffusion Coefficient
E'	Storage Modulus
E''	Loss Modulus
e	Internal energy
f	Frequency
h	Thickness
k	Kinetic Energy
M	Mach Number
m_0	Dry Specimen Mass
m_∞	Saturated Specimen Mass
P	Permeability
P_0	Total Pressure
p	Pressure
S	Sorption Coefficient
T	Temperature
T_0	Total Temperature
t	Time
U	Velocity
y^+	Dimensionless Wall Distance

Greek letters

γ	Turbulent Intermittency/Specific Heat Ratio
$\boldsymbol{\gamma_L^T}$	Water Surface Tension
ΔG_{SL}	Surface Free Energy
Δy	First-off-the-wall Cell Distance

δ	Phase (loss) Angle; Boundary layer thickness
ε_e	Engineering Strain
ε_t	True Strain
θ	Water Contact Angle/Momentum Thickness
μ	Viscosity
ρ	Density
σ_e	Engineering Stress
σ_t	True Stress
ω	Dissipation Rate, Angular velocity

Acronyms

AEP	Annual Energy Production
AoA	Angle of Attack
ASTM	American Society for Testing and Materials
CFD	Computational Fluid Dynamics
CNT	Carbon Nanotubes
DI	Deionised
DSC	Differential Scanning Calorimetry
DMA	Dynamic Mechanical Analysis
EDX	Energy Dispersive X-Ray spectroscopy
EL	Elongation at Break
Re	Reynolds Number
SEM	Scanning Electron Microscopy
FTIR	Fourier Transform Infrared Spectroscopy
GNP	Graphene Nanoplatelets
GR	Glide Ratio
LE	Leading Edge
LEE	Leading Edge Erosion
LEP	Leading Edge Protection
MWCNT	Multi-Walled Carbon Nanotube
O&M	Operation & Maintenance
PU	Polyurethane
PS	Pressure Side
RANS	Reynolds-Averaged Navier–Stokes
RT	Room Temperature

TKE	Turbulent Kinetic Energy
TGA	Thermogravimetric Analysis
TSST	Transition Shear Stress Transport
SA	Spalart–Allmaras
SFE	Surface Free Energy
SS	Suction Side
SST	Shear Stress Transport
UTS	Ultimate Tensile Strength
WCA	Water Contact Angle

Chapter 1: Introduction

1.1 Motivation and Scope

Wind turbine blades are subjected to erosion due to environmental factors such as rain and sand, which damage the leading edge of the blades. Most published research focuses on rain erosion, implying that rain is the predominant causal factor. However, the impact of airborne particles from seawater aerosols or from adverse local environments, such as nearby quarries, greatly increases the levels of leading-edge erosion (LEE). LEE affects almost all wind turbines, reducing their annual energy production (AEP) and lifetime profitability. Erosion can also eventually expose the underlying fibre reinforced polymer (FRP) composite of the blade structure, causing damage and thus reducing the lifespan of wind turbine blades. Hence, developing an efficient protective coating for the blades is important.

The use of polymer coatings has emerged as a promising solution to mitigate erosion on wind turbine blades. These coatings offer enhanced erosion resistance, providing protection against the wear and tear caused by harsh environmental conditions. They also contribute to surface protection, ensuring the longevity and structural integrity of the wind turbine blades. In addition, their weather resistance allows them to withstand various climatic conditions, while their cost-effectiveness makes them a practical option for large-scale use.

The protective coatings for wind turbines must possess several important attributes. Firstly, these coatings should demonstrate strong adhesion between the substrate and the coating, ensuring durability and longevity. In addition, they must be capable of operating over a wide temperature range, providing flexibility in both low and high-temperature environments

The coatings must be able to withstand erosion caused by rain, sand, organic solvents, and hydraulic and lubricating oils. High mechanical strength and flexibility, along with the ability to undergo elastic deformation, are critical for maintaining structural integrity under load.

In addition to these mechanical properties, the coatings should be stable against UV radiation to prevent degradation over time. An efficient application process is also vital, characterized by high production efficiency, quick drying times, and ease of use, allowing for effective coverage of large areas with complex contours. Cost-effectiveness in both materials and processing methods is key to ensuring economic viability.

Finally, the coatings must have a smooth surface finish to reduce drag and possess superhydrophobic and anti-icing properties to enhance their performance in various operational environments. These attributes contribute significantly to the overall effectiveness and reliability of wind turbine protective coatings.

Currently polyurethane, an elastomer, is used as a coating for leading-edge protection. Improving the mechanical properties of polyurethane coating using nano additives is the primary hypothesis of this project. For this project, three nanomaterials — graphene (GNP), carbon nanotubes (CNT), and fumed silica (SiO_2) — either individually or in a combination, are investigated. Graphene is a two-dimensional nanomaterial, with exceptional thermomechanical properties and is favoured for many innovative and practical applications. Carbon nanotubes (CNT) are one-dimensional nanomaterials that possess great thermomechanical properties. Fumed silica (SiO_2) is an amorphous (non-crystalline) polymorph of silicon dioxide, and it has been used as a reinforcing system in elastomers [1].

The outcomes of this research have significant societal and environmental impacts by extending the life of wind turbine blades, which will be a major problem at the end of their lifespan. This project aims to develop novel polyurethane nanocomposite with enhance mechanical properties.

1.2 Problem Definition

The performance of a wind turbine depends on the appropriate design of the blades and the maintenance of their shape and geometrical dimensions during operation and throughout their lifespan. The blades are the most expensive parts of wind turbines and are made from fibre reinforced polymer (FRP) composites. They are prone to erosion due to the environmental conditions such as heat, moisture, ultraviolet radiation, rain, hailstones. It is reported that AEP loss due to LEE is between 3-25%, depending on the extent and location of the damage. For example, Sareen et al. [2] reported that for moderately to heavily eroded blades, an increase in drag by 6-500%, coupled with the loss in lift, led to an AEP loss as high as 25%. They also reported that even a small amount of LEE can result in an AEP loss of approximately 3–5% [2]. Law, et al. [3] studied wind farms and reported an average AEP loss of 1.8% for medium levels of erosion, with the worst affected turbine experiencing an AEP loss of 4.9%.

Power generation by a Horizontal Axis Wind Turbine (HAWT) is directly proportional to the swept area, the circular area covered by the rotating blades. This swept area plays a crucial role in determining the amount of wind energy the turbine can capture and convert into electricity. In essence, the larger the swept area, the greater the volume of wind the blades can intercept, leading to higher potential power output.

The power that can be extracted from the wind by a wind turbine is governed by a key equation in wind energy theory:

$$P = \frac{1}{2} C_P \rho A v^3 = \frac{1}{2} C_P \rho \pi R^2 v^3 \tag{1.1}$$

In this equation P is the power output of the turbine, ρ is the air density, A is the swept area, $A = \pi R^2$ where R is the blade length, v is the wind velocity, and C_P is the power coefficient, which reflects the efficiency of the turbine in converting wind energy into mechanical energy. Equation (1.1) highlights the strong dependence of wind turbine power generation on both the swept area and wind speed, with power increasing in proportion to the swept area and rising with the cube of wind speed. This relationship has driven the trend toward increasing blade length over time to maximize energy capture as shown in Figure 1.1. The most powerful wind turbine is MySE 22MW with a rotor diameter of over 310 m, and nacelle height at 319 m, and swept area of 75,438 m^2, equivalent to 60 Olympic swimming pools. Overall characteristics of the rotor for a 22 MW wind turbine is presented in Table 1.1. However, the tip speed increases linearly with blade radius, and for longer blades, this creates additional challenges, particularly with leading edge erosion (LEE), especially near the outer third of the blade, where the speed is highest.

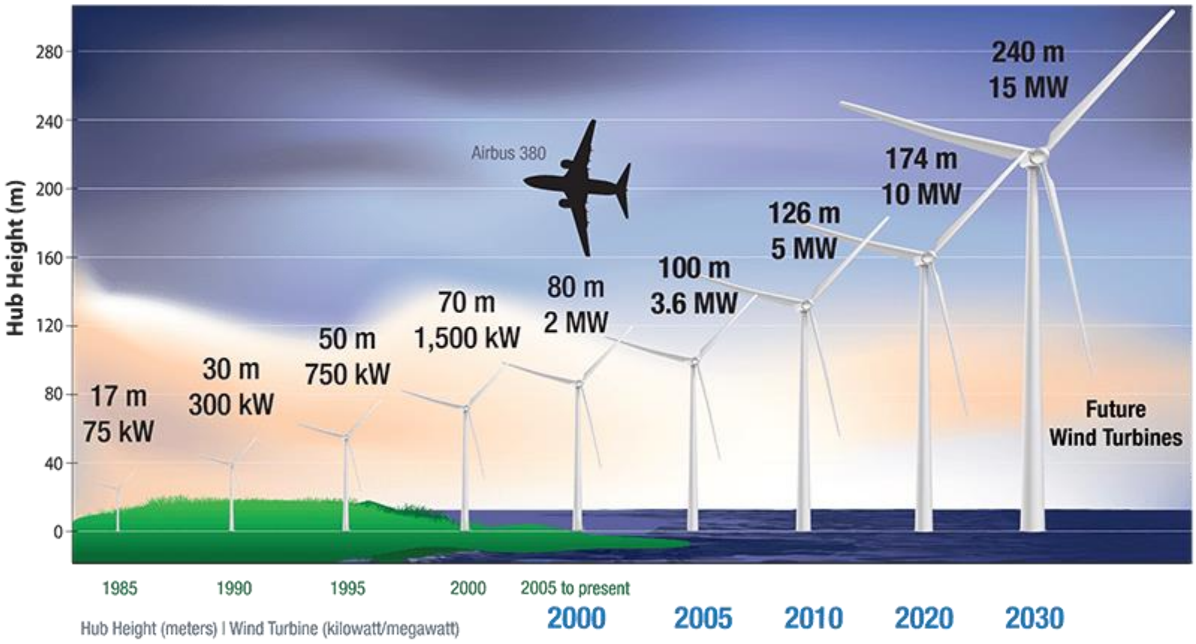

Figure 1.1. Increase in turbine heights and rotor diameter over time.

Table 1.1. Overall characteristics of the rotor for a 22 MW turbine [4].

Quantity	**Value**
Blade mass [t]	82.3
Blade length [m]	137.8
Blade prebend [m]	7.0
Blade precone [deg]	4.0
Blade root diameter [m]	5.8
Blade max. chord [m]	7.2
Max. tip speed [m s^{-1}]	105.0
Tip-speed ratio [-]	9.15
Rated rotor speed [rpm]	7.06
Rated torque [kN m]	31,465.0
Rated thrust [kN]	2,793.0
Rated blade root flapwise moment [kN m]	79,528.0
Aerofoil family	FFA-W3
Minimum aerofoil relative thickness	21%
Blade 1st moment mass* [kg m]	3.033E+06
Blade 2nd moment mass* [kg m^2]	2.052E+08
Blade 1st flapwise mode* [Hz]	0.384
Blade 1st edgewise mode* [Hz]	0.520
Blade 1st torsional mode* [Hz]	3.961

* *Evaluated using HAWCStab2.*

In addition, repairing wind turbines is costly due to various obstacles in reaching their location, such as a mountainous road in highlands and sea water. Hence, it is necessary to minimise repairs, particularly to the blades, as the cost of repair and loss of energy production adversely affect the economics of running the wind turbines. Therefore, maintaining the structural integrity of the wind turbine blades is essential to ensure their efficiency over time and to operate a wind turbine economically. Developing novel coatings for erosion protection of wind turbines blades is of utmost importance.

There are number of challenging issues regarding rain erosion of wind turbine blades, including:

- Tailoring a computational framework for analysing the aerodynamics of eroded blades for high-fidelity digital twin systems.
- Creating barrier properties to restrict water ingress and reduce the impact of water uptake into the blade structure.
- Developing a molecular mechanism within the coating film for energy dissipation upon rain droplet impact.

The drive to enhance the rain erosion resistance of wind turbine blades is driven by the need to ensure the reliability, efficiency, and longevity of wind turbines in demanding environmental conditions. Polymer coatings offer a promising, adaptable, and cost-effective approach to protecting turbine blades from erosion, helping to maintain energy output at optimum level, and reduce operational costs of the wind farms.

1.3 Aim and Objectives

The primary focus of this project is to enhance the mechanical properties of polyurethane elastomer using nano additives materials for the protection of wind turbine blades against rainwater droplet.

To achieve this aim, the following objectives are set:

1. Investigate the effect of eroded blades on lift and drag forces using CFD modelling.
2. Establish a manufacturing method for polyurethane nanocomposites by incorporating GNP, MWCNT and SiO_2 nanoparticles into the polyurethane matrix.
3. Determine the hydrophobicity and damping of each nanocomposite by measuring their water contact angle.
4. Characterise the mechanical properties of the developed nanocomposites
5. Use accelerated water absorption testing to determine their water diffusivity coefficients and mechanical performance after long-term exposure to water.

1.4 Thesis Outline

The structure of the thesis is as follows:

Chapter 2 reviews the background literature on the effects of leading-edge erosion on the annual energy production of wind turbines. It also examines the state-of-the-art of protective coating techniques currently used for turbine blades, the polymer matrices used for these coatings, and the impact of additive nanomaterials on enhancing the mechanical and erosion resistance of polymers and elastomers.

Chapter 3 discusses the impact of leading-edge damage on the aerodynamics performance of wind turbine blades using computational fluid dynamics (CFD). The CFD modelling is conducted for both two- and three-dimensional undamaged and eroded aerofoils. The study also investigates grid independency and the effects of different turbulence models.

Chapter 4 explores the manufacturing process of various coating materials. After establishing the manufacturing methods, the physicochemical characterisation of the coating materials is performed using the Fourier-transform infrared spectroscopy (FTIR), thermogravimetric analysis (TGA), Differential Scanning Calorimetry (DSC), and dynamic mechanical analysis (DMA) techniques. Water contact angle (WCA) and surface free energy are measured. The morphological features of fracture surfaces are studied using scanning electron microscopy (SEM) and optical microscopy.

Chapter 5 delves into the mechanical characterisation of the base polyurethane (PU) matrix and five nanomodifed PU nanocomposites. Tensile, tearing, and wear tests were conducted, and the results of these tests are presented. The morphological features of the fracture surfaces of tensile and tear specimens are studied using SEM and Energy Dispersive X-ray (EDX) spectroscopy.

Chapter 6 investigates the accelerated water absorption of pure PU and the five modified PU nanocomposites at three different temperatures: 22°C, 32°C and 45°C. The applicability of Fickian law is explored and thermal diffusivity and permeability for each coating material are reported.

Chapter 7 summarises the outcome of this project and provides recommendations for future work.

Chapter 2: Literature review

2.1. Introduction

Leading edge erosion of wind turbine blades is a formidable challenge for the wind turbine industry as it affects their performance and structural integrity. Various studies have examined the mechanisms underlying this phenomenon, ranging from the erosive impact of raindrops to the abrasive action of airborne particles. Understanding these mechanisms is essential in determining mitigating strategies to safeguard continuous wind turbine operation throughout its design lifespan.

One way to protect turbine blades from erosion is by selecting durable and cost-effective coating materials. Several researchers have proposed coatings and suitable protection strategies to protect blades from the impact of rain and particles [5]. Numerical simulations have emerged over the years as vital tools for studying and understanding the dynamics of rain erosion and assessing its effects on wind turbine blades [6]. Computational fluid dynamics (CFD) alongside the finite element method (FEM) have been utilized to replicate real-world performance of the blades, explore different scenarios, and evaluate the effectiveness of protective measures against rain and particles erosion [7].

In this chapter the background literature was explored to identify the effects of LEE on the annual energy production loss of wind turbines and examines the protective coating techniques currently used for turbine blades, the polymer matrices employed for these coatings, and the impact of additive nanomaterials on enhancing the mechanical and erosion resistance of polymers and elastomers. Finally, the research gaps are identified, and a summary of finding from the literature is presented, which is relevant to further work in this project.

2.2. Effects of leading-edge erosion on the annual energy production of wind turbines

The energy production of wind turbines is proportional to its swept area, and by continuous enhancement in materials properties and design during the last 30 years, wind turbine industries have effortlessly increased the size of the wind turbine. Currently, the biggest installed wind turbine is Siemens Gamesa SG 14-222 DD with nominal rated power of 14MW and rotor diameter of 222m, while a single General Electric Haliade-X turbine has a nominal capacity of 12-14.7MW with rotor diameter of 220m [8].

The increased size of the blades resulted to an increase in tip speeds, reaching to 80 m/s to 110 m/s at the biggest wind turbines [9]. At such speed, the impact of rain droplet on the blades leading-edge is significant, which could cause LEE.

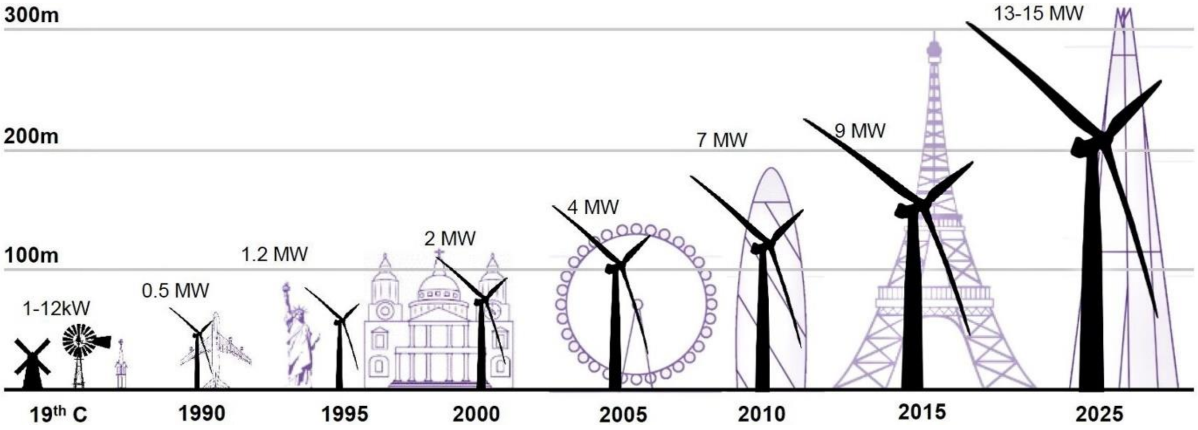

Figure 2.1. Evolution of wind turbine heights and output [10].

The erosion of the blade deteriorates the aerodynamics performance of the blade, and adversely affect the lift and drag forces and ultimately, reduces energy production [2]. Özçakmak et al. [11] showed that there was a 4.3 % reduction in the AEP for a severe erosion case, which was spanned the last third of the blade. It is reported that by using laser scanning and machine learning prediction, AEP losses varied from 0.3 to 0.8% of the nominal AEP [12]. Campobasso, et al. used the NREL AeroDyn blade element momentum theory code [13], and by making use of a variant of the NREL 5MW turbine obtained by replacing the NACA 64-618 with the DU 96-W-180 aerofoil, showed that an AEP loss between 2.1% and 2.6%, based on both experiments and simulations, can occur. Law, et al. studied wind farms and reported an average AEP loss of 1.8% for medium levels of erosion, with the worst affected turbine experiencing an AEP loss of 4.9% [3]. Sandia National Laboratories estimated the AEP losses to be between 5–8% [14]. Experimental [15] and numerical [16] studies reported AEP losses of 4%, increasing to 6% when top coat on the leading edge is damaged [17].

The blades is protected with polymeric coatings against erosion, either applied in-mould or post-mould. However, the coating can start to show signs of degradation after 2–5 years while the lifetime of wind turbines is expected to be at least 25 years.

2.3. Erosion classifications

Damages caused by erosion can occur on any part of the wind turbine blade, but they are particularly significant and noticeable at the blade's leading edge [7]. *Figure* 2.2 demonstrate an actual LEE on a blade. The variety of the damage intensity mostly occurs because of the linear speed experienced at various radii.

Various authors have suggested different criteria for categorising the severity of LEE. Eisenberg, et al. [7] divided the severity of erosion damage into the following four levels:

- Level 1: Minor holes are established in the blade coating.
- Level 2: Although the coating is not completely removed, the underlying epoxy of the blade structure starts to become apparent at irregular intervals.
- Level 3 & 4: The epoxy of the structure becomes entirely exposed to the surroundings due to the coating being completely removed, leaving different scale of damage on the blade.

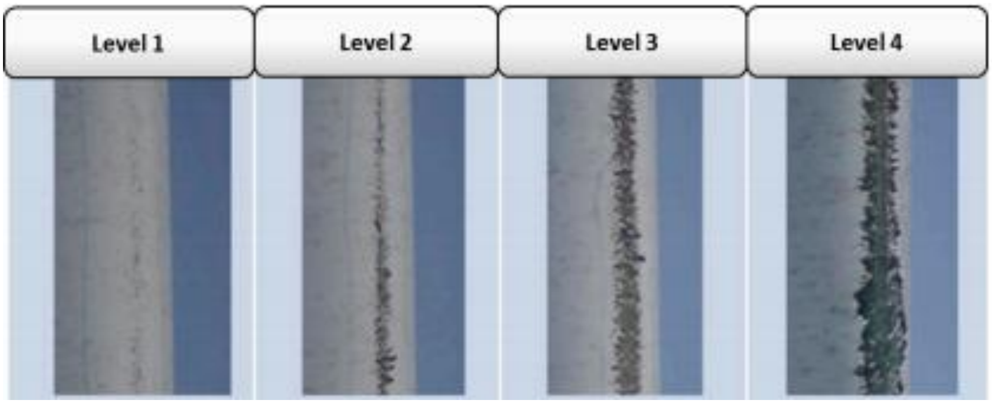

Figure 2.2. Leading edge erosion damage level at various radii [7]

The tip of a wind turbine blade suffers the most severe erosion in comparison to other parts of the blade. This is because the blade's linear speed, $v = r\omega$, is maximum at the tip [18]. Such losses of the coating and structural materials can occur within only two years of service, eventually leading to rapid inefficiency, decreased durability, reduced power generation, and expensive repair costs.

In a similar study, Law and Koutsos [19] inspected 18 wind farms in the UK after around two years of service to evaluate the severity of leading edge erosion on wind turbine blades. They used a grading system to indicate the erosion level on the blades, as shown in *Figure* 2.3.

(a) Grade 0 (b) Grade 1

(c) Grade 2 (d) Grade 3

Figure 2.3. (a) No erosion, (b) Minor erosion, (c) Larger erosion, and (d) Wider erosion (Adapted from [19])

According to *Figure* 2.3, the severity of degradation of the blade is categorised from 0 to 3:

- Grade 0: The coating material of the blade is in great condition with no erosion present.
- Grade 1: The coating material starts to show minor signs of damage with small areas of erosion visible.
- Grade 2: The coating shows clear signs of significant erosion in long patches, with large areas affected.
- Grade 3: The coating is almost entirely eroded in wide areas, exposing the blade surface to the surroundings.

Bartolome, and Teuwen [20] reported the degree of severity of LEE on a blade using *Figure* 2.4. The erosion progresses through the following stages:

- Stage A: Pitting effects are distributed coarsely throughout the blade surface.
- Stage B: Cracks start forming.
- Stage C: When cracks form at high concentrations, crater begins to manifest, leading to severe erosion.
- Stage D: Complete exposure of the laminates occurs due to the removal of the coating material, resulting in delamination.

It is crucial to evaluate the potential of new materials for erosion protection. Key parameters that affect the performance of erosion-resistant coatings include resistance to abrasive wear, damping properties, fracture energy, rebound resilience, and the mechanical loss factor which quantifies the energy lost within a material when subjected to cyclic stress.

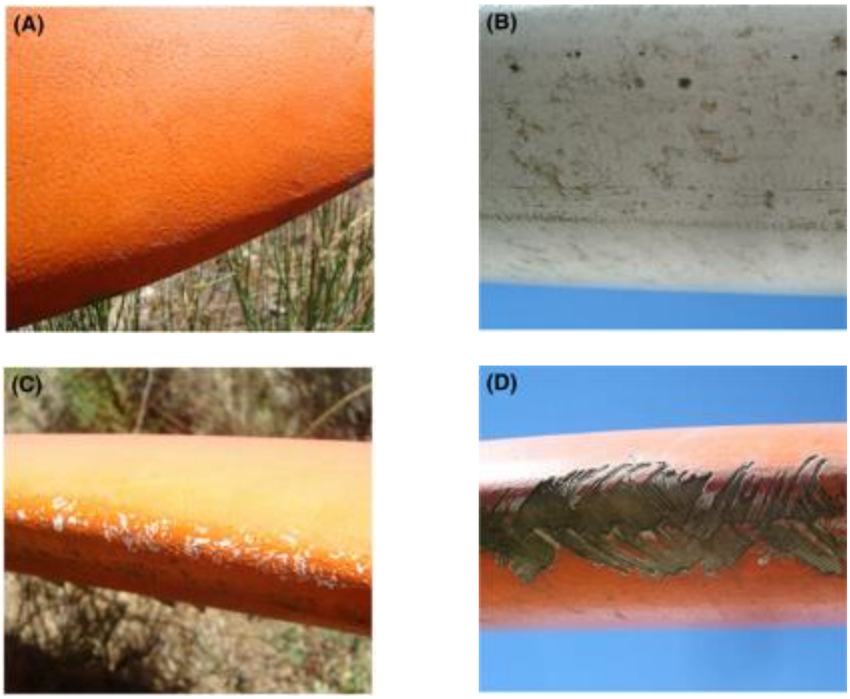

Figure 2.4. (A) Pitting, (B) Cracking; (C) Cratering, and (D) Delamination, adapted from [20]

2.4. Erosion Mechanism

Tendencies in wind energy development include the creation of large and extra-large wind turbines, often located far from coast (e.g., floating wind turbines), and expansion into new regions such as Northern Regions, Northern Sea, and monsoon areas with severe weather conditions. These new developments share a common challenge: They make the wind turbine maintenance more difficult and expensive, requiring more frequent repairs due to high mechanical and environmental loads from stronger sea wind, icing, monsoon rains, and higher rotational speeds. [6]

Surface erosion of the blades is the only damage typically observed during the first year of operation after the installation. It remains the most critical damage in the first five years of service for wind turbines in Europe, along with lightning strikes and manufacturing defects. It is also the most expensive degradation mechanism due to the frequency of required repairs [21]. Minor surface damage can cost up to 12 times as much as major structural damage. *Figure* 2.5 shows how wind turbine erosion occurs due to rain droplet impacts.

Many coatings and leading edge protection systems are available on the market, including ProBlade Collision Barrier by LM Wind Power, PowerEdge® Care Leading Edge Protection by Siemens, and products from 3M, Bergolin, Duromar, Enercon, Belzona, PolyTech (Ever Lasting Leading Edge soft shell ELLE), and Hempel (Hempablade Edge 171), among others. Despite these options, the problem has not been fully resolved, especially for larger blades with higher tip speeds located in regions with frequent intensive rain and hail.

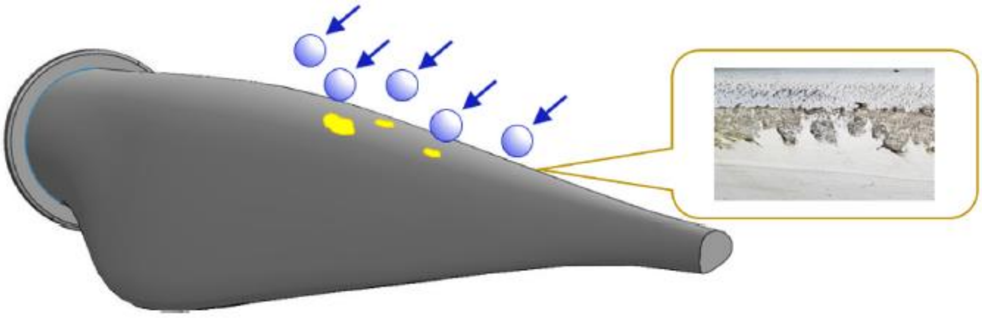

Figure 2.5. Schema: Erosion of wind turbine blades due to rain droplet impact. (adapted from [6])

The analysis of erosion damage caused by raindrop impacts primarily relies on the static concept of direct impact on a rigid surface. However, evidence indicates that the damage is a dynamic event involving the propagation of shock waves, as shown in *Figure* 2.6. When a water droplet strikes the surface at a normal angle, it creates two wave fronts: a longitudinal compressional normal stress wave and a transverse shear wave. A third wave, the Rayleigh wave, arises from the deformation of the droplet itself. This wave is confined to the surface of the target and contains about two-thirds of the impact energy [22].

The pressure generated upon droplet impact, known as water-hammer pressure, varies depending on the acoustic properties of both the target material and the liquid [23]. The peak pressure does not occur at the epicentre of impact at the moment of first contact. Instead, it is delayed and occurs in a ring around the midpoint, where the initial shockwave generated by the impact reaches the edge of the contact circle [24]. Maximum shear stresses are observed at these radial locations and have a very short duration compared to the central compressional pressures. The duration of the impact pressure on the surface is directly related to the radius of the droplet. Erosion failure can be initiated by a local imbalance of tensile and shear stresses in regions that may lie outside the direct impact area [22].

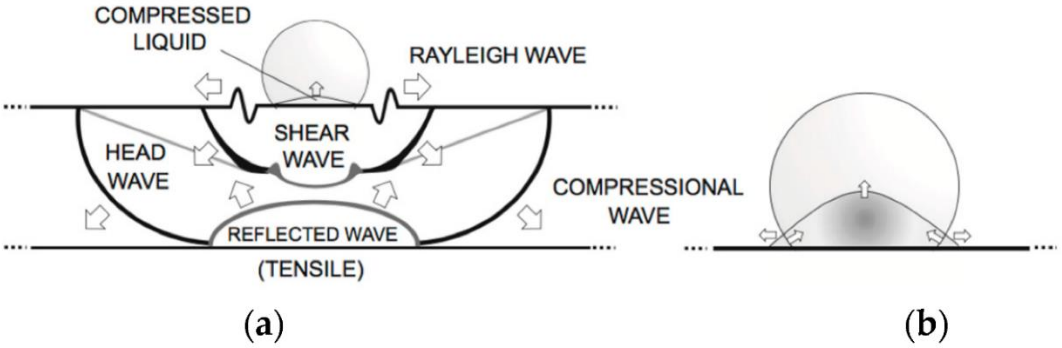

Figure 2.6. Liquid droplet–solid surface impact interaction, showing shockwave behaviour (from [22]). (a) the three waves that develop following the droplet collision, (b) the lateral jetting upon movement of the contact boundary ahead of the shock wave in the drop initiating a release wave across the solid surface.

2.4.1. Computational modelling of wind-turbine blade erosion

Leading-edge erosion results from repeated impacts by raindrops and hailstones. Each impact generates contact pressure on the surface and initiate wave propagation in the protective layers. Over time, this process progresses from initial damage to materials degradation, fatigue, coating cracking, debonding, cracks in the composite and surface roughening. *Figure* 2.7 provides a schematic of these key processes.

Computational modelling of wind-turbine blade erosion can predict blade erosion and optimize blade protection. Rain erosion is a complex phenomenon, influenced by numerous physical mechanisms, necessitating the use of various modelling tools. The deformation and impact of raindrops can be described using fluid dynamics and contact mechanics.

In numerical modelling of materials response to rain impacts, multiple, time-dependent raindrop impacts are simulated using stochastic rain scenario models [25]. The droplet impacts generate stress-wave propagation in the blade coatings and laminate, which can be simulated using solid mechanics and dynamics. As these stress waves travel through the materials and reflect at interfaces, they cause deformation of polymer chains. Over months and years, this repeated deformation leads to fatigue damage in both the coating materials and the interfaces.

As stress waves propagates through the coatings, part of the stress energy is dissipated through internal friction and heating of the polymer coatings. These effects are described by the theory of viscoelasticity.

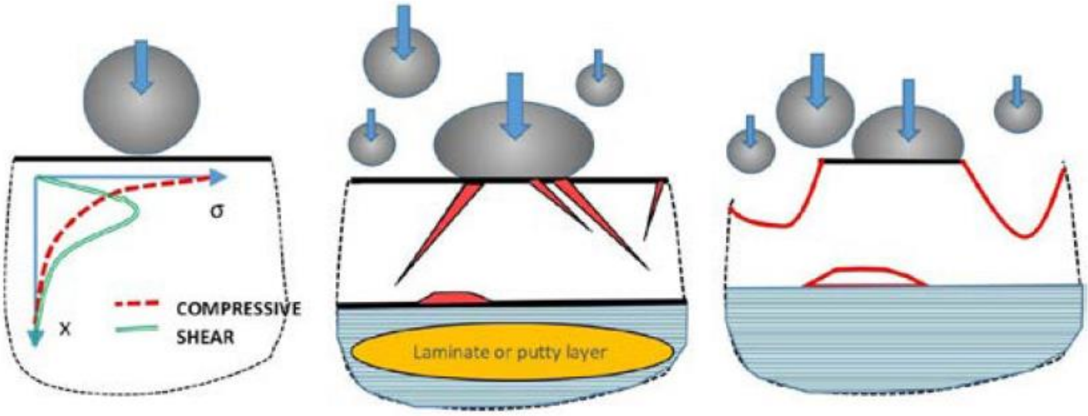

Figure 2.7. Schematic of the erosion of coating: (left) impact, stress state and wave propagation, (middle) formation of cracks and debonding, (right) material removal and roughening, Adapted from [26]

Fraisse et al. [27] developed a FEA model in ABAQUS and studied the impact of a water droplet on a resin-coated laminate and the resulting the internal transient stresses. *Figure* 2.8 shows the stages of droplet impact on the surface and stress distributions within the material. The target laminate was modelled using the Eulerian domain, while the water droplet was modelled using the Lagrangian domain, allowing the material to move through the mesh. Observations showed that during the initial stage of the impact, the highest stress was localised beneath the contact surface. In the quasi-static stage, the high-stress region formed deeper under the surface.

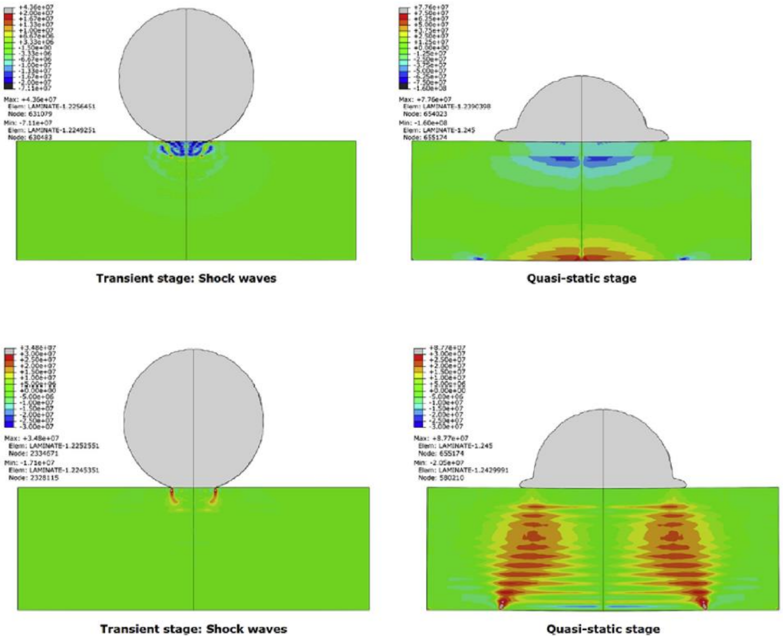

Figure 2.8. Deformation of droplet and stresses in the laminate under loading (adapted from [27])

The effect of viscoelasticity of the coating material on the stress field under liquid impact was studied numerically [6]. A computational finite element model of liquid drop impact was implemented using the Smoothed Particle Hydrodynamics (SPH) method. *Figure* 2.9 compares the stress fields in hyper-viscoelastic and elastic coatings, showing maximum von Mises stress over time (a) and von Mises stress distributions (b). For purely elastic coatings, deformation and strain levels are lower, and the high stress area is localized near the impact contact area. In contrast, for viscoelastic coatings, the high-stress region is located beneath the surface. This demonstrates that the viscoelastic behaviour of coatings alters the stress distribution and the damage mechanisms of the coatings.

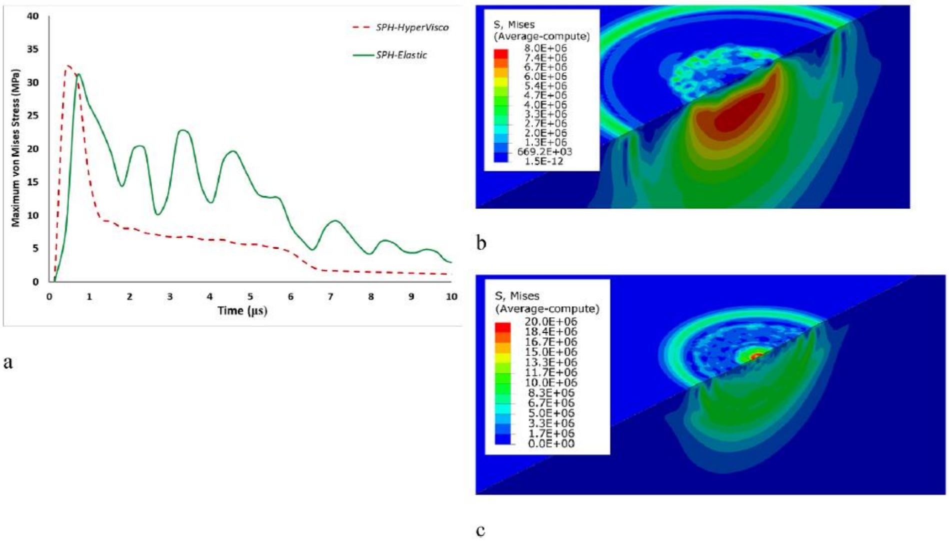

Figure 2.9. Comparison of hyper-viscoelastic and elastic coatings: Maximum Mises versus time (a) and stress fields for viscoelastic (b) and elastic coatings (c) under liquid impact (adapted from [6])

2.4.2. Polyurethane coating

Segmented polyurethanes (PUs) are highly versatile materials with extensive applications across various fields, including textile fibres, coatings, adhesives, biomaterials, membranes, damping and energy absorbing materials, and anti-erosion coatings. PUs are composed of alternating “soft” and “hard” segments that are chemically bonded along a macromolecular backbone, as shown in *Figure* 2.10. The soft segments typically have glass transition temperatures (Tg) significantly below ambient temperature, offering elasticity akin to elastomeric springs under normal conditions. In contrast, the hard segments which are relatively small (approximately 150 nm in length) and formed by the reaction of diisocyanates with diol or diamine chain extenders, features strongly hydrogen bonded urethane, urea and urethaneurea groups. These hard segments generally exhibit Tg well above the operational temperature range, behaving like relatively short rigid units depending on their specific chemical composition and structures.

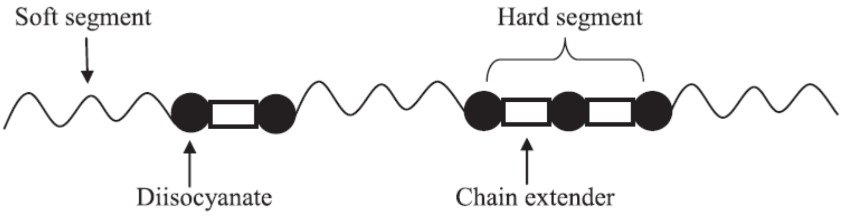

Figure 2.10. Schematic representation of a segmented TPU (adapted from [28])

Increasing the molecular weight of the flexible block in PU has a noticeable impact on its properties. Specifically, higher molecular weight leads to decreased tensile strength, modulus, hardness, and tear strength as indicated in [20]. Conversely, abrasion resistance tends to improve under these conditions. Chemical cross linking typically accompanies an increase in tensile strength, modulus of elasticity, and elongation at break. Higher proportion of hard segments significantly enhances the Young’s modulus, tensile strength, yield strength, and hysteresis behaviour during initial cycle [36].

The final structure, morphology and properties of PUs are influenced by numerous chemical, physical and structural factors. These include:

(i) The polymerization method used, and synthesis condition employed.

(ii)The chemical structure, hydrogen bond strength, structural symmetry, average chain length, and length distribution of the hard segments in the copolymer,

(iii) The chemical structure, solubility parameter, and molecular weight of the soft segments in the copolymer,

(iv) The extent of competitive intermolecular interactions, such as hydrogen bonding between hard-hard and hard-soft segments, and considerations related to their packing and crystallization.

(v) The composition of the copolymer or the volume fraction of hard and soft segments within it.

The performance of PU coating in erosion protection hinges significantly on their viscoelastic properties and damping of coating materials [29]. These factors collectively dictate the effectiveness and durability of PU coatings in practical applications.

New advancement in materials for future applications include multilayer coatings, reinforced coatings, and interpenetrating polymer networks. Multilayer coatings, featuring alternating layers of stiff and ductile materials (see Figure 2.11), are integral to various protective systems. Examples include multilayer polyurethane/polyurea coatings, polycarbonate diol-polyurethane-based coatings, polymer-metal laminates, and electroformed metallic solutions like nickel-cobalt alloys used for leading-edge protection.

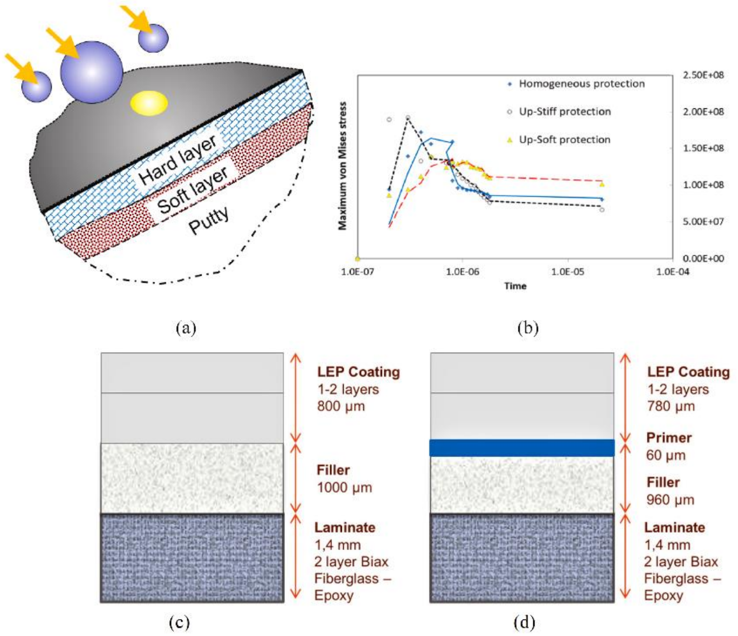

Figure 2.11. (a) Multilayer coating (upper stiff layer, lower soft layer), (b)maximum von Mises stress plotted versus the time [6], (c) LEP coating with an intermediate filler layer; (d) additional primer layer included to improve adhesion to the substrate [9].

Reinforced coatings incorporate microscale and nanoscale particles such as graphene (GNPs), carbon nanotubes (CNTs), and silica within the polymer matrices. These particles enhance energy dissipation, effectively mitigating damage and improving durability.

Interpenetrating polymer networks (IPN) are a polymer made up of two or more networks that are partly intertwined on a molecular scale but not chemically bonded to each other. IPN enhance the damping properties of PU by integrating epoxy components. This results in polyurethane/epoxy IPNs, which offer superior damping characteristics compared to traditional materials. These innovations represent significant strides in enhancing the performance and functionality of protective and damping materials for diverse applications.

2.4.3. Additive nanomaterials for coatings

Enhancing the mechanical properties and erosion resistance of polyurethanes can be achieved by using additive nanomaterials. These nanomaterials improve the damping effect of the coatings, thanks to the viscoelasticity of the material, which leads to attenuation, dispersion, and scattering of stress waves. Inhomogeneities, mode conversion at interfaces, and the redirection and conversion of deformation energy into heat through molecular relaxation processes also contribute to this improvement.

As discussed in Section 2.4, the impact of raindrops on the blade surface generates various stress waves. The dissipation of these waves in composite materials is facilitated by the viscoelastic nature of the resin and the scattering on inclusions. At high frequencies, the wavelength becomes comparable to the size of the reinforcements, allowing particles to influence wave propagation. Multiple scattering of waves on particles results in frequency-dependent changes in the velocity and attenuation of coherent waves [30].

To explore the potential of structural modifications in anti-erosion coating materials, a series of computational studies were conducted [30]. *Figure* 2.12 shows three damping mechanisms: (a) viscoelasticity, (b) disc-shaped particle reinforcement, and (c) pulp-induced damping from multiple elastic fibres.

This study examined the effect of discs and fibre pulp reinforcements on stress wave propagation, wave scattering, and damping in the coating under rain droplet impact. The results showed that coatings embedded with a network of stiff elastic curved fibres exhibited enhanced damping and energy dissipation, leading to improved erosion protection. The embedded particles introduced additional wave scattering mechanisms, and significant viscoelastic energy dissipation was observed in highly stressed regions between closely located fibres.

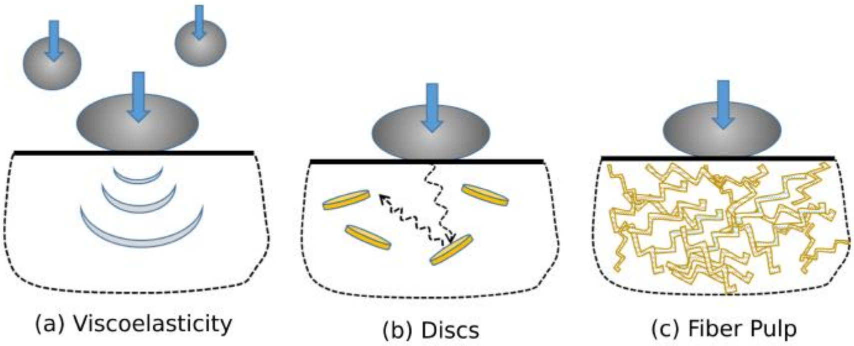

Figure 2.12. Considered damping mechanisms: (a) viscoelastic damping, (b) disc particle reinforcement induced damping, (c) fibre pulp enhanced damping. (adapted from [30])

Consequently, coating with a higher volume fraction of fibres are expected to dissipate the impact energy of a rain droplet more quickly than pure PU coatings. The scattering of stresses and increased damping properties enhance the erosion resistance of the coatings. Therefore, fibres or similar particles have significant potential in developing improved LEE solutions [30].

Pham, et al. [31] used a solution blending process to produce polyurethane/graphene (PU/G) composite for high mechanical and anti-corrosive coatings. In these composites, graphene flakes functioned both as structural components and as corrosion inhibitor, enhancing the mechanical and anti-corrosive properties of PU/G coatings.

As shown in *Figure* 2.13, the preparation involved mixing polyol with HDI based modified polyisocyanate coronate HX (C-HX), xylene, and graphene fakes using a mechanical propeller stirrer at 1200 rpm for 30 minutes to form PU/G composites. Finally, the composites were sonicated for 30 mins.

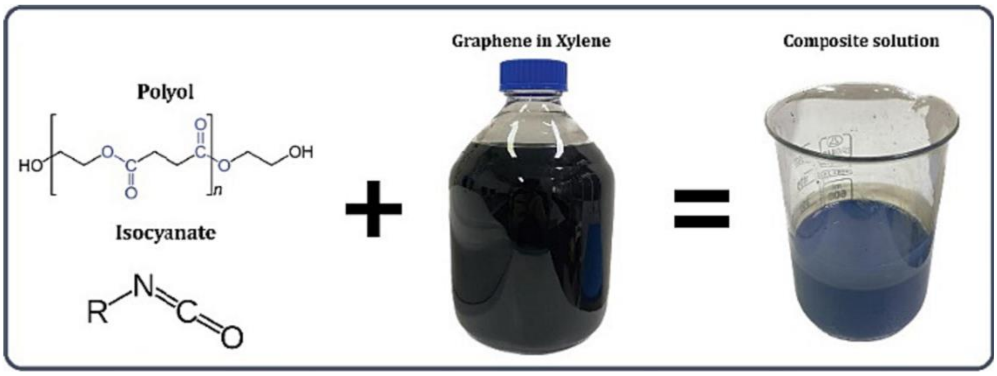

Figure 2.13. Scheme of solution blending of PU/G composites. Adapted from [31]

The combination of graphene nanoplatelet (GNP), graphene oxide (GO), and carbon nanotubes (CNTs) for polymer reinforcement has been explored previously. Verma, et al. [32] acid-treated CNTs to introduce oxygen-containing groups, such as carboxyl groups and hydroxyl groups, to the CNT tips and sidewalls. This treatment resulted in a fine dispersion of functionalised CNT (FCNT) in water. They then mixed GO with FCNT in an aqueous solution, where the oxygen functionalities on the GO basal planes acted as surfactant, allowing strong interactions with FCNT.

Figure 2.14 shows the synthesis procedure for creating the graphene nanoplatelets with CNT. In addition to the π-π interaction between the FCNTs surface and the GO basal planes, hydrogen bonds formed between GO and FCNT, causing FCNT to strongly adsorb to the basal planes of GO sheets [33]. Subsequently, the chemical reduction of GO was performed in the presence of FCNTs using hydrazine hydrate to obtain GCNT hybrid.

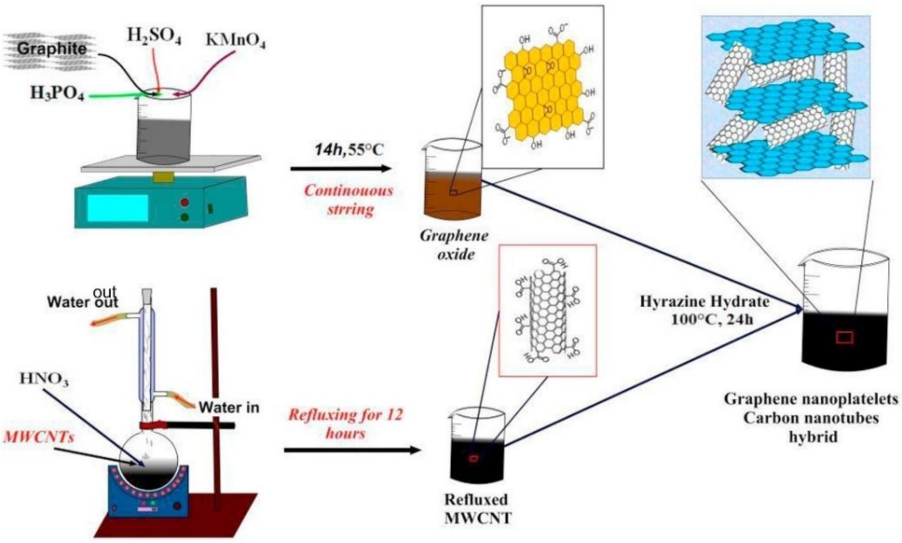

Figure 2.14. Schematic representation of the synthesis procedure adopted for synthesizing graphene nanoplatelets-CNT hybrid, adapted from [32]

The mechanical properties of polyurethane and modified PU elastomers with carbon nanotubes (CNTs) and graphene have been extensively investigated by Nadvidfar and Trabzon [34]. They combined graphene nanoplatelets (GNPs) and multi-walled carbon nanotubes (MWCNTs) with PU to study their synergistic effect on the thermal conductivity of the resulting nanocomposites. Pourmohammadi et al. [35] prepared composites of CNT and CNT-halloysite (HNT) hybrids at different loading with polyurethane through melt mixing. They observed that adding CNT resulted in greater phase separation, while the hybrid samples formed a network of nanoparticles.

In the work conducted by Legge, et al. [36] a commercially available powder containing few-layer graphene (FLG) flakes was characterized before and after plasma or chemical functionalization with nitrogen or oxygen species. Various measurement techniques, including tip-enhanced Raman spectroscopy (TERS), time-of-flight secondary ion mass spectrometry (ToF-SIMS), and NanoSIMS, were used to examine the physical and chemical changes in the graphene material at both the micro- and nanoscale. These analyses revealed the location of the defects (edge versus basal plane) and variations in the level of functionalization.

PU-GNP composites were then produced, and the dispersion of the GNPs in the matrix was visualized using ToF-SIMS. Mechanical tests compared the properties of the original polyurethane with the nanocomposites after adding both unfunctionalized and plasma-O graphene nanoplatelets. Stress–strain plots for each sample type are shown in *Figure* 2.15a. Both PU composites samples demonstrated improved mechanical properties compared to pure PU, achieving higher UTS (*Figure* 2.15c) and elongation at break (*Figure* 2.15d), while the initial elastic modulus remained unaffected (*Figure* 2.15b).

The unfunctionalized GNP showed a slightly larger improvement than the functionalized one; but both performed better than pure PU. The commercially available GNPs (unfunctionalized and plasma-O) showed substantial improvement in UTS (85% and 75%, respectively) and EL (54% and 40%, respectively) indicating their potential for reinforcing PU [36].

However, despite the improved dispersion observed in ToF-SIMS results after the functionalization process, the UTS values were similar for both types of GNPs, and the EL slightly decreased for the functionalized material. This discrepancy is likely due to the introduction of defects into the basal plane of some flakes during functionalisation. These defects may offset the benefit of improved dispersion by decreasing the mechanical robustness of the nanofiller [36].

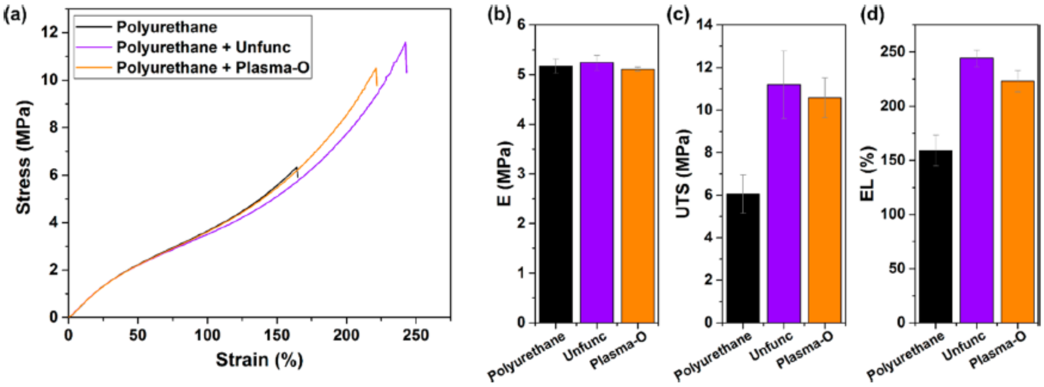

Figure 2.15. Mechanical testing of polyurethane, polyurethane with the addition of the unfunctionalized graphene, and polyurethane with the addition of the functionalized, plasma-O graphene. (a) The stress−strain curve for representative specimens taken from the samples tested. Mean results for the (b) initial elastic modulus (E), (c) ultimate tensile stress (UTS), and (d) elongation at break (EL) determined from 5 individual tests (adopted from [36].

Ma and Zhang [37] conducted a systematic review analysing the potential of using CNTs to develop polymer-based nanocomposites for wind turbine blades, leveraging their distinctive functional and structural features. They showed that CNT/polymer nanocomposites, whether used as blade coatings or as a matrix for fibre-reinforced polymer composite, can enhance strength and improve erosion resistance. However, they also identified several challenges in using CNT for wind turbine applications:

- Poor CNT dispersion and interfacial interaction with polymer matrix: This can lead to the deterioration of CNT/polymer composite materials. The issue may be addressed by functionalising CNTs to improve interfacial adherence with polymers and enhancing their solubility and dispersion in polymers.
- High cost of CNTs: The cost of CNTs can limit their use in FRP structures for blades. This challenge may be mitigated by seeking lower cost alternatives, such as hybridizing the CNTs with more affordable fillers (e.g. clay or silica) to reduce the overall cost of CNT/polymer nanocomposites.

2.5. Aerodynamics Analysis of wind turbines

2.5.1. Aerofoils parameters

Figure 2.16 depict various parameters of an aerofoils which will be used in Chapter 3. Important parameters are angle of attack (AoA), which is the angle between the relative wind velocity and the chord line, chord length (c), leading edge and trailing edge.

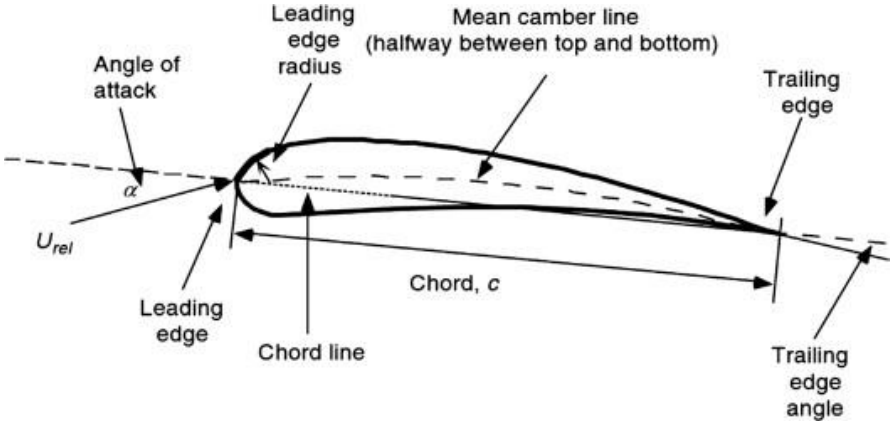

Figure 2.16. Aerofoil design parameters [38]

2.5.2. Scaling the governing equations

All CFD modelling presented in Chapter 3 is on scaled models of the wind turbine blade. In this section, we explore the conditions under which the flow on an scaled model can be representative of a real blade.

For a 2D incompressible flow, the continuity and Navier-Stokes equations are:

$$u_x + v_y = 0 \tag{2.1}$$

$$u_t + uu_x + vu_y = -\frac{1}{\rho}p_x + \nu(u_{xx} + u_{yy}) \tag{2.2}$$

$$v_t + uv_x + vv_y = -\frac{1}{\rho}p_y + \nu\left(v_{xx} + v_{yy}\right) - g \tag{2.3}$$

The independent variables for the flow are x, y and t; the dependent variables are velocities u, v and pressure p. The constant gravitational acceleration in the y-direction is g, and the density ρ and viscosity ν are both assumed to be constant (or, alternatively, g, ρ and μ can be used).

By transforming the Navier-Stokes equations of motion to dimensionless form, a set of dimensionless parameters associated with fluid flow can be identified, which completely characterises the behaviour of a system [39]. Eqs. (2.1) to (2.3) can be expressed in dimensionless form as

$$u_x + v_y = 0 \tag{2.4}$$

$$u_t + uu_x + vu_y = -p_x + \frac{1}{Re}(u_{xx} + u_{yy}) \tag{2.5}$$

$$v_t + uv_x + vv_y = -p_y + \frac{1}{Re}\left(v_{xx} + v_{yy}\right) - \frac{1}{Fr^2} \tag{2.6}$$

The Reynolds number and the Froude number are defined as $Re = \frac{UL}{\nu}$, and $Fr = \frac{U}{\sqrt{gH}}$, respectively, where the kinematic viscosity ν = μ/ρ. Equations (2.4) to (2.6) are dimensionless, and their solutions depend only on the parameters Re and Fr.

Therefore, if flow fields associated with two geometrically similar objects have the same Reynolds and Froude numbers, they will have the same scaled velocity and pressure fields. In turn, from the equations of motion, this implies that they will exhibit the same scaled forces at all locations in the flow. For geometrically similar objects, the unscaled forces will be in a constant ratio at all corresponding points of the two flow fields, achieving dynamic similarity. Hence, for flows in or around geometrically similar objects, dynamic similarity is achieved if all dimensionless parameters associated with these flows are the same.

2.5.3. Lift, drag, and pressure coefficients

In an aerofoil lift and drag coefficients are determined for a range of angles of attack and Reynolds numbers. The lift and drag coefficients are defined by the following equation:

$$C_l = \frac{L}{l/2\rho U^2 c} \tag{2.7}$$

$$C_d = \frac{D}{l/2\rho U^2 c} \tag{2.8}$$

Where L is the lift force, D is the drag force, ρ is the air density, U is the free stream velocity, and c is the chord length of the aerofoil. The definition of pressure coefficient for an aerofoil flow is:

$$C_P = \frac{p - p_\infty}{l/2\rho U^2} \tag{2.9}$$

2.5.4. CFD modelling of leading-edge defects

Gharali & Johnson [40] investigated the lift reduction at two erosion lengths, 4%c and 14%c under dynamic conditions, where c represent the chord length of the aerofoil and the erosion length denotes the eroded portion along the chord from the leading edge. Wang, et al. [41] examined the impact of various defect cavity lengths (*h*) and thicknesses (*t)* on the aerodynamic coefficients and flow pattern of an aerofoil, as shown in *Figure* 2.17. Their study included defect lengths from 0.5%c to 14%c and defect thicknesses from 6%tc to 25%tc, determining the critical length/thickness ratio of defect affecting the aerodynamic performance.

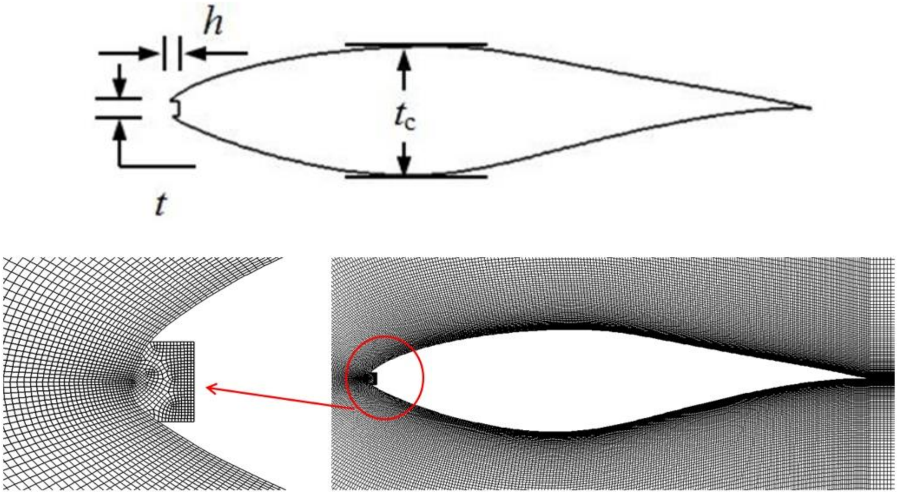

Figure 2.17. The leading edge defect model for S809 aerofoil, adapted from [41]

Figure 2.18 shows the results of the lift/drag ratio versus defect length/thickness for two angles of attacks. The C_l/C_d ratio varies widely from approximately 10 to 70, but it stabilises when the defect length/thickness ratio exceeds 0.5. Consequently, the critical defect length/thickness ratio (h/t_c) for this kind of leading edge defect is 0.5, beyond which the aerodynamics remains unaffected.

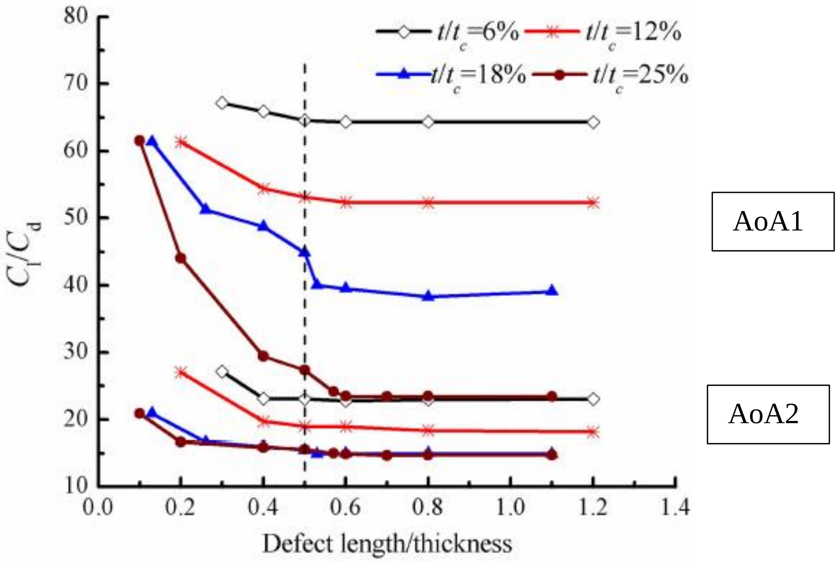

Figure 2.18. Lift/drag coefficients for aerofoils with various defect length/thickness [41]

Ge et al. [42] studied the LEE for the following two cases:

1. Surface concaved deep defects (SDD) on the aerofoil leading edge which represent the serious damage caused by severe impact or erosion. Such defects are more concentrated in distribution, with the equivalent depth of $h \sim t$; here, *t* represents the defect opening size, h=s/t indicates the defect equivalent depth, and *s* represents the defect area.

2. Surface distributed shallow defects (SSD) on the aerofoil leading edge, which is a kind of blade surface damage caused by slight erosion, usually composed of small shallow pits distributed on the leading surface, with $h \ll r$; here, the defect range *r* is defined by the length of defect along the aerofoil profile, and the corresponding equivalent depth is defined as $h = s/r$.

Both defects on the aerofoil leading edge are shown in *Figure* 2.19. They investigated both static and dynamic aerodynamic performances using the shear stress transport (SST) k-ω transition turbulence model (TSST), focusing on key parameters such as the defect range, shape, and equivalent depth.

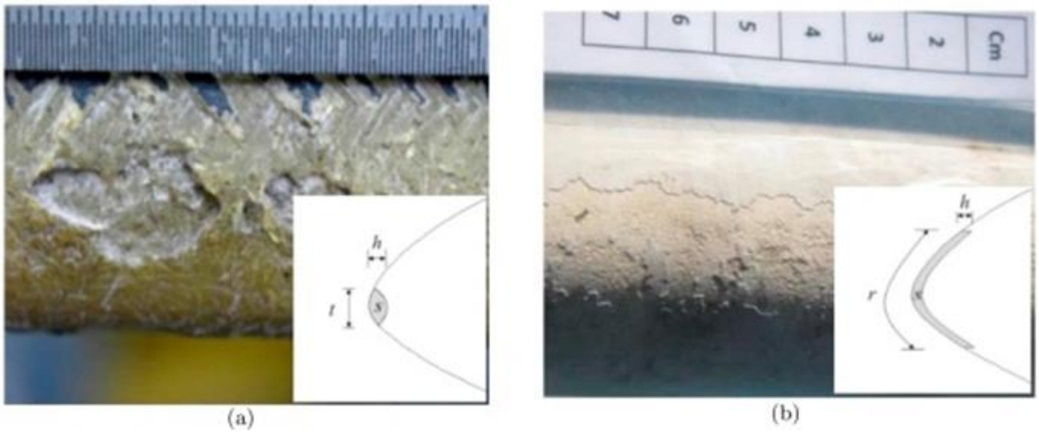

(a) (b)

Figure 2.19. Two types of surface defects on leading edge: (a) SDD and (b) SSD [42]

They calculated the glide ratio (C_l/C_d) versus AoAs for various defect shapes shown in *Figure 2.20*. The results of eroded aerofoil with SDD defect and smooth aerofoil are shown in *Figure* 2.21, where $t^* = t/t_a$ and $h^* = h/c$. It can be seen that both coefficients for an aerofoil with leading edge SDD defect are relatively insensitive to the defect shape. This indicates that for SDD, the defect opening size is the critical parameter, whereas the defect's equivalent depth and shape have only minimal influence.

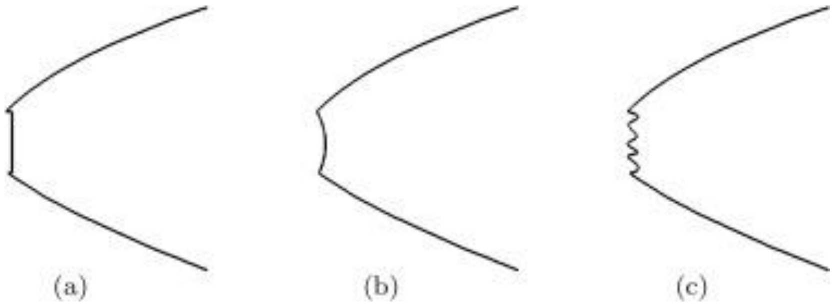

(a) (b) (c)

Figure 2.20. Schematics of SDD on the leading-edge: (a) Rectangular defect; (b) Smooth sunken deformation; (c) Random deep pits.

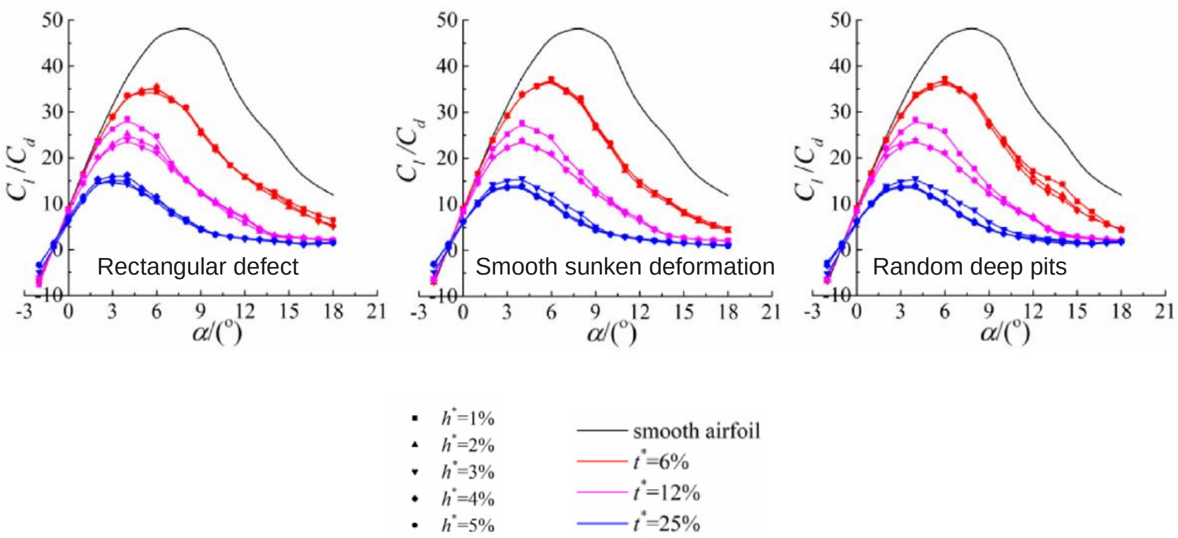

Figure 2.21. Variation of Cl/Cd with the angle of attack for SDD aerofoils with different defect shapes, opening sizes and equivalent depths, adapted from [42].

Han, et al. [43] investigated the impact of blade contamination and erosion on the AEP loss of a large wind turbine with a NACA64-618 aerofoil, similar to NREL 5-MW wind turbine tip aerofoil. The CFD simulation results at high Reynolds number of 6 ×10^6 as shown in *Figure* 2.22. To protect wind turbines from contamination and erosion, they recommended implementing systematic inspection and O&M plans that consider blade surface conditions. However, most wind farms suffer from inefficient O&M due to a lack of quantitative data on how contaminant accumulation and erosion affect power performance and load variation.

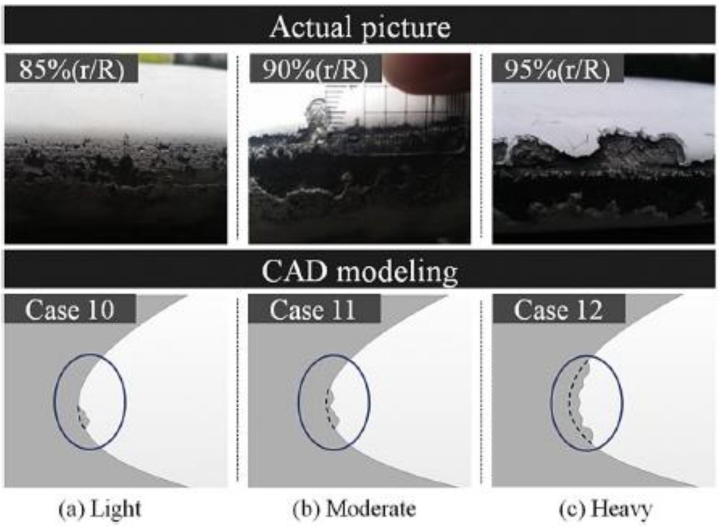

Figure 2.22. Erosion condition at the leading edge of a 12-year-old Vestas V47 blade, adapted from [43]

The effects of turbulence models were compared with the wind tunnel test results reported by Abbott et al. [44]. The inflow wind speed was set as 89.6326 m/s, and turbulence intensity was set to 0.01%. The y+ was set such that it satisfied the recommended values for the given characteristics of the turbulence model. Shear stress transport (SST) k–ω and SST k–ω transition models (TSST) fulfil the condition of y+ < 1, and the k–ε model fulfils the condition of y+ > 30. Except for the lift–drag ratios at an angle of attack is 4°, the results from the SST k–ω transition turbulence model (TSST) closely matched the wind tunnel test results for most angles of attack. Fully turbulent models, on the other hand, tend to underestimate drag, resulting in significantly high relative errors in the lift–drag ratios. Therefore, the TSST model was recommended in their study.

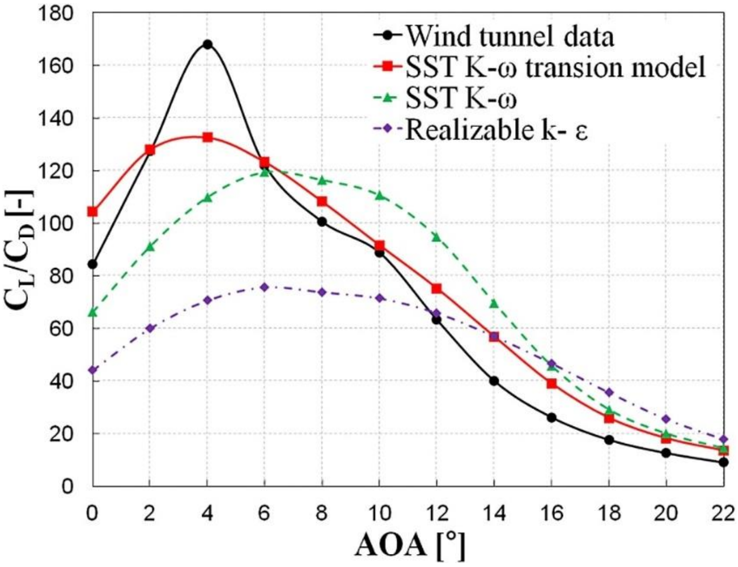

Figure 2.23. Lift–drag ratios in various turbulence models, adapted from [43]

2.6. Research gaps

Rain erosion of wind turbine blades has been researched for many decades with two major trends emerging. One line of research focuses on quantifying the effect of rain erosion on energy production loss caused by LEE. The other line is dedicated to developing protection system for the blades' leading-edges.

Polyurethane is one of the most commonly used coating materials for protection systems. A primary research gap in this area is enhancing the mechanical properties and erosion resistance of pure polyurethanes using additive nanomaterials such as graphene, carbon nanotubes, and fumed silica. These nanomaterials, individually or in combination, have the potential to improve the damping effect of the coatings through attenuation, dispersion, and scattering of stress waves. Inhomogeneities, mode conversion at interfaces, and the redirection and conversion of deformation energy into heat through molecular relaxation processes also contribute to this improvement.

When raindrops impact the blade surface, they generate various stress waves. The dissipation of these waves in composite materials is facilitated by the viscoelastic nature of the resin and the scattering by nanomaterials particles. At high frequencies, the wavelength becomes comparable to the size of the reinforcements, allowing additive particles to influence wave propagation.

Based on the above summary, this research will focus on three main topics:

1. Computational fluid dynamic analysis of two- and three-dimensional damaged blades, and the effect of leading edge damage on lift and drag coefficients.
2. Using GNP, CNTs and fumed silica, individually or in combination, to improve the mechanical properties and erosion resistance of polyurethane.
3. Investigating water absorption behaviour of nanomodified polyurethane coatings.

In summary, CFD analysis of damaged wind turbine blades provides a detailed understanding of the impact of leading-edge damage on aerodynamic performance and energy efficiency. This analysis helps identify critical areas where performance deteriorates, enabling targeted repairs and optimizations. As a result, protective coatings for the blades are essential. According to the literature, polyurethane is identified as a strong candidate for the base coating material. Enhancing its properties with nanomaterials such as GNPs, CNTs, and fumed silica further improves blade durability by increasing erosion resistance, mechanical strength, and reducing water absorption. Together, these approaches extend blade lifespan, lower maintenance costs, and enhance overall turbine efficiency in harsh environmental conditions.

2.7. Literature Summary

This chapter investigated various aspects related to the causes and consequences of leading-edge erosion (LEE) on wind turbine blades. It presented classifications of LEE severity from multiple sources and explored its impact on annual energy loss in wind turbines by compiling data from various studies.

A primary focus of blade protection system development is enhancing the erosion resistance of polymer coating materials, particularly those with polyurethane matrices. The literature review underscored the critical importance of understanding the underlying mechanisms of LEE to develop effective mitigation strategies. Analysis of scholarly works emphasised the pivotal role of integrating numerical simulations and advanced computational modelling techniques to study the dynamics of erosion caused by rain and other particles. Using these techniques can provide a better understanding of the effect of coating material properties and structure on the erosion, debonding, and the impact of humidity and weathering.

Another crucial factor that requires special attention is the characterisation of coating-laminate interphase adhesion to effectively achieve a high-quality LEE protection system. Experimental methods in this area include accelerated water absorption testing, pull-off testing, peeling adhesion testing, and nanoindentation testing.

Additional experiments involve applying typical LEP system to scaled-modelled blade sections and conduction rain erosion testing (RET) to characterise the erosion performance of the developed coating materials and determine their incubation time for erosion damage.

The ageing of wind turbine fleets and the use of larger wind turbines with higher tip speeds ensure that LEE remains a topic of significant interest to the industry. Therefore, the wind turbine industry and operators of wind farms will continue to seek the development and testing of new repair and prevention solutions. Understanding the primary causes of damage at specific wind farm sites is essential for accurately predicting the repair needs. This allows for maintenance scheduling based on adequate damage monitoring, such as seasonal cycles, moving from unplanned to well-planned maintenance, which ultimately reduces overall maintenance costs and improve financial outcomes from wind turbines.

Chapter 3: CFD modelling of undamaged and leading edge eroded blades

3.1 Introduction

Computational Fluid Dynamics (CFD) simulation is used in this chapter to evaluate the aerodynamic performance of both undamaged and eroded wind turbine blades. The effect of Leading-Edge Erosion (LEE) of wind turbine blades on lift and drag forces is investigated, as the energy production of a wind turbine directly correlate with these forces as the optimum operating condition of a wind turbine is achieved when glide ratio, the ratio of lift to drag coefficients, is maximised. For this study, the NACA0012 aerofoil was chosen for the blade, as many published experimental results are available in the literature for validation of the CFD models.

The CFD modelling is conducted for two- and three-dimensional undamaged and eroded aerofoils. All the CFD modelling was performed with ANSYS Fluent Workbench R2021 software. Various turbulence models are analysed, and the results are compared with the experimental data to identify the most suitable turbulence model. Prior to determining the most appropriate turbulence model, a mesh sensitivity analysis was carried out to find an acceptable cell size that provides accurate results while computationally cost-effective.

3.2 Turbulence modelling

Turbulent flow is characterised by irregular, and chaotic motion, in which various components of the flow field fluctuate over time around a mean value. According to Kundu and Cohen [45], turbulence has specific characteristics including randomness, nonlinearity, and a rapid rate of diffusivity of heat and momentum due to the macroscopic mixing of fluid particles. There is high vorticity, with fluctuating eddies of various sizes, where large eddies contain most of the energy. The energy is transferred from larger to smaller eddies by nonlinear interactions until it is dissipated by viscous diffusion in the smallest eddies. Energy dissipation occurs as the vortex stretching mechanism transfers energy and vorticity to increasingly smaller scales until the gradients become so large that they are dissipated by viscosity. Therefore, turbulent flows require a continuous supply of energy to compensate for the viscous losses.

In the CFD modelling context, there are various approaches for modelling of turbulence as shown in *Figure 3.1.* These models are:

- **RANS** (Reynolds-Averaged Navier-Stokes): This is most common approach in industrial applications which is used in modern design to reduce the number of experiments where the Navier-Stokes equations are solved, and the average quantities are obtained directly. As a result, the small scales are not present in the equations and less demand is put on the numerical method and mesh requirement.
- **LES** (Large Eddy Simulation): Large eddies in the turbulent flow are resolved by the governing equations, while the effect of the Sub-Grid Scales (SGS) is not completely neglected but properly modelled. The scale separation is obtained by applying a filter to the governing equations which also influences the form of the SGS models. This approach can be thought as an intermediate between the DNS and the RANS approaches.
- **DES** (Detached Eddy Simulation): DES is a hybrid method that treats near-wall regions with a RANS approach, switching to the LES for the bulk flow.
- **DNS** (Direct Numerical Simulation): Resolves all scales of turbulence by directly solving the Navier-Stokes equations numerically without any turbulence modelling.

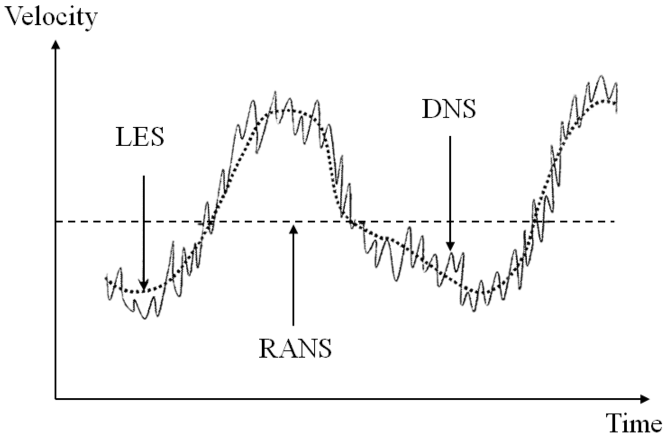

Figure 3.1. Flow resolved by RANS, LES, and DNS. Typical time evolutions of velocity that these three methods would provide. (adapted from Foale [46])

Due to the high computing cost of DNS, the engineering approach to CFD are based on the RANS equations. In this approach the starting point is the Reynolds decomposition of the flow variables into "average" quantities and fluctuating parts, where the insertion of the Reynolds-decomposed variables into the Navier–Stokes equations, followed by an averaging of the equations themselves, gives rise to the Reynolds-stress tensor, an unknown term that must be modelled in order for the RANS equations can be solved. The closure problem of the Navier–Stokes equations system is essentially included in this operation. For example, the Reynolds decomposition of the instantaneous velocity u_{inst} results in a mean value $\bar{u}$ and a fluctuating value $u'(\boldsymbol{x}, t)$ as shown in *Figure* 3.2.

$$u_{inst}(\boldsymbol{x}, t) = \bar{u}(\mathbf{x}) + u'(\mathbf{x}, t) \tag{3.1}$$

The same can be applied to any other flow field properties. Then, time average velocity, $\bar{u}$, is calculated over a sufficiently large time Δt from:

$$\bar{u}(\boldsymbol{x}, t) = \frac{1}{\Delta t} \lim_{\Delta t \to \infty} \int_{t_0}^{t_0+\Delta t} u(\boldsymbol{x}, t) dt \tag{3.2}$$

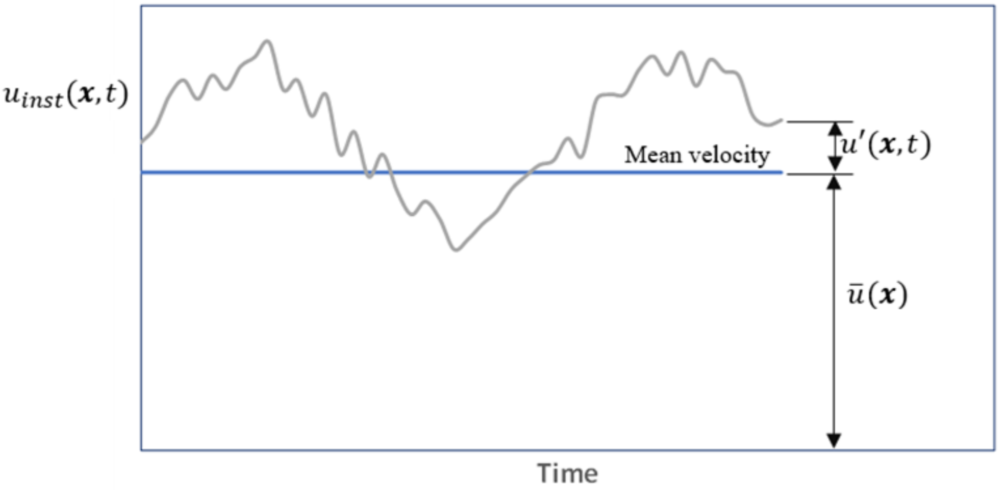

Figure 3.2. Reynolds decomposition for turbulent flow, adapted from Sun [47]

Δt is the averaging time interval. We assume that $\Delta t \to \infty$ which corresponds to the steady RANS model. For an Unsteady RANS (URANS), this time interval must be sufficiently large with respect to the time scale T_1 of the turbulent fluctuations (*Figure* 3.3), and small with respect to the time scale T_2 of large scale unsteadiness [48]. So, for unsteady problems, Equation (3.2) takes the form:

$$\bar{u}(\boldsymbol{x}, t) = \frac{1}{\Delta t} \int_{t_0}^{t_0+\Delta t} u(\boldsymbol{x}, t) dt \tag{3.3}$$

The Turbulent Kinetic Energy (TKE), the kinetic energy (k) per unit mass, is based on the turbulent fluctuations' velocity (u'_i) in a turbulent flow, and it is expressed by:

$$TKE = k = \frac{1}{2} \overline{u'_\iota u'_\iota} = \frac{1}{2} \left(\overline{u'^2_x} + \overline{u'^2_y} + \overline{u'^2_z} \right) \tag{3.4}$$

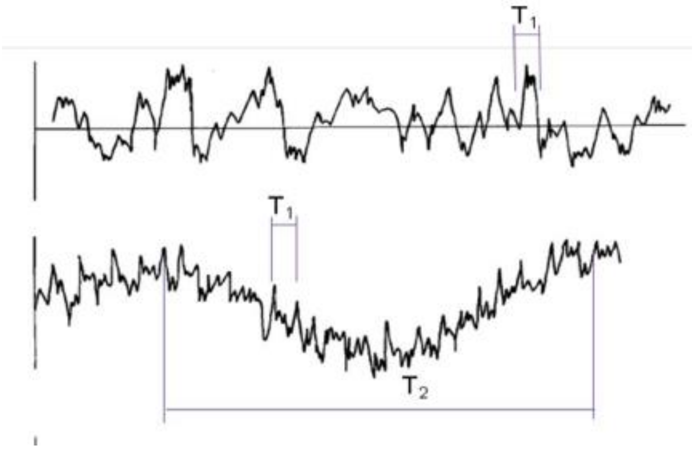

Figure 3.3. Time-averaging windows. $\Delta t = T_1$ *– time scale of turbulent fluctuations,* $\Delta t = T_2$ *– time scale of unsteady motion. The time-averaging window T should be:* $T_1 < \Delta t < T_2$ *[48]*

The results from RANS simulation with experiments are compared in *Figure 3.4*. *Figure 3.5* compares the resolution of eddies in LES and DNS approaches.

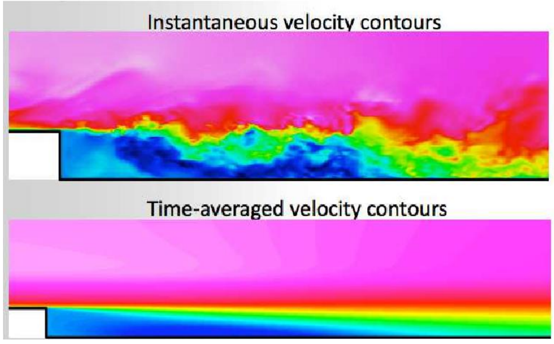

Figure 3.4. Comparison between experimental (top) and a simulation with RANS (bottom) (Source: adapted from ANSYS training course)

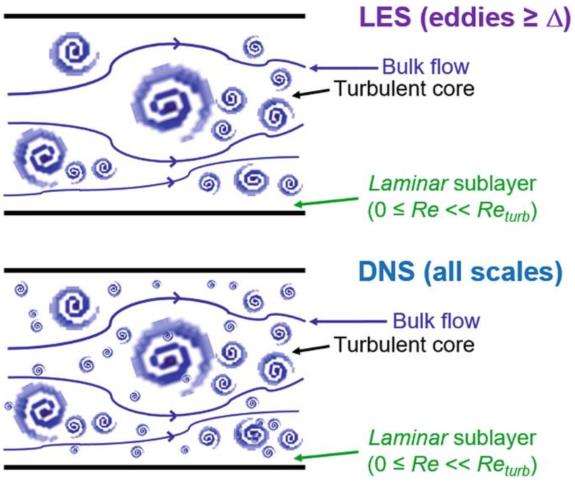

Figure 3.5. Comparison of LES and DNS. (adapted from Rodriguez [49])

Figure 3.6*(a)* compares the computational cost of various approach for modelling turbulence. DNS is computationally the most expensive one, but as shown in *Figure* 3.6*(b)*, the details of the flow are at the highest resolution.

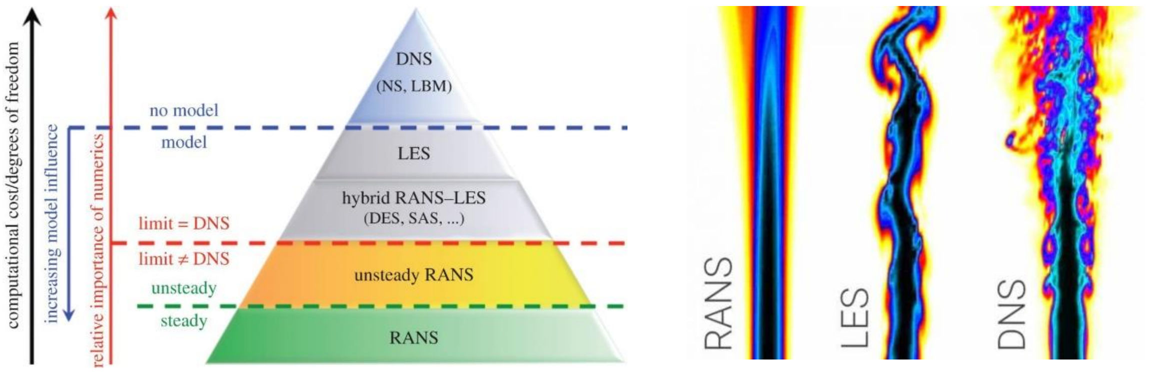

(a) (b)

Figure 3.6. (a) Classification of unsteady approaches according to levels of modelling and readiness (adapted from Sagaut et al. [50]), and (b) Comparison of flow results from CFD modelling with RANS, LES, and DNS.

The Navier-Stokes *(N-S) e*quations are the governing equations for describing a fluid flow. The N-S equations are based on Newton's Law of motion (momentum equation), the first law of thermodynamics (conservation of energy), and the conservation of mass. These equations form a set of coupled, nonlinear partial differential equations, which forms the basis for flow simulations. These set of equations for compressible Newtonian fluids are [51]:

Conservation of mass:

$$\frac{\partial \rho}{\partial t} + \nabla.\left(\rho \vec{V}\right) = 0 \tag{3.5}$$

Conservation of momentum:

$$\begin{aligned}
\frac{\partial(\rho u)}{\partial t} + \nabla.\left(\rho u \vec{V}\right) &= -\frac{\partial p}{\partial x} + \frac{\partial \tau_{xx}}{\partial x} + \frac{\partial \tau_{yx}}{\partial y} + \frac{\partial \tau_{zx}}{\partial z} + \rho f_x \\
\frac{\partial(\rho v)}{\partial t} + \nabla.\left(\rho v \vec{V}\right) &= -\frac{\partial p}{\partial y} + \frac{\partial \tau_{xy}}{\partial x} + \frac{\partial \tau_{yy}}{\partial y} + \frac{\partial \tau_{zy}}{\partial z} + \rho f_y \\
\frac{\partial(\rho w)}{\partial t} + \nabla.\left(\rho w \vec{V}\right) &= -\frac{\partial p}{\partial z} + \frac{\partial \tau_{xz}}{\partial x} + \frac{\partial \tau_{yz}}{\partial y} + \frac{\partial \tau_{zz}}{\partial z} + \rho f_z
\end{aligned} \tag{3.6}$$

and conservation of energy:

$$\begin{aligned}
&\frac{\partial}{\partial t}\left[\rho\left(e + \frac{V^2}{2}\right)\right] + \nabla.\left[\rho\left(e + \frac{V^2}{2}\right)\vec{V}\right] = \\
&\rho \dot{q} + \frac{\partial}{\partial x}\left(k\frac{\partial T}{\partial x}\right) + \frac{\partial}{\partial y}\left(k\frac{\partial T}{\partial y}\right) + \frac{\partial}{\partial z}\left(k\frac{\partial T}{\partial z}\right) \\
&-\frac{\partial(up)}{\partial x} - \frac{\partial(vp)}{\partial y} - \frac{\partial(wp)}{\partial z} + \frac{\partial(u\tau_{xx})}{\partial x} + \frac{\partial(u\tau_{yx})}{\partial y} + \frac{\partial(u\tau_{zx})}{\partial z} \\
&+\frac{\partial(v\tau_{xy})}{\partial x} + \frac{\partial(v\tau_{yy})}{\partial y} + \frac{\partial(v\tau_{zy})}{\partial z} + \frac{\partial(w\tau_{xz})}{\partial x} + \frac{\partial(w\tau_{yz})}{\partial y} + \frac{\partial(w\tau_{zz})}{\partial z} + \rho \vec{f}.\vec{V}
\end{aligned} \tag{3.7}$$

where ρ is the fluid density, p is the pressure and k is thermal conductivity. For a perfect gas, the equation of state is $p = \rho RT$ where R is the specific gas constant, and a thermodynamic relation between state variables such as $e = e(T, p)$ complete the seven equations required.

When averaging processes are applied to the Navier-Stokes equations, the RANS momentum equations become:

$$\frac{\partial(\rho\bar{u}_i)}{\partial t} + \frac{\partial(\rho\bar{u}_i\bar{u}_j)}{\partial x_j} = -\frac{\partial\bar{p}}{\partial x_i} + \frac{\partial}{\partial x_j}\left(\tau_{ij} - \rho\overline{u'_i u'_j}\right) \tag{3.8}$$

where $\bar{u}_i$ is the vector of the averaged velocity field, $\bar{p}$ is the averaged pressure and τ_{ij} is the Stokes (laminar) stress tensor. For incompressible flows:

$$\tau_{ij} = \mu\left(\frac{\partial\bar{u}_i}{\partial x_j} + \frac{\partial\bar{u}_j}{\partial x_i}\right) = 2\mu S_{ij} \tag{3.9}$$

Where S_{ij} is the strain-rate tensor $S_{ij} = \frac{1}{2}\left(\frac{\partial\bar{u}_i}{\partial x_j} + \frac{\partial\bar{u}_j}{\partial x_i}\right)$, and μ is the dynamic molecular viscosity.

The last term in equation (3.8) $-\rho\overline{u'_i u'_j}$ is so-called ‘Reynolds Stress Tensor’ and results from the averaging of the non-linear convection terms. This tensor represents the influence of the turbulent fluctuations on the mean velocity field.

The above momentum equations are ‘unclosed’ as no equations are yet available for the Reynolds Stress Tensor. Turbulence models are needed to provide formulations for this tensor. In addition, the RANS momentum equations above are derived under the assumption that there are no significant density variations due to turbulence. This is typically the case for flows with Mach numbers $M < 0.3$.

In this work, RANS method was used for flow analysis. In this approach, turbulence models are required to feedback information to allow physically correct simulations. For most industrial applications, eddy-viscosity turbulence models provide the optimal balance between accuracy and robustness. The most relevant turbulence models for low Reynolds numbers are discussed below.

$k - \omega$ SST turbulence model

This model is a two-equation eddy-viscosity model that is used in various aerodynamic applications (Wilcox [52]). It consists of combined $k - \omega$ and $k - \varepsilon$ expressions, where for anticipating fluid flow characteristics in areas away from the wall the $(k - \varepsilon)$ is used, and for replicating fluid flow in the viscous sub-layer $(k - \omega)$ is used. The Shear Stress Transport (SST) constraint aids the $k - \omega$ in preventing the accumulation of immoderate turbulent kinetic energy near stagnant points. It is also insensitive to free stream conditions and can model laminar-turbulence transition.

$k - \varepsilon$ realizable turbulence model

This model consists of two transport expressions which are the turbulent dissipation (ε) and the turbulent kinetic energy (k), in which they both depict the turbulent effects of a fluid flow and hence take into consideration past effects of turbulent energy (e.g., diffusion). The expression (k) evaluates the energy within the turbulence, while (ε) is related to the turbulence relative size. The realizable constraint assists in enhancing the model's sensitivity to adverse pressure gradient and handling low Reynolds formulations for laminar-turbulence transition (since the model is technically a high Reynolds model) [53].

Spalart-Allmaras (S-A) turbulence model

The one-equation Spalart-Allmaras model [54] consists of a single transport equation that calculates the kinematic eddy viscosity. This model provides improved performance relative to $k-\varepsilon$ models for flows with adverse pressure gradients and boundary layer separation. The model has become popular for aerodynamic and turbo-machinery applications [55, 53] and it gives satisfactory results for aerofoil and turbine blade applications, for which it is calibrated. However, it is not appropriate for applications involving jet-like free shear regions.

Transition Shear Stress Transport model (TSST)

This model is known as the Langtry-Menter four-equation transitional SST model or the four-equation Transition Shear Stress Transport model (TSST). The model consists of two extra transport variables alongside the $k-\omega$ model. These are the transition momentum-thickness Reynolds number, Re_θ, and the turbulence intermittency, γ. Hence, there are two additional transport equations for the γ and Re_θ in this model. The transition momentum-thickness Reynolds number is defined by

$$Re_\theta = \frac{\rho\bar{u}\theta}{\mu} \tag{3.10}$$

where the momentum thickness is calculated by

$$\theta = \int_0^\delta \frac{u}{\bar{u}}\left(1-\frac{u}{\bar{u}}\right)dy \tag{3.11}$$

This model is useful for transitional flows. γ and Re_θ assist in anticipating the transition process which usually occurs naturally and is induced by separation. These variables, coupled with the $k-\omega$ model, also assist in predicting fully turbulent fluid flows and thus prevents turbulent kinetic energy accumulation in the stagnated points [56].

Multiple simulation works have been done by several researchers in the past to predict which of these turbulence models most accurately predicts the aerodynamic behaviour of the flow at various Reynolds numbers. *Table 3.1* and *Table 3.2* summarise the turbulent models used in these works for low and high Reynolds numbers, respectively.

Table 3.1. Turbulence models in previous CFD modelling for low Reynolds number $Re \leq 5 \times 10^5$

Authors	Reynolds number	Angle of attack (°)	Aerofoil type	Turbulence model	Ref.
Suvanjurmat	1.6×10^5-3.6×10^5	0 to 20	NACA 0015	k-ω SST	[57]
Andres et al.	3×10^5	5 to 25	DU-06-W-200	k-ω SST	[58]
Aftab et al.	1.2×10^5	6 and 18	NACA 4415	γ-Re_θ SST	[59]
Rahimi et al.	7×10^5	6 to 20	FX 79-W-151A and NACA 63-430	kkl- ω transition	[60]
Lin and Sarlak	1×10^5	0 to 14	NREL S826	k-k_L-ω (best) γ-Re_θ (adequate) (both models are transitional)	[61]
Cakmakcioglu et al.	1.45×10^5	0 to 12	NREL S826	2D γ-Re_θ transitional	[62]
Yao et al.	5×10^5	-8 to 13	NACA 0018	Reynolds Stress Model (RSM) 5-equations	[63]

As observed from *Table 3.1* and *Table 3.2* each turbulence model proves to be the best model depending on the aims and objectives of the studies conducted (e.g., aerodynamic performance, pressure distribution around the aerofoil, etc.), along with the type of aerofoils utilised, which have different profiles in each study. From reviewed works at low Reynolds number flows, the two-equation $k - \omega$ models are among the most used turbulence models. This model includes two additional transport equations - turbulent kinetic energy (k) and the specific dissipation rate (ω)- to represent the turbulent properties of the flow.

The $k - \omega$ model is known to perform better for boundary layers, and low Reynolds number flows compared to the $k - \varepsilon$ models. Furthermore, the shear stress transport (SST) variant of the $k - \omega$ model has advantages and is suitable for complex boundary layer flows under adverse pressure gradient and separation, and hence was chosen in this work.

Accurate prediction of the stalling angle of attack must be ensured to avoid significant overestimation of drag. At low Reynolds number, the TSST $\gamma - Re_\theta$ transitional model has proven effective in addressing the issue of overprediction of stalling angle. The accuracy of a model's computational results is due to the TSST model's precise prediction of leading-edge separation in the stall and post-stall zones.

Table 3.2. Turbulence models in previous CFD modelling for high Reynold number $Re \geq 1 \times 10^6$

Authors	**Reynolds number**	**Angle of attack (°)**	**Aerofoil type**	**Turbulence model**	**Ref.**
Karim et al.	1×10^6	-18 to 18	NACA0012 and NACA 2412	S-A, k-ω SST and k-ε RNG	[53]
Douvi et al.	3×10^6	-12 to 16	NACA0012	k-ω SST	[64]
Fernando et al.	Not given (turbulent Reynolds number indicated)	0 to 28	NACA 63-415	k-ω SST (best) S-A and k-ε RNG (adequate)	[65]
Rahimi et al.	1.5×10^6	6 to 20	FX 79-W-151A and NACA 63-430	kkl- ω transition	[60]
Basha and Ghaly	2×10^6 - 4×10^6	-16 to 16	NLF (1)-0416 and NLR-7301	S-A*	[66]
Badran and Bruun	0.36×10^6	15	NACA 4412	k-ε RNG & Realizable, and RSM	[67]
Genc	5.8×10^6	2 to 11	NACA 64A006	k-k_L-ω	[68]

* S-A gave poor quality lift and drag results hence a transitional model was developed to counter this issue.

In conclusion, the TSST model stands out in applications where transition prediction plays a vital role, such as low Reynolds number aerodynamics such as for wind turbines aerodynamic analysis. It strikes an excellent balance between accuracy and efficiency, making it a preferred choice in situations where both laminar and turbulent flow regions coexist and must be modelled accurately to predict performance metrics like drag, lift, and flow separation effectively.

3.3 Flow analysis with ANSYS Fluent

The regime of a flow depends on the flow Reynolds number and *Figure 3.7* illustrates typical Reynolds numbers in various boundary layer applications.

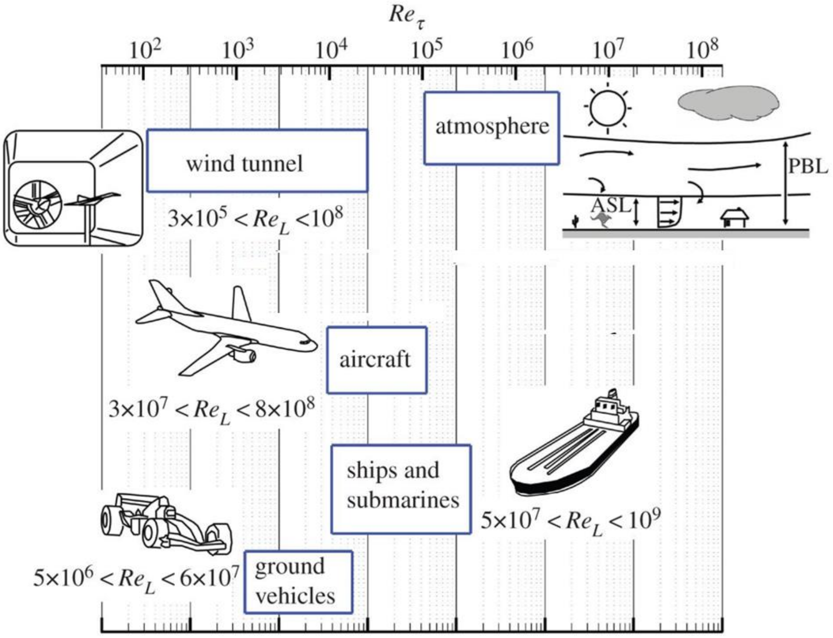

Figure 3.7. Typical Reynolds numbers in various boundary layer applications. Re_L denote the Reynolds numbers based on the streamwise characteristic length, and Re_τ denotes the friction Reynolds number.(Adapted from Deck et al. [69])

For CFD modelling, the volume of the fluid domain was discretized into cells of finite dimensions. In ANSYS Fluent software, the finite volume method was used to solve general conservation (transport) equations for mass, momentum, energy, species, etc. on this set of cells. The equations were discretized as well. The transport partial differential equations then convert to a system of algebraic equations which were solved in every cell of the domain to compute the field variables such as pressure and velocities at the cells' centre. Gradients are required for calculating scalar values at the cell faces, and also for computing secondary diffusion terms and velocity derivatives. The three gradient methods which are available in ANSYS Fluent are:

- Green-Gauss Cell Based
- Green-Gauss Node Based
- Least Squares Cell Based

In all CFD simulations presented in this chapter, the 'Least Squares Cell-Based' gradient method was used. This method was selected for its optimal balance of accuracy, robustness, and computational efficiency, making it an excellent choice for engineering simulations, particularly when dealing with complex geometries and unstructured grids.

For the pressure, the PRESTO! (PREssure STaggering Option) scheme is adopted. It uses the discrete continuity balance for a "staggered" control volume about the face to compute the "staggered" (i.e., face) pressure. The PRESTO! scheme is available for all meshes guaranteeing a good stability.

By default, considering the unsteady conservation equation for transport of a scalar quantity φ, ANSYS Fluent stores discrete values of φ at the cell centres. However, face values φ_f are required for the convection terms in the unsteady conservation equation for transport of a scalar quantity φ which must be interpolated from the cell centre values. This is accomplished using an upwind scheme.

Upwinding means that the face value φ_f is derived from quantities in the cell upstream, or "upwind", relative to the direction of the normal flow velocity. Fluent gives the possibility to choose from several upwind schemes: first-order upwind, second-order upwind, power law, and QUICK.

First-Order Upwind Scheme: In this scheme quantities at cell faces are determined by assuming that the cell-centre values of any field variable represent a cell-average value and hold throughout the entire cell. When first-order upwinding is selected, the face value φ_f is set equal to the cell-centre value φ in the upstream cell. First-order upwind is available in the pressure-based and density-based solvers.

Second-Order Upwind Scheme: In this scheme, a higher-order accuracy is achieved at cell faces through a Taylor series expansion of the cell-centred solution about the cell centroid. Thus, when second-order upwinding is selected, the Second Order Upwind (SOU) face value $\varphi_{f,SOU}$ is computed using the following expression:

$$\varphi_{f,SOU} = \varphi + \nabla\varphi . \vec{r} \tag{3.12}$$

where φ and $\nabla\varphi$ are the cell-centred value and its gradient in the upstream cell, and $\vec{r}$ is the displacement vector from the upstream cell centroid to the face centroid. This formulation requires the determination of the gradient $\nabla\varphi$ in each cell. Second-order upwind is also available in the pressure-based and density-based solvers.

All the subsequent simulations have been solved with a second-order scheme, which has a smaller truncation error, leading to better results despite some minor instability.

3.4 Aerodynamic analysis of undamaged blades

For analysis of undamaged aerofoil, parameters that influence the accuracy of CFD simulations including the grid resolution and iterative convergence, the order of the discretization schemes, the choice of turbulence models, near-wall treatment, and boundary conditions are considered.

In this part, RANS with four different turbulence models are used to predict the lift and drag coefficient alongside pressure coefficient around the undamaged aerofoil. NACA0012 aerofoil is selected as the basis for the aerodynamic analysis.

3.4.1 Mesh sensitivity analysis

To establish the accuracy of the CFD solution and to keep the computational costs low, a grid dependency study is performed by meshing the domain with varying cells densities from coarse, to medium, and fine grids. For each grid density, the lift (C_L), the drag (C_D), and pressure (Cp) coefficients are calculated to determine how the cell size affects the CFD simulation results. In a mesh sensitivity study, high-gradient areas require finer cells than the low-gradient areas. The time-to-solution of a CFD simulation is highly dependent on the number of cells in the model.

To create a high-quality mesh, it is helpful to have some approximate formulas for the development of boundary layers. The boundary layer develops in streamwise direction (x-direction) for a flat plate with origin at $x = 0$. The boundary layer thickness is δ, the freestream velocity is U, and the wall shear stress (local wall friction) is $\tau_{wall} = \frac{\mu \partial u_p}{\partial y}$, where u_p is the local flow speed near wall and parallel to the flow. The wall friction coefficient is $C_f = \tau_{wall}/(0.5\rho U^2)$ and $Re_x = \rho U x/\mu$. Reynolds number Re_x is calculated at half the running length of the boundary layer (e.g., half chord of an aerofoil).

In laminar flows, the wall shear stress coefficient and boundary layer thickness can be calculated from:

$$C_f = 0.664 Re_x^{-1/2} \tag{3.13}$$

$$\frac{\delta}{x} = 5.0 Re_x^{-1/2} \tag{3.14}$$

And in turbulent flows, based on Prandtl formula (1927), they are calculated from:

$$C_f = 0.058 Re_x^{-1/5} \tag{3.15}$$

$$\frac{\delta}{x} = 0.37 Re_x^{-1/5} \tag{3.16}$$

More accurate shear stress coefficient and boundary layer thickness than the above Prandtl formula for turbulent flow are:

$$C_f = 0.027 Re_x^{-1/7} \tag{3.17}$$

$$\frac{\delta}{x} = 0.16 Re_x^{-1/7} \tag{3.18}$$

$$Re_\delta = 0.16 Re_x^{6/7} \tag{3.19}$$

Finally, the viscous sublayer thickness, y^+, is estimated from:

$$y^+ = \frac{u_\tau . \Delta y}{v} \tag{3.20}$$

Where the wall friction velocity is calculated from:

$$u_\tau = \sqrt{\frac{\tau_{wall}}{\rho}} = 0.17. U. Re_x^{-1/10} \tag{3.21}$$

Hence, the first-off-the-wall cell distance, Δy, can be found from:

$$\Delta y = 5.87\, y^{+} \frac{v}{U} Re_x^{1/10} \tag{3.22}$$

Since near-wall regions involve steep gradients in velocity and temperature variation, they pose significant difficulties in turbulent flows simulations, making accurate treatment of this region very important. The two main approaches to treat the near-wall regions are: (i) using wall functions and (ii) using wall-resolved methods, which typically require the first grid point to be in the viscous sublayer corresponding to $y^{+} \leq 1$. In wall-bounded RANS models, wall-functions can be used to model the near-wall region. The use of wall-functions assumes that, under many flow conditions, the nature of the solution between the wall and the outer edge of the logarithmic layer is invariant, provided appropriate scaling is used. This assumption allows the first cell to be placed within the logarithmic layer which leads to substantial reduction in the computational time. However, the use of wall-functions can lead to inaccuracies and can be difficult to formulate for cases involving complex geometries. Hence, in this work, the wall-resolved method is chosen, and the selected meshes have near-wall resolution with $y^{+} < 1$, resulting the first cell being located within the laminar sublayer.

Note that when $y^{+} > 30$, the first cell is located outside the viscous sublayer. When $1 < y^{+} < 30$, the first cell is located within the buffer layer but not too close to the surface wall. In our case, $y^{+} < 1$ was used for capturing the boundary layer near the wall.

Initially, multiple mesh cases were generated to study the effect of mesh density near the aerofoil walls and farther in the domain, establishing the best mesh that provides accurate results without excessive computational cost.

Comparing different meshes and their proximity to experimental and/or numerical benchmarks is crucial for selecting the proper mesh. When the results such as C_D or C_P do not change significantly with further mesh refinement, the mesh is considered acceptable.

As illustrated in *Figure 3.8*, the mesh constructed around the NACA0012 aerofoil was of a C-type structured mesh. This mesh type was chosen since it usually provides better flow convergence over the aerofoil and hence providing better results alongside the fact that the grid curves align well with leading edge profile. Structured cells are used in the proximity of the aerofoil wall to improve resolution in the boundary layer and ensure that proper wall y^+ values define in Eq. (3.20) are kept. The first guess of the first-off-the-wall cell distance, Δy, is obtained by enforcing a y-plus value of $y^{+} = 0.5$ to flat-plate empirical estimations presented in equation (3.22).

Different mesh seeds from (a) to (i) shown in *Figure 3.9* were generated along all edges of the domain boundary and aerofoil, resulting in different cell sizes. The meshes around the aerofoil are made finer than those further away from aerofoil by setting proper biases. This together with inflation layers produced meshes with a $y^{+} < 1$ as required. However, mesh cases (g), (h) and (i) were discarded for further modelling since for these cases the $y^{+} > 1$. The mesh cases (a) to (f) met the y^+ criteria of being less than one and they were used for evaluating lift, drag and pressure coefficients and the results are validated with Ladson's experimental data [70, 71].

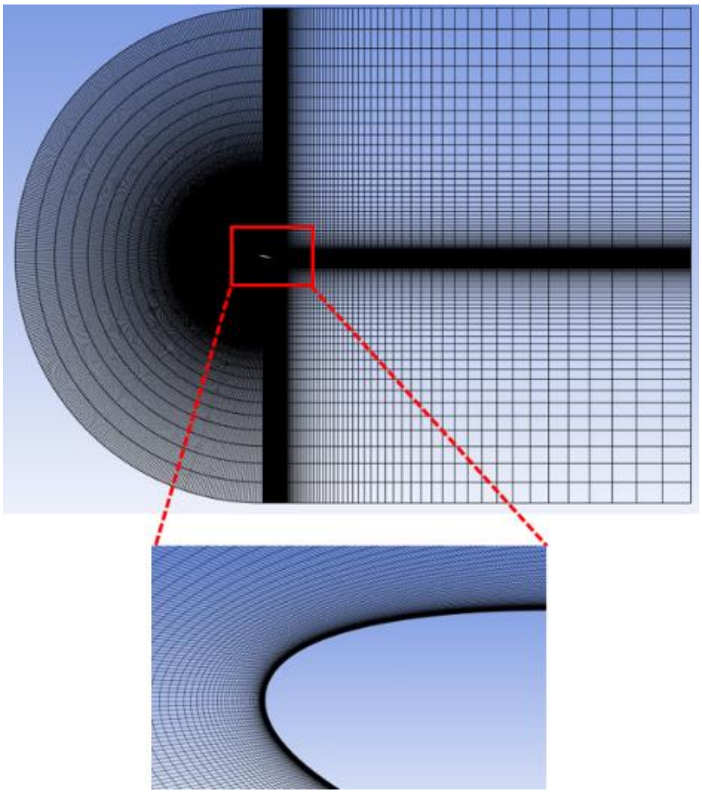

Figure 3.8. C-type mesh surrounding NACA0012

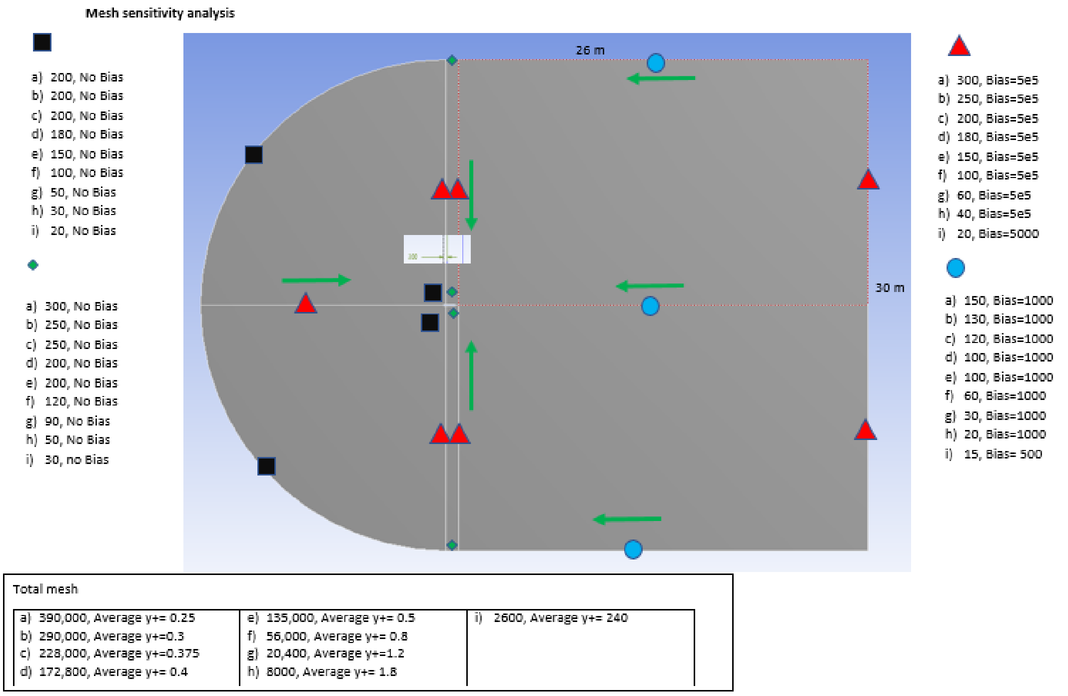

Total mesh

a) 390,000, Average y+= 0.25
b) 290,000, Average y+=0.3
c) 228,000, Average y+=0.375
d) 172,800, Average y+= 0.4
e) 135,000, Average y+= 0.5
f) 56,000, Average y+= 0.8
g) 20,400, Average y+=1.2
h) 8000, Average y+= 1.8
i) 2600, Average y+= 240

Figure 3.9. Number of elements for each mesh case

The set boundary conditions are:

- No slip wall on the aerofoil surface
- Farfield pressure condition for the farfield
- Velocity at the inlet of the domain (on the C section)
- Atmospheric pressure at the outlet

Zero heat flux, constant thermal conductivity and specific heat, ideal gas law for density, and Sutherland law for viscosity were selected. The aerofoil's chord was set to be 1 m in length.

For mesh sensitivity analysis, the testing condition of Ladson's experiments [70, 71] were chosen, i.e., angle of attack $AoA = 1.55°$, and Mach number $M = 0.7$, hence the flow is transonic. These values resulted in the flow Reynolds number of $Re = 16.7 \times 10^6$, with total temperature of $T_0 = 311$ K.

Static pressure P is calculated from Eq. (3.23) by assigning the specific heat ratio $\gamma = 1.4$, and the total pressure $P_0 = 101325\ Pa$.

$$\frac{P_0}{P} = \left(1 + \frac{\gamma - 1}{2} M^2\right)^{\frac{\gamma}{\gamma - 1}} \qquad (3.23)$$

Static temperature is calculated from Eq. (3.24) for the total temperature ($T_0 = 311$ K).

$$\frac{T_0}{T} = 1 + \frac{\gamma - 1}{2} M^2 \qquad (3.24)$$

The CFD results of drag and pressure coefficients for all mesh densities are shown in *Figure 3.10* and *Figure* 3.11, respectively.

The results in *Figure 3.10* shows that the drag coefficient for meshing case (d) with 172,800 cells, and meshing case (e) with 135,000 cells has not changed noticeably and the drag has been stabilised and the results barely change with further mesh refinement, which increases the computational costs.

The pressure coefficient distribution around the aerofoil for various mesh densities are shown in *Figure* 3.11. The results for the pressure coefficients obtained from all mesh densities are in good agreement with Ladson's experimental data [70, 71].

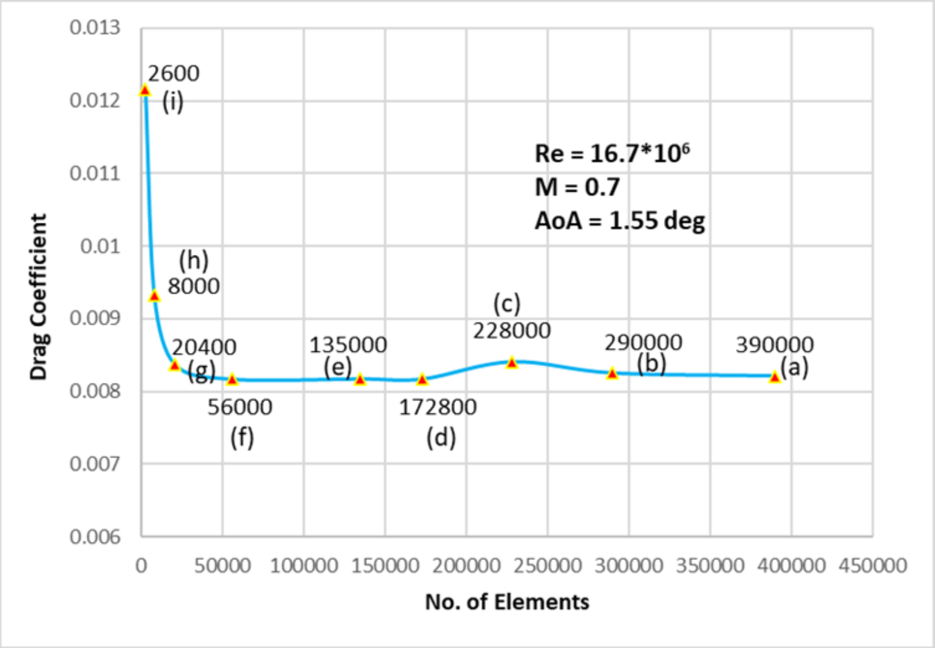

Figure 3.10. Drag coefficients versus number of cells.

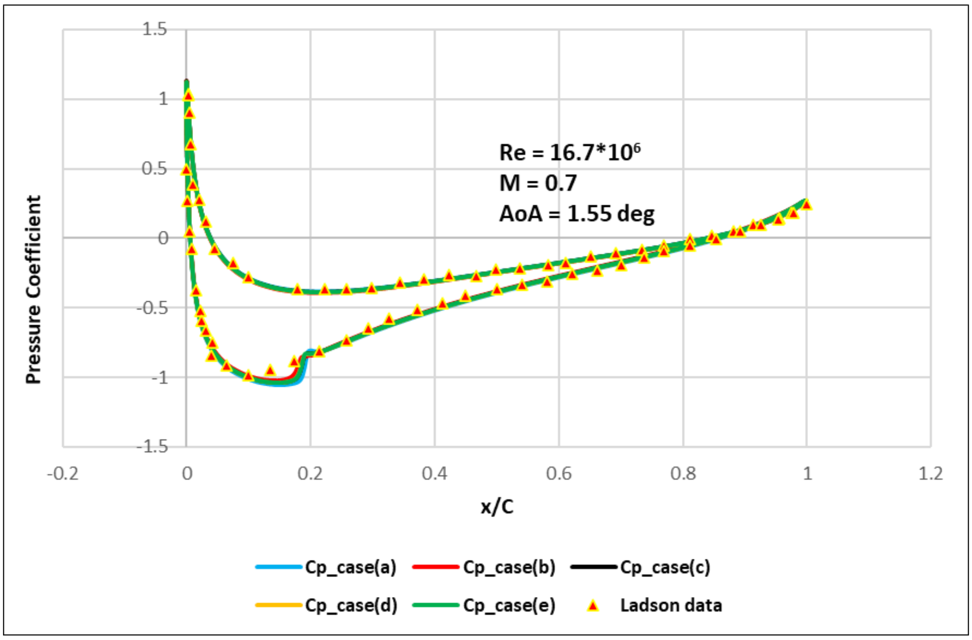

Figure 3.11. Pressure coefficients around the aerofoil for all mesh densities.

The contour plots of pressure and velocity distribution around the aerofoil profile at AoA=1.55° are shown in *Figure 3.12*. The pressure on the suction side (SS) is below atmospheric pressure, while the velocity on the upper surface accelerating and reaches $M \approx 1.1$, slightly above sonic speed.

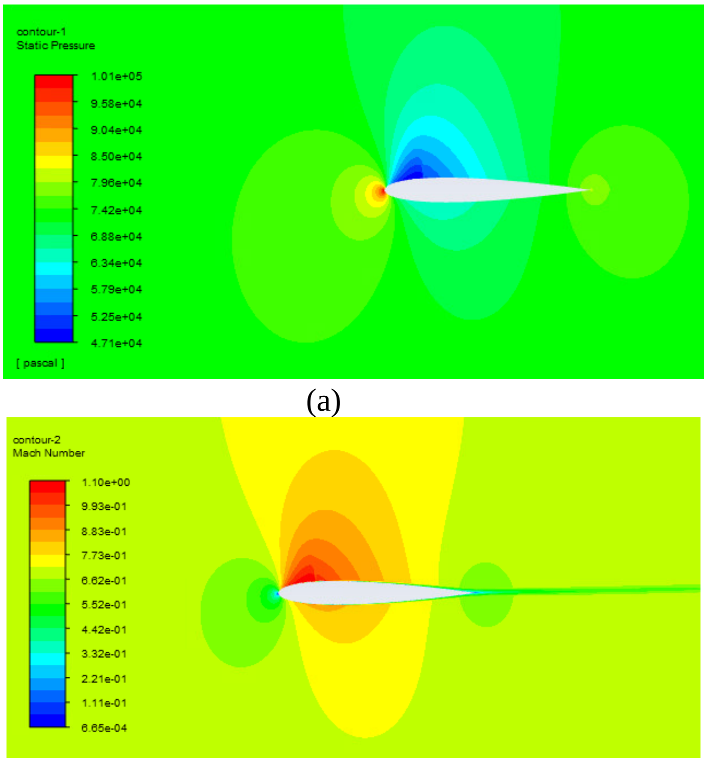

(a)

(b)

Figure 3.12. (a) Pressure, and (b) Velocity contour plots for NACA0012 at AoA=1.55° for inlet air velocity at M=0.7

The maximum pressure occurs at the stagnation point at the aerofoil’s tip where the air velocity is zero. As the air passes over the upper surface of the aerofoil, the pressure substantially decreases and reaches its minimum value while the air velocity significantly increases. On the lower surface of the aerofoil, the air velocity decreases from the free flow velocity to $M < 0.7$. The Mach contour plot in *Figure 3.12(b)* also shows that at the aerofoil’s tip, the velocity is zero (a stagnation point).

Figure 3.13 shows the velocity vector plot around the aerofoil. No reverse flow nor any flow separation can be seen at any point around the aerofoil.

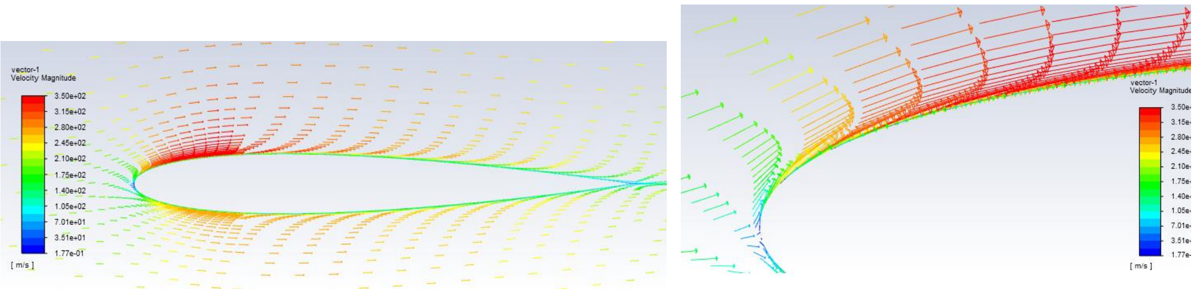

(a)

(b)

Figure 3.13. (a) Velocity vector around NACA0012 aerofoil at AoA=1.55°, and (b) Close up around the aerofoil’s tip

The y^+ value around the aerofoil for mesh densities (a) to (e) are shown in *Figure* 3.14. The results indicate that for meshes (a) to (e) $y^+ < 1$. This assures that the first cell is close to the aerofoil boundary, and it is within the viscous sublayer of boundary layer. Therefore, there is sufficient number of cells within the viscous sublayer thus the outcome is accurate.

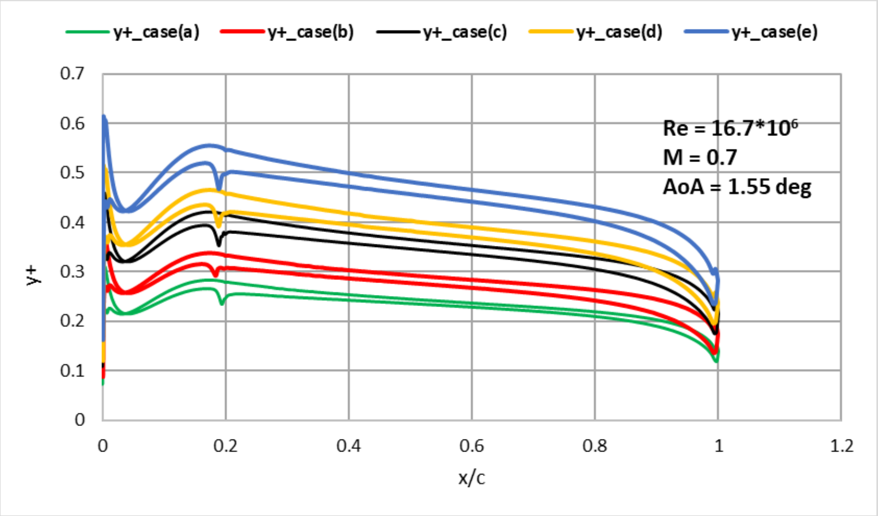

Figure 3.14. y^+ values around the NACA0012 aerofoil for mesh densities (a) to (e),

The above analysis demonstrated that the results from both meshes (d) and (e) are satisfying all conditions for accurate results and the mesh (d) is chosen for investigating the effect of turbulence model on the CFD results.

3.4.2 Selection of Turbulence model

In this section, the four turbulence models briefly discussed in Section 3.3 are employed and the results of each model are compared with Ladson's data [70, 71] for validation. The selected turbulence models were:

- k-ω SST
- k-ε Realizable
- Spalart-Allmaras (S-A)
- γ-Reθ SST (TSST)

For each turbulence model, the accuracy of lift and drag coefficients, and the computational costs are calculated. For this part, Ladson's experimental data at M=0.25, resulting in Reynolds number of 6×10^6, and AoA= 10° is selected [70]. The chord length was kept at 1m as before. All other boundary conditions are the same as explained in previous section.

The results of pressure coefficient distribution around the aerofoil for all four selected turbulence models are shown in *Figure 3.15*. The results show that all turbulence models are in good agreement with the Ladson experimental data in [70].

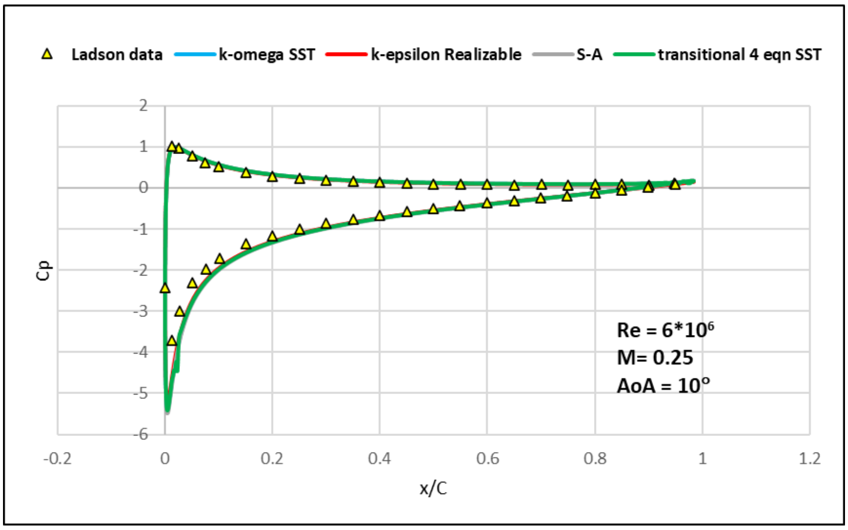

Figure 3.15. Pressure coefficients for the four turbulence models

The results of lift and drag coefficients obtained from these turbulence models are shown in *Figure* 3.16. The results shows that the drag from the TSST turbulence model is the closest to Ladson's experimental data in [70] as well as S-A turbulence model. It is expected that the TSST model will capture separation more accurately, and possibly it could also capture reverse flow at higher angle of attacks. The pressure contour plots from the four turbulence models for AoA=10° are shown in *Figure* 3.17 and the velocity contour plots are shown in *Figure 3.18*.

From such observations, it is concluded TSST model to be the most suitable turbulence model for further work.

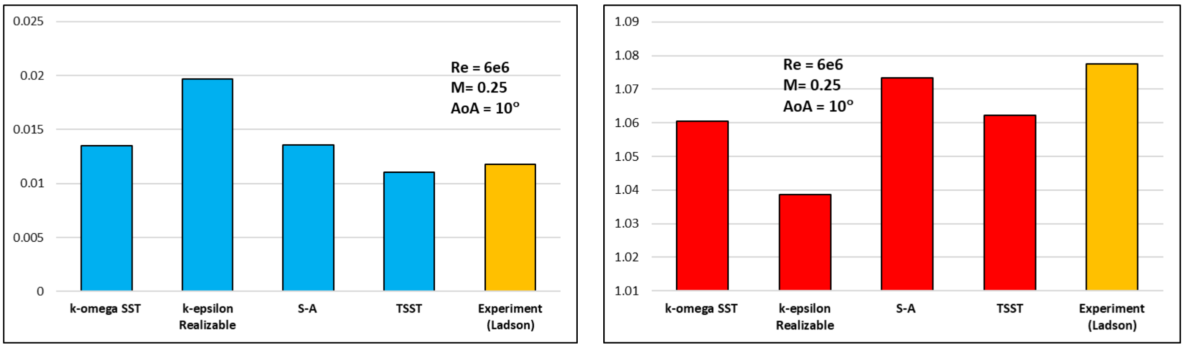

(a) (b)

Figure 3.16. Comparison of (a) lift, and (b) drag coefficients obtained from the four turbulence models and Ladson experimental data

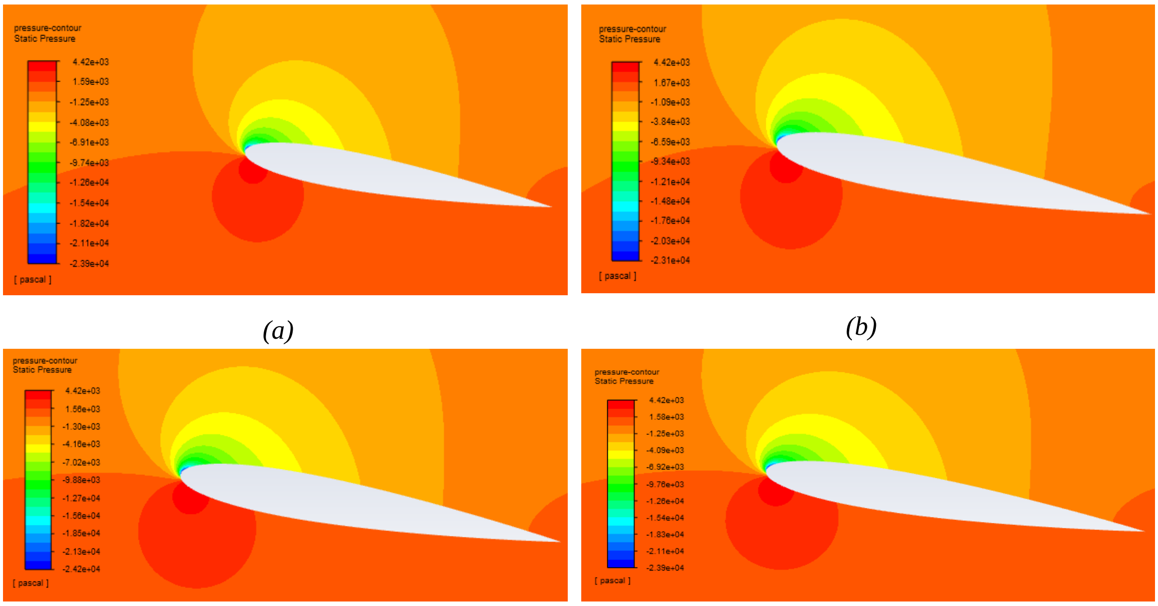

(a) *(b)*

(c) *(d)*

Figure 3.17. Pressure contour plot for M=0.25 and AoA=10° for turbulence model (a) k-ω SST, (b) k-ε Realizable, (c) S-A, and (d) TSST

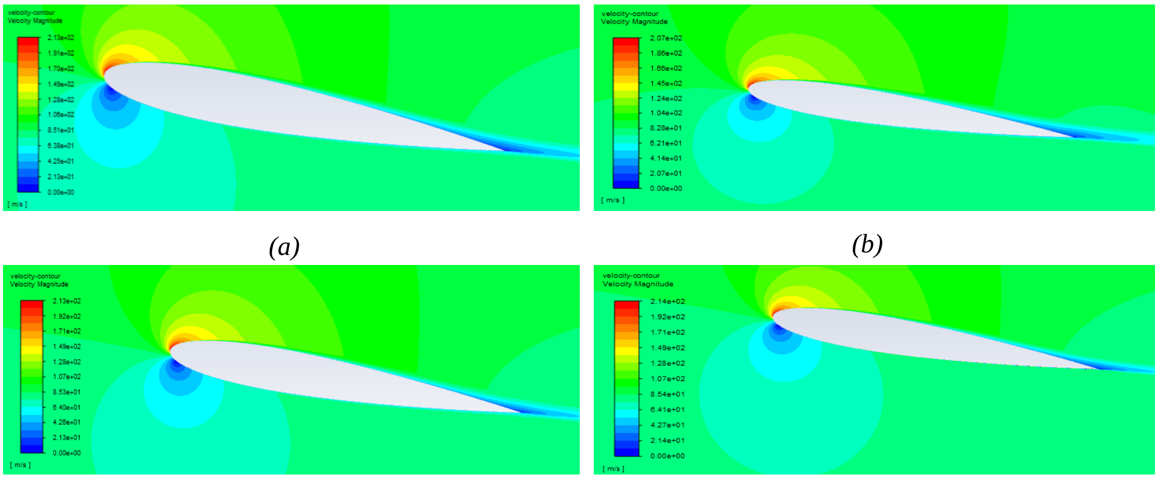

(a) *(b)*

(c) *(d)*

Figure 3.18. Velocity contour plot for M=0.25 and AoA=10° for turbulence model (a) k-ω SST, (b) k-ε Realizable, (c) S-A, and (d) TSST

The velocity contours plots of the selected turbulence models in Figure 3.18 show that the air velocity reaches to its maximum value near the leading edge at the SS of the aerofoil. It also noted that near the trailing edge of the aerofoil, the velocity on the SS is much lower than pressure side (PS). This could create some degree of reverse flow in that region (see *Figure* 3.19).

The result of this section shows that the TSST model is similar to the k-ω SST. Generally, in the case of stationary flows, where the boundary layer is under equilibrium, this is the case. However, if the flow is strongly unsteady, as it could happen in heavily eroded blade with non-symmetrical damage along the span or for high AoA, the TSST model is preferred, and it is the most suitable model to be used for the aerodynamics of aerofoils.

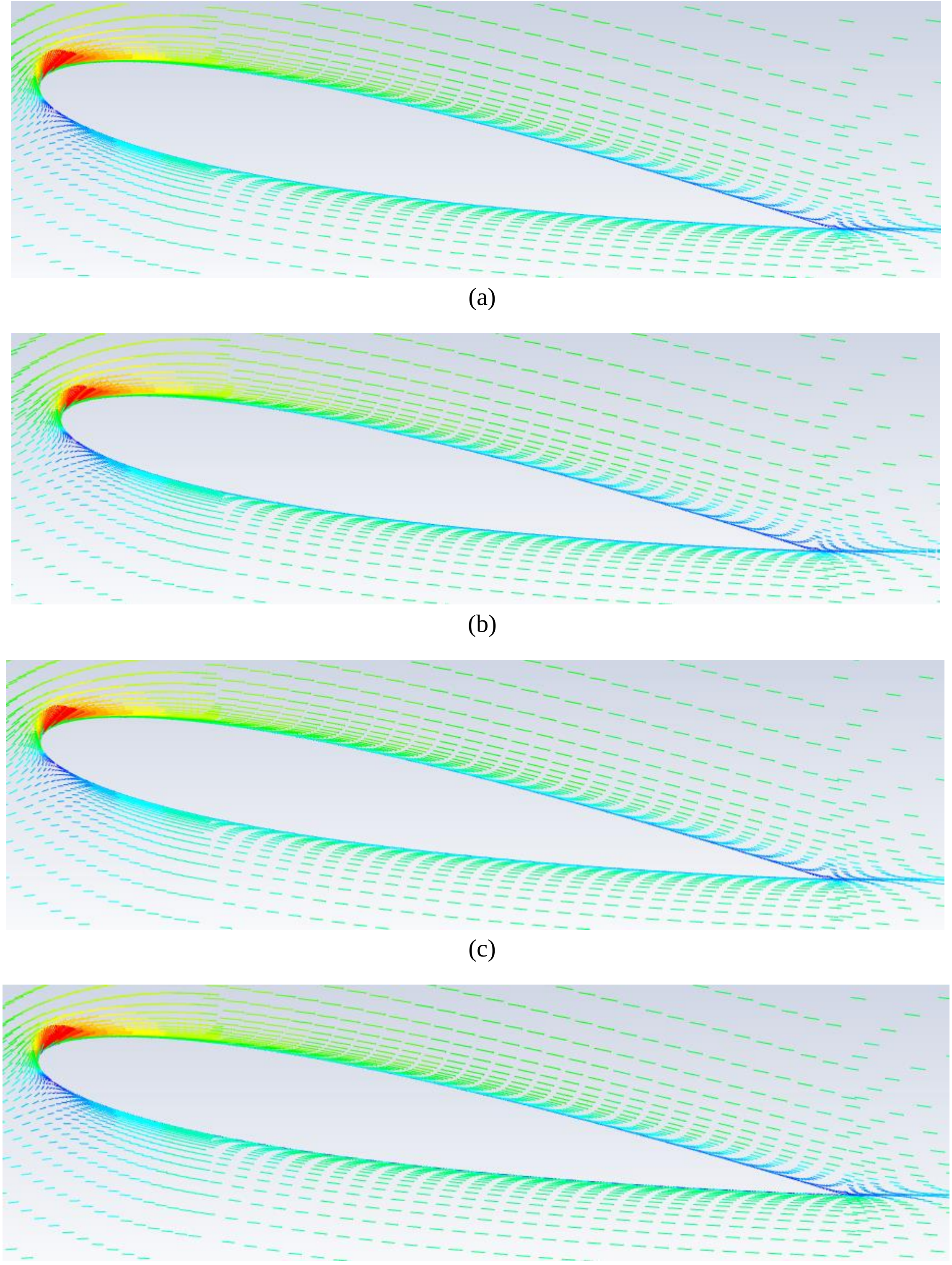

(a)

(b)

(c)

(d)

Figure 3.19. Velocity vector for AoA=10° for turbulence model (a) k-ω SST, (b) k-ε Realizable, (c) S-A, and (d) TSST

3.4.3 Lift and drag coefficient at various angles of attack

The performance of the aerofoil at different angles of attack was investigated using Fluent and XFOIL software. The angle of attack was varied from -10° to 15° with a 2.5° increment. The results of lift and drag coefficients are shown in *Figure 3.20,* and *Figure 3.21*, respectively.

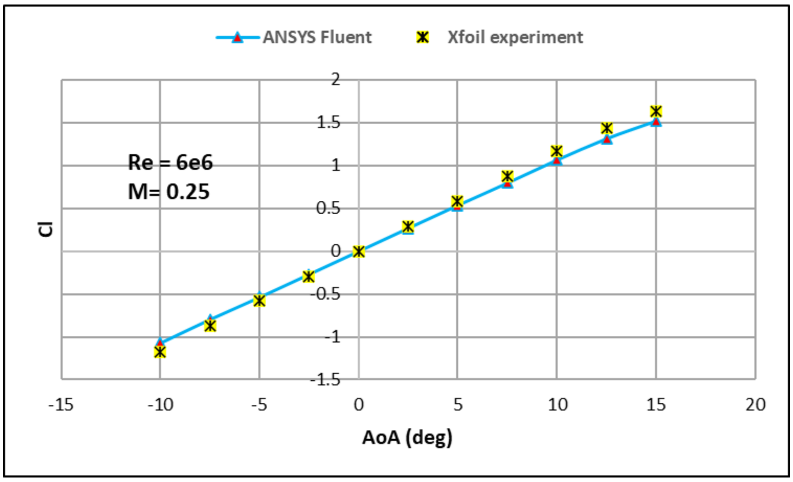

Figure 3.20. Lift coefficient versus angle of attached for NACA0012 aerofoil

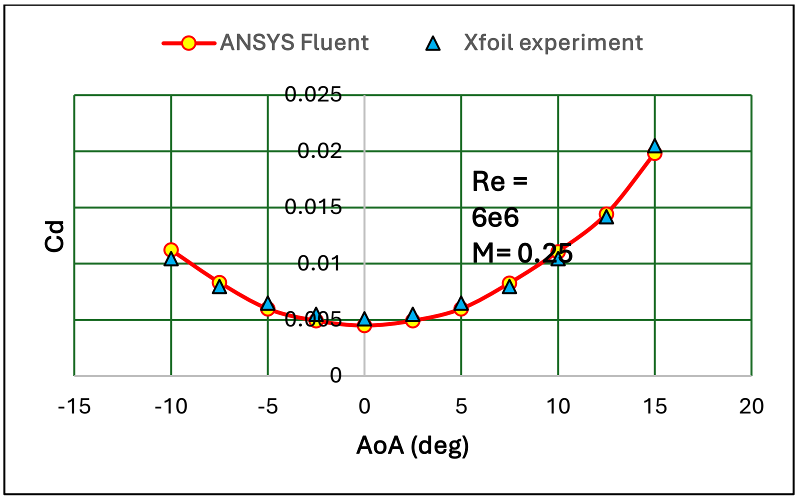

Figure 3.21. Drag coefficient versus angle of attached for NACA0012 aerofoil

The drag coefficient initially decreases as the AoA increases from -10°, and it reaches to its minimum value at AoA=0°. Then it increases as the AoA increases to 15° as shown in *Figure 3.21*. The lift and drag coefficients were also calculated using the XFOIL software and they are presented in *Figure 3.20,* and *Figure 3.21*. The proximity of the XFOIL results and CFD validate the results of the CFD modelling.

For a NACA 0012 aerofoil, the lift coefficient (C_L) increases approximately linearly with the angle of attack (α) in the low to moderate range, typically between 0° and 10°. In this range, the airflow remains largely attached to the aerofoil's surface, and the aerodynamic behaviour follows thin aerofoil theory, where lift is proportional to the angle of attack. However, as the angle of attack increases beyond a critical value, usually around 12° to 15°, flow separation begins near the trailing edge. This reduces the aerofoil's lift-generating capacity, and beyond this point, known as stall, the relationship between lift and angle of attack becomes non-linear, with the lift coefficient decreasing rapidly.

From the results of lift and drag coefficient, the glide ratio ($GR = C_L/C_D$) was calculated, and the results are presented in *Figure 3.22*. The maximum glide ratio is obtained at $AoA = 7.5\,°$with $GR \approx 96$. The glide ratios obtained from ANSYS Fluent are in very good agreement with those data obtained from XFOIL software, confirming the accuracy of CFD modelling.

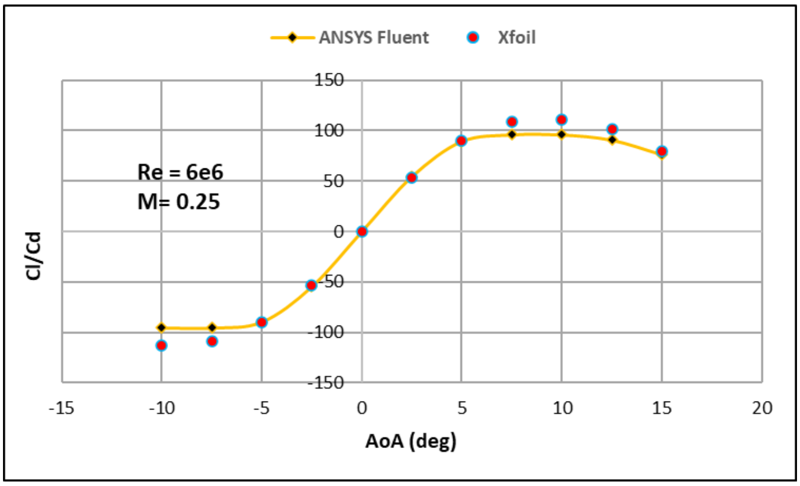

Figure 3.22. Comparison of glide ratio vs AoA, at M=0.25 and Re=6×10^6 calculated by Fluent and XFOIL

Pressure and velocity contour plots for -10° $< AoA < 15°$ are shown in Table 3.3. It is important to note that for $AoA > 5°$ or $AoA < -5°$, flow separation and reverse flow occur, becoming particularly noticeable near the trailing edge of the aerofoil. The static pressure is relatively high on the upper surface of the aerofoil, while there is suction on the lower surface for $-10° < AoA < 0°$. Since the NACA0012 is a symmetric aerofoil, at $AoA = 0$, both the velocity and pressure distributions are symmetric. For $AoA > 0°$, the aerofoil operates normally, with suction on the upper surface and pressure on the lower surface, thereby generating lift.

Table 3.3. Velocity and pressure contours for each AoA

AoA (deg)	**Pressure Contour**	**Velocity Contour**
-10	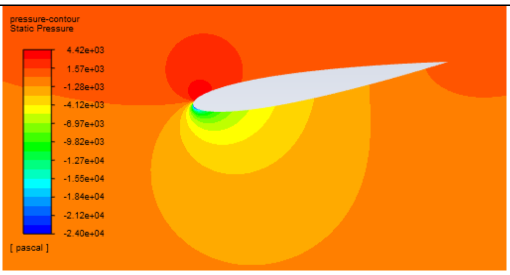	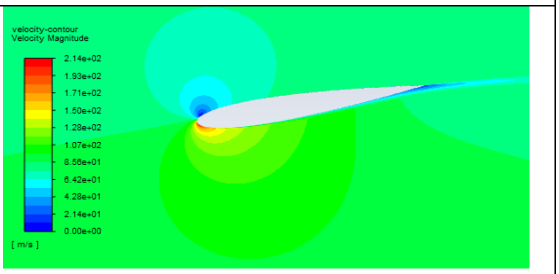
-7.5	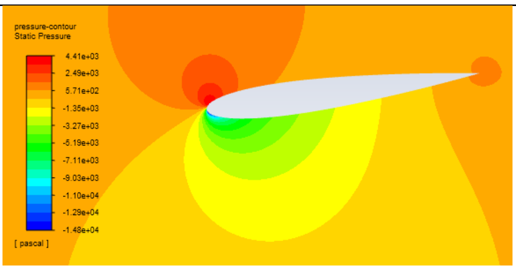	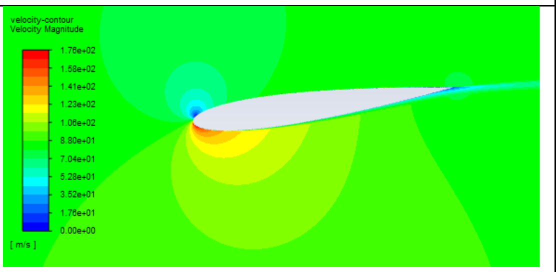
-5	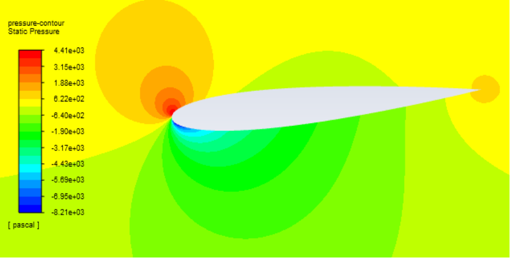	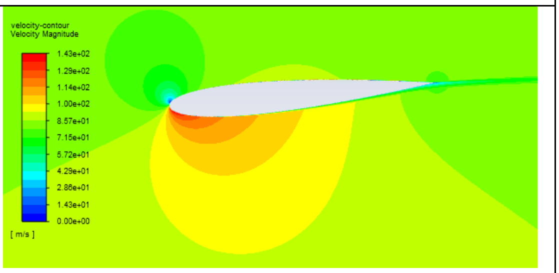
-2.5	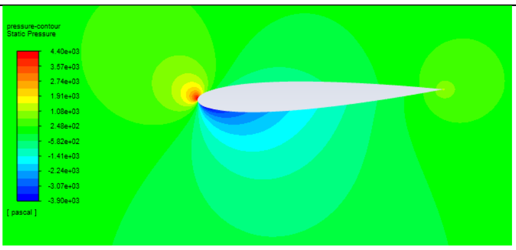	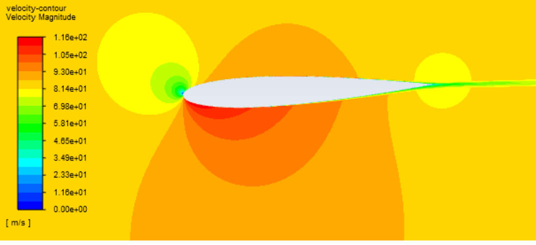
0	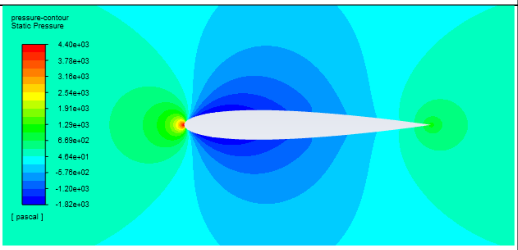	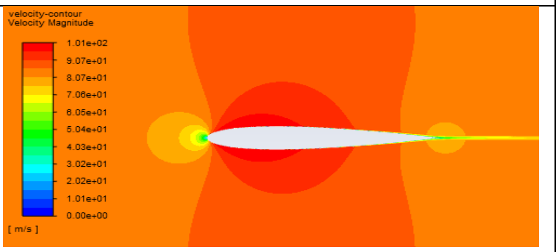

2.5	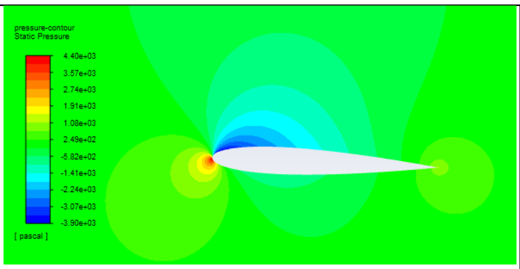	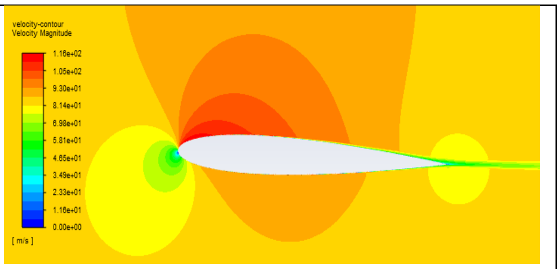
5	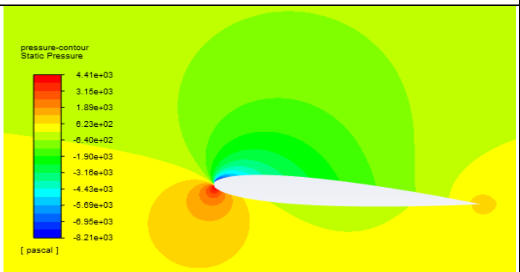	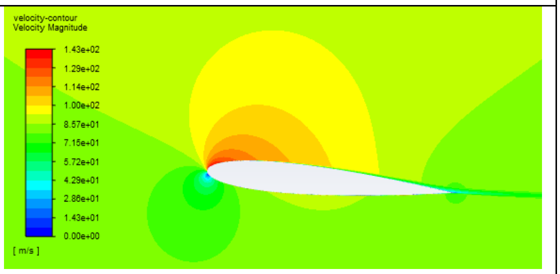
7.5	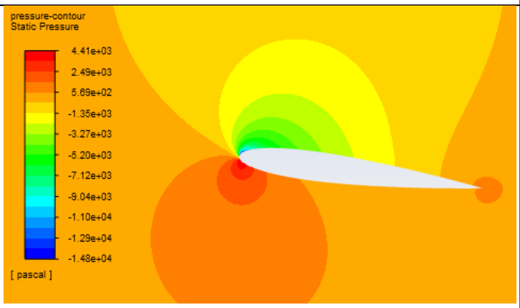	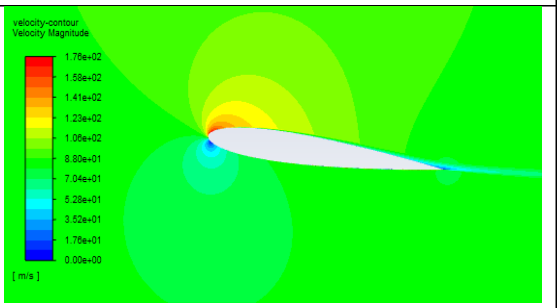
10	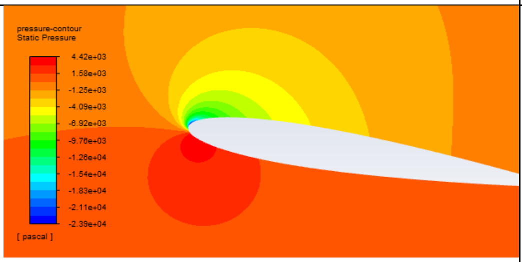	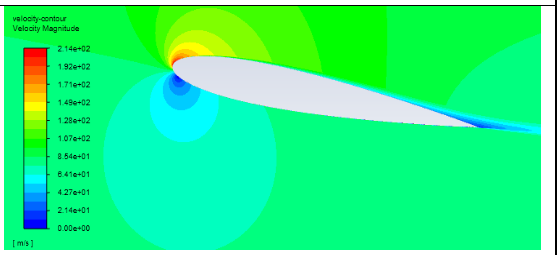
12.5	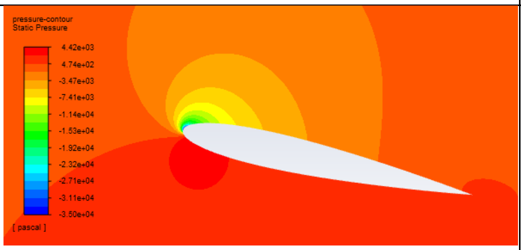	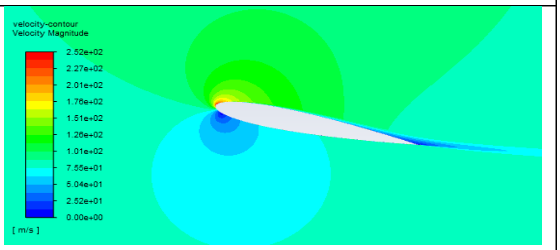
15	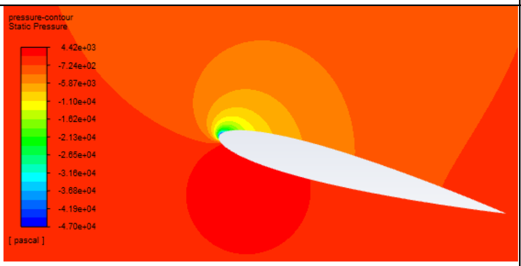	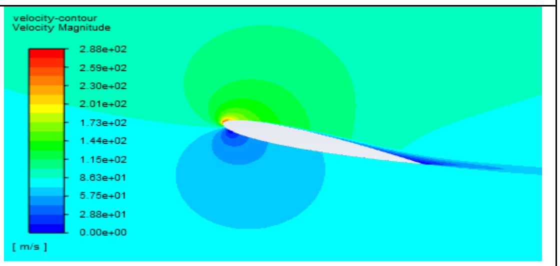

3.5 Aerodynamic analysis of leading-edge eroded blades

The reported Annual Energy Production (AEP) loss due to LEE varies from 3-25% depending on the extent and location of the damage. Sareen et al. [2] reported that for many moderate to heavy eroded blades, an increase in drag of 6-500%, coupled with the loss in lift, led to an AEP loss as high as 25%. They also reported that even a small amount of LEE can result in an AEP loss of approximately 3–5% [2]. Özçakmak et al. [11] calculated the thrust and power losses using both CFD and OpenFAST, finding comparable results with both methods. In a severe erosion case, spanning the last third of the blade, a 4.3% reduction in the AEP was reported. Using laser scans and machine learning prediction, it is reported that AEP losses varied from 0.3% to 0.8% of the nominal AEP [12]. Campobasso, et al. [13] used the NREL AeroDyn blade element momentum theory code, and by making use of a variant of the NREL 5MW turbine obtained by replacing the NACA 64-618 with the DU 96-W-180 aerofoil, showed that an AEP loss between 2.1% and 2.6%, based on both experiments and simulations, can occur. Law, et al. studied wind farms and reported an average AEP loss of 1.8% for medium levels of erosion, with the worst affected turbine experiencing an AEP loss of 4.9% [3]. Sandia National Laboratories estimated the AEP losses to be between 5–8% [14]. Experimental [15] and numerical [16] studies reported AEP losses of 4%, increasing to 6% when top coat on the leading edge is damaged [17].

In this section, the effect of erosion of lift and drag coefficient of a blade with NACA0012 is investigated using two- and three- dimensional CFD modelling.

3.5.1 Two-dimensional eroded aerofoil modelling

LEE, among other form of damages, can severely affect the aerodynamic performance of a wind turbine blade, significantly impacting its efficiency and lifespan. The severity of LEE's effect on an aerofoil's aerodynamic performance depends on the damage depth, and area of the damage. In this study, as shown in *Figure 3.23*, the aerofoil type chosen was a NACA0012 profile with an erosion length of 10% of the chord length (0.1*c*, with *c* being the chord of the aerofoil). The damage depth (h) was varied to investigate its effect on the generated lift and drag forces.

The model was simulated using a C-mesh with a radius of 12c and a wake region length of 12c in the streamwise direction. The fluid domain was obtained using Boolean subtraction of the aerofoil from the C region. The meshing process was carried out using the meshing software of the ANSYS Fluent. The quality of each grid is monitored by measuring mean skewness and mean orthogonal quality, both of which were acceptable. The boundary layer's resolution and near wall meshing was ensured, with wall y+ distribution being less than 1, guaranteeing adequate resolution of the near-wall flow.

CFD simulations were performed in ANSYS Fluent, using second-order upwind schemes for spatial discretization. The Transition SST (TSST) turbulence model was employed. The convergence tolerance for all the residuals set to 1×10^{-6}. The boundary conditions included an inlet velocity on the domain C edge, specified to achieve a Reynolds number Re = 3×10^5. A pressure-outlet condition was set on the outlet section by specifying reference value for the static pressure.

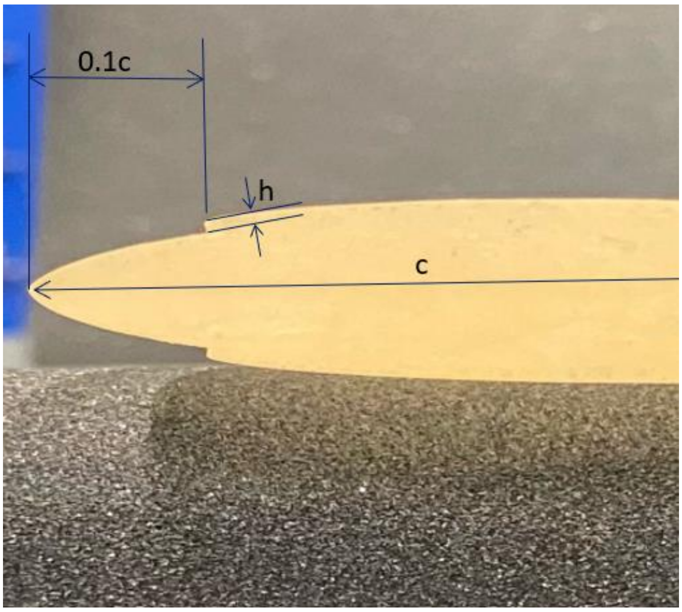

Figure 3.23. Geometrical representation of eroded aerofoil showing the chordwise delamination length of 0.1c and the delamination depth h

Four different aerofoil models analysed are shown in *Figure 3.24*. The undamaged blade is the control one, and the severity of erosion was increased by increasing the erosion depth *h* to 0.6mm, 1mm and 1.4mm.

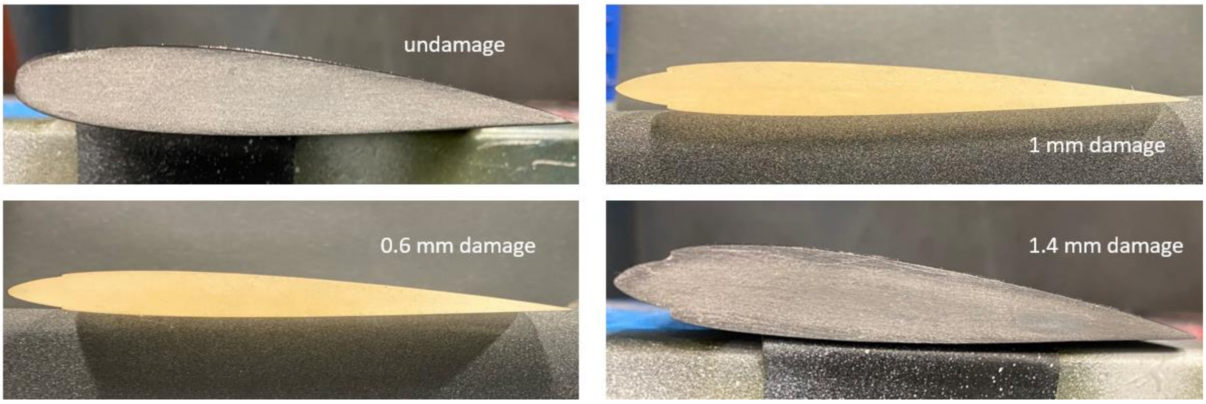

Figure 3.24. NACA0012 aerofoil with different degree of LEE: Undamaged, h=0.6 mm, h=1mm and h=1.4mm

The lift and drag coefficients for each case were computed at an angle of attack of 5°. The pressure and velocity contour plots for each aerofoil are obtained to monitor if reverse and/or separation flows occurred. The results of velocity and pressure contours plot for the undamaged and the three eroded aerofoils for AoA=5° are shown in *Figure 3.25*.

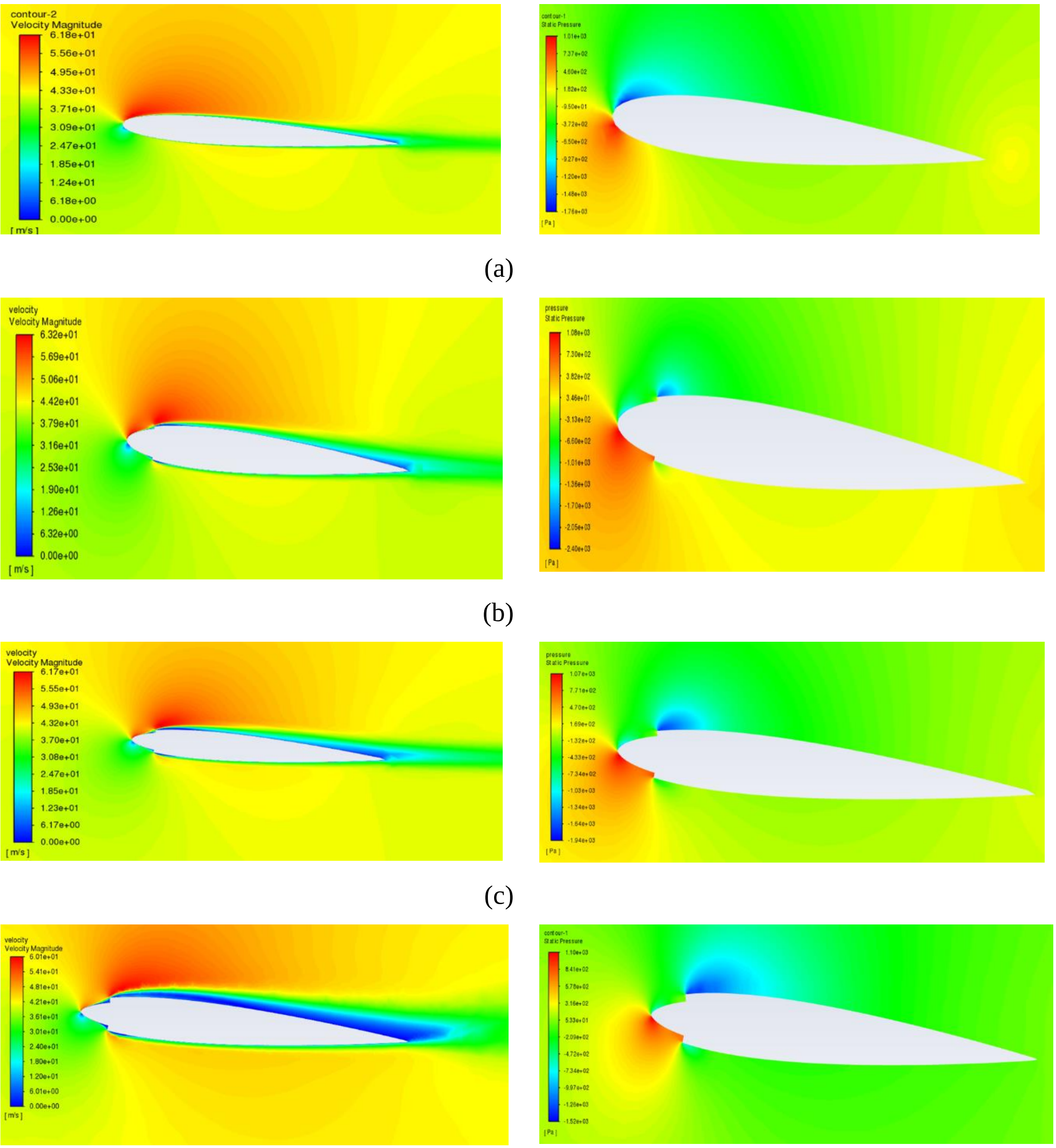

(a)

(b)

(c)

(d)

Figure 3.25. Velocity and pressure distribution contour plots for NACA0012 for (a) undamaged and eroded with erosion depth h (b) 0.6mm, (c) 1.0mm, and (d) 1.4mm at Re=300,000.

For undamaged aerofoil, the flow was smooth across the aerofoil, and flow separation or reverse flow was not detected at any point around the aerofoil. For eroded aerofoil with h=0.6mm, the velocity and pressure distribution around the eroded area started to change; resulting an increase in the pressure on the suction side. In addition, because of the damage, reverse flow from the end of damaged point was formed, causing some disruption to the air flow pattern as shown in *Figure 3.26*(a). By increasing the depth of erosion (higher h=1.0mm), the length of the reverse flow at the SS extended further as shown in *Figure 3.26*(b), hence resulting in a lower lift and a higher drag force.

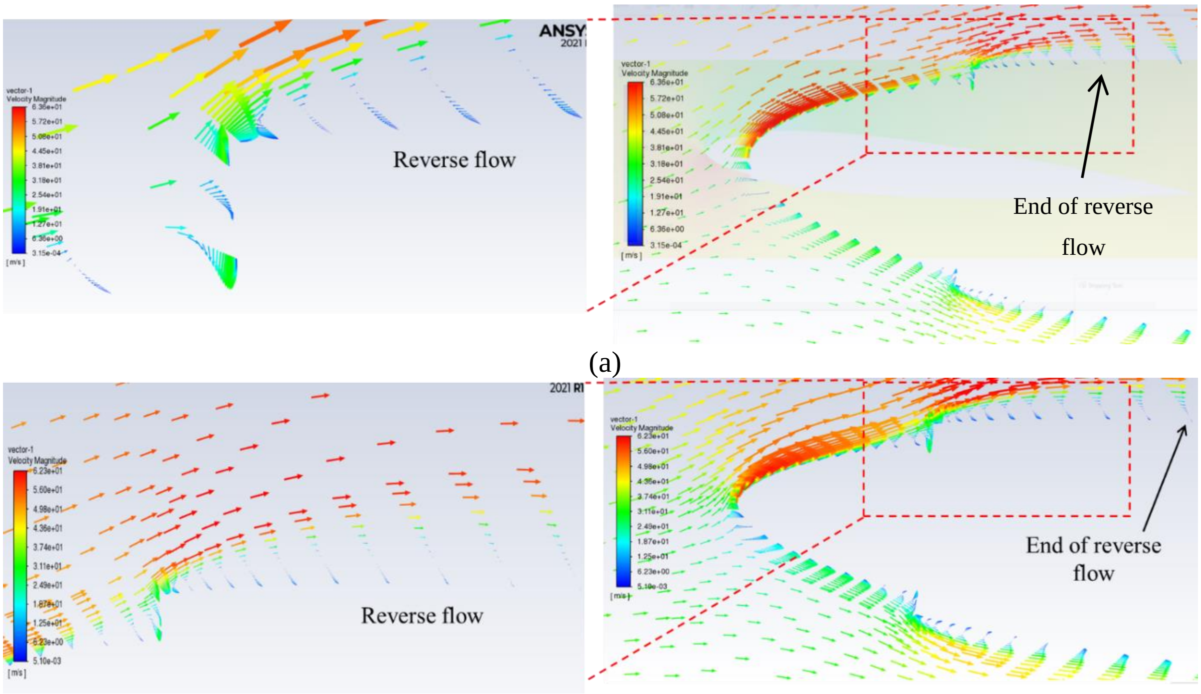

(a)

(b)

Figure 3.26. Velocity vector for eroded NACA0012 with (a) h=0.6 mm, and (b) h=1.0mm showing the extension of reverse flow as the depth of erosion increased at Re=300,000.

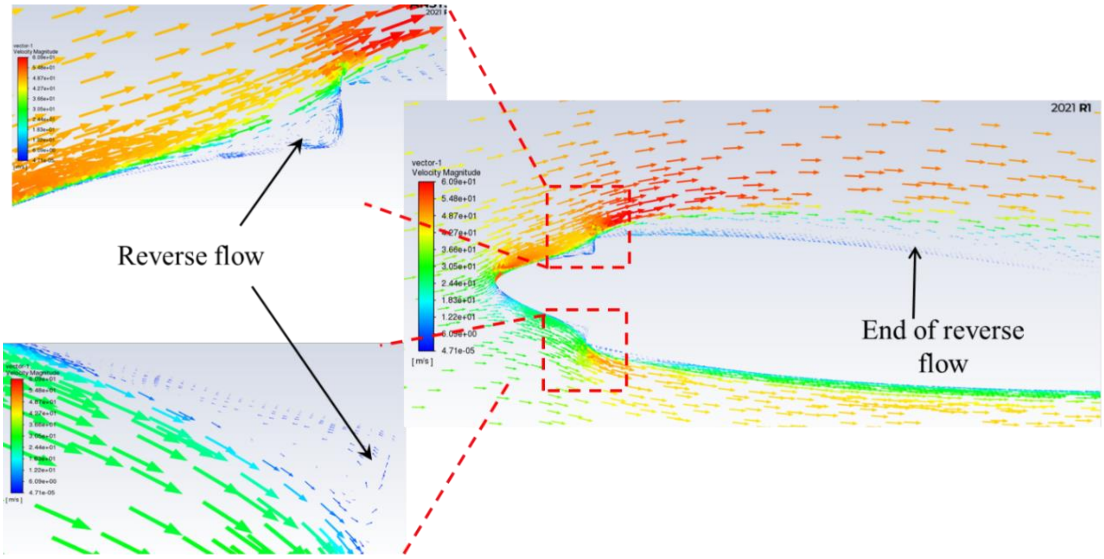

(a)

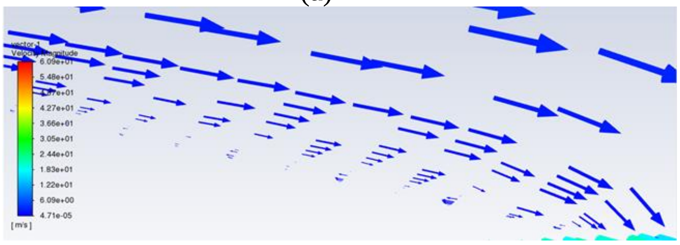

(b)

Figure 3.27. Velocity vector for leading edge damage h=1.4 mm depicting the severity of reverse flow at (a) suction and pressure side, and (b) near the trailing edge at Re=300,000.

With the increase in erosion depth to the maximum value of 1.4mm, the distribution of pressure around the aerofoil was adversely affected, as seen in *Figure 3.25(d)*, severely impacting lift generation. In addition, as shown in *Figure 3.27*, the reverse flow extended further, reaching the trailing edge of the aerofoil. This, coupled with the increase in flow separation and the presence of circulation, substantially increased the drag force. The combination of lower lift and the much higher drag force will result in a loss of energy production for the wind turbine.

The results of lift and drag coefficients for various value of erosion depth for AoA=5° are shown in *Figure* 3.28. The lift coefficient decreased by about 32.5% and the drag coefficient increased by 101% as the leading-edge damage increased to a depth of 1.4mm. Consequently, the overall effect of the leading-edge erosion is the reduction in power generation of wind turbine while there will be a threat to the structural integrity of the blade as well.

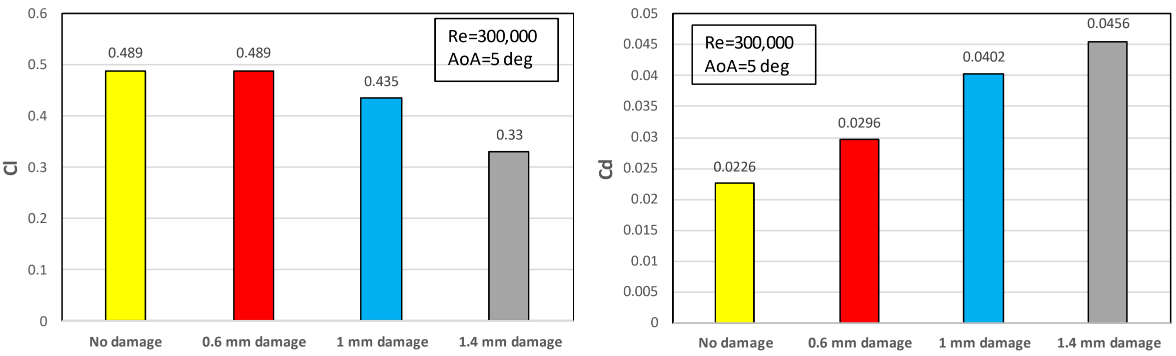

(a) (b)

Figure 3.28. (a) lift, and (b) drag coefficients for the NACA0012 aerofoil with LEE damage depth from h=0.6mm to h=1.4mm at AoA=5°, Re=300,000, and TSST turbulence model.

3.5.2 Three-dimensional eroded aerofoil modelling

Three-dimensional eroded NACA0012 aerofoils were created at various LEE severity as shown in *Figure 3.29*. These models are representative of a blade element, hence there is no twist or tip effects. The model underwent a C-type mesh with a radius of 12c and a wake region length 12c in the direction of the stream flow. The fluid domain was obtained using Boolean subtraction of the blade from the domain region.

All blade elements have a span of 0.65*c*, an average eroded length of 0.1c, and a delamination depth of 0.014c, where c is the chord length. The sever case (d) of LEE has been observed in real blades after 10+ years of operation [2]. For case (d), three hybrid refined mesh grids were produced: coarse, medium, and fine, resulting in 1.25, 2.5 and 5 million cells, respectively. Using ANSYS Fluent, the meshing was generated, and the quality of each grid was tested, resulting in an average orthogonal quality of 0.65 and skewness of 0.34. As reported in Carraro, et al. [72], a hybrid structured-unstructured mesh is generated, where the unstructured mesh is used to construct the blade's 3D features around the eroded area. Structured cells, on the other hand, are placed in the flow areas close to the blade's walls to enhance the resolution within the boundary layer and to maintain proper wall y^+ values. An overview of the whole grid is shown in *Figure* 3.30. Damage to the leading edge was created by randomly subtracting spheres (a to c) and cylinders (d) from the aerofoil, within 10% of the chord length from the leading edge.

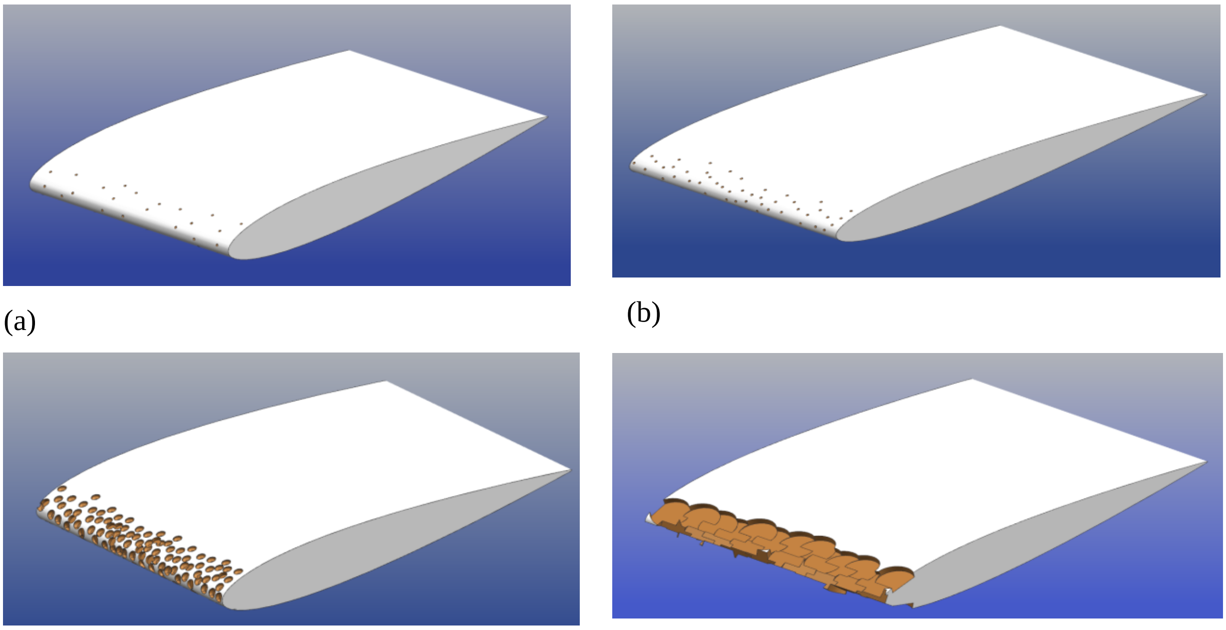

(a) (b)

(c) (d)

Figure 3.29. CAD models of the 3D blade element with NACA0012 aerofoil at four level of leading edge erosion: (a) minor, (b) low, (c) medium, and (d) sever erosion cases.

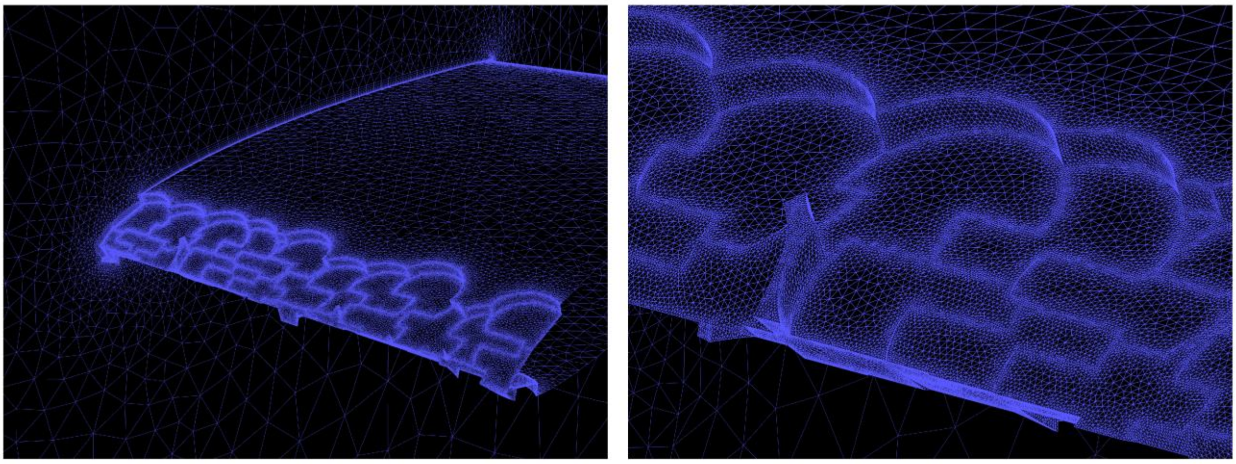

(a) (b)

Figure 3.30. Mesh overview of the 3D NACA0012 with leading edge damage (fine grid), adapted from Carraro, et al. [72]

As before, the CFD simulations were executed using the Coupled scheme in ANSYS Fluent. Spatial discretization was handled with a 2nd order upwind scheme, while the Least Squares Cell-Based approach was implemented for the calculation of gradients. A convergence tolerance of 10^{-6} was set for all parameters for the iterative Navier–Stokes residuals. The applied boundary conditions, shown in *Figure 3.31*, include an inlet velocity on the C-domain edge (red area) and a reference static pressure on the outlet section (yellow area). All surfaces of the blade section were treated as wall with a no-slip condition. A flow symmetry condition was imposed on the lateral boundaries (blue areas). The free stream velocity was set to achieve a Reynolds number of $Re = 3\times10^5$, which is typical for a wind turbine. Finally, the model was initialised using hybrid initialization with 10 iterations [72].

To validate the CFD results for the 3D aerofoil, a mesh sensitivity analysis was performed to establish the level of grid refinement required to make the results mesh-independent. The turbulence models considered were the 4-equation transitional SST (TSST), S-A, and k-ω SST models. The analysis was performed for the three mesh grids with 1.25, 2.5 and 5 million cells. The drag coefficient values were scaled with the corresponding outcome obtained with the most refined mesh and with the TSST turbulence model, $C_{d\text{-Fine,TSST}}$. The results of the analysis are shown in *Figure 3.32*. The results show that for all three turbulence models, the scaled drag coefficient reached and maintained the value of 1 as the mesh refinement level increased from 1.25 million cells (1) to 5 million cells (4). The TSST did not outperform the other turbulence models. This is due to the damage on the leading edge triggering the separation of the boundary layer of the turbulence flow. Based on the y^+ values for the TSST turbulence model shown in *Figure 3.32(b)*, the near-wall resolution for the TSST model is considerably higher than the recommended y^+ thresholds for wall-resolved RANS simulations, which is $y^+<1$. Hence, the TSST model coupled with the fine mesh grid (with 5 million cells) was chosen for the 3D CFD modelling of the wind turbine blade element with a severely eroded blade section [72].

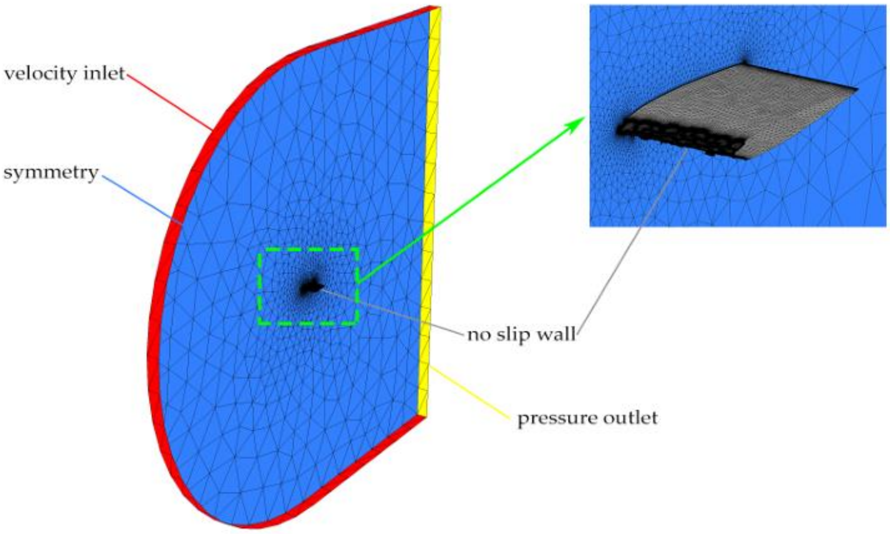

Figure 3.31. Boundary condition overview: inlet velocity is highlighted in red; outlet pressure is highlighted in yellow, and symmetry boundary condition is highlighted in blue, adapted from Carraro, et al. [72]

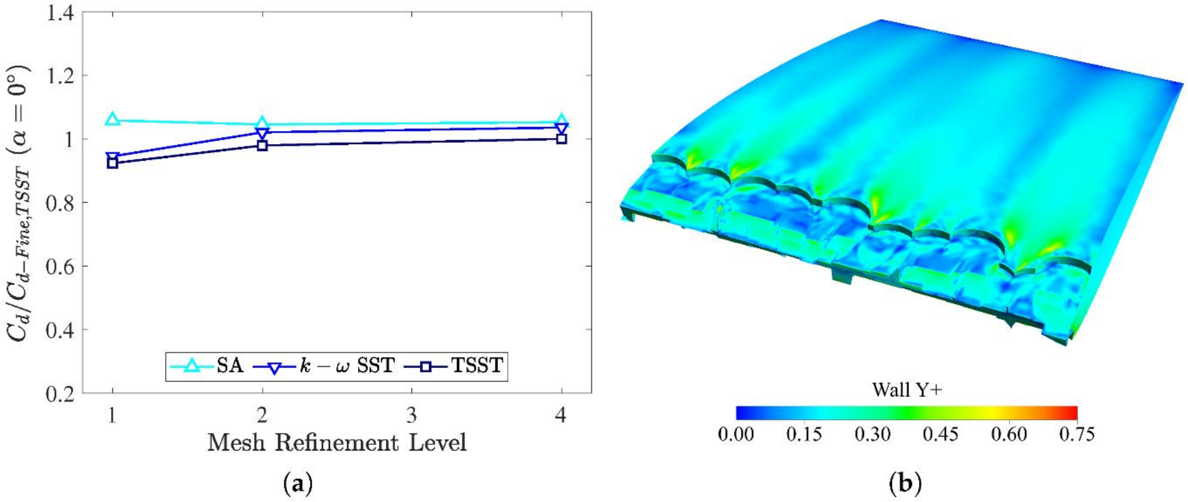

Figure 3.32. 3D model validation: (a) drag coefficients for the eroded aerofoil accounting for different turbulence models and mesh refinement levels, (b) y^+ contour generated with the fine mesh grid with TSST turbulence model at AoA= 0° [72]

The lift and drag coefficients computed from 2D and 3D models were compared for a range of angle of attack in *Figure 3.33*. The results show that the lift coefficients for the 2D and 3D models are in close proximity, whereas the drag coefficients for the 3D model are approximately 17% higher than those of the 2D model across the entire range of angles of attack. The close similarity in lift coefficients for both models is attributed to their similar pressure fields over a considerable range of angles of attack, whilst the difference in drag coefficients is attributed to the various wall dynamics faced by the 3D geometry near the leading edge in the 3D model.

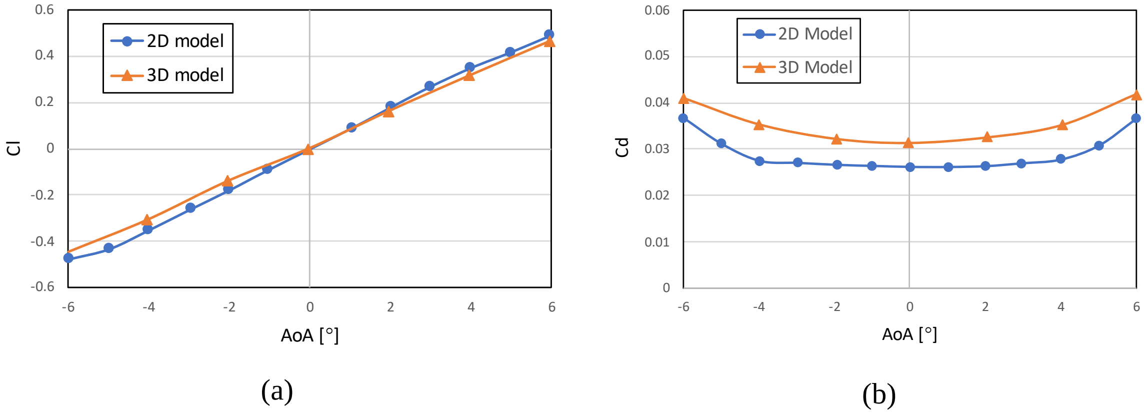

Figure 3.33. Comparison of (a) lift, and (b) drag coefficients for 2D and 3D aerofoils models [72]

Even though the friction coefficient is important for predicting the blade aerodynamics, for any digital twin model that relies on estimating a wind turbine's life span should primarily aim to accurately evaluate the lift coefficient. Lift is the main contributor to AEP by a wind turbine; hence and is, therefore, the fundamental basis for estimating maintenance interventions. As a result, a calibrated 2D model has been demonstrated to thoroughly represent the overall aerodynamics of a wind turbine blade under leading edge erosion conditions at a lower computational cost than a 3D model.

The advantage of 2D modelling is its lower computational cost. A 2D simulation took roughly 30 minutes to converge the flow quantities, while the 3D simulation took approximately 15 hours, 30 times higher than 2D model. This makes the computational cost for the 2D model trivial and allows it to serve as the basis for defining a digital twin to estimate the wind turbine's lifespan [72].

The difference in pressure and friction coefficients between the undamaged and the eroded blades induces a significant reduction in the off-design performance of the eroded blade. In this regard, *Figure 3.34* compares the lift and drag coefficients of these two 2D geometries. The flow angle of attack values up to the stall condition were investigated. To analyse the behaviour of the aerofoil beyond this condition, a non-stationary model would be required, which is beyond the scope of this work. As shown in *Figure 3.34*(a), simulations predict that erosion has a small impact on the lift coefficient at low flow incidences, while a more pronounced discrepancy is observed at higher angles of attack. On the other hand, the eroded aerofoil's drag polar plot is systematically shifted upward between 18% and 125% across the entire operating range. Thus, both the C_l and C_d curves reveal a degradation of the aerodynamic performance of the eroded aerofoil, which generally increases at higher angle of attack.

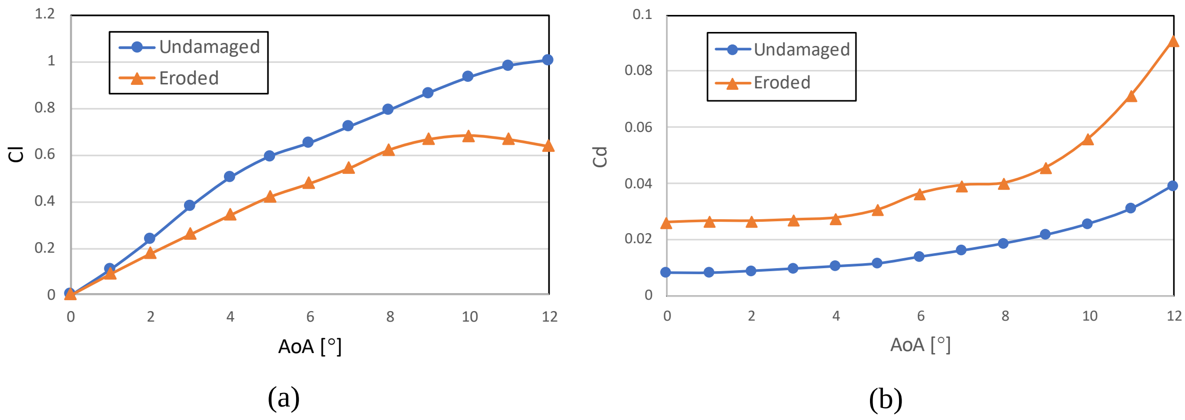

(a) (b)

Figure 3.34. Comparison between coefficients of (a) lift, and (b) drag versus AoA for undamaged and eroded aerofoil from 2D models [72]

3.6 Conclusion

In this chapter, the effect of leading-edge erosion on the performance of two- and three-dimensional aerofoils is investigated. The impacts of grid resolution, and turbulence model on the lift and drag coefficient were evaluated, and the appropriate mesh size and turbulence model were identified. A validation campaign with experimental data is reported for global and local quantity convergence, determining the optimal mesh refinement level and the most appropriate turbulence model for predicting the aerofoil and blade aerodynamic performance at low-Reynolds numbers experienced during wind turbines operation.

The significance of mesh quality on computational accuracy was scrutinised by carrying out a mesh sensitivity analysis. For this part, different mesh densities cases were set up, and dimensionless wall distance (y^+) values were examined to determine their validity and suitability for subsequent modelling and simulation studies. It was shown that a 2D mesh with 500k cells coupled with the TSST turbulence model provides a good balance between computational time and accuracy, while a 3D model with five million cells, in combination with the TSST model, ensures grid independency for blade aerodynamics.

The performances of undamaged and eroded blades were investigated for 2D and 3D geometries. It is shown that 2D modelling has a lower computational cost relative to 3D modelling by a factor of 30. The 2D model provides acceptable results and could serve as the basis for defining a digital twin to estimate the wind turbine’s lifespan.

The Mach number for wind turbines primarily depends on the rotor size and the rotational speed of the blades. Generally, large wind turbines operate at Mach numbers in the range of 0.2 to 0.3 at the blade tips. In this range no shock wave is expected to form on an aerofoil and the flow remains subsonic. Although there are some minor compressibility effects, these are insufficient to generate shock waves. Shock waves only become a concern at higher Mach numbers (approaching or exceeding transonic speeds, around Mach 0.7 or above).

Finally, the results showed that erosion has a small impact on the lift coefficient at low flow incidences, while a more pronounced discrepancy is observed at higher angles of attack. In addition, the eroded aerofoil’s drag polar plot increases between 18% and 125% across the entire operating range. Thus, both the C_l and C_d results reveal a degradation of the aerodynamic performance of the eroded aerofoil, which generally increases at higher angle of attack, leading to the loss of annual energy production of a wind turbine.

Chapter 4: Processing of polyurethane nanocomposites and their physicochemical analyses

4.1 Introduction

This chapter discusses the manufacturing processes and procedures for pure polyurethane (PU) and its modified nanocomposites, which include PU+GNP, PU+GNP+CNT, PU+SiO_2, PU+SiO_2+GNP and PU+SiO_2+CNT. Physicochemical characterisations are essential for the development of new materials. In this work, the Fourier-Transform Infrared spectroscopy (FTIR), Differential Scanning Calorimetry (DSC), Thermogravimetric Analysis (TGA), and Dynamic Mechanical Analysis (DMA) techniques were used to determine various properties of pure PU and PU nanocomposites including mechanical, thermal, and chemical properties.

DSC was used for the measurement of heat flow and temperature changes during thermal transitions. FTIR is used for analysing the chemical composition and molecular structure of the PU nanocomposites. TGA was performed to study the thermal stability and composition of materials by measuring the change in their weight as a function of temperature. DMA is used to determine the glass transition temperature and damping coefficient. Finally, water contact angle (WCA) measurement has been done to assess the water contact angle of modified PUs.

4.2 Manufacturing of pure PU and modified PU nanocomposites

Additive nanomaterials, including graphene nanoplatelets (GNP), carbon nanotubes (CNT), and fumed nanosilica (SiO2), as well as binary combinations of these nanomaterials, were used to enhance the mechanical properties and hydrophobicity of pure polyurethane [73]. In this work, various PU nanocomposites were manufactured, followed by a series of experiments, including tensile, tearing and abrasion tests, which are reported in Chapter 5. Specific moulds were designed for each test, and the resin casting method was employed to manufacture the specimens. Pure polyurethane (PU) was used as the control material to monitor the improvements achieved by modifying the pure PU. The preparation of PU and PU nanocomposites were conducted partly in the chemistry research lab at the Faculty of Science and the material lab at the Department of Mechanical of Engineering at Kingston University.

The specimens prepared for all the aforementioned tests were based on either single or combinations of binary nanoparticles to explore their potential synergistic effects. In addition to pure PU, the PU nanocomposites investigated were:

- PU + graphene nanoplatelet (GNP-COOH or simply GNP)
- PU + GNP + carbon nanotubes (CNT)
- PU + fumed nanosilica (SiO_2)
- PU + SiO_2 + GNP
- PU + SiO_2 + CNT

The production of PU was carried out using polyether polyol (BAYTEC CG9 9005 60A MF) and diphenylmethane diisocyanate (MDI) (DESMODUR B9M10), supplied by Covestro Company. PU nanocomposites were made by blending polyol with different weight percentages of individual SiO_2, CNT, and GNP or a binary combination of these nanomaterials followed by mixing with MDI. The concentration of MDI required for a complete reaction with polyol is determined by the isocyanate (NCO) content, and the recommended weight ratio of polyol to MDI by the manufacturer (100:37) was used for the manufacturing of PUs.

The general chemical structure of polyether polyurethane consists of repeating units of polyether polyols (like Polypropylene Ether Glycol PPG: $-[CH_2CH(CH_3)O]-_n$ or Polytetramethylene Ether Glycol PTMEG: $-[CH_2-CH_2-CH_2-CH_2-O]-_n$) and hard segments derived from diisocyanates (MDI) and chain extenders like 1,4-butanediol (BDO). The reaction of polyisocyanates (R-NCO), such as methylene diphenyl diisocyanate (MDI), which has two -N=C=O groups attached to a methylene-linked phenyl ring or toluene diisocyanate (TDI), with polyether polyols (HO-R'-OH) results in:

$$n\ R\text{-}NCO + n\ HO\text{-}R'\text{-}OH \rightarrow \text{-}[R\text{-}NH\text{-}CO\text{-}O\text{-}R']_n$$

Here, R-NCO represents the isocyanate group attached to an organic substituent (R), and in the diisocyanate there are two isocyanate groups (-NCO) attached to the same organic backbone, one on each end (OCN-R-NCO), and HO-R'-OH is the polyether polyol. The resulting product is polyether polyurethane, with repeating urethane linkages (-NH-CO-O-), which form the backbone of the polyurethane by connecting the isocyanate and polyol segments (R').

Graphite consists of many layers of carbon atoms arranged in a hexagonal lattice structure. Graphene nanoplatelets (GNP), made from graphite, are nanoscale platelets particles composed of multiple small stacks of graphene layers. GNP are often considered a substitute for graphite due to its desirable properties, such as higher surface area and improved mechanical, thermal, and electrical properties [74]. Due to these superior properties, GNPs are a desirable additive material for producing nanocomposites on a large scale at a lower cost. They are used for various applications, such as reinforcing polymer matrices to enhance the mechanical properties of polymer composites, and for advanced coatings in surface protection applications, such as wind turbine blades [75]. The GNP used in this project was HDPlas^{TM} GNP-COOH, supplied by Haydale Graphene Industries. This GNP underwent surface functionalization with carboxyl groups through a plasma functionalization process called "split plasma" in oxygen. Haydale, the supplier of the GNP for this project, conducted this process [74, 76].

Figure 4.1 shows graphene, an allotropic form of elemental carbon, as a planar monolayer of carbon atoms arranged on a two-dimensional hexagonal lattice with a carbon–carbon bond length of 0.142 nm [77]. Graphene serves as the building block for other allotropes, including graphite (layered graphene), carbon nanotubes (CNTs) (graphene sheets seamlessly rolled up into nanoscale cylinders), and buckminsterfullerene (buckyballs) (graphitic molecular cages) all shown in *Figure 4.1(a-d)* [78]. Scanning electron microscopy (SEM) of HDPlas^{TM} GNP-COOH used in this project has been conducted, and the SEM image is shown in *Figure 4.1(e)*.

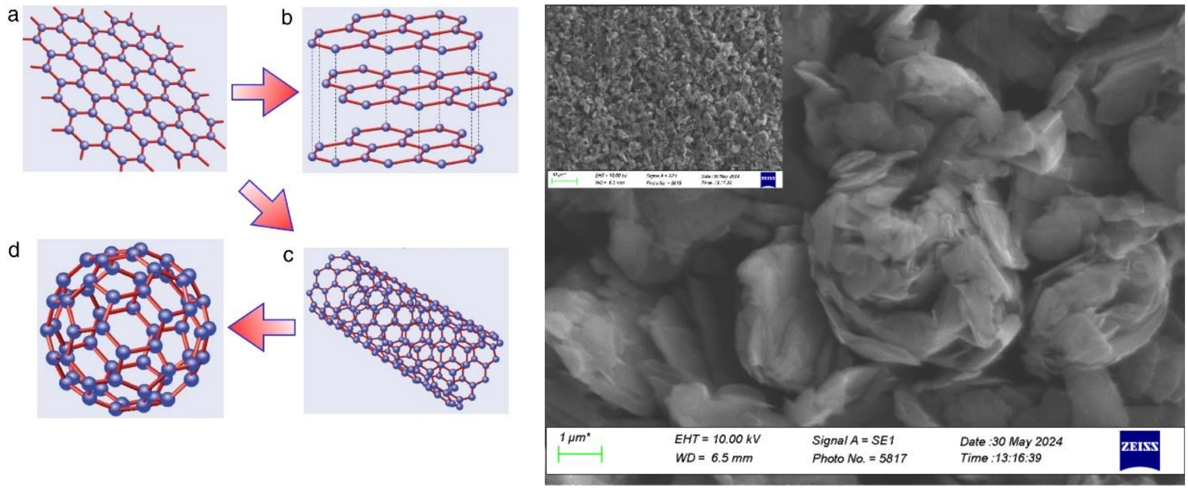

(e)

Figure 4.1. Various forms of carbon: (a) graphene; (b) graphite; (c) nanotube; (d) buckyball [79], and (e) an SEM image of HDPlas^{TM} GNP-COOH used in this project.

For this project, carbon nanotubes were supplied by NANOCYL Company in Belgium. NANOCYL® NC7000™ series, which are thin multi-walled carbon nanotubes (MWCNTs), are produced via the Catalytic Chemical Vapor Deposition (CCVD) process. MWCNTs were used due to their properties essential for erosion prevention applications. These includes: [80, 81, 82]

- Great tensile strength
- High electrical conductivity

- Good processability
- Retention of key mechanical properties
- High recyclability in thermoplastics
- Flame retardancy (synergy in combination with other flame retardants)
- Thermal dissipation
- UV resistance

In wind turbine blade coating, CNTs have exhibited excellent mechanical performance to withstand fatigue loading and the blade's substantial weight, factors that typically lead to material failure. CNT-based nanocomposites have also been proven to enhance the blades' matrices, making them tougher, and resulting in higher resistance to fatigue crack growth. These enhancements stem from the unique nanostructure of MWCNTs and the strong bonds between the carbon atoms [83]. *Figure* 4.2 illustrates the structure of SWCNT, DWCNT and MWCNT, along with an SEM image of NC7000 MWCNTs.

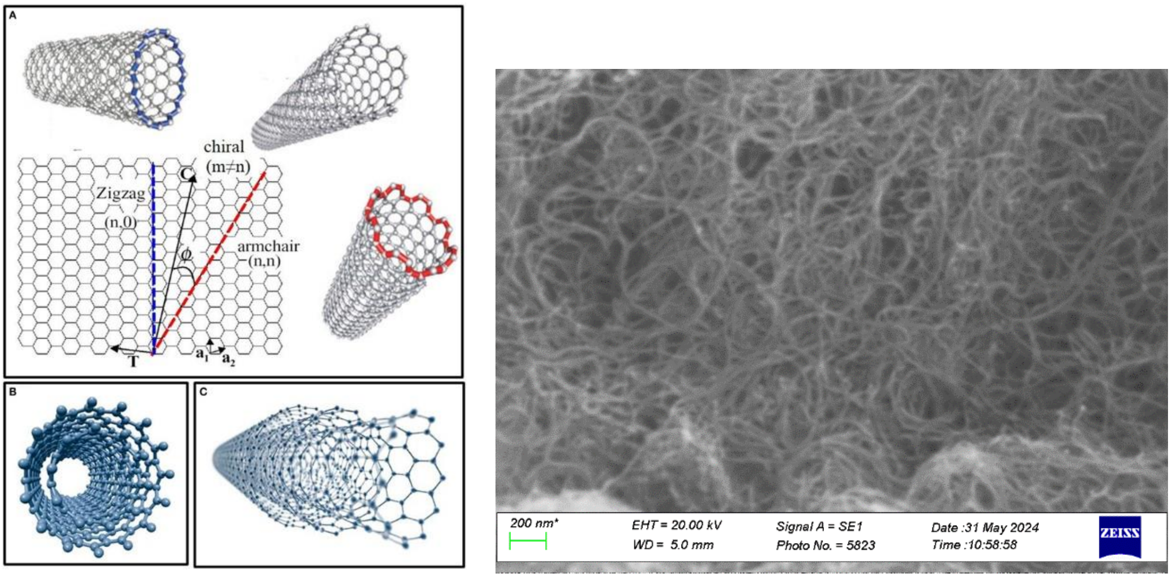

(D)

Figure 4.2. CNT chemical structure: (A) SWCNT, (B) DWCNT, (C) MWCNT [82], and (D) an SEM of NC7000 MWCNT used in this project.

The chemical structure of silica (SiO_2) is shown in *Figure 4.3(a).* Nanosilica is a high-purity structureless powder with nanoscale spherical particles. This substance is well-known for exhibiting unique properties such as heat resistance, anti-corrosiveness, high chemical purity, strong surface absorption, and high surface energy [84]. Coatings incorporating nanosilica have demonstrated excellent performance in anti-icing, water repellence, abrasion resistance, and the capability of self-cleaning from pollutants. These attributes promote the use of nanosilica in combination with PU and other polymers to develop effective coating materials for erosion prevention in various structures, including wind turbine blades [85]. The nanosilica used for this project is amorphous fumed silica (IV) provided by Alfa Aesar. An SEM image of the powder is shown in *Figure 4.3(b).*

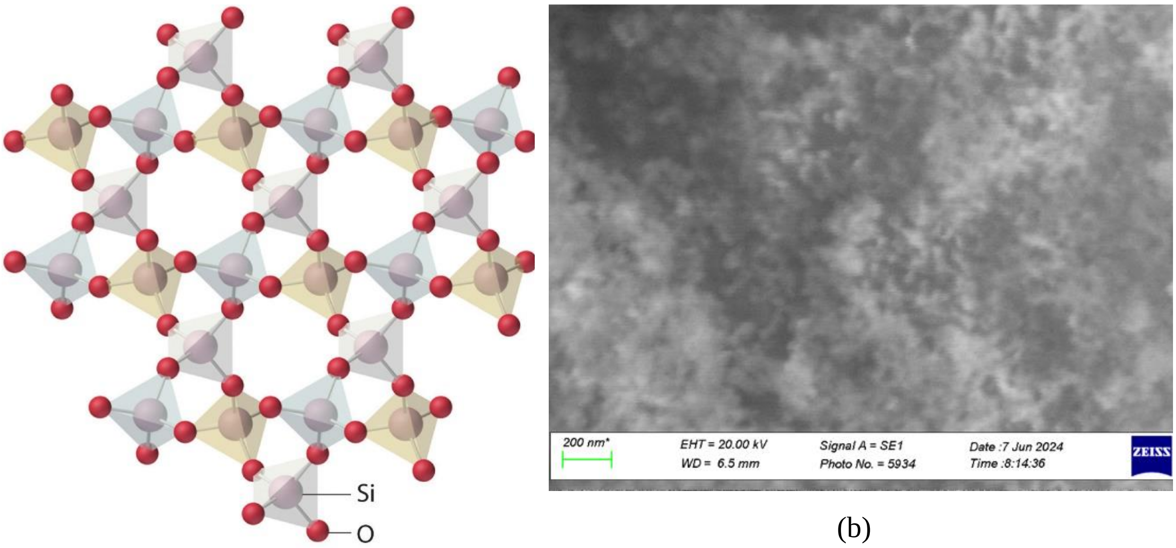

(b)

(a)

Figure 4.3. (a) The lattice of crystalline SiO_2 , (b) an SEM image of the amorphous fumed SiO_2 used in this project

4.2.1 Processing of pure PU

The polyether polyol was mixed with diphenylmethane isocyanate (MDI) at 100:37 weight ratio. The mixture was stirred at 200 rpm using a mixing pad rotating inside an MK Technology MK-Mini vacuum chamber for 3 min as shown in *Figure 4.4*. The MK-Mini vacuum chamber was equipped with a Leybold single stage oil-sealed rotary vane vacuum pump, model SOGEVAC SV25, with nominal pumping speed of 25 m^3/h and an ultimate total pressure of less than 0.5 mbar. Inside the chamber, the mixture underwent additional stirring for another 2-3 minutes, facilitated by a propeller installed within the chamber (*Figure 4.4(b))*. The end result was then poured onto preheated moulds made from aluminium manufactured by CNC machining, as shown in *Figure 4.5*.

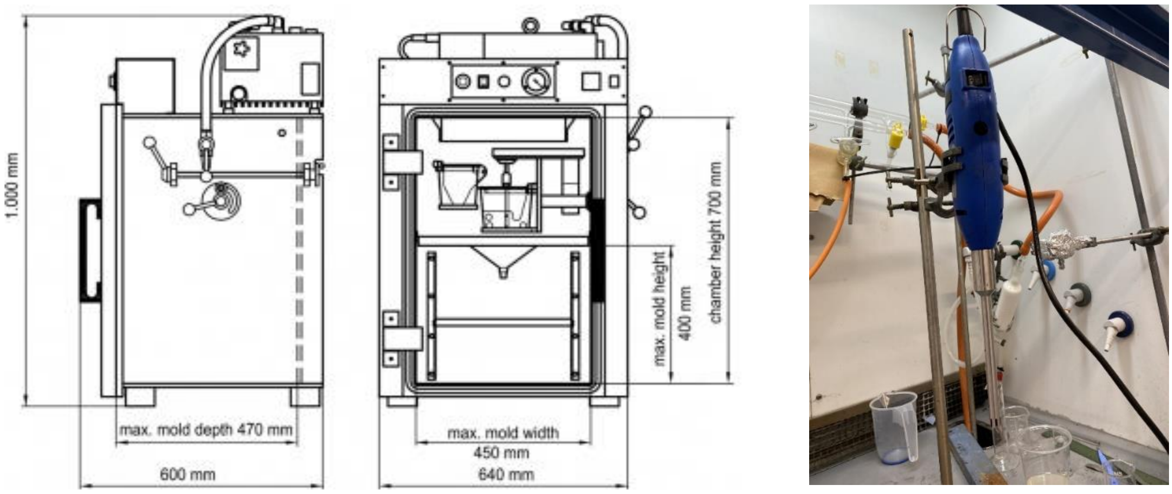

(a)

(b)

Figure 4.4. (a) MK-Mini vacuum chamber and (b) D130 homogenizer used in processing of PUs.

(a)

(b)

Figure 4.5. CNC machining process of (a) water absorption, (b) tensile moulds manufacturing

4.2.2 Processing of PU nanocomposites with unary additive nanomaterial

PU + GNP and PU + SiO_2: polyether polyol (100 g) was stirred with GNP (0.41 g) or SiO_2 (0.41 g) for 18 minutes at 8000 rpm using a homogeniser shown in *Figure 4.4b*, then MDI (37 g) was added to the mixture inside MK-Mini vacuum chamber and stirred for another 3 min with a mechanical mixing pad at 200 rpm to give 0.3 wt.% GNP or 0.3 wt.% SiO_2 polyurethane nanocomposite.

4.2.3 Processing of PU nanocomposites with binary additive nanomaterial

PU + GNP + CNT: polyether polyol (100 g) was stirred with GNP (0.21 g) and CNT (0.21 g) for 18 minutes at 8000 rpm using a homogeniser, then MDI (37 g) was added to the mixture inside MK-Mini vacuum chamber and stirred for another 3 min with a mechanical mixing pad at 200 rpm to give 0.15 wt.% GNP + 0.15 wt.% CNT PU nanocomposite.

PU + GNP + SiO_2 and PU + CNT + SiO_2: polyether polyol (100 g) was mixed with SiO_2 (0.21 g) and GNP (0.21 g) or CNT (0.21 g) for 18 minutes at 8000 rpm using a homogeniser, then MDI (37g) was added to the mixture inside MK-Mini vacuum chamber and stirred for another 3 min with a mechanical mixing pad at 200 rpm to give 0.15 wt.% SiO_2 + 0.15 wt.% GNP or 0.15 wt.% SiO_2 + 0.15 wt.% CNT PU nanocomposites.

As previously mentioned, isocyanate was blended with mixture of PU and the additive nanomaterials inside a vacuum chamber to prevent the formation of bubbles in the mixture. Pure PU was also prepared outside the vacuum chamber, and the morphology of both undegassed and degassed samples prepared inside vacuum chamber was investigated using an optical microscope. The images presented in *Figure 4.6* clearly demonstrate that mixing isocyanate outside the vacuum chamber results in the formation of numerous air bubbles within the PU. Therefore, mixing inside the chamber is essential for processing both PU and modified PU. In all subsequent work, isocyanate mixing was performed inside the vacuum chamber.

For each manufacturing process, the relevant moulds were preheated in an oven at 80°C for approximately 5-7 minutes before pouring any mixture into them. This preheating minimised the temperature differential between the resin and the mould, thus preventing premature solidification and potential formation of defects, thereby enhancing the quality of the specimens.

Once the mixtures were poured into the moulds, they were left in a well-ventilated room for 24 hours until the mixture solidified into a rubber-like state, ensuring that they are not tacky and ready for testing.

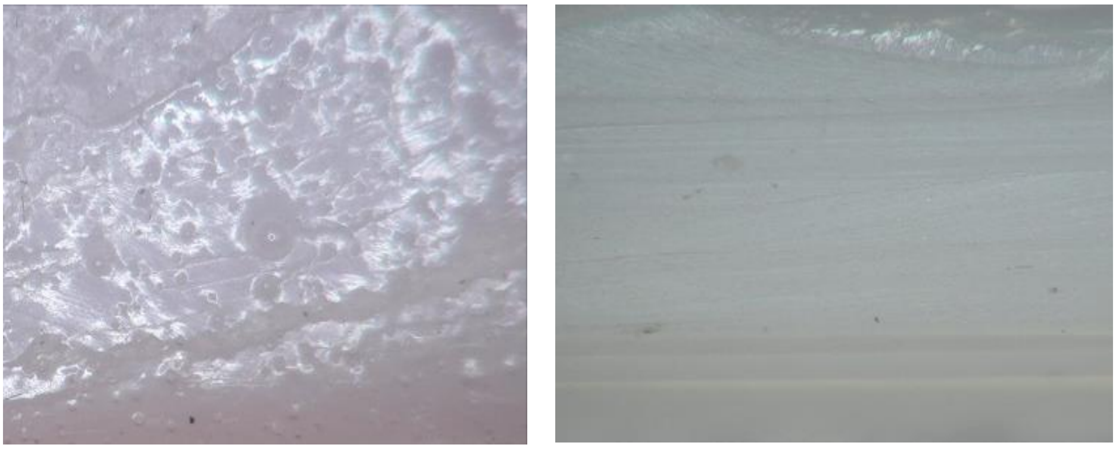

(a) (b)

Figure 4.6. Optical microscope image of (a) Undegassed, (b) Degassed.

4.3 Physicochemical analysis

Several instruments were employed to conduct necessary physicochemical experiments and analyse the thermal stability, crystallization, molecular fingerprint, and oxidation behaviour of the nanocomposites.

The following sections provide a detailed description of each instrumental technique and present the corresponding results obtained for both PU and modified PU nanocomposites manufactured.

4.3.1 Fourier-transform infrared spectroscopy analysis

FTIR is a technique that measures how a sample absorbs infrared (IR) light. Molecules absorb IR light at specific wavelengths, which correspond to vibrations of the chemical bonds between atoms. The resulting spectrum shows peaks at different wavelengths, representing the molecular fingerprint of the material. FTIR is used to identify the types of chemical bonds, such as C-H, O-H, or C=O, present in a sample.

A Thermo Nicolet iS5 FTIR spectrometer was used for ATR-FTIR (Attenuated Total Reflection Fourier-Transform Infrared) spectroscopy. A diamond ATR crystal is used to analyse solid or liquid samples with minimal preparation. The ATR accessory typically consists of a crystal with a surface area of about 2 mm² and a clamp that uniformly presses solid or powdered samples onto the crystal (*Figure 4.7b*). During measurement, the sample is in direct contact with the ATR crystal, allowing infrared (IR) radiation to travel through the crystal and interact with the sample. Due to the difference in refractive indices between the crystal and the sample, total internal reflection occurs, generating an "evanescent wave" that extends into the sample. A portion of the IR light is absorbed when the wave interacts with the sample, producing a slightly attenuated reflection. This absorption generates the FTIR spectrum, which provides information on the sample's molecular composition.


(a) (b)

Figure 4.7. (a) Thermo Nicolet iS5 FTIR spectrometer, and (b) iD5 Diamond ATR accessory

The analysis was carried out over a wavenumber range of 4000 to 500 cm^{-1}, which covers a wide portion of the infrared spectrum. The instrument had a resolution of 4 cm^{-1}, meaning it could distinguish between different wavelengths with that level of precision. The ATR unit attached to the spectrometer was cleaned with ethanol and a cloth. Subsequently, each specimen representing one of the six different nanocomposites was clamped on the ATR for testing (*Figure 4.7b*).

Both pure PU and modified PU specimens were exposed to IR radiation in the FTIR spectrometer to analyse their chemical properties and various types of bonding within their structure, using high-resolution spectral data generated during the analysis. *Figure 4.8* and *Figure 4.9* show the FTIR spectra results for pure PU and all nanocomposites.

As shown in *Figure 4.8* there was no noticeable difference in spectra among pure PU and PU nanocomposites. This consistent behaviour across all materials was due to the high percentages of PU in the nanocomposite structures (99.7 wt%). This is also evidence suggesting effective incorporation and homogenous dispersion of GNP, CNT, and SiO_2 within the PU matrix. However, PU+GNP+CNT showed a noticeable deviation in the fingerprint region (500-750 cm^{-1}), distinguishing it from other PU nanocomposites. This deviation might be attributed to incomplete incorporation of either GNP or CNT into the PU matrix. Characteristic peaks attributed to key functional group of PU and its modified nanocomposites including N-H stretching and O-H stretching at 3200-3400 cm^{-1}, C-H stretching at 2800-3000 cm^{-1}, N-H bending at 1530 cm^{-1}, C=O stretching at 1700-1750 cm^{-1}, and C-O stretching at 1000-1300 cm^{-1}. These characteristic peaks in the FTIR spectrums confirm the presence of polyurethane and its functional groups in the examined PU and PU nanocomposites.

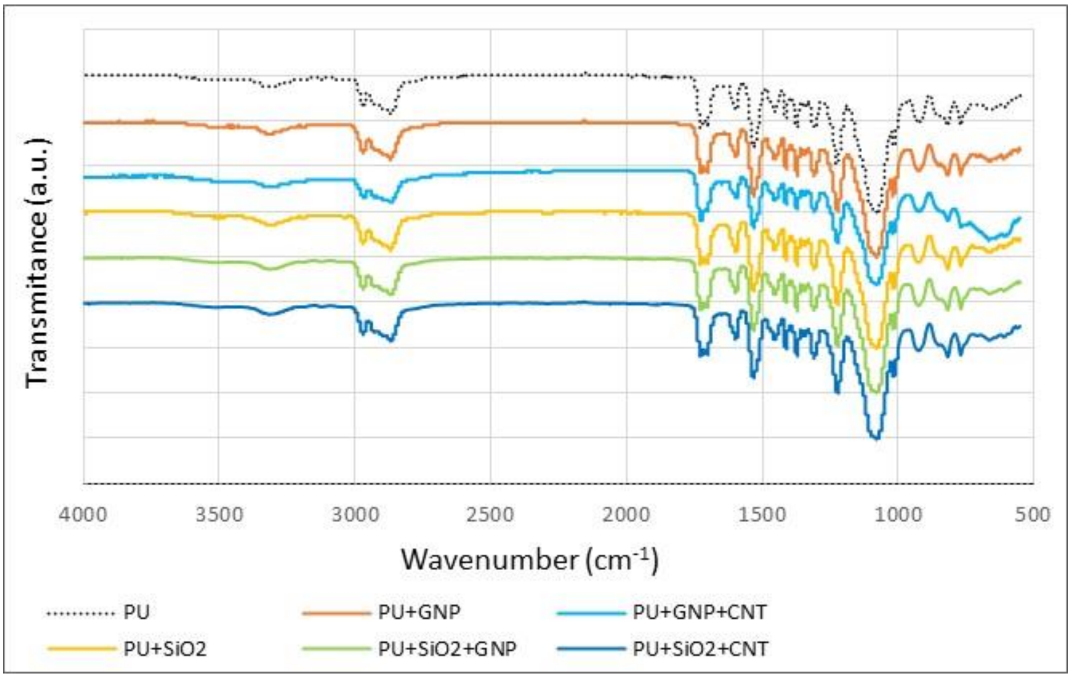

Figure 4.8. Shifted overlay of ATR-FTIR spectral for pure PU and all PU nanocomposites

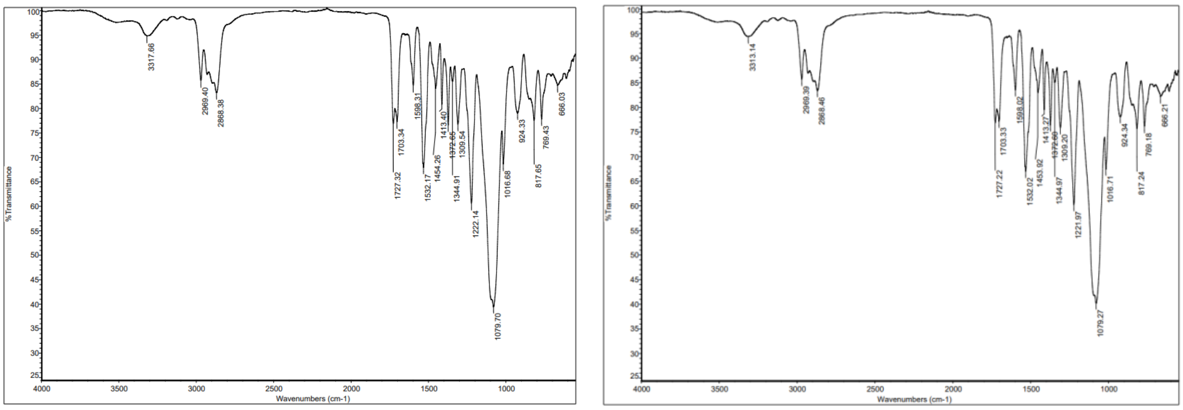

(a) Pure PU

(b) PU+GNP

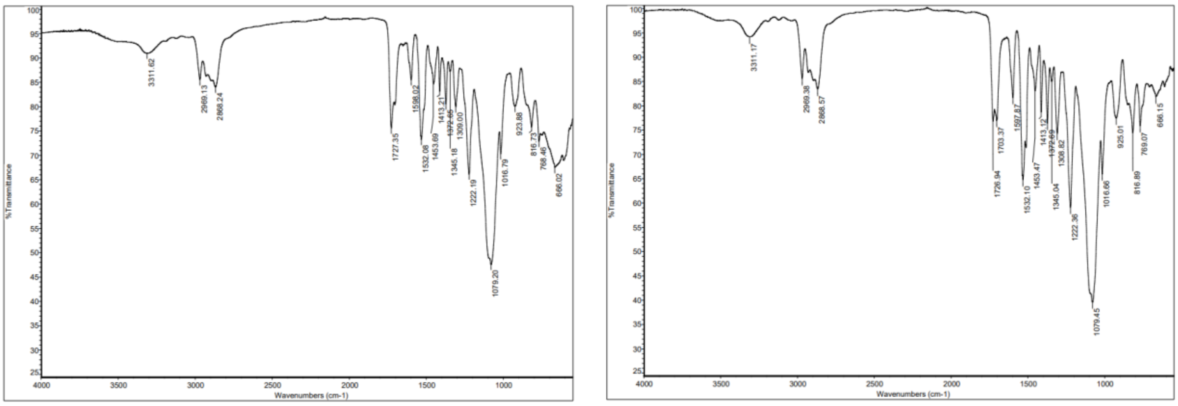

(c) PU+GNP+CNT

(d) PU+SiO$_2$

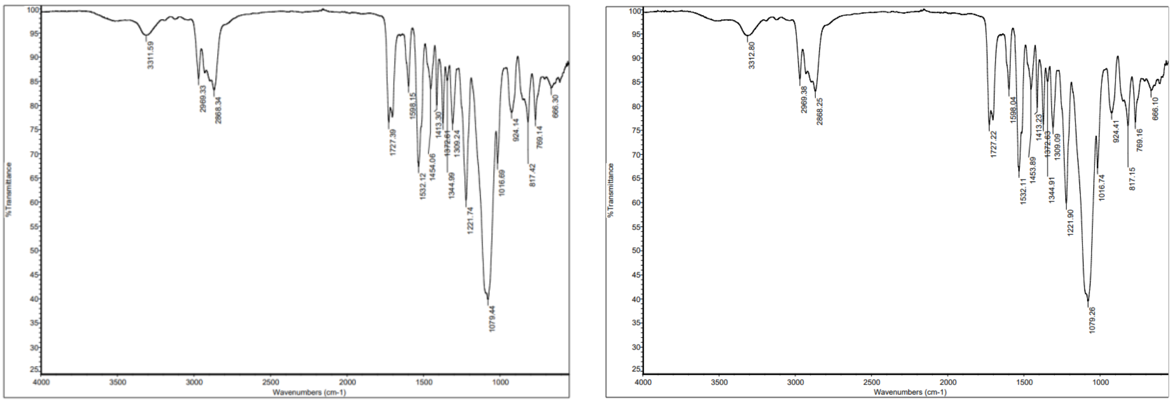

(e) PU+GNP+SiO$_2$

(f) PU+CNT+SiO$_2$

Figure 4.9. FTIR spectral data for (a) PU, (b) PU+GNP, (c) PU+GNP+CNT, (d) PU+SiO$_2$, (e) PU+GNP+SiO$_2$ and (f) PU+CNT+SiO$_2$

4.3.2 Differential scanning calorimetry analysis

Differential Scanning Calorimetry (DSC) is a thermal analysis technique in which a specimen is exposed to controlled temperatures while monitoring changes in its heat capacity with respect to temperature. A sample of known mass undergoes either heating or cooling, and changes in heat capacity are tracked as heat flows. This method is valuable for detecting transitions such as melting, glass transitions, phase changes, and curing. DSC technique has proven to be robust and versatile in assessing material properties like thermal stability, crystallization, and oxidation behaviour. The DSC instrument is capable of providing test data for various types of materials, including organic materials, polymers, and composites [86, 87].

(a) (b)

Figure 4.10. (a) TA DSC 25 instrument, and (b) pans where fragments of each nanocomposite are placed

In this study, a TA DSC 25 instrument, shown in *Figure 4.10*, was used for thermal analysis of both pure PU and nanomodified PUs. A small portion of each nanocomposite was cut and placed on a pan, as shown in *Figure 4.10(b)*. The pan with the nanocomposite sample was then placed on a digital scale to ensure it fell within the acceptable weight range (between 2.5mg to 5mg). Once the weight fell within this range, the pan containing the specimen was transferred to a specimen encapsulation press tool to securely encapsulate it with a lid, as shown in *Figure 4.11*. Subsequently, encapsulated pan was carefully positioned on the DSC instrument for analysis.

DSC analysis of both pure polyurethane (PU) and PU nanocomposites was conducted to examine changes in their physical properties at a heating rate of 10 K/min within a specified temperature range of -75°C to 320°C. The results of the DSC analysis for pure PU and nanomodified PU are shown in Figure *4.12*. Notably, the DSC curve does not indicate a glass transition phase for any of the PU nanocomposites. The absence of a glass transition phase can be attributed to several factors, including the size and preparation of the specimens, the high heating rate, or potential calibration issues with the DSC instrument.

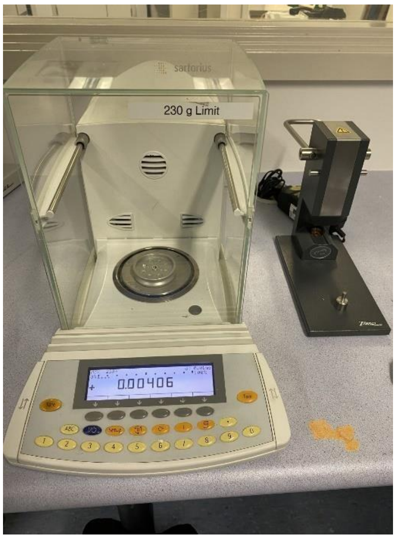

Figure 4.11. A digital scale (on the lefthand side), and a Tzero specimen press (on the righthand side).

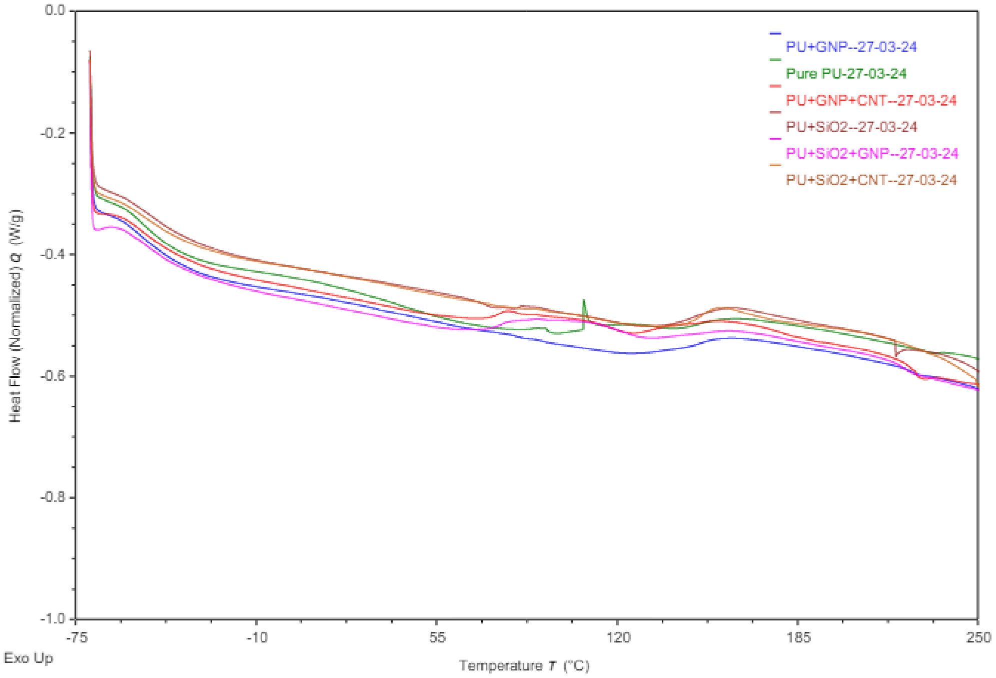

Figure 4.12. DSC results for all the nanocomposites

4.3.3 Thermogravimetric analysis

Thermal Gravimetric Analysis (TGA) is a thermal analysis technique that measures the relative change in the mass of a specimen over time or temperature. By gradually increasing the specimen's temperature over time, TGA effectively detects changes in its composition. This versatile technique finds application across various fields such as research, failure analysis, and product development to characterize materials including petrochemicals, polymers, and rubbers. TGA enables the measurement and determination of important factors such as filler content in polymers, absorbed moisture, solvent content, thermal stability, decomposition temperature, among others [88, 89].

There are numerous of applications of the TGA, including:

- Ensuring products meet safety requirements.
- Establishing optimal operating temperatures for different gases.
- Quality control to meet product specifications.
- Analysing carbon content in materials.
- Evaluating kinetic parameters using Arrhenius model.

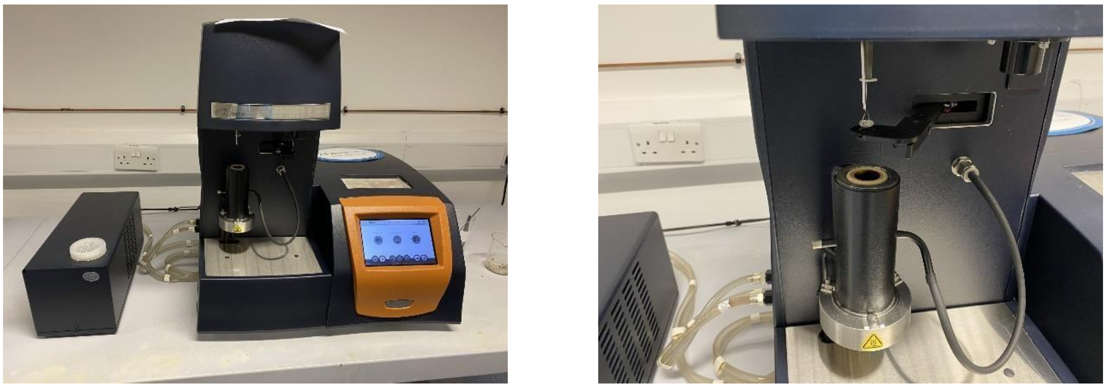

(a) (b)

Figure 4.13: (a) TA TGA 550 instrument and (b) furnace where the pan containing the specimen piece will be inserted

The TGA 550 instrument, located at PR campus (*Figure 4.13*), was used to conduct TGA analysis on the six PU nanocomposites. A small portion of each nanocomposite, ranging from 3mg to 9mg, was cut and placed on a specimen pan designed for automatic loading into the TGA furnace. TGA analysis was conducted to examine the thermal stability and weight loss of each nanocomposite within temperature range of 20°C to 600°C. The TGA and DTG results for both pure PU and the modified PU nanocomposites are shown in *Figure 4.14,* and with individual nanocomposite results detailed in *Figure 4.15*.

At early stages of thermal degradation, up to 280°C, the initial weight loss observed in the TGA curve was related to the loss of volatiles and the breakup of weaker bonds before the main thermal decomposition of the polymer matrix begins. These volatiles include adsorbed water (around 100°C), low molecular weight volatile such as solvents, and small molecular fragments that were not fully reacted during the polymerisation process (around 200°C). In addition, the breakup of weaker bonds such as hydrogen bonds and low-energy chemical bonds between phases of segmented polyurethane contribute to this initial weight loss. The minimal weight loss observed before 280°C is attributed to the evaporation of substances physically adsorbed on the surfaces. The weight loss observed between 280°C and 410°C in TGA of polyurethane is primarily due to the thermal degradation of the polymer structure, specifically the breakdown of urethane linkages and the degradation of polyol chains. Understanding the magnitude of this weight loss can provide valuable insights into the thermal stability and performance of the polyurethane at elevated temperatures.

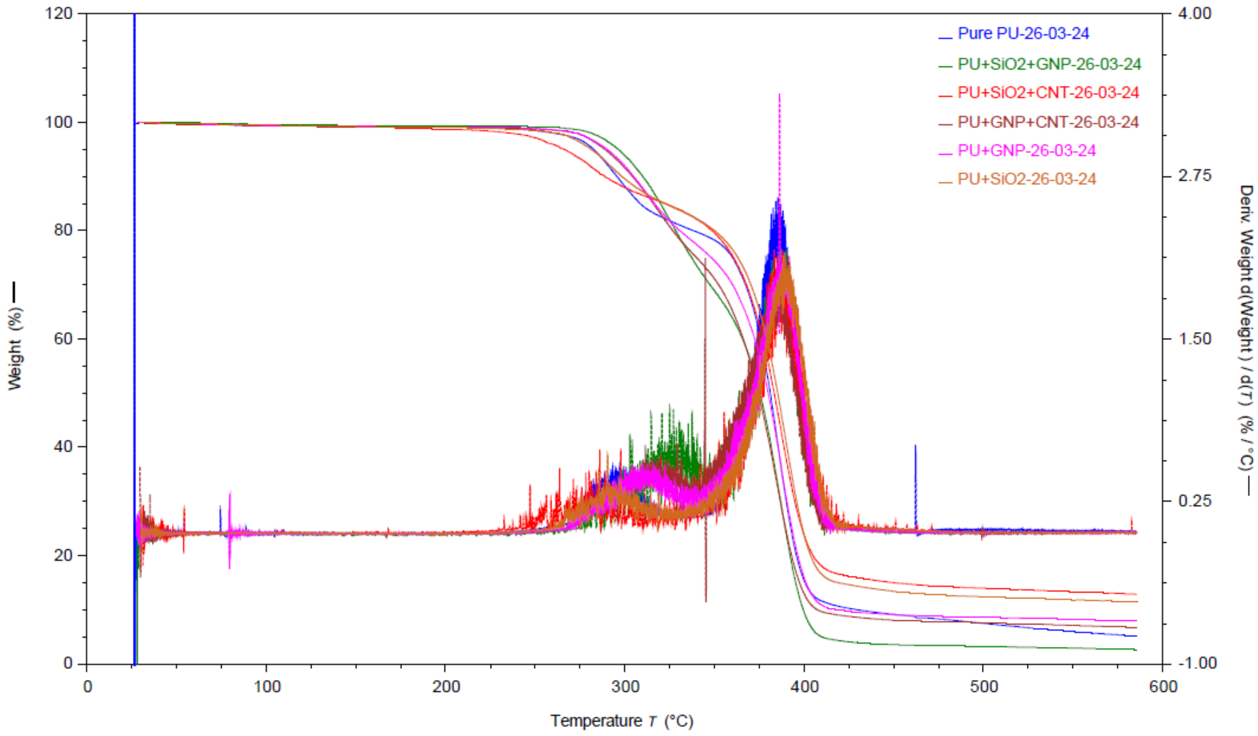

Figure 4.14. TGA results for all nanocomposites.

Figure 4.15 depicts the TGA and DTG results for pure PU and individual modified PU nanocomposites. The results show that the decomposition of the five PU nanocomposites followed a two-step degradation process. Polyurethane elastomers are polymers composed of alternating hard and soft segments. The soft segments in our polyurethane (PU) are made of flexible polyether, which generally begin to decompose around 250°C, with significant weight loss observed between 300°C and 400°C. The uniform structure of the soft segments among all nanomodified PUs contributes to their similar degradation behaviour. In contrast, the hard segments are formed from methylene diphenyl diisocyanate (MDI) and chain extenders, such as 1,4-butanediol. Hard segments typically decompose at higher temperatures, starting around 350°C and continuing up to about 500°C. The exact decomposition temperature can depend on various factors, including the type of diisocyanate and the presence of any additives or stabilizers.

Table 4.1 summarizes the temperatures corresponding to weight loss of 5%, 15%, 50% and the onset temperature of final unchanged mass. The thermal stability of PU is determined by T_5 representing the temperature at which 5% of the mass is lost. The results in *Table 4.1* show that all PU nanocomposites exhibited thermal stability up to approximately 278°C, beyond which decomposition occurred. This characteristic makes PU a suitable candidate for coating wind turbine blades, as they are typically not exposed to temperatures exceeding 60°C. The TGA tests results show that PU+GNP+CNT had a higher residue than PU+GNP. This can be attributed to the combined thermal stability of GNP and CNT. The synergistic effects of GNP and CNT enhance the thermal stability of the nanocomposite. In addition, better dispersion and improved thermal barrier properties slow down the decomposition of the polymer matrix. Potential catalytic effects that might also alter the decomposition pathways of the PU, affecting char formation. These factors collectively contribute to a more thermally stable PU+GNP+CNT nanocomposite, resulting in a higher residual mass. The residual mass for PU+SiO_2 at 600°C is the highest. In addition to a char residue formed during thermal decomposition, the residual mass includes contribution from incomplete combustion and the remains of thermally stable inorganic SiO_2.

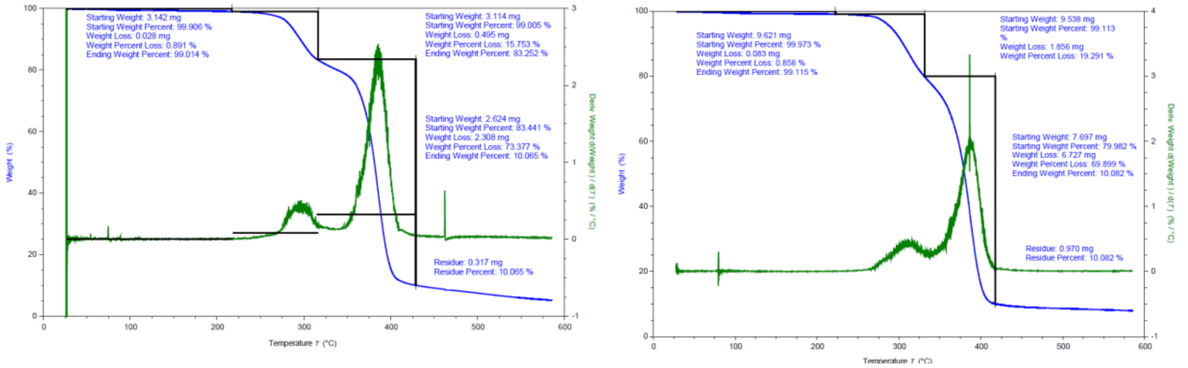

(a) Pure PU

(b) PU+GNP

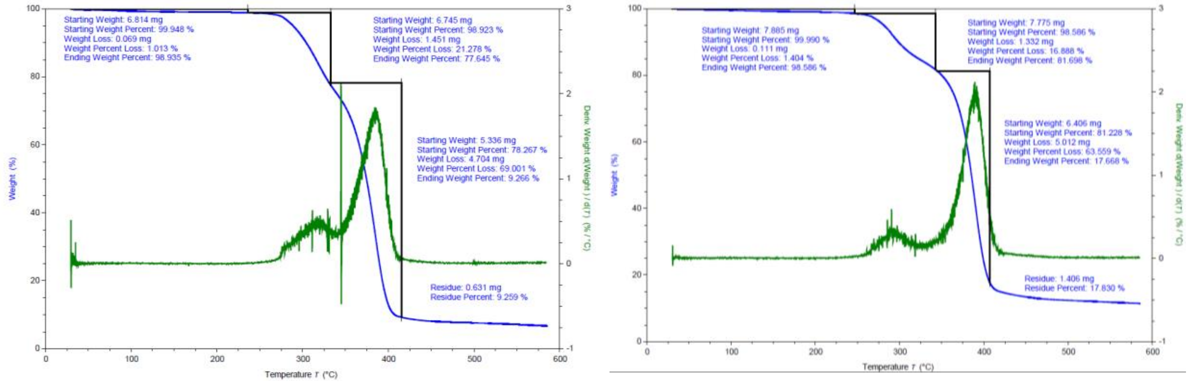

(c) PU+GNP+CNT

(d) PU+SiO_2

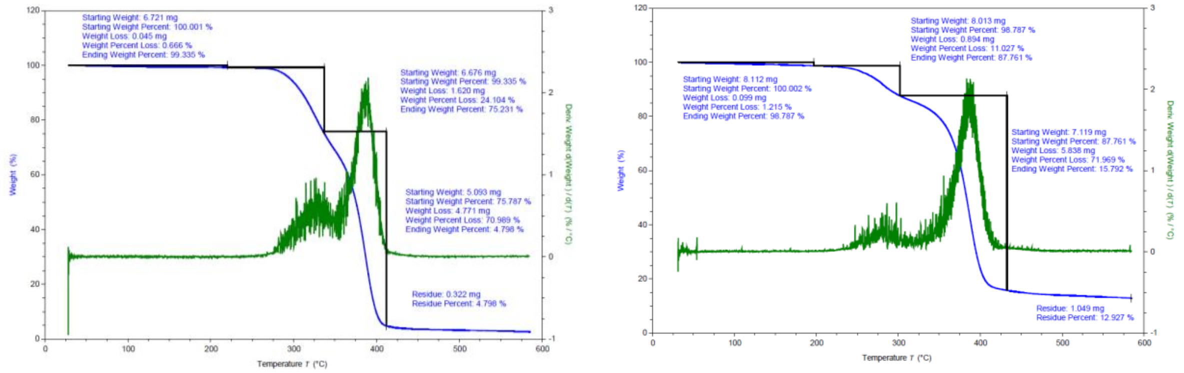

(e) PU+SiO_2+GNP

(f) PU+SiO_2+CNT

Figure 4.15. TGA and DTG results for (a) pure PU, (b) PU+GNP, (c) PU+GNP+CNT, (d) PU+SiO_2, (e) PU+SiO2+GNP and (f) PU+SiO_2+CNT nanocomposites.

Table 4.1. Characteristic parameters of PU determined by TGA and DTG

Nanocomposite	T_5 (°C)	T_{15} (°C)	T_{50} (°C)	$T_{residues}$ (°C)
Pure PU	278	302	378	410
PU+GNP	278	302	380	410
PU+GNP+CNT	284	308	378	407
PU+SiO_2	284	313	378	410
PU+SiO_2+GNP	284	308	370	404
PU+SiO_2+CNT	293	318	382	410

T_5, T_{15}, and T_{50} are temperature at 5%, 15% and 50% weight loss.

4.3.4 Dynamic mechanical analysis

In DMA tests, a sample is subjected to a periodic (sinusoidal) loading, causing deformation with the same period as shown in *Figure 4.16*, and the force, displacement, and the phase between the force and displacement signals are measured. The deformation follows the force with a loss angle δ which is related to frequency and time lag according to:

$$\delta = 2\pi f \Delta \tag{4.1}$$

Where f is frequency in Hz, and Δ is a time lag between force and displacement signal.

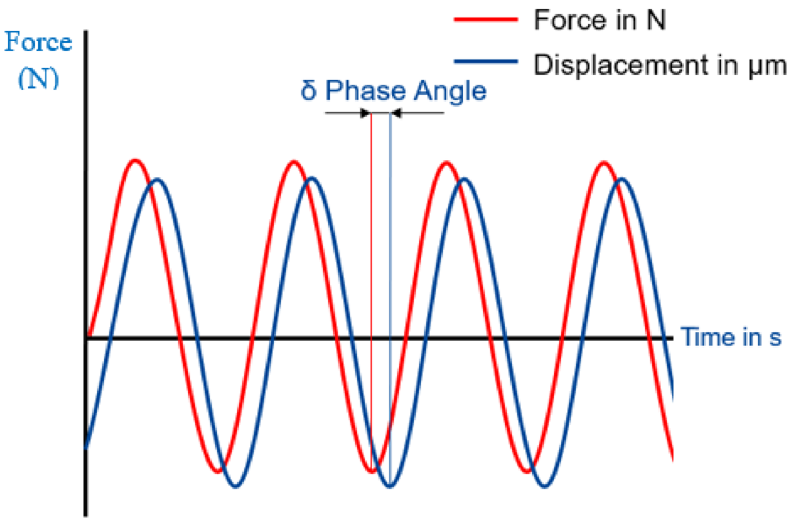

Figure 4.16. Force and displacement in a DMA test at a frequency f.

The applied load amplitude to the sample must be within the linear elastic region. The measured storage modulus of the specimen represents the elastic behaviour which is related to the storage of mechanical energy during a stress period. The loss modulus indicates the viscous behaviour which is related to energy dissipation by transformation of mechanical energy into heat in the material. The ratio of stress amplitude to strain amplitude is complex modulus E^*, which consists of an in-phase component (storage modulus E') and a 90° out-of-phase component (loss modulus E'').

$$E^*(\omega) = \frac{\sigma(t)}{\varepsilon(t)} = E' \sin \omega t + E'' \cos \omega t \qquad (4.2)$$

Where:

$$\sigma(t) = \sigma_A \sin(\omega t + \delta) \qquad (4.3)$$

$$\varepsilon(t) = \varepsilon_A \sin(\omega t) \qquad (4.4)$$

The storage modulus E' is expressed by:

$$E'(\omega) = \frac{\sigma_A}{\varepsilon_A} \cos \delta \qquad (4.5)$$

And the loss modulus E'' is measured by:

$$E''(\omega) = \frac{\sigma_A}{\varepsilon_A} \sin \delta \qquad (4.6)$$

The damping factor ($\zeta = \frac{c}{2\sqrt{mk}}$) and tan δ are related through the equation:

$$\zeta = \frac{1}{2} tan\ \delta \qquad (4.7)$$

Both parameters provide valuable insights into the damping characteristics of materials, particularly in vibrational analysis and dynamic mechanical analysis contexts.

In shear mode, DMA measures the shear modulus G^*. In this mode G' is the storage modulus and G'' is the loss modulus. The key aspect of the DMA instrument is its sensitivity to the glass transition temperature (T_g), hence making it a very suitable tool for evaluating the T_g of polymers with very high accuracy. A typical DMA test result of G' and $\tan \delta$ for a thermoplastic polymer is shown in *Figure 4.17*. It can be seen that the mechanical properties of the material are changed markedly in the region of glass transition temperature: the storage modulus G' decreases typically from glassy by several orders to rubbery state and the loss factor $\tan \delta$ shows a distinct maximum after which there is a region in which the material is soft.

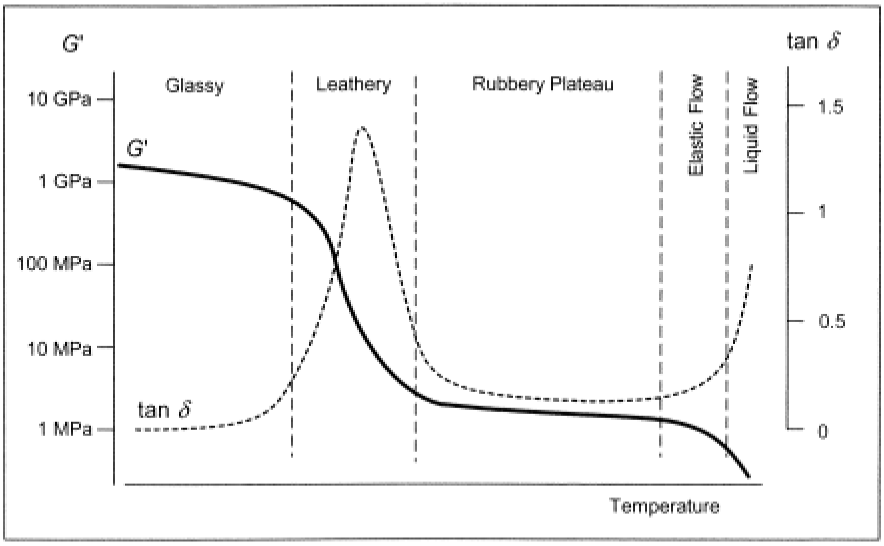

Figure 4.17. DMA curve of a typical thermoplastic in shear mode. [90]

The loss factor $\tan\delta$, also called damping factor, is the ratio of E''/E':

$$\tan\delta = \frac{E''(\omega)}{E'(\omega)} \tag{4.8}$$

A high loss factor indicates a high non-elastic strain component, and in contrast, a low value shows the material is more elastic. The loss factor is an indicator of the degree of energy dissipation as heat during each cycle. For purely elastic material the phase angle $\delta = 0$ and sample oscillate without loss of energy. When phase angle $\delta = \pi/2$, the material is pure viscous, and the deformational energy entirely convert to heat. For phase angle $0 < \delta < \pi/2$, the material behaviour is viscoelastic and the larger the phase angle, the stronger the oscillation is damped.

Mettler Toledo DMA 1 Dynamic Mechanical Analysis (DMA) was used in dual cantilever mode at a fixed frequency of 1 Hz and a heating rate of 3 K/min to evaluate the impact of various nanofillers on the viscoelastic properties, such as storage modulus, loss modulus, and loss factor, of PU nanocomposites over a temperature range from -80°C to 50°C. The glass transition temperature (Tg) and damping factor of each PU nanocomposite were determined. Liquid nitrogen was used for cooling the specimens, and the tests were performed in an air environment. The measurement point for Tg was taken from the peak of the $\tan\delta$ curve. The tests were performed in displacement control with a displacement amplitude of 10µm.

(a) (b)

Figure 4.18. (a) Mettler Toledo DMA 1 instrument, and (b) dual cantilever measuring mode fixture.

The results of the storage modulus (E'), loss modulus (E''), and loss factor ($\tan\delta$) for a composite material in 3-point bending mode are shown in *Figure 4.19* [90]. The temperature at the peak of $\tan\delta$ curve represent the glass transition temperature (T_g), which in this case is 137°C. T_g can also be measured from the storage modulus curve, shown in *Figure 4.19*, and for this case, it is 124.16°C. This value corresponds to the onset of transformation from the glassy phase to the leathery phase. However, in the literature, the T_g measured form $\tan\delta$ is more commonly reported, and in this project the reported T_g value is determined from peak of $\tan\delta$.

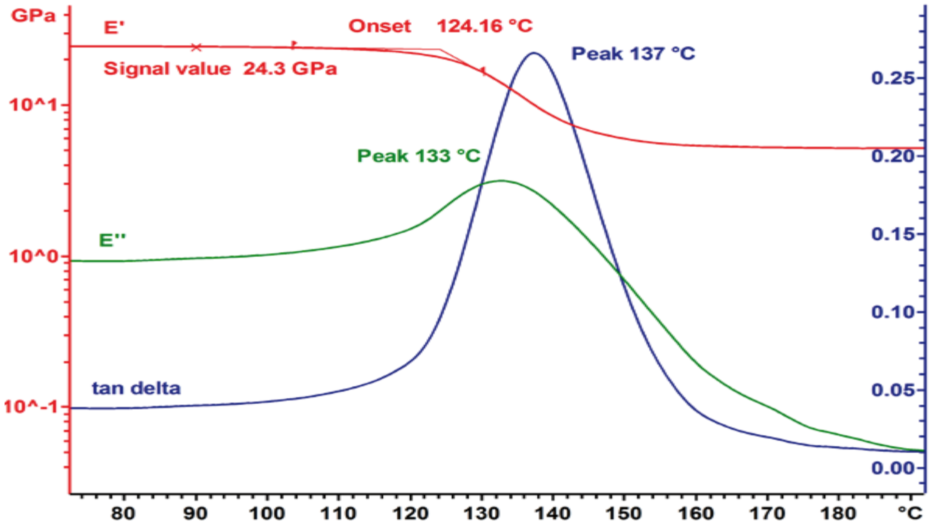

Figure 4.19. DMA thermal scan of a composite in 3-point bending [90]

Polyurethane elastomers are amorphous and highly crosslinked linear chain molecules that form a wide-meshed three-dimensional network, behave glassy and brittle at low temperature in the range of -80°C to -20°C. They do not melt but begin to degrade and decompose at high temperatures.

Specimens with a rectangular cross-section of 4mm × 5mm and a length 35mm were made from each nanocomposite. DMA analysis was conducted to examine the response of each sample to temperature at a frequency of 1 Hz, and a heating rate of 3°C/min. The tests were performed in displacement control with a displacement amplitude of 10µm. Liquid nitrogen was supplied to the instrument to cool the specimen to freezing temperatures. Once the specimen reached the set starting temperature of -80°C, the nitrogen valves were closed. The temperature continued to decrease by a few degrees before it began to increase. As the temperature returned to the set starting temperature, the loading cycle started, and data for the storage module, loss modulus, and $\tan\delta$ were recorded. The results of storage modulus and $\tan\delta$ versus temperature for both pure PU and the modified PU nanocomposites are shown in *Figure 4.20* and *Figure 4.21*, respectively.

The glass transition temperatures (Tg) of soft segments in polyurethanes is usually observed in the range of -80°C to 0°C, depending on the type of soft segment used, while hard segments are typically more crystalline or highly crosslinked, giving them much higher Tg compared to the soft segments. The Tg of hard segments often occurs at temperatures significantly above room temperature, sometimes well above 100°C or even higher, depending on the specific chemistry.

The relatively flat regions at lower temperatures in *Figure* 4.20 correspond to the glassy state of each PU. The onset of the glass transition (Tg) for the polyurethanes started at around -43°C, where the curves initially bend downward. Beyond this point, all the curves show a rapid decrease in modulus, resulting from significant softening and rubbery flow. However, it is generally preferred to calculate Tg using the peak in the $tan\,\delta$ diagram shown in *Figure* 4.21, which is summarised in

Table 4.2, and these values are from -22°C to -18°C for all PU nanocomposites. This preference is due to the greater uncertainty in accurately placing the tangents compared to identifying the apex of a peak in the $tan\,\delta$ diagram. It can be seen that the Tg temperatures calculated by E' tangent method and the $tan\,\delta$ method are not identical. This emphasises the fact that polymer glass transitions occur over a temperature range, not at a single temperature. From

Table 4.2, PU+GNP+CNT nanocomposite has the maximum damping factor while PU+SiO2+GNP has the lowest damping factor.

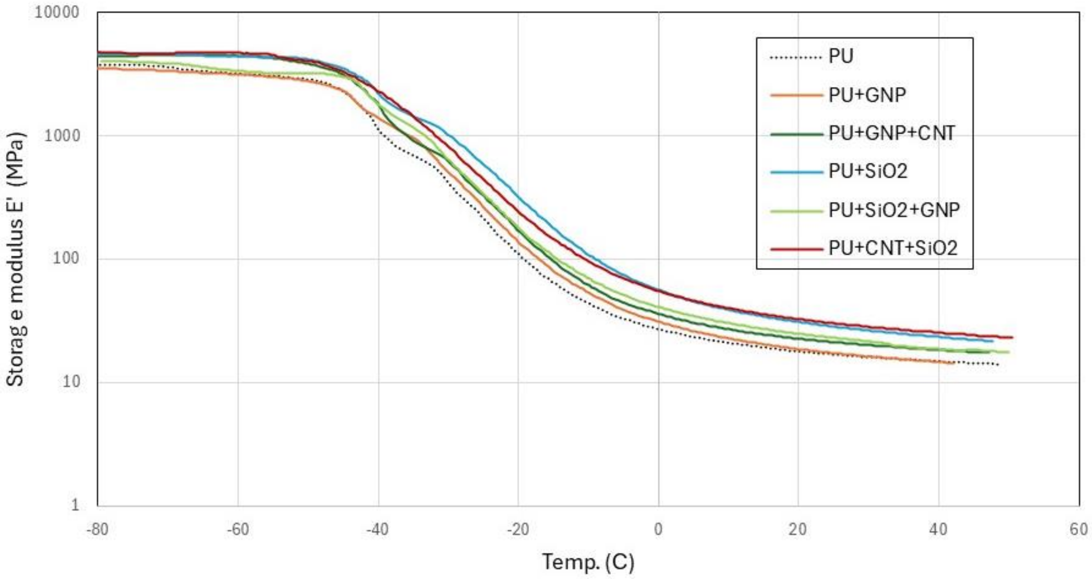

Figure 4.20. Variation of storage modulus versus temperature for all PU nanocomposites.

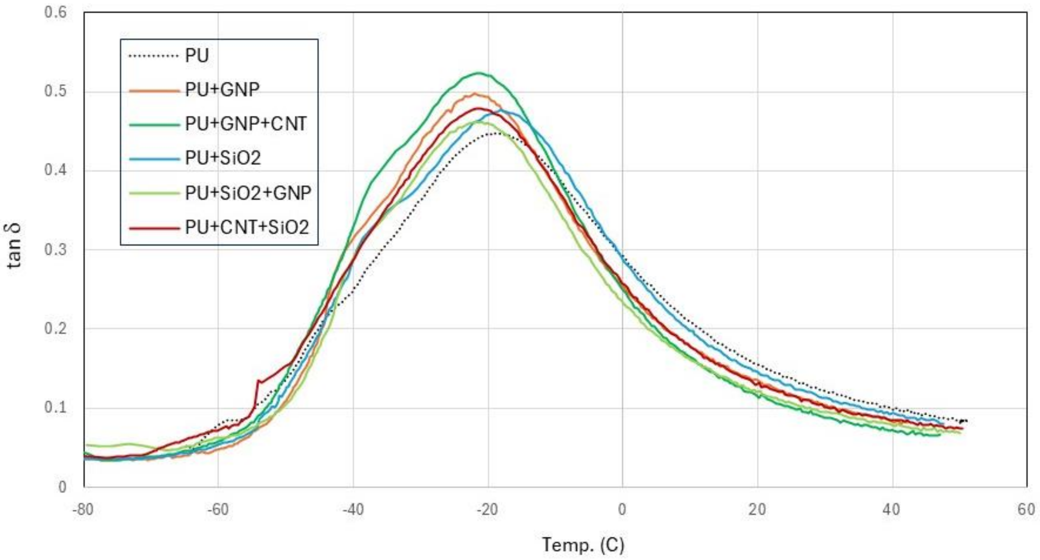

Figure 4.21. Variation of tan δ versus temperature for all PU nanocomposites.

Table 4.2. Glass transition temperature and damping coefficient of pure PU and PU nanocomposites

Material	Tg (°C)	Damping factor	% increase of damping factor
PU	-19.2	0.447	-
PU+GNP	-22.1	0.498	11.4
PU+GNP+CNT	-21.5	0.523	17.0
PU+SiO_2	-18.1	0.476	6.5
PU+SiO_2+GNP	-21.7	0.475	6.3
PU+SiO_2+CNT	-21.4	0.478	6.9

The measured loss moduli, E'', for all PU nanocomposites are shown in *Figure 4.22*. The peaks of E″ are around -43°C to -40°C for all nanocomposites, which corresponds to the onset of significant segmental motion of the polyurethane chains. During cyclic loading of specimens in DMA tests, the input mechanical energy is dissipated as heat due to the internal friction caused by chain motion, resulting in damping. In comparison, the $\tan\delta$ peak, usually reported for Tg, represents longer-range cooperative molecular motion consistent with rubbery flow, permanent deformation, or both, depending on the molecular structure.

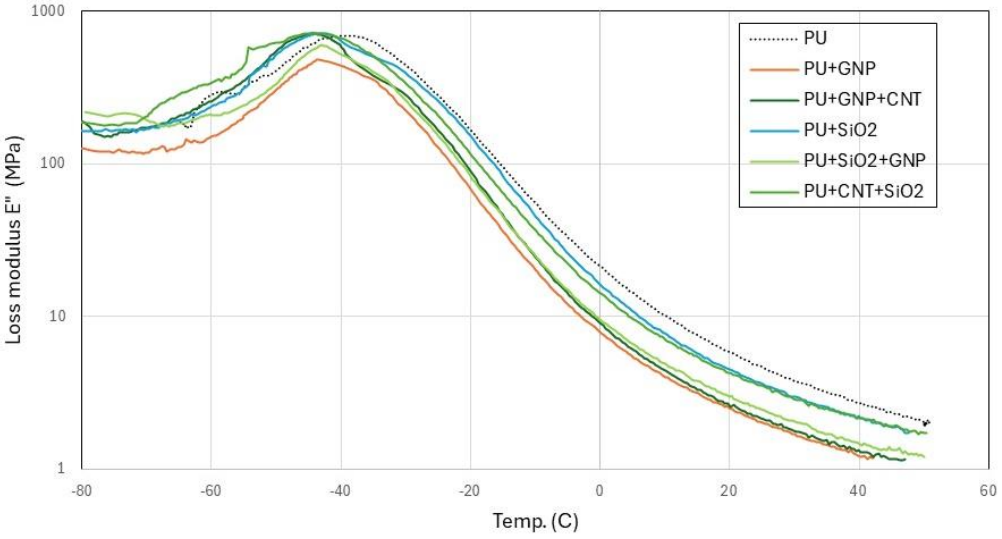

Figure 4.22. Variation of loss modulus versus temperature for all PU nanocomposites.

4.4 Water Contact Angle

A liquid drop suspended on a solid substrate either spreads throughout the surface or forms a segment that is semi-spherical, depending on the Surface Free Energy (SFE) of the solid and liquid. The liquid will spread across the surface if its surface tension is lower than the solid's SFE; otherwise, it will form a semi-spherical circle, causing a contact angle between the solid-liquid interphase and solid-liquid-vapor triphase tangent [91]. The static contact angle, also known as the wetting angle, is measured by placing a liquid drop on a solid surface and measuring the angle between the solid surface and the tangent to the liquid droplet at the point of contact, as shown in *Figure 4.23*. The magnitude of the contact angle indicates the wettability of the solid by the liquid. A contact angle of 0° represents a superhydrophilic surface, indicating complete wetting. For contact angles $0° < \theta < 90°$, the surface is hydrophilic, while for angles greater than 90°, the surface becomes hydrophobic. As the contact angle increases beyond 90°, the degree of hydrophobicity also increases. When the contact angle exceeds 150°, the surface is considered superhydrophobic, see *Figure 4.23*. In general, increasing the WCA reduces the wetting surface, thereby decreasing water absorption by the coating during rain.

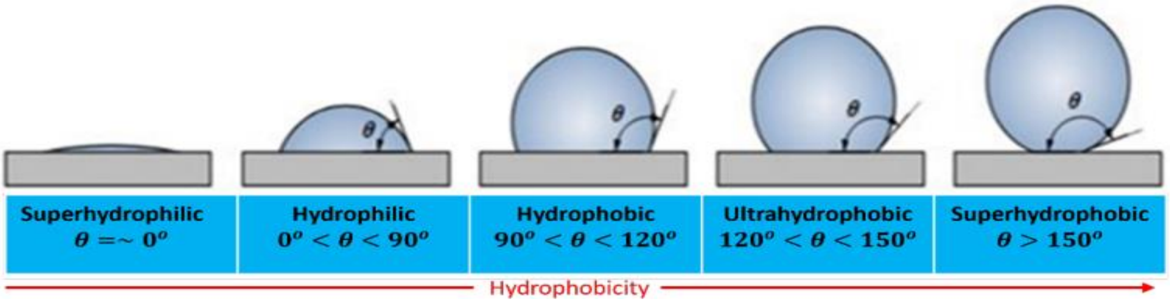

Figure 4.23. Range of WCA from superhydrophilic to superhydrophobic [92].

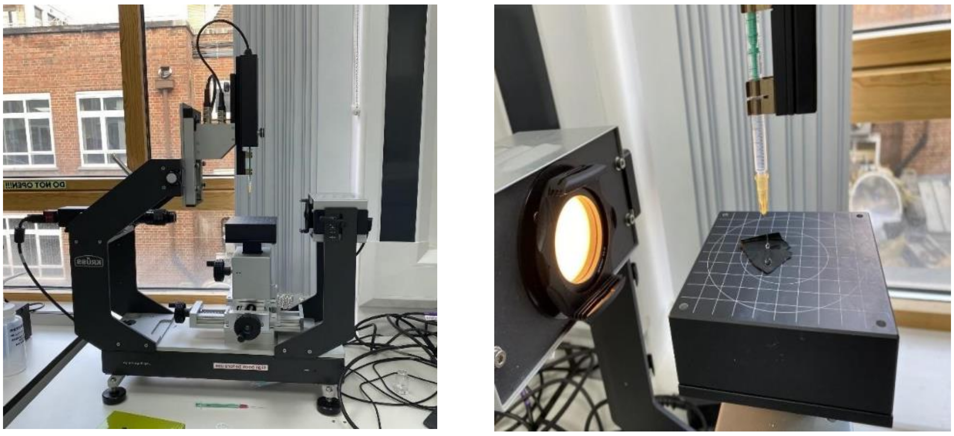
(a) (b)

Figure 4.24. (a) DSA30 Krüss drop shape analyser and (b) water droplet contacting PU+GNP+CNT surface after dispensing from the syringe.

The DSA30 Krüss contact angle measuring instrument, available at PR campus as shown in *Figure 4.24(a)*, was used to measure the water contact angle (WCA) of both pure PU and modified PU nanocomposites. These tests aimed to measure the angle between the surface of each nanocomposite and a water droplet upon contact, providing insight in the wettability of each nanocomposite material. A higher water contact angle result in a smaller wetting surface. Consequently, such nanocomposites are preferable for coating wind turbine blades, as they repel rain droplets, reduce water absorption, and improve the coating's erosion resistance over time

Samples of each nanocomposite were placed on a table, where a water droplet dispensed from a syringe attached to the instrument contacted the surface of each sample *Figure 4.24(b)*. Using a camera mounted opposite each specimen, the contact angle was measured 2 minutes after the droplet made contact. This allowed for a comparison of the water contact angles among different PU nanocomposites after the same exposure period to water. The results of these WCA measurements are shown in *Figure 4.25*. The surface free energy ($-\Delta G_{SL}$) can be calculated using the following Young-Dupre equation [73]:

$$-\Delta G_{SL} = (1 + \cos\theta)\gamma_L^T \tag{4.9}$$

Where the water surface tension γ_L^T = 72.8 mJ/m^2 and θ is the measured water contact angle.

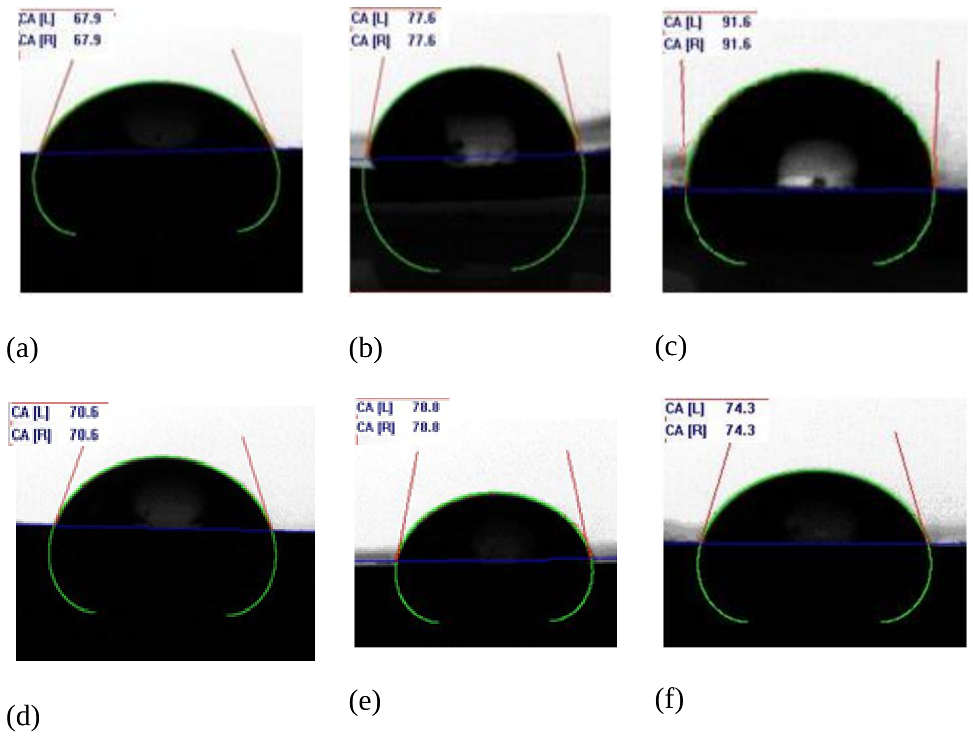

Figure 4.25. Water contact angle for (a) Pure PU [67.9°], (b) PU+GNP [77.6°], (c) PU+GNP+CNT [91.6°], (d) PU+SiO2 [70.6°], (e) PU+GNP+SiO2 [78.8°], and (f) PU+CNT+SiO2 [74.3°]

The measured contact angles along with the calculated free surface energies are summarised in *Table 4.3*. The addition of hydrophobic silica, GNP and CNT nanomaterials reduced the surface free energy of PU from 100.2 mJ/m^2 to 70.8 mJ/m^2 for the PU+GNP+CNT nanocomposite. All other modified PUs exhibited lower surface free energies compared to pure PU. This decrease in surface free energy indicates an improvement in the water repellence of the PU-modified coatings, potentially enhancing the durability of structures exposed to rain.

The surface free energy of pristine graphene is approximately 44.8±14.7 mJ.m^{-2} [93], while for CNTs, it varies depending on their type (single-walled or multi-walled) and functionalization, typically ranging from 27-45.3 mJ.m^{-2} [94]. The surface free energy of fumed silica also varies significantly depending on its surface treatment, typically around 46-54 mJ.m^{-2} [95]. Adding GNP, CNT, and SiO_2 nanoparticles, either individually or in combination, to the PU matrix reduces the surface free energy of resultant nanocomposite.

According to the Wenzel [96] and Cassie-Baxter [97] model, rougher surfaces can amplify the intrinsic hydrophobicity of a material, resulting in a larger contact angle between the liquid and the surface. Incorporation of GNP, CNT, and SiO_2 increases the surface roughness of the nanocomposites. In addition, the presence of nanoparticles within the PU matrix creates a more tortuous path for water molecules, acting as barriers to their penetration into the PU matrix.

Finally, the polarity of a material's surface affects its surface free energy, with more polar surfaces generally exhibiting higher surface free energy. Adding CNTs or graphene to a polymer matrix reduces the overall polarity of the composite due to their inherent apolar characteristics. These factors contribute to the decrease in surface free energy of modified PU matrices, leading to improved water repellence relative to the pure PU coatings. This improvement can enhance the water resistance of wind turbine blades exposed to rain.

Table 4.3. Water contact angle (WCA) and surface free energy for PU and nanomodified PUs.

Specimen	**WCA**	**$-\Delta G_{SL}$ (mJ/m^2)**
Pure PU	67.9°	100.2
PU+GNP	77.6°	88.4
PU+GNP+CNT	91.6°	70.8
PU+SiO_2	70.6°	97.0
PU+SiO_2+GNP	78.8°	86.9
PU+SiO_2+CNT	74.3°	92.5

4.5 Conclusion

In this chapter, physicochemical characterisation tests including FTIR, DSC, TGA, DMA, and water contact angle measurement, were carried out. A comparative analysis of various physicochemical properties including thermal stability, hydrophobicity and heat flow was conducted to determine the optimal PU nanocomposite.

The DSC test showed that the glass transition of the soft segment in PU nanocomposites occurred around -68.6°C, while DMA tests identified the glass transition temperature of hard segment in pure polyurethane and its nanocomposites around -20°C. TGA results demonstrated that all PU nanocomposites exhibit thermal stability up to approximately 278°C, beyond which decomposition occurs, making them applicable for coating under extreme weather conditions. PU+SiO_2 showed the highest residual mass at 600°C, attributed to the thermal stability of SiO_2, a inorganic material.

Water contact angle measurements showed that the incorporation of hydrophobic fumed nanosilica, GNP, and CNT reduced the surface free energy of PU, with the PU+GNP+CNT nanocomposite exhibiting the lowest value at 70.8 $mJ \cdot m^{-2}$. In addition, all modified PU formulations showed lower surface free energy compared to pure PU. The water contact angle of PU+SiO_2+GNP and PU+SiO_2+CNT nanocomposites also increased compared to pure PU, making them suitable candidates as optimal coatings depending on their mechanical properties in dry and wet environments.

Chapter 5: Mechanical testing of pure and nanomodified polyurethane

5.1 Introduction

In this chapter the mechanical properties of unmodified polyurethane (PU) and its unary and binary nanomaterial modified nanocomposites including PU+GNP, PU+CNT+GNP, PU+SiO_2, PU+GNP+SiO_2, PU+CNT+SiO_2 in dry condition were investigated. In all cases the weight percentage of nanoparticles were kept constant at 0.3 wt.% for unary and 0.15 wt.% for each nanomaterial for binary additive nanomaterials systems, making the additive nanomaterial for all cases at 0.3 wt.%. Tensile, tearing and abrasion tests were conducted, and the results are presented, and various mechanical properties were extracted and compared. From the results the best performing material was identified.

Fracture surfaces of broken tensile and tearing test specimens were inspected using scanning electron microscopy (SEM), and Energy Dispersive X-ray (EDX) spectroscopy. The digital image correlation (DIC) technique was used for measuring the full field strain distribution for tearing specimens during the tests and their results are presented.

5.2 Tensile tests

All specimens for tensile testing were prepared by polymer casting methods. For this process an aluminium mould was designed in a CAD software and subsequently by using a CNC machine the mould was manufactured. All stages of manufacturing of the tensile mould are shown in *Figure 5.1*. The dimension of the specimen was according to ASTM D412 standard C-type with gauge length of 25mm, a width of 6 mm in the gauge interval and thickness of 3 mm (see *Figure 5.1a*). For each nanocomposite material five specimens were manufactured. Negligible variations in the dimensions occurred during manufacturing due to mixture’s contact with the walls when being poured onto the mould.

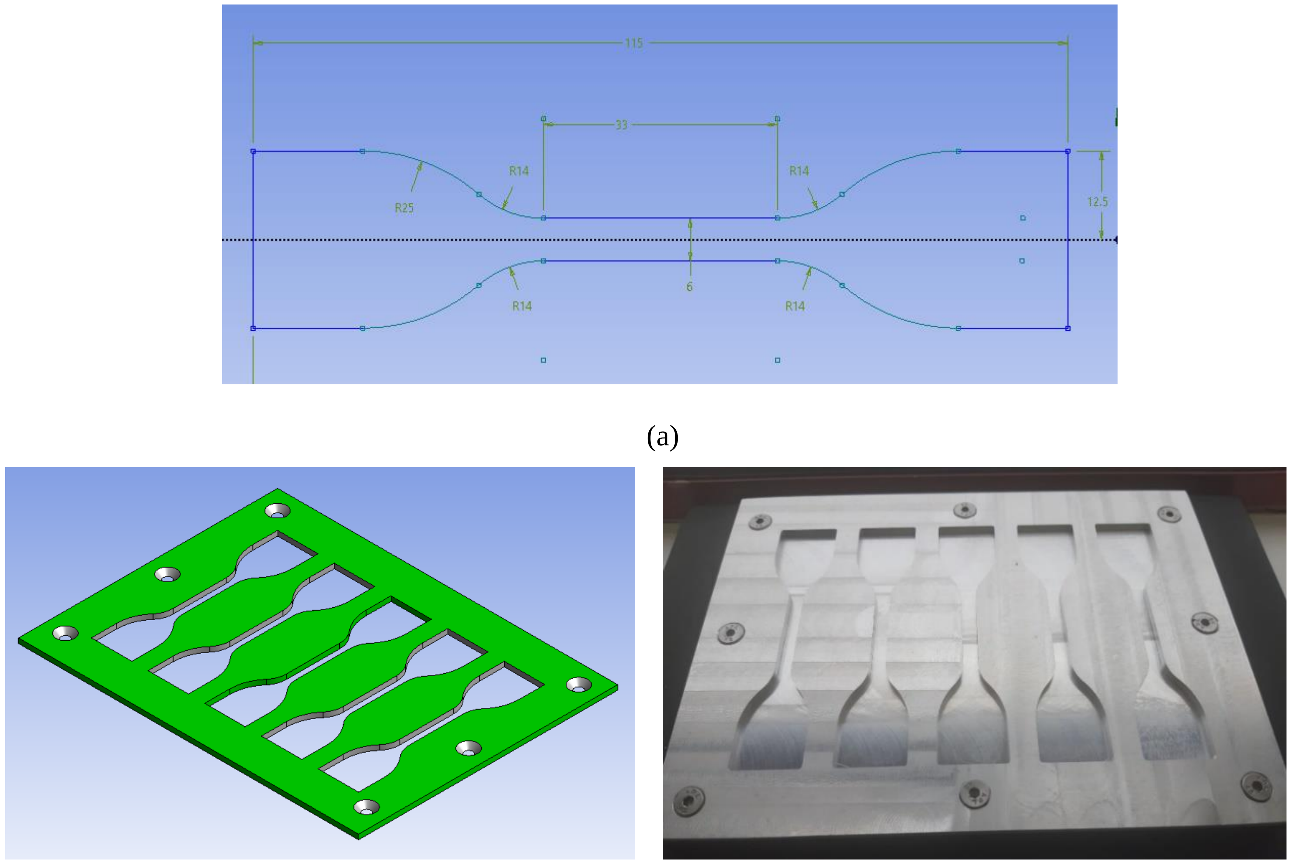

(a)

(b)

(c)

Figure 5.1. (a) Tensile specimen dimensions according to ASTM D412 standard C-type, (b) Aluminium tensile mould machined by CNC machine, (c) Final tensile mould with back plate.

(a)

(b)

Figure 5.2. (a) Various casted tensile test specimens, (b) Tensile specimen fitted between the grips of HTE universal testing machine.

Figure 5.2a shows samples of the manufactured tensile specimens. After preparing the tensile specimens, tensile tests were conducted using an HTE Hounsfield universal testing machine (see *Figure 5.2(b)*). During the testing, the specimens were firmly griped to the fixed grip at the bottom and to the crosshead at the top. A built-in extensometer with the gauge length of 50 mm was attached to the centre of the specimens and the tests were carried out at a constant crosshead speed of 30 mm/min for all specimens.

During the tests, the applied load and extension were recorded, and the engineering strain (ε_e) and the engineering stress (σ_e) were calculated. The engineering stress was calculated by:

$$\sigma_e = \frac{F}{A} \tag{5.1}$$

Here, F represents the applied load measured by the machine's load cell, and A is the original cross-sectional area of a tensile specimen. This area was determined by averaging three measurements of the specimen's width and thickness within the gauge length.

The engineering strain was computed using the following equation:

$$\varepsilon_e = \frac{\delta}{L_0} \tag{5.2}$$

Where δ is the gauge extension measured by the extensometer, and L_0 is the original extensometer gauge length.

The true stress (σ_t) is calculated using:

$$\sigma_t = \sigma_e \times (1 + \varepsilon_e) \tag{5.3}$$

and the true strain (ε_t) is calculated using:

$$\varepsilon_t = ln(1 + \varepsilon_e) \tag{5.4}$$

The collected data from the tensile tests were analysed, and true strain versus true stress was plotted for all tested specimens. From the stress-strain diagrams, Young's modulus, ultimate tensile strength (UTS), strain at rupture, and modulus of toughness were determined.

These mechanical properties were used to evaluate which material performed best, with the potential to improve the erosion resistant of coating for the leading edges of wind turbine blades.

The fracture surface of broken specimen from each material were investigated by a ZEISS Crossbeam 550 Scanning Electron Microscope (SEM) (see *Figure 5.3*).

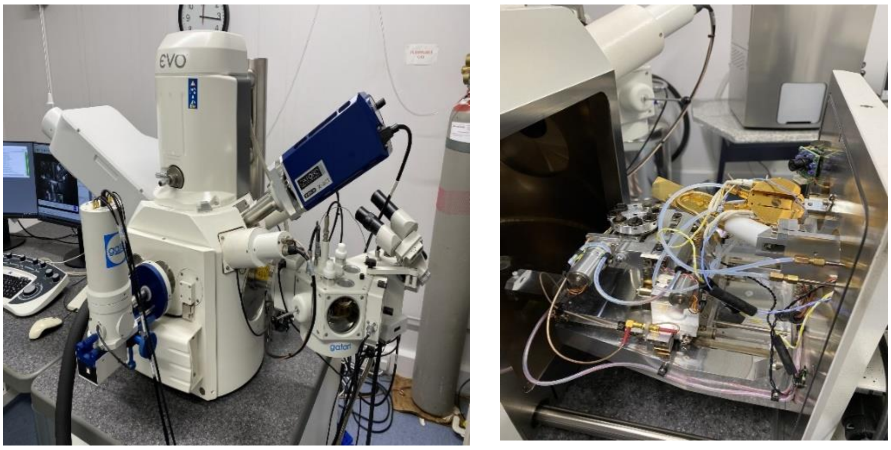

(a) (b)

Figure 5.3. (a) The ZEISS Crossbeam 550 SEM machine and (b) SEM's interior where specimens are placed.

The SEM specimens were each obtained by cutting samples from the fractured area of tensile and tear specimens and they were thoroughly cleaned with ethanol and pressured air to remove debris from the fracture surfaces. It is essential for the specimens to have electrical conductivity for SEM imaging. Making the polymer specimens electrically conductive, the fracture surfaces were coated with 10-15 nm of carbon to make them electrically conductive and thus prevent electrical charge accumulation. All the SEM specimens were mounted on stubs using carbon tape and the SEM images were taken at 25 kV and at different magnifications (see *Figure 5.4*).

Figure 5.4. Specimens mounted on stubs for SEM imaging.

5.2.1 Tensile test results of pure PU

The true stress-strain results for pure PU specimens are illustrated in *Figure 5.5*. All specimens showed similar behaviour which indicates that the testing, and the manufacturing of pure PU specimens were consistent. Table 5.1 summarises the mechanical material properties of pure PU. As shown in Table 5.1, the average measured Young's modulus of pure PU is 4.2 MPa, UTS 14.5 MPa, strain at rupture is 130.5%, and modulus of toughness, the area under strain-strain curve, is 589 J/mm^3. The modulus of toughness is related to resistance to fracture and a higher value is desirable.

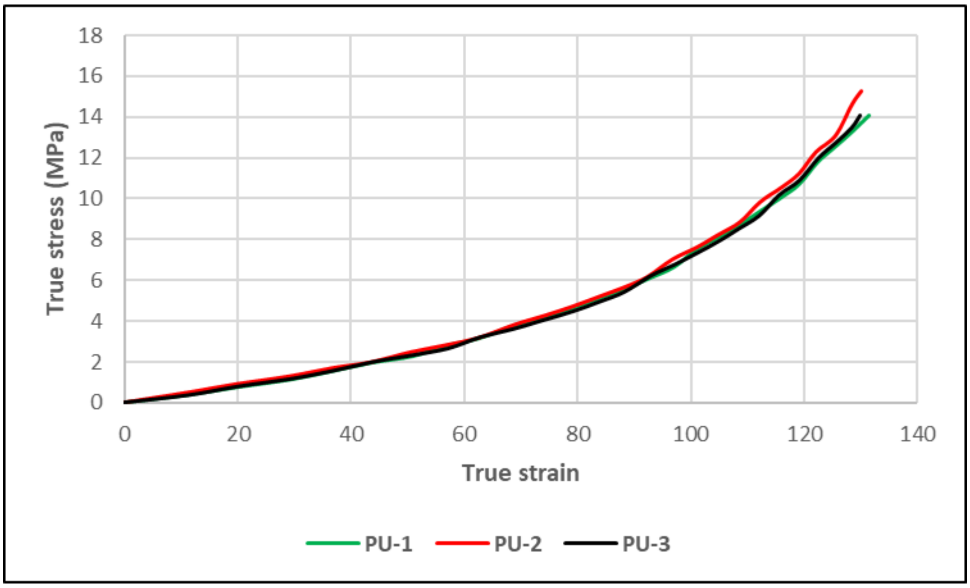

Figure 5.5. True stress-strain curves for pure PU specimens.

Table 5.1. Key mechanical properties for PU tensile tests.

Material	Young's modulus (MPa)	UTS (MPa)	Strain at rupture (%)	Modulus of toughness (J/mm3)
PU-1	4.2	14.1	131.5	595
PU-2	4.4	15.3	130.1	601
PU-3	4.1	14.1	129.8	570
Average	4.2±0.2	14.5±0.7	130.5±0.9	589±16

The SEM and EDX analysis were carried out on the fracture surface of *PU* specimen. The SEM images shown in *Figure 5.6* at two different magnifications (scale bars of 3μm and 20μm) indicate that the pure PU have a relatively smooth fracture surface and minimum microcracks occurred during failure. The presence of few microcracks and voids at the fracture surface indicates that the energy absorption of the pure PU was dominated by plastic deformation.

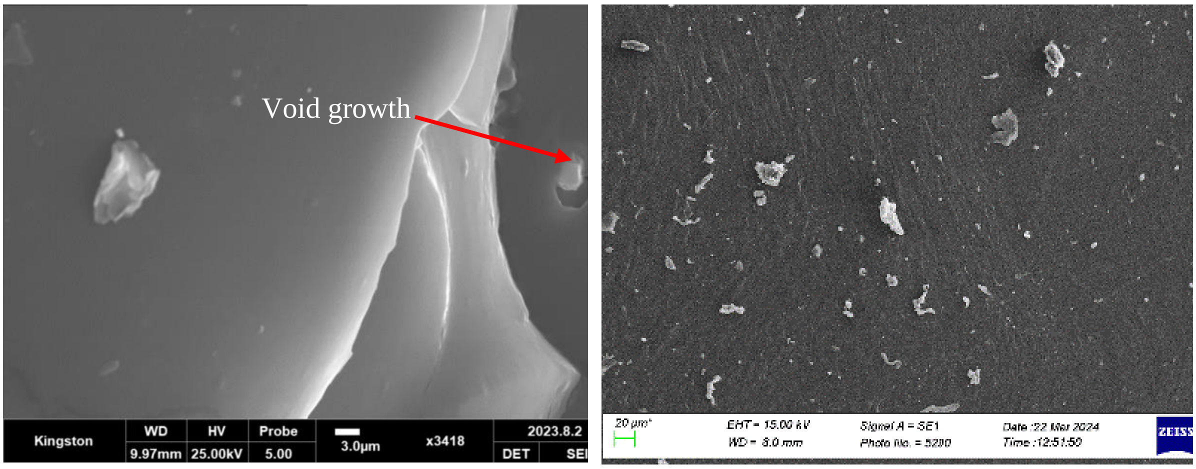

(a) (b)

Figure 5.6. SEM images for a pure PU specimen at two different magnifications.

The EDX and elemental mapping in PU specimen are shown *Figure 5.7*. The EDX analysis obtained when an electron beam is two-dimensionally scanned over the specimen surface, and the characteristic X-ray spectra generated by the electron beam are acquired pixel by pixel. The result shown in *Figure 5.7(a)* demonstrate that carbon has the highest concentration compared to the other elements. The mapping also detected nitrogen which is a key element in the PU chemical composition. In addition, other elements such as sulphur and silver may have been captured due to contamination of the specimen's environment. The elemental mapping of PU shown in *Figure 5.7(b) and (c)* demonstrate a uniform distribution of carbon (C) and oxygen (O) across the entire specimen, showing a homogenous polymerisation of PU. These images confirmed the presence of both carbon and oxygen elements within the PU's chemical structure which agrees with the stoichiometric composition of PU (along with nitrogen and hydrogen).

It should be noted that in SEM and EDX concerning all PU nanocomposites, determining the source of carbon can be challenging when the specimen has been carbon-coated. To address this, elemental mapping was performed across the surface of the specimen, where areas with the polymer will often show additional elements associated with it like nitrogen or oxygen, which is not present in the carbon coating. Also, carbon coatings for SEM are typically thin so the signal from this coating is theoretically weak compared to that of a bulk polymer.

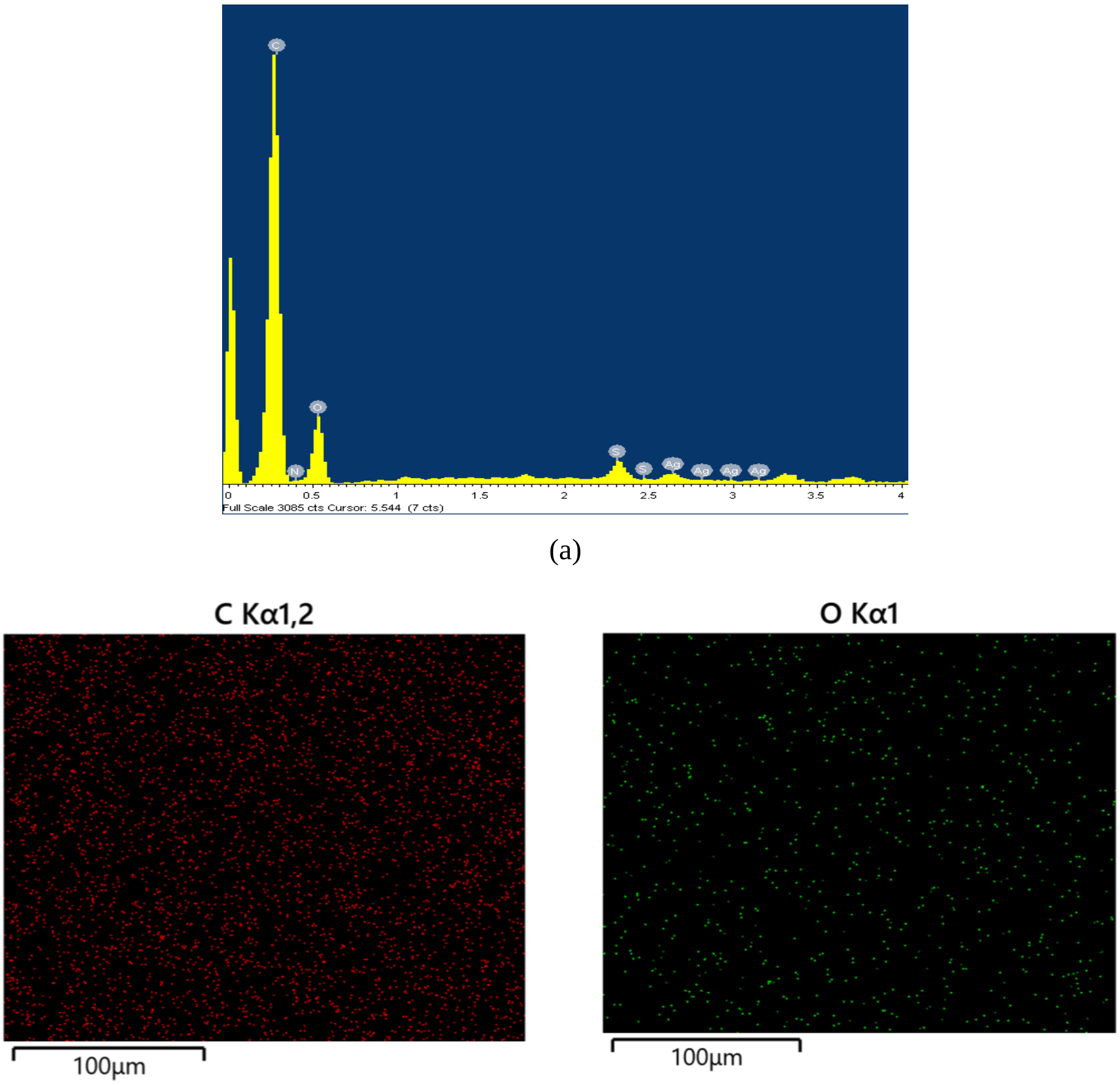

(a)

(b)

(c)

Figure 5.7. (a) EDX and elemental mapping for (b) carbon, and (c) oxygen in a pure PU specimen.

5.2.2 Tensile test results of PU+GNP

GNP has poor dispersion within polymer matrix. An effective solution to enhance GNP dispersion and interfacial strength with the polymer matrices is the functionalization of GNPs [98, 75]. Studies report that surface functionalization of GNPs through covalent bonding improves filler/matrix interactions and promotes uniform distribution [99]. Several other researchers have also employed covalent functionalisation of GNP to enhance the properties of epoxy/graphene nanocomposites (e.g. see [100, 101]). The graphene used in this project is carboxyl (COOH) functionalised nanoplatelets (f-GNP) which the free radical bond creates a covalent bond with polymer backbone. For brevity from here on the f-GNP will be referred to as GNP.

The specimens of PU+GNP with GNP loading of 0.3 wt.% underwent the tensile tests, each at a crosshead speed of 30 mm/min until specimen failed. The true stress-strain results in *Figure 5.8* indicated that the data for the PU+GNP-3 specimen showed average performance, making it a suitable representative of the true stress-strain behaviour of PU+GNP specimens for comparative studies.

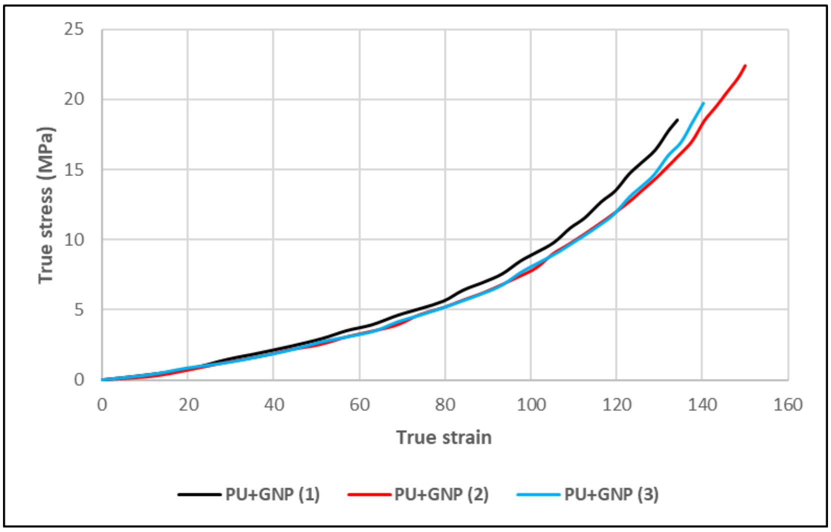

Figure 5.8. True stress-strain curves of all PU+GNP specimens at 0.3 wt.% GNP loading.

Table 5.2 summarizes the results for Young's modulus, UTS, strain at rupture, and modulus of toughness for PU+GNP at a 0.3 wt.% loading. Young's modulus and UTS increased by 2.4% and 39.3%, respectively, while strain at rupture and modulus of toughness rose by 8.4% and 46%, respectively, compared to pure PU specimens.

Table 5.2. Key mechanical properties for PU+GNP specimens from tensile tests.

Material	Young's modulus (MPa)	UTS (MPa)	Strain at rupture (%)	Modulus of toughness (J/mm^3)
PU+GNP-1	4.6	18.5	134.1	778
PU+GNP-2	4	22.4	149.9	988
PU+GNP-3	4.3	19.7	140.2	807
Average	4.3±0.4	20.2±2	141.4±8	858±114

SEM and EDX analysis were carried out on the selected *PU+GNP* specimen fracture surface and the results are shown in *Figure 5.9* and *Figure* 5.10. Microcracking, creation of ridges, crack branching and fragments of nanocomposite were observed on the fracture surface and unlike the pure PU, the fracture surface was not smooth, and some ridges were visible on the surface. These extra features on the fracture surfaces contributed to the higher modulus of toughness relative to pure PU as reported in *Table 5.2*.

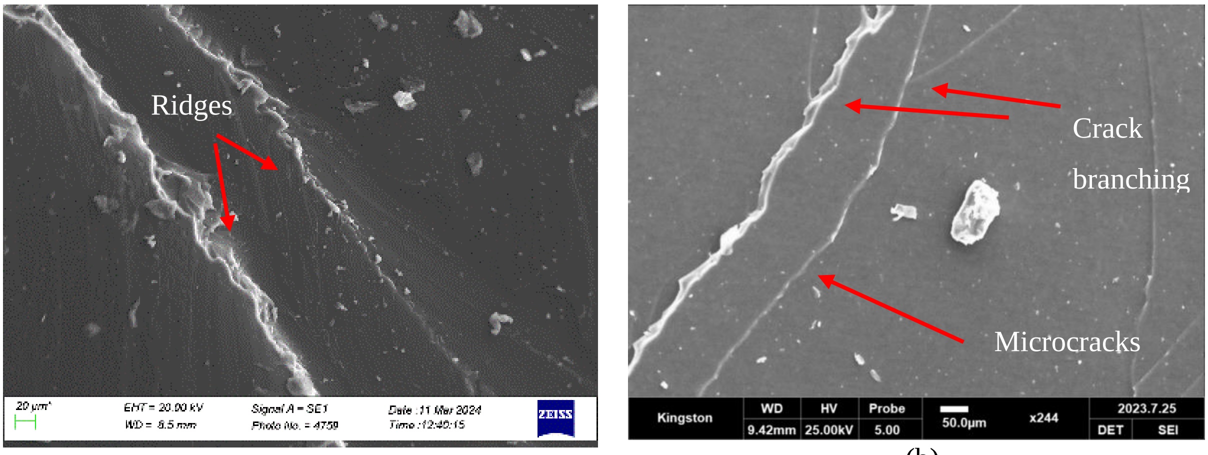

(a) (b)

Figure 5.9. SEM images for a PU+GNP specimen at two different magnifications.

The EDX and elemental mapping of PU+GNP specimen surface are shown in *Figure 5.10*. The result shown in *Figure 5.10(a)* demonstrate that carbon has the highest concentration compared to the other elements. The mapping also detected nitrogen which is a key element in the PU chemical composition. In addition, other elements such as sulphur and silver may have been captured due to contamination of the specimen's environment. The elemental mapping of PU+GNP shown in *Figure 5.10(b) and (c)* demonstrate a uniform distribution of C and O across the entire specimen hence confirming the presence of both carbon and oxygen elements within the PU+ GNP's chemical structure which agrees with the stoichiometric composition of PU+GNP (along with nitrogen and hydrogen).

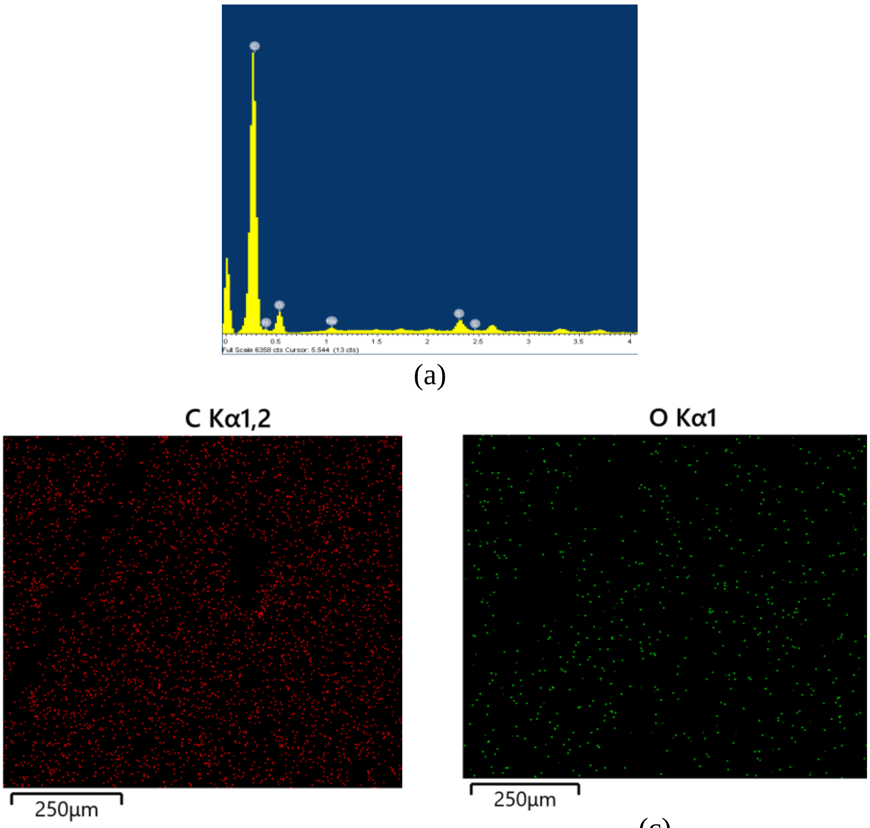

(a)

(b) (c)

Figure 5.10. (a) EDX and elemental mapping for (b) carbon, (c) oxygen in a pure PU+GNP specimen.

5.2.3 Tensile test results of PU+GNP+CNT

In this case, the PU is modified by the binary GNP and CNT nanoparticles equally at 0.15 wt.% at a total loading of 3 wt.%. The carbon nanotubes are a multiwalled CNT (MWCNT). The true stress-strain results for PU+GNP+CNT specimens are illustrated in *Figure 5.11*.

The true stress-strain results indicated that the data for the PU+GNP+CNT-2 specimen showed average performance, making it a suitable representative of the true stress-strain behaviour of PU+GNP+CNT specimens for comparative studies.

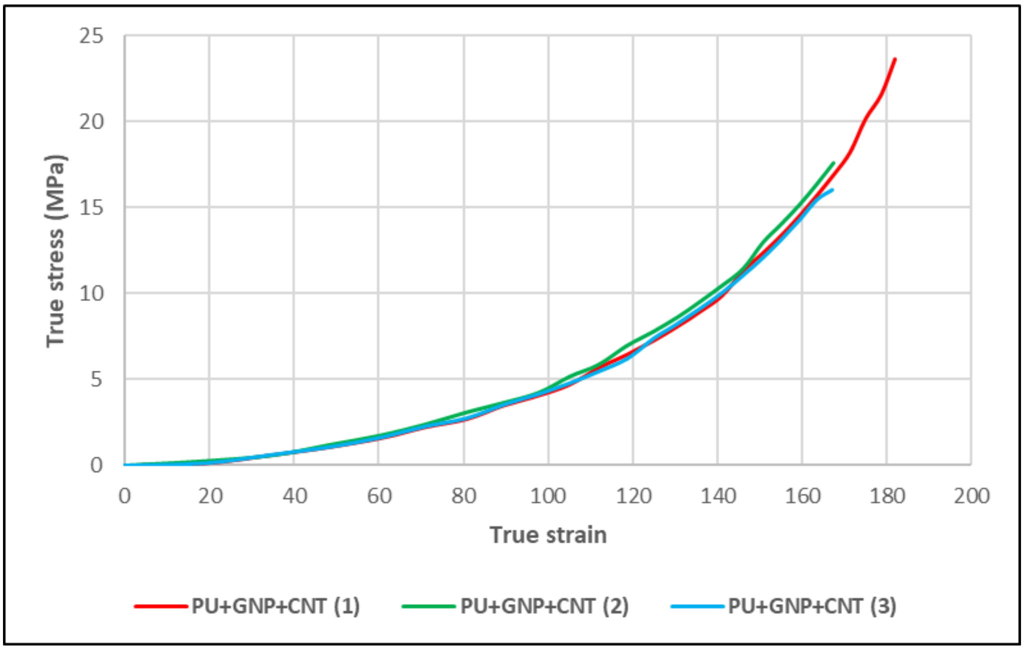

Figure 5.11. True stress-strain curves of all PU+GNP+CNT specimens.

Table 5.3 summarizes the results for Young's modulus, UTS, strain at rupture, and modulus of toughness for PU+GNP+CNT at a 0.3 wt.% loading. Young' modulus decreased by 42.9%, while the UTS, the strain at rupture, and modulus of toughness increased by 31.7%, 32%, and 50.3%, respectively, compared to pure PU specimens. The decrease in Young's modulus was probably related to the agglomeration of CNT and GNP nanoparticles. It was reported that MWCNTs inhibit stacking of GNPs, improve their dispersion, and can bridge between GNPs, leading to an increased contact surface [102]. Pontefisso, and Mishnaevsky Jr. [103] by using finite element analysis showed that while graphene particles cause the crack deviation at the early stages of fracture, the CNTs ensure the debonding and fibre bridging mechanisms after the main crack is formed. They also reported that Young's modulus decreases when going from exfoliated to low and then high aggregated structures. SEM and EDX analysis were carried out on the *PU+GNP+CNT* fracture surface to study its chemical elemental composition and the energy absorbing mechanism.

Table 5.3. Key mechanical properties for PU+GNP+CNT specimens from tensile tests.

Material	Young's modulus (MPa)	UTS (MPa)	Strain at rupture (%)	Modulus of toughness (J/mm^3)
PU+GNP+CNT-1	2.6	23.7	181.9	1065
PU+GNP+CNT-2	2.3	17.6	167.5	824
PU+GNP+CNT-3	2.1	16.0	167.2	767
Average	2.4±0.3	19.1±4	172.2±8	885±158

The SEM image of PU+GNP+CNT in *Figure 5.12* shows a wavy pattern. More fragments of the nanocomposite are visible on the fracture surface, along with elongated microcracks and crack branching. These features contributed, in part, to the higher modulus of toughness compared to pure PU.

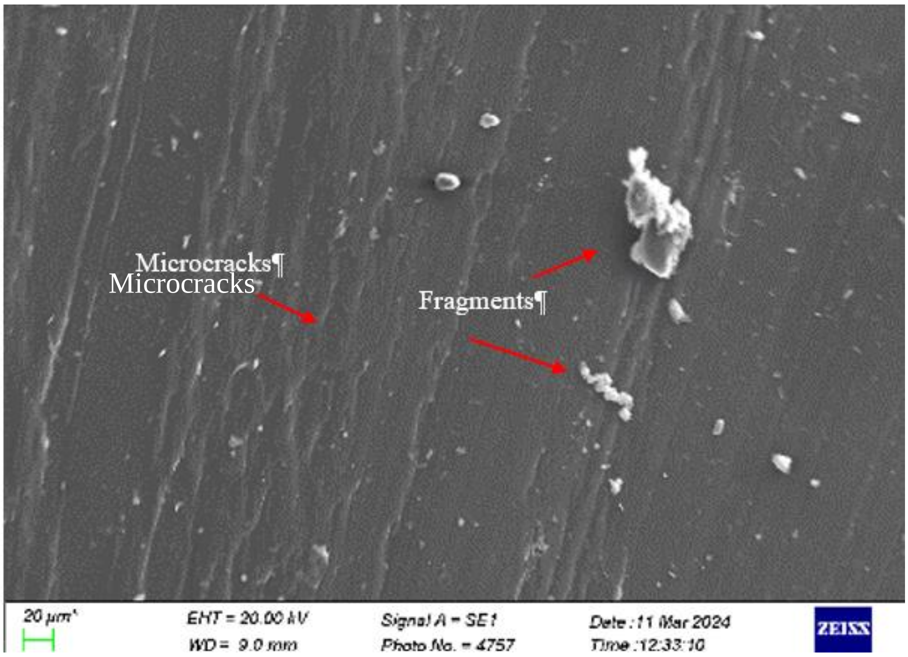

Figure 5.12. An SEM image for a PU+GNP+CNT specimen.

The EDX and elemental mapping of PU+GNP+CNT specimen surface are shown in *Figure 5.13.* The result in *Figure 5.13(a)* demonstrate that carbon has the highest concentration compared to the other elements. The mapping also detected nitrogen as this is a key element in the PU+GNP+CNT chemical composition. The elemental mapping of PU+GNP+CNT shown in *Figure 5.13(b)* and *(c)* demonstrate a uniform distribution of C and O across the entire specimen.

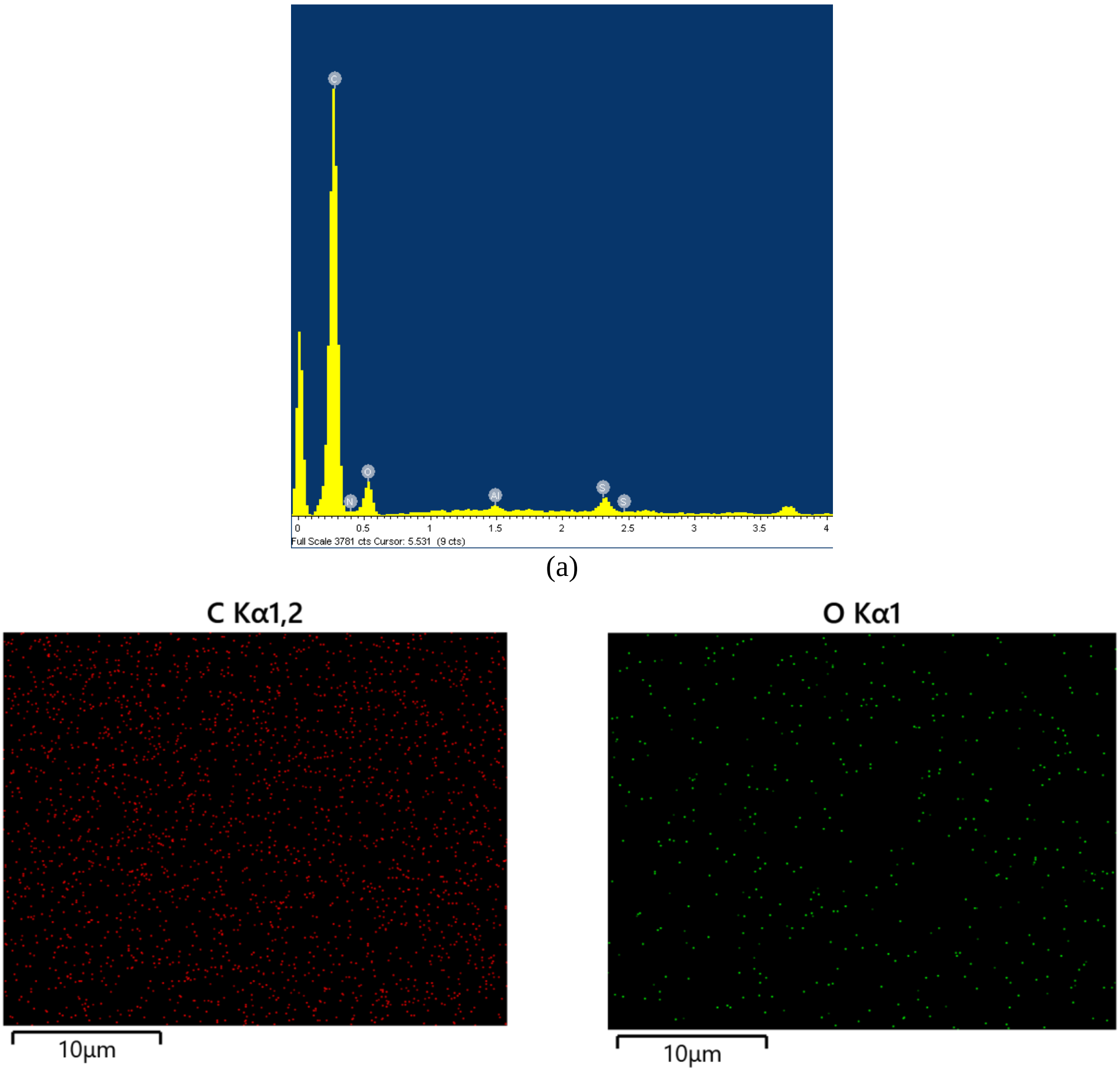

(a)

(b)

(c)

Figure 5.13. (a) EDX and elemental mapping for (b) carbon, (c) oxygen in a PU+GNP+CNT specimen.

5.2.4 Tensile test results of PU+SiO_2

Silicon dioxide, also known as silica, is an oxide of silicon with the chemical formula SiO_2. Previous study by Johansen, et al. [104], Dashtkar, et al. [73], and Malaki et al. [105] showed that by increasing nanosilica loading in the PU, a considerable increase in mechanical properties and the erosion resistance of the resultant coating will be achieved. It is also reported that the presence of the nanosilica particles improve the tribological properties, which in turn protects the surface against harsh weathering conditions. [106] In this part fumed nanosilica was used for reinforcement of PU.

Tensile tests of PU+SiO_2 specimens with nanosilica loading of 0.3 wt.% have been carried out at a crosshead speed of 30 mm/min and the tests were continued until specimens' failure. The true stress-true strain results for PU+SiO_2 specimens are illustrated in *Figure 5.14* and the extracted mechanical properties are summarised in *Table 5.4*.

Although the mixing process of nanosilica with the polyol and isocyanate has been done in a vacuum chamber, still SEM images showed that not all air bubble were extracted (see *Figure 5.15*(b)). Depending on the locations of these voids, premature failure of specimens were observed. From the results it was determined that the stress-strain of the PU+SiO_2-2 specimen is a representative for PU+SiO_2 material. The graph of this specimen will be used later in comparative studies.

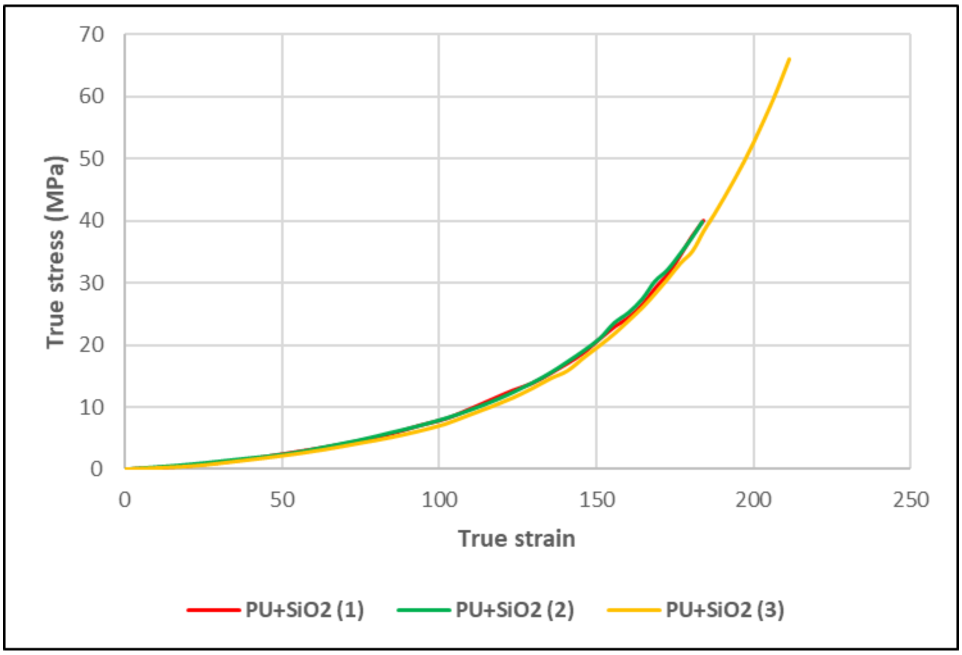

Figure 5.14. True stress-strain curves of all PU+SiO_2 specimens

In Table 5.4. Key mechanical properties for PU+SiO_2 specimens from tensile test., the Young's modulus, UTS, strain at rupture and modulus of toughness of PU+SiO_2 at 0.3 wt.% SiO_2 loading are summarised. The Young's modulus, UTS, strain at rupture and modulus of toughness had all increased by 9.5%, 235%, 48% and 303%, respectively, relative to pure PU specimens.

SEM and EDX analysis of the fracture surface were carried out on the *PU+SiO_2-2* specimen to study its chemical elemental composition and the mechanisms contributing to higher energy absorption. As it can be seen from *Figure 5.15*(a) and (b), the fracture surface of PU+SiO_2 is very rough which resulted in a fracture area much higher than PU specimens. Severe microcracks and presence of the voids and their expansion upon loading resulted in significant increase in modulus of toughness relative to unmodified PU.

Table 5.4. Key mechanical properties for PU+SiO_2 specimens from tensile test.

Material	Young's modulus (MPa)	UTS (MPa)	Strain at rupture (%)	Modulus of toughness (J/mm^3)
PU+SiO_2-1	4.7	40.0	184.1	1941
PU+SiO_2-2	4.9	39.9	183.9	1959
PU+SiO_2-3	4.2	66.0	211.3	3212
Average	4.6±0.4	48.6±15	193±16	2371±729

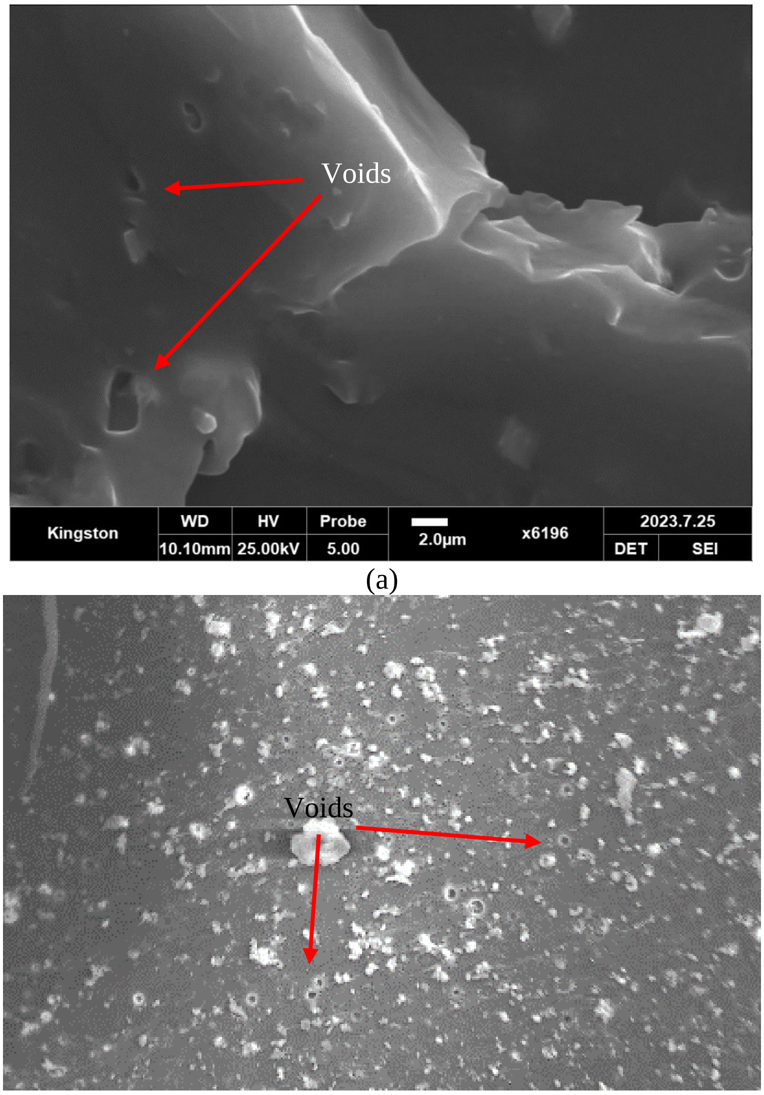

(a)

(b)

Figure 5.15. SEM images for PU+SiO_2 at two different magnifications.

The EDX and elemental mapping in PU+SiO_2 specimen are shown *Figure 5.16*. The result shown in *Figure 5.16(a)* demonstrate that carbon has the highest concentration compared to the other elements. The mapping also detected nitrogen and silica as both elements are key element in the PU+SiO_2 composition. The elemental mapping of PU shown in *Figure 5.16(b), (c)* and *(d)* demonstrate a uniform distribution of carbon, oxygen and fumed nanosilica (Si) across the entire specimen, hence confirming the presence of these three elements within the PU nanocomposite.

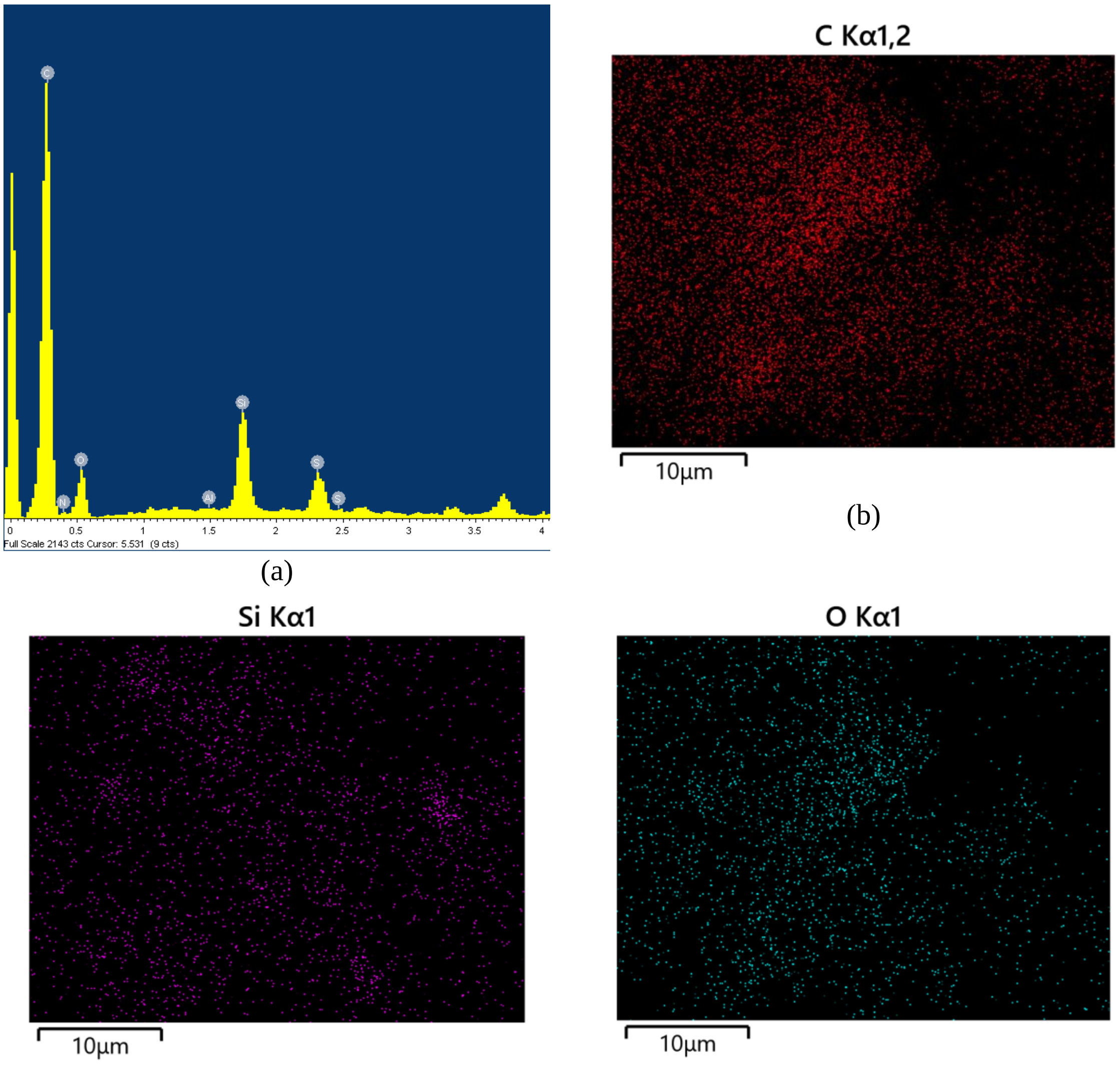

(a)

(b)

(c)

(d)

Figure 5.16. (a) EDX and elemental mapping for (b) carbon, (c) silica, and (d) oxygen in a PU+SiO_2.

5.2.5 Tensile test results of PU+SiO_2+GNP

Since the mechanical properties of PU are significantly improved when modified individually with GNP and SiO_2, it was decided to explore their combined synergistic effect on enhancing the mechanical properties of PU. To maintain a consistent total nanomaterial inclusion of 0.3 wt.%, equal amounts of each nanoparticle were added to the PU.

Tensile tests of PU+SiO_2+GNP specimens were carried out at a crosshead speed of 30 mm/min until specimens' failure. The true stress-strain results for PU+SiO_2+GNP specimens are illustrated in *Figure 5.17*. Compared to the other specimens, PU+SiO_2+GNP-1 showed deviations in stress-strain response, particularly in yield strength, UTS, modulus of toughness, and strain at rupture. These differences suggest potential variations in material properties for this specimen, possibly due to the location and size of defects. From the results it was determined that the stress-strain of the PU+SiO_2+GNP-2 specimen is a representative for PU+SiO_2+GNP material. The graph of this specimen will be used later in comparative studies.

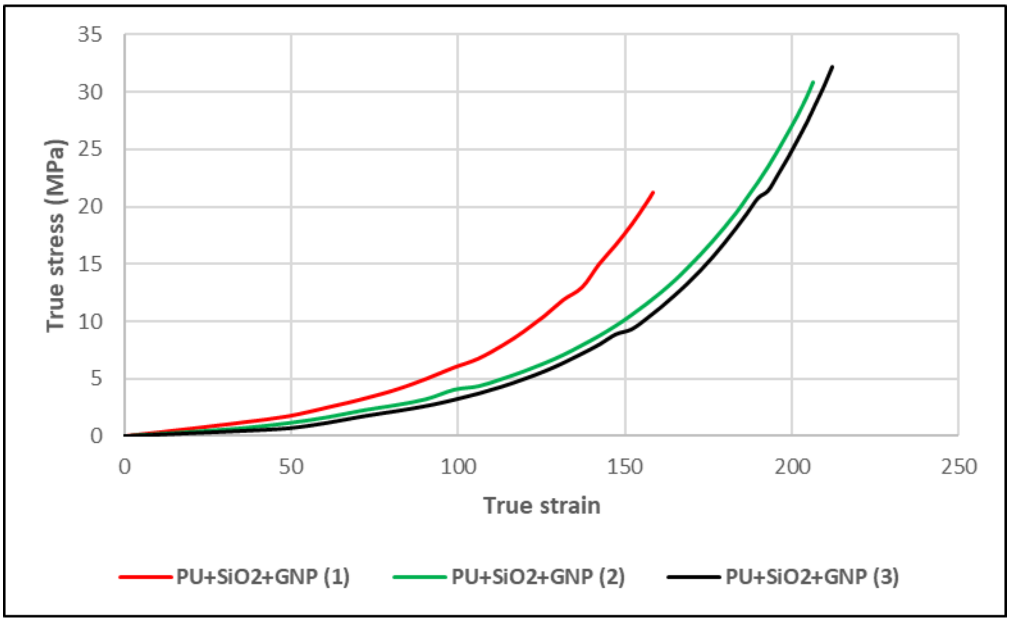

Figure 5.17. True stress-strain curves of all PU+SiO_2+GNP specimens.

Table 5.5 summarises the Young's modulus, UTS, strain at rupture and modulus of toughness of PU+SiO_2+GNP at 0.3 wt.% total nanomaterials loading. Relative to pure PU, the Young's modulus decreased by 33.3%, but the UTS, strain at rupture and the modulus of toughness all increased by 93.8%, 47.4% and 125%, respectively.

Table 5.5. Key mechanical properties for all PU+SiO_2+GNP tensile tests.

Material	Young's modulus (MPa)	UTS (MPa)	Strain at rupture (%)	Modulus of toughness (J/mm^3)
PU+SiO_2+GNP-1	3.4	21.2	158.5	927
PU+SiO2+GNP-2	2.6	30.9	206.4	1522
PU+SiO2+GNP-3	2.3	32.2	212.2	1535
Average	2.8±0.6	28.1±8	192.3±35	1328±347

An SEM and EDX analysis were carried out on the selected PU+SiO_2+GNP fracture surface to study its elemental composition and the energy absorbing mechanism. Some microcracks, wrinkle and lots of debris of polymer fragments were observed on the fracture surface rendering it rough. These features contributed to substantial higher modulus of toughness (see *Figure 5.18*).

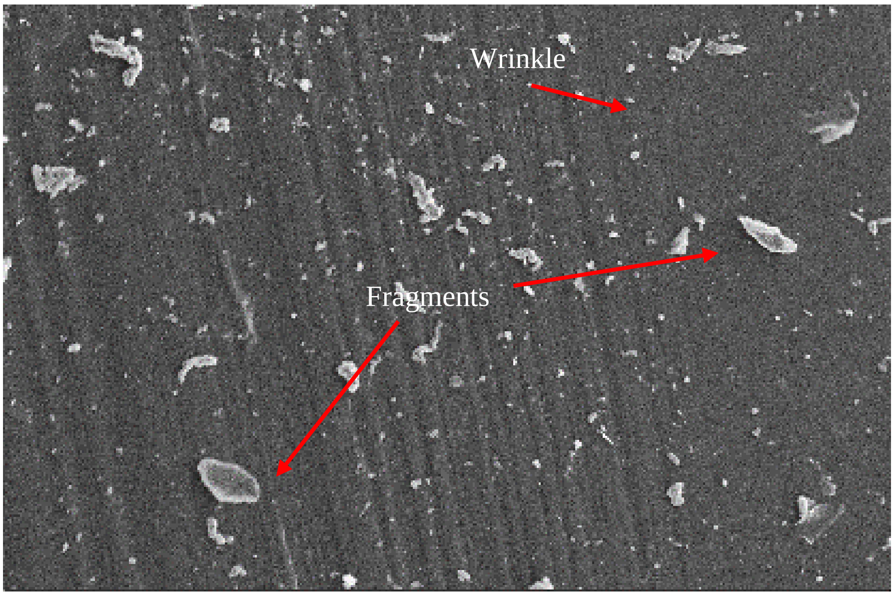

Figure 5.18. SEM image for PU+SiO_2+GNP.

The EDX of PU+SiO_2+GNP specimen is shown *Figure 5.19*. The result demonstrate that carbon has the highest concentration compared to the other elements. The mapping also detected nitrogen and silica as both elements are key element for this chemical composition. In addition, other elements such as sulphur and silver may have been captured due to contamination of the specimen's environment.

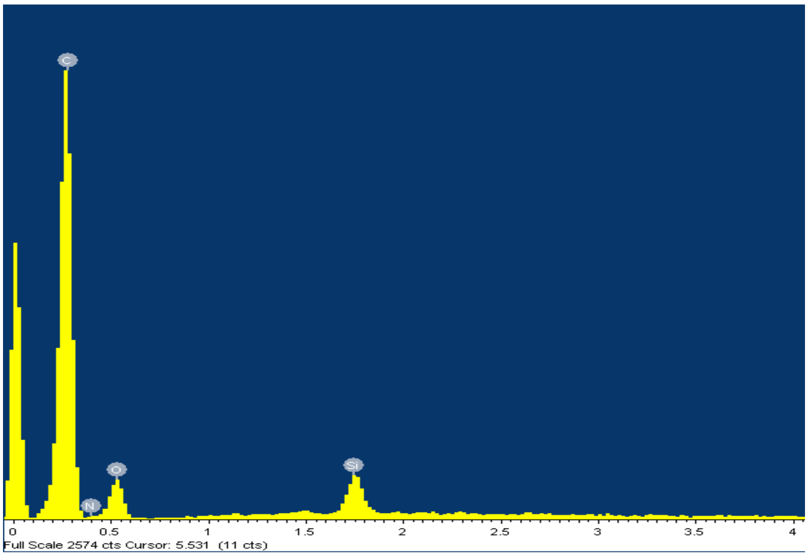

Figure 5.19. EDX and elemental mapping for a PU+SiO2+GNP specimen.

5.2.6 Tensile test results of PU+SiO_2+CNT

The synergistic effect of the binary nanoparticle system comprising SiO_2 and CNT for reinforcing PU was also investigated. In this binary system, the total nanoparticle loading was maintained at 0.3 wt.%, with equal contributions from each nanomaterial. Tensile tests on PU+SiO_2+CNT specimens were conducted at a crosshead speed of 30 mm/min, continuing until the specimens failed. The true stress-strain results for the PU+SiO_2+CNT specimens are illustrated in *Figure 5.20*.

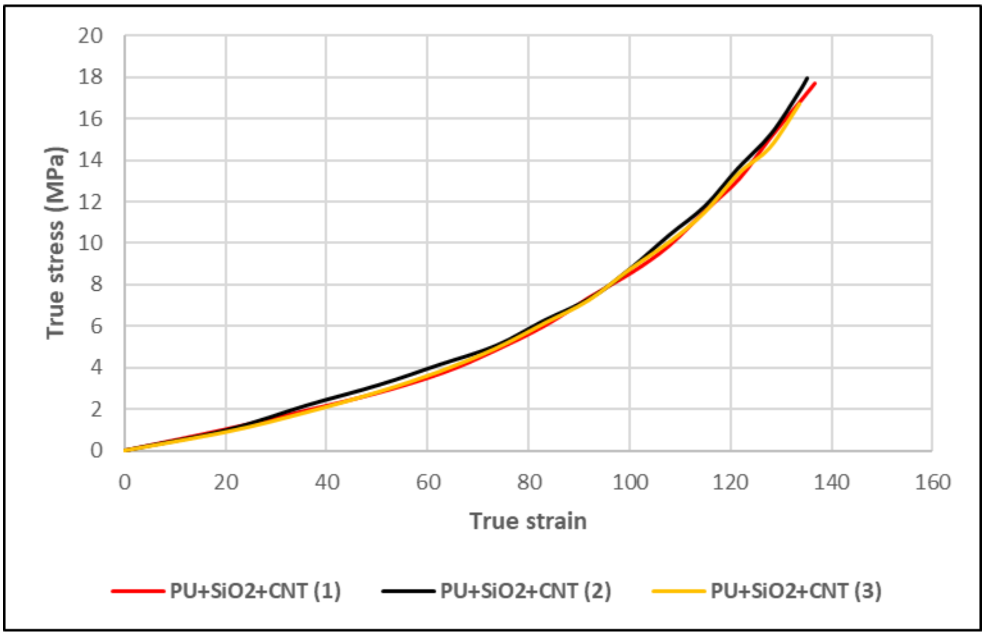

Figure 5.20. True stress-strain curves of all PU+SiO_2+CNT specimens

The stress-strain results show that all specimens performed similarly indicating the consistency in manufacturing the specimens. From the results it was determined that the stress-strain of the PU+SiO_2+CNT-3 specimen is a representative for PU+SiO_2+CNT material. The graph of this specimen will be used later in comparative studies.

Table 5.6 summarises the Young's modulus, UTS, strain at rupture and modulus of toughness of PU+SiO_2+CNT at total 0.3 wt.% nanomaterials loading. Relative to pure PU, the Young's modulus, UTS, strain at rupture and modulus of toughness all increased by 14.3%, 20.7%, 3.6% and 31.7%, respectively.

Table 5.6. Key mechanical properties for all PU+SiO2+CNT tensile tests.

Material	Young's modulus (MPa)	UTS (MPa)	Strain at rupture %	Modulus of toughness (J/mm^3)
PU+SiO2+CNT-1	5.1	17.7	136.7	792
PU+SiO2+CNT-2	4.9	17.9	135.5	796
PU+SiO2+CNT-3	4.5	16.7	133.8	741
Average	4.8±0.3	17.5±0.7	135.2±1.5	776±31

SEM and EDX analysis were carried out on the PU+SiO_2+CNT fracture surface to study its chemical elemental composition and features on the fracture surface which contribute to the higher energy absorption relative to pure PU. On the fracture surface shown in *Figure 5.21*, ridges, some microcracks and polymer fragments are visible, and the fracture surface is uneven which resulted in much higher fracture surface area relative to pure PU. All these features resulted in an increase of 31.7% in module of toughness.

The EDX and elemental mapping in PU+SiO_2+CNT specimen are shown *Figure 5.22*. The result shown in *Figure 5.22(a)* demonstrate that carbon has the highest concentration compared to the other elements. The mapping also detected nitrogen and silica as both elements are key element in the PU+*SiO_2*+CNT chemical composition. The elemental mapping of PU shown in *Figure 5.22(b)* and *(c)* demonstrate a uniform distribution of carbon and oxygen across the entire specimen.

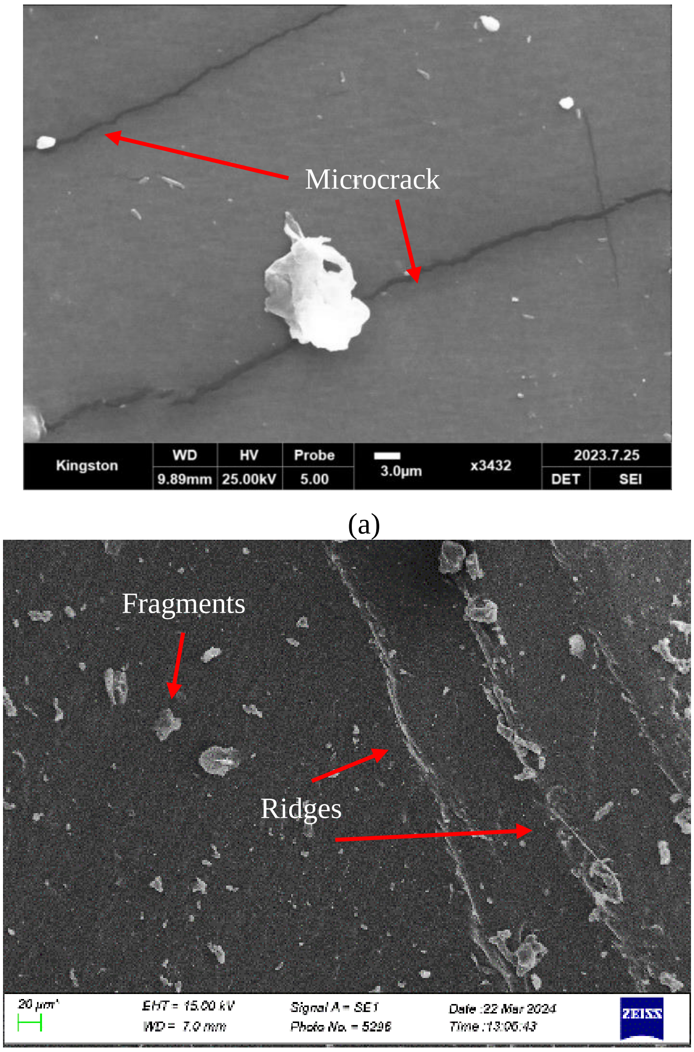

(a)

(b)

Figure 5.21. SEM images for a PU+SiO_2+CNT specimen at two different magnifications: (a) High magnification, (b) Low magnification.

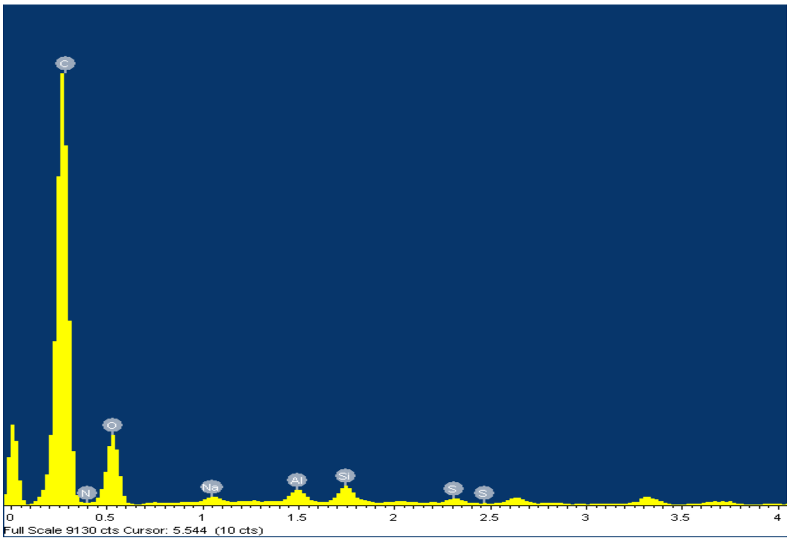

Figure 5.22. EDX of PU+SiO_2+CNT specimen.

The average mechanical properties of PU and all modified PUs are summarized in Table 5.7. The results show that UTS, strain at rupture, and the modulus of toughness of all nanomodified PUs have improved compared to pure PU. However, this is not the case for Young’s modulus. PU+SiO_2 has the highest UTS and modulus of toughness compared to the other specimens and has the highest strain at rupture, second only to PU+SiO_2+GNP. The increase in Young’s modulus from adding fumed nanosilica particles is relatively small. Except for Young’s modulus, the mechanical properties of the PU+SiO_2+GNP nanocomposite have improved significantly, while for the PU+SiO_2+CNT nanocomposite, all mechanical properties, including Young’s modulus, have improved to varying degrees.

Table 5.7. Key mechanical properties for pure PU and all modified PUs.

Material	Young’s modulus (MPa)	UTS (MPa)	Strain at rupture %	Modulus of toughness (J/mm^3)
PU	4.2±0.2	14.5±0.7	130.5±0.9	589±16
PU+GNP	4.3±0.4	20.2±2	141.4±8	858±114
PU+GNP+CNT	2.4±0.3	19.1±4	172.2±8	885±158
PU+SiO_2	4.6±0.4	48.6±15	193±16	2371±729
PU+SiO_2+GNP	2.8±0.6	28.1±8	192.3±35	1328±347
PU+SiO_2+CNT	4.8±0.3	17.5±0.7	135.2±1.5	776±31

Average values of Young’s modules, UTS, strain at rupture and modules of toughness of PU and all PU nanocomposites are compared in *Figure 5.23(a) to (d)*.

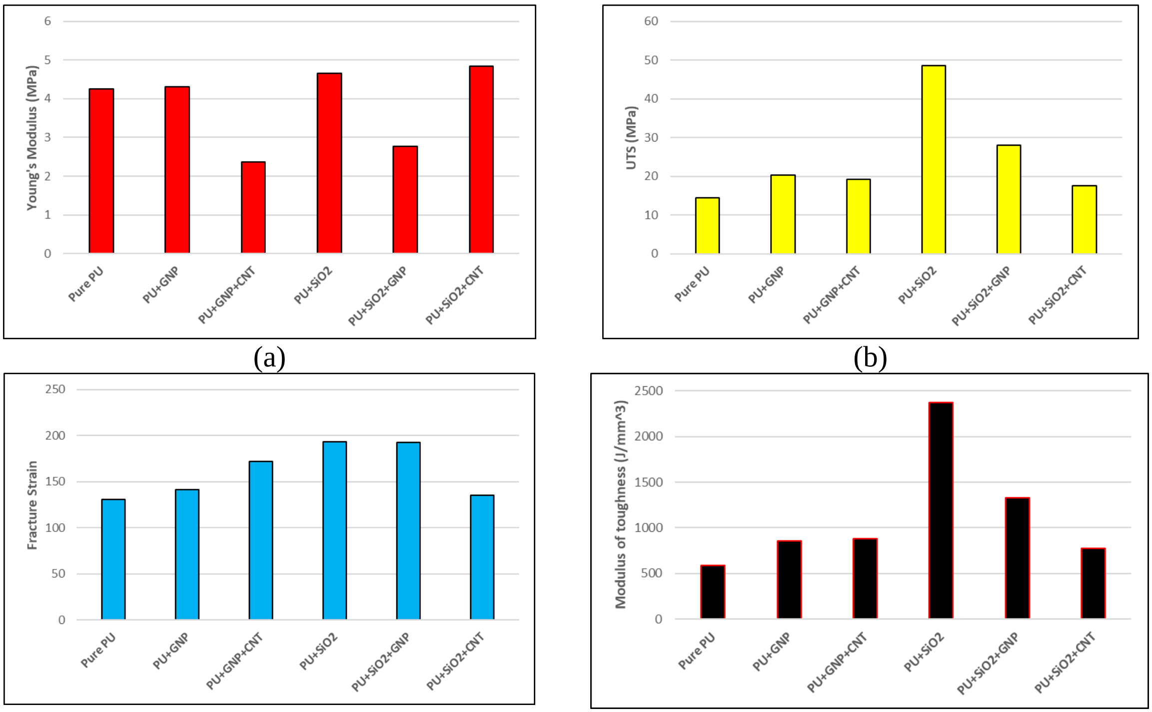

(a) (b)

(c) (d)

Figure 5.23. Average (a) Young's Modulus, (b) UTS, (c) strain at rupture, and (d) toughness of modulus for all tensile specimens.

5.3 Tearing tests

Tearing testing is an essential step to measure a material's resistance to tear. The force required to propagate crack from an initial notch, along with the tear's path, offers insights into the material's structural integrity and durability. For this project, the ASTM D624 standard was adhered to for the tearing test procedures.

The CAD model of the tearing mould was designed based on the ASTM D624 standard as shown in *Figure* 5.24(a). A CNC machine was used, and the mould was machined from an aluminium block in order to cast a set of tearing specimens for each type of coating material (*Figure* 5.24(b)). The overall length of tearing specimens was 102 mm and the width 19 mm and thickness of 2.5 mm.

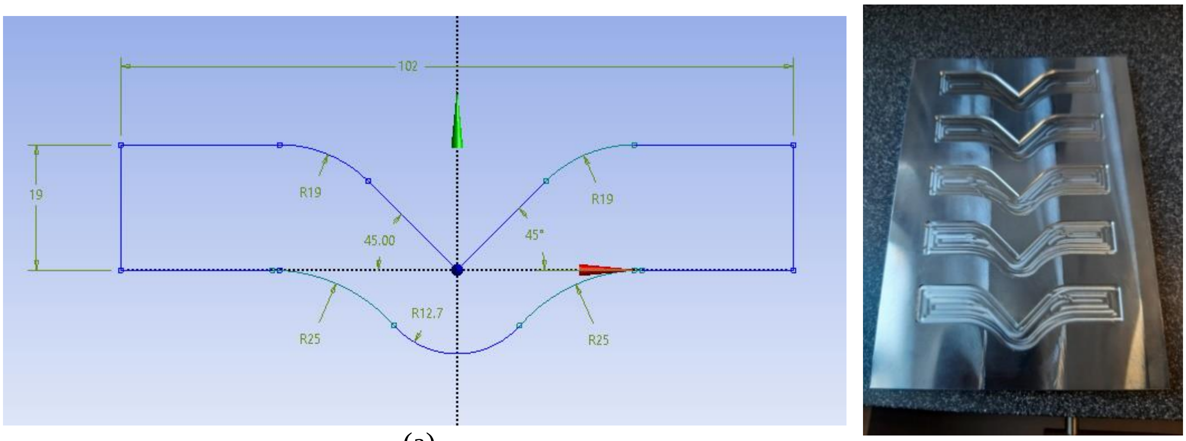

(a) (b)

Figure 5.24. (a) Tearing specimen dimensions, (b) Aluminium tearing mould made from CNC machining.

After preparing the tearing specimens, each one had a sharp notch of approximately 1 mm cut by a razor blade at the tip of the V-notch where the stress concentrates. The tearing tests were carried out using Zwick/Roell universal testing machine with a 5 kN load cell. One side of each specimen was securely clamped to cross-head connected the load cell, while the other side was firmly secured by the bottom grip (*Figure 5.25b*). All tearing tests were conducted at a crosshead speed of 500 mm/min.

(a) (b)

Figure 5.25. (a) Samples of tearing specimens, (b) A tearing specimen gripped in Zwick-Roell Universal Testing Machine.

The following parameters were obtained from tearing tests.

- Tearing strength (T_S), which is the ratio of the maximum applied load during the tearing test (F_{max}) to the specimen's thickness (t), its unit is *N/mm*.

$$T_S = \frac{F_{max}}{t} \tag{5.5}$$

- Tearing energy, which is the total energy required to fracture the specimens. This value was determined by calculating the area under the load-displacement recorded by the testing machine and its unit is *mJ*.
- Percentage of elongation at break (EL%), which is the percentage increase in the length before the specimen ruptures. The EL% is calculated based on the maximum recorded displacement at break.

In addition, hardness, the material's resistance to indentation, is determined using a Shore D Durometer.

5.3.1 **Tearing test results of pure PU**

Five specimens of pure PU underwent the tearing test each at a crosshead speed of 500 mm/min and kept stretching by the tearing load until rupture. The measured load-displacement results for pure PU specimens are illustrated in *Figure 5.26*.

All the pure PU tearing specimens demonstrated relatively similar behaviour during the tearing tests. The tearing force gradually increased up to an elongation between 13 mm to 17 mm, at which point crack propagation started from the sharp notch, causing the force to start decreasing until the specimen ruptured. The crack propagation paths were not exactly identical in all specimens. The discrepancy can be attributed to small variation in thickness, and variation in distribution of internal defect such as micro air bubbles.

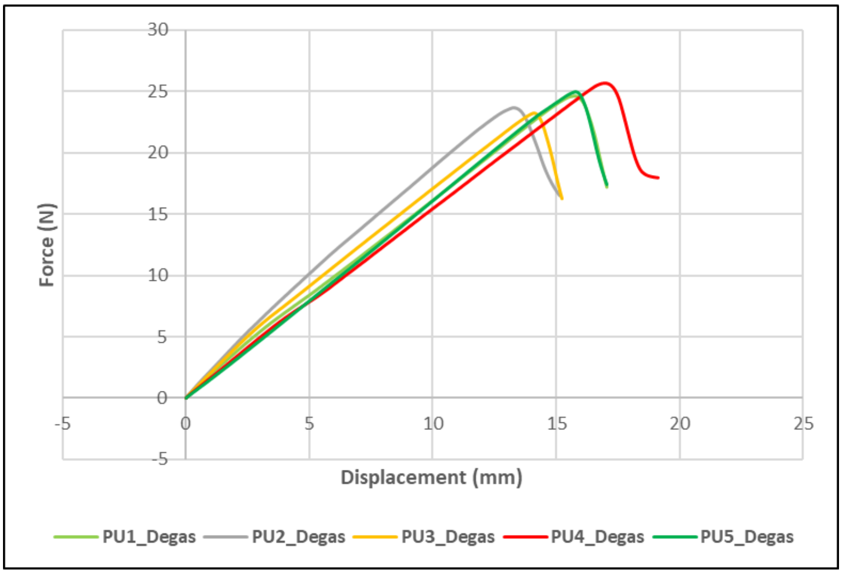

Figure 5.26. Load-displacement of pure PU specimens in tearing tests.

The key parameters of tearing tests for each specimen were obtained and summarised in *Table 5.8*. The average measured tearing strength is 10.3 N/mm, elongation at break is 33.4%, and tearing energy, the area under load-displacement curve, is 226 mJ. A higher value of tearing energy corresponds to more resistance to tearing, indicating that the material is more tolerant to rupture.

The hardness of PU specimens is measured by a Shore D durometer, and the results are also summarised in *Table 5.8*. According to Shore D scale, the average Shore D hardness of PU is 20.2 which falls within the range of semi-rigid (medium-hard), thus showing minimal flexibility.

Table 5.8. Key parameters from tearing tests for pure PU.

Material	Tearing strength (N/mm)	EL%	Tearing energy (mJ)	Shore D hardness
PU-1	10.6	34.1	231	20.5
PU-2	9.9	30.3	208	18.5
PU-3	10.1	30.5	196	21.5
PU-4	10.6	38.2	269	22.0
PU-5	10.3	34.1	228	18.5
Average	10.3±0.3	33.4±3.2	226±28	20.2±1.6

Scanning electron microscopy was carried out on the fracture surface of *PU* specimen. The results of SEM analysis, shown in *Figure 5.27*, at two different magnifications, reveal that the pure PU fracture surface is very rough, with a significant presence of microcracks and crack branching, which contributed to the tearing energy.

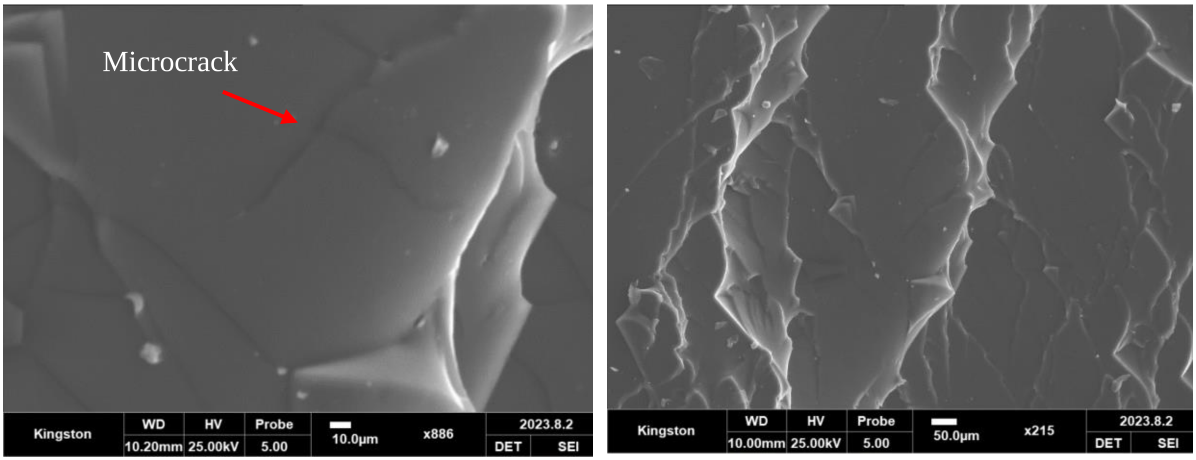

(a) (b)

Figure 5.27. SEM images for pure PU-5 at two different magnifications.

5.3.2 Tearing test results of PU+GNP

Five specimens of PU+GNP with a GNP loading of 0.3 wt.% underwent the tearing test, each tested at a crosshead speed of 500 mm/min and continuously stretched until failure. The load-displacement results for all PU+GNP specimens are illustrated in *Figure 5.28.*

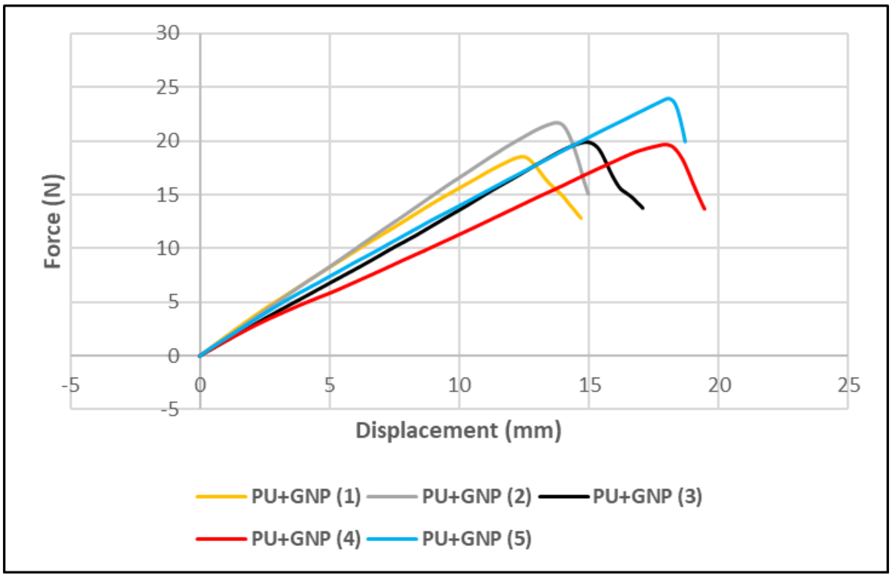

Figure 5.28. Load-displacement of PU+GNP specimens in tearing tests.

Figure 5.28 shows that all the PU+GNP tearing specimens demonstrated relatively similar behaviour during the tearing tests. At the early stage of loading, the load-displacement relationship of PU is linear because the material initially responds elastically. As the load increases further, microcracks begin to form within the PU, gradually growing and propagating, which results in a nonlinear response. The force reached to its maximum at elongations between 12 mm to 18 mm, at which point crack propagation started from the sharp notch, causing the force decreasing until the specimen failed. The crack propagation paths were not exactly identical in all specimens. This discrepancy can be attributed to variation in thickness, and the distribution of size and location of internal defect such as micro air bubbles inside the material.

Table 5.9 summarises the results of tearing strength, elongation (EL%), tearing energy, and shore D hardness of PU+GNP at 0.3 wt.% GNP loading. Tearing strength, tearing energy and hardness had decreased by 14.6%, 13.3% and 13.9%, respectively, while the EL% had increased by 1.5% compared to pure PU specimens.

Table 5.9. Key parameters for PU+GNP tearing tests.

	Tearing strength (N/mm)	EL%	Tearing energy (mJ)	Shore D Hardness
PU+GNP-1	7.9	29.4	159.4	16.0
PU+GNP-2	9.0	29.9	179.8	17.5
PU+GNP-3	8.3	34.1	187.7	18.0
PU+GNP-4	8.6	38.9	210.8	18.5
PU+GNP-5	10.2	37.5	241.8	17.0
Average	8.8±0.9	33.9±4.3	195.9±31.6	17.4±0.9

SEM images were taken at two different magnifications from *PU+GNP* fracture surface and they are shown in *Figure 5.29*. Microcracking, crack branching, voids and fragments of nanocomposite were observed on the fracture surface. The fracture surface was also observed to be rough and contains ridges on the surface.

The EDX images taken for PU+GNP specimen are shown in *Figure 5.30* showing a uniform distribution of carbon and oxygen across the entire specimen.

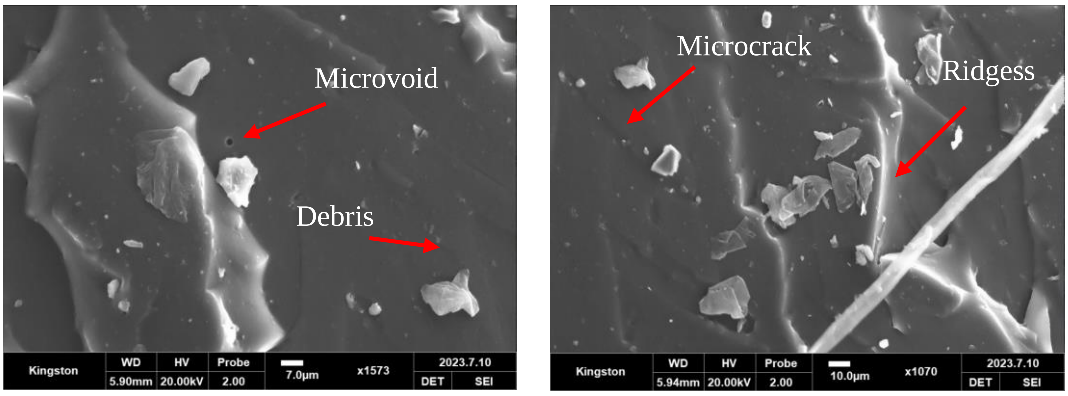

(a) (b)

Figure 5.29. SEM images for PU+GNP-5 at two different magnifications.

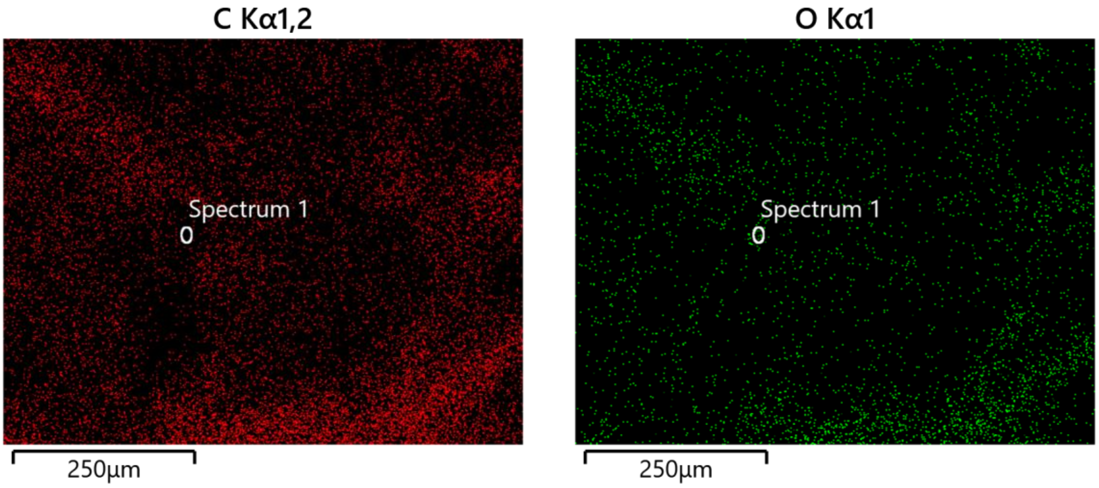

Figure 5.30. EDX images showing the composition of PU+GNP-5

5.3.3 Tearing test results of PU+GNP+CNT

Five specimens of PU+GNP+CNT with 0.15 wt.% of GNP and 0.15 wt.% of CNT underwent the tearing test at a crosshead speed of 500 mm/min until the rupture. The load-displacement results for all PU+GNP+CNT specimens are illustrated in *Figure 5.31*.

Figure 5.31 shows that initially the PU+GNP+CNT tearing specimens demonstrated linear behaviour and then began to increase nonlinearly due to the growth and propagation of defects. The tearing load reached its maximum value for elongations between 11 mm and 13 mm, at which point crack propagation initiated from the sharp notch, leading to a continuous reduction in load until the specimen ruptured. The crack propagation paths were not exactly identical in all specimens. This discrepancy can be attributed to variation in thickness, and the distribution and size of internal defects such as air bubbles. Specimen *PU+GNP+CNT-1* was chosen as the average representative for this nanocomposite for comparative analysis.

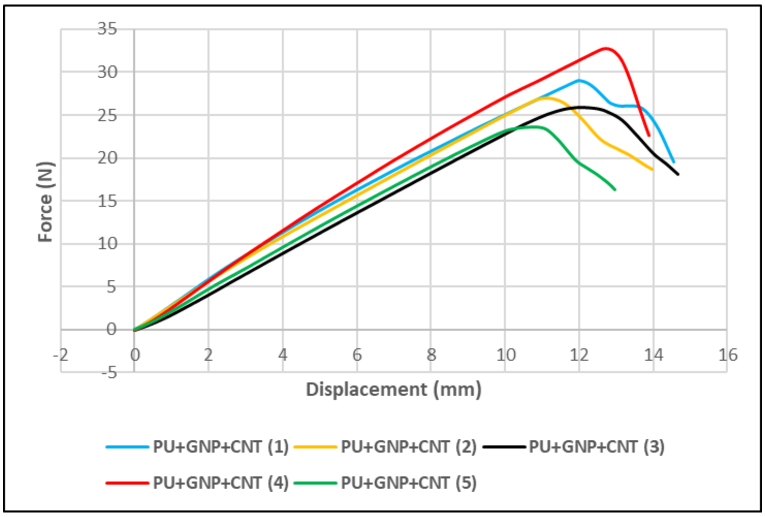

Figure 5.31. Load-displacement of PU+GNP+CNT specimens in tearing tests.

Table 5.10 summarises the results of tearing strength, elongation, tearing energy and hardness of PU+GNP+CNT at 0.3 wt.% loading. Tearing strength and tearing energy had both increased by 9.7% and 0.5%, respectively. The elongation and hardness had both decreased by 16.1% and 12.4%, respectively, relative to pure PU specimens.

An SEM and EDX analysis were carried out on a *PU+GNP+CNT* specimen to study its chemical elemental composition on its surface and to detect any occurring cracks or debris within the surface.

The SEM images shown in *Figure* 5.32, taken at two different magnifications, indicate that PU+GNP+CNT exhibits a significant presence of microcracks, with only minor debris observed. The presence of microcracks on the fracture surface contributes to the roughness of PU+GNP+CNT and increases its tearing energy.

Table 5.10. Key parameters for PU+GNP+CNT tearing tests.

Material	Tearing strength (N/mm)	Elongation percentage (%)	Tearing energy (mJ)	Shore D Hardness
PU+GNP+CNT-1	12.3	29.1	254.0	19.5
PU+GNP+CNT-2	10.7	27.9	224.3	16.0
PU+GNP+CNT-3	10.4	29.3	223.0	16.5
PU+GNP+CNT-4	13.2	27.8	255.6	19.0
PU+GNP+CNT-5	9.9	26.0	180.5	17.5
Average	11.3±1.4	28.02±1.3	227.5±30.5	17.7±1.5

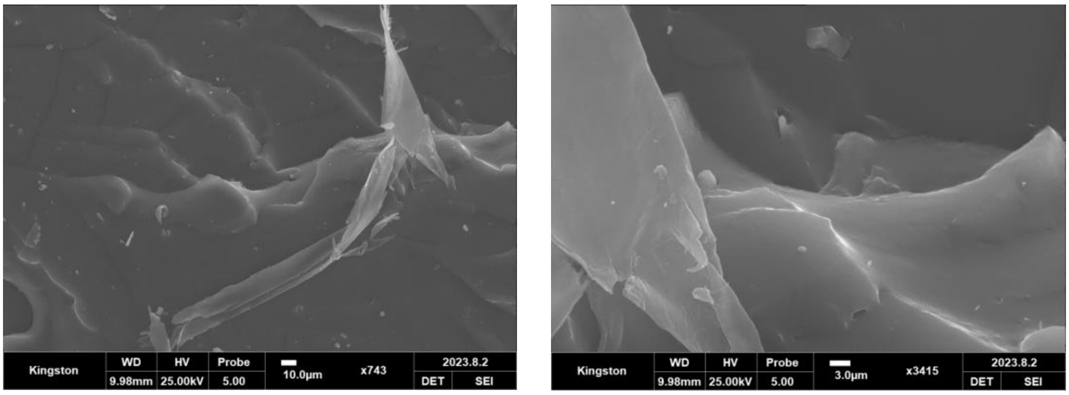

(a) (b)

Figure 5.32. SEM images for PU+GNP+CNT-1 at two different magnifications.

The EDX images of PU+GNP+CNT fracture surface, shown in *Figure 5.33,* exhibits the distribution of C and O across the entire specimen. These images confirmed the presence of both carbon and oxygen elements within the PU's chemical structure which agrees with the stoichiometric composition of PU+GNP+CNT.

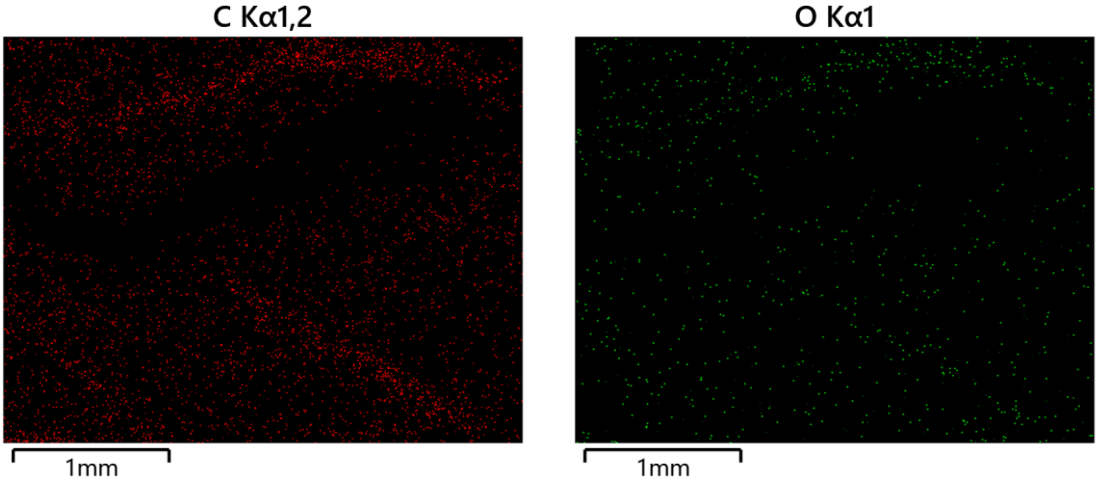

Figure 5.33. EDX images showing the composition of PU+GNP+CNT-1

5.3.4 Tearing test results of PU+SiO_2

Five specimens of PU+SiO_2 with 0.3 wt.% SiO_2 loading underwent the tearing tests, at a crosshead speed of 500 mm/min until specimens ruptured. The load-displacement results for these specimens are illustrated in *Figure 5.34*. The tearing force was gradually increased for elongation between 13 mm to 17 mm, at which point crack propagation started from the sharp notch, causing the force to start drop gradually until the specimen ruptured.

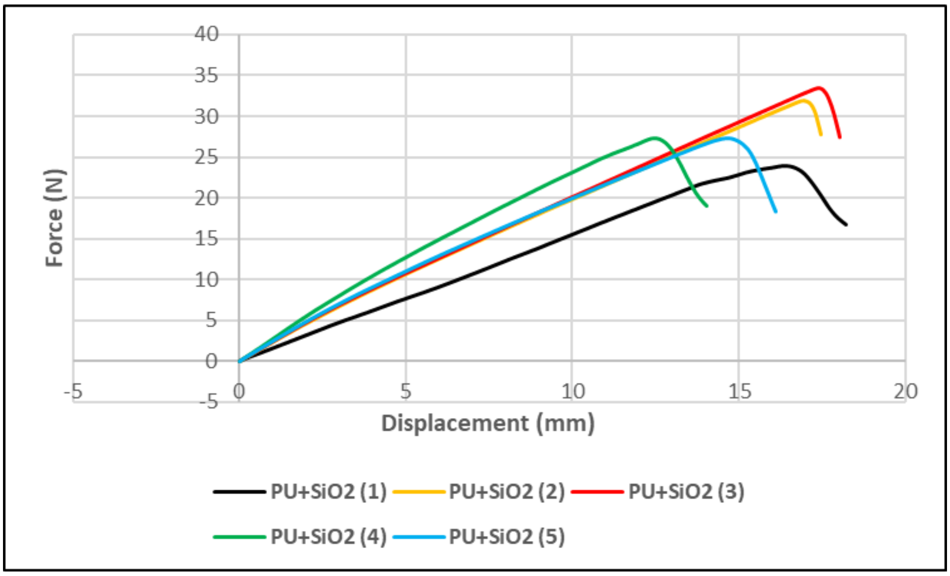

Figure 5.34. Load-displacement of PU+SiO_2 specimens in tearing tests.

The crack propagation paths were not exactly identical in all specimens. This discrepancy can be attributed to variation in thickness, and distribution and sizes of internal defect such as air bubbles.

Table 5.11 summarises the results of tearing strength, elongation, tearing energy and Shore D hardness of PU+SiO_2 at 0.3 wt.% loading. Compared to pure PU, tearing strength, and tearing energy increased by 15.5% and 19.4% respectively, while elongation at break remained unchanged. In contrast, hardness decreased by 18.3% .

Table 5.11. Key parameters for PU+SiO_2 tearing tests.

Material	Tearing strength (N/mm)	EL%	Tearing energy (mJ)	Shore D Hardness
PU+SiO_2-1	9.7	36.5	246.0	15.5
PU+SiO_2-2	13.3	35.0	301.4	19
PU+SiO_2-3	13.7	36.1	325.7	17
PU+SiO_2-4	11.7	28.1	223.5	16
PU+SiO_2-5	11.6	32.3	253.9	15
Average	11.9±1.6	33.6±3	270.1±42.1	16.5±1.6

The SEM images taken at two different magnifications for the PU+SiO_2 specimen is shown in *Figure 5.35* shows presence of significant microcracking, void elongation and fragments of nanocomposite on the fracture surface, making it rough, resulting in higher energy absorption.

The EDX images shown in *Figure 5.36* demonstrated the distribution of carbon, oxygen, and silica in the specimen.

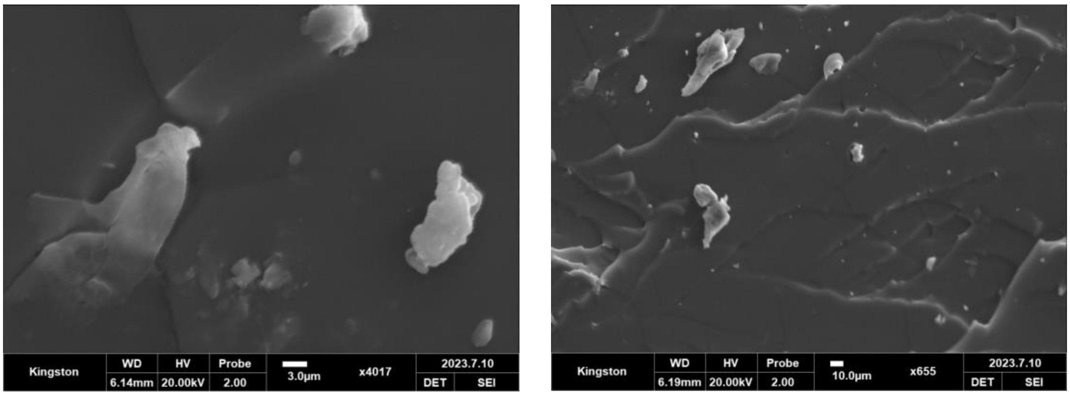

(a) (b)

Figure 5.35. SEM images for PU+SiO2-3 at two different magnifications.

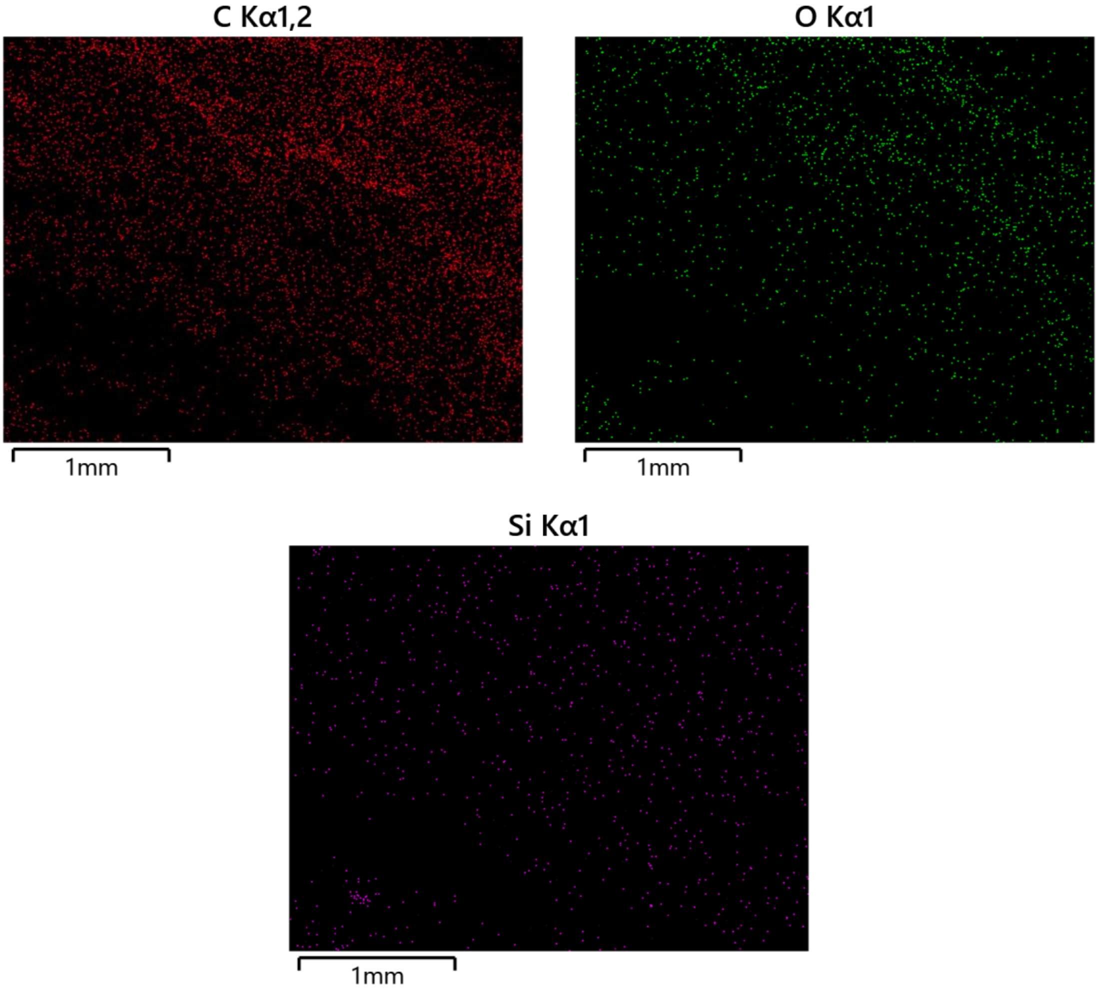

Figure 5.36. EDX images showing the surface composition of PU+SiO_2-3

5.3.5 Tearing test results of PU+SiO_2+GNP

Five specimens of PU+SiO_2+GNP with 0.15 wt.% fumed silica and 0.15 wt.% GNP underwent the tearing test at a crosshead speed of 500 mm/min until rupturing. The load-displacement test results for these specimens are illustrated in *Figure 5.37*. The results show that for all the specimens the tearing force increased gradually up to an elongation between 13 mm to 16 mm, when crack propagation started from the sharp notch, causing the force to decrease gradually until the specimen ruptured.

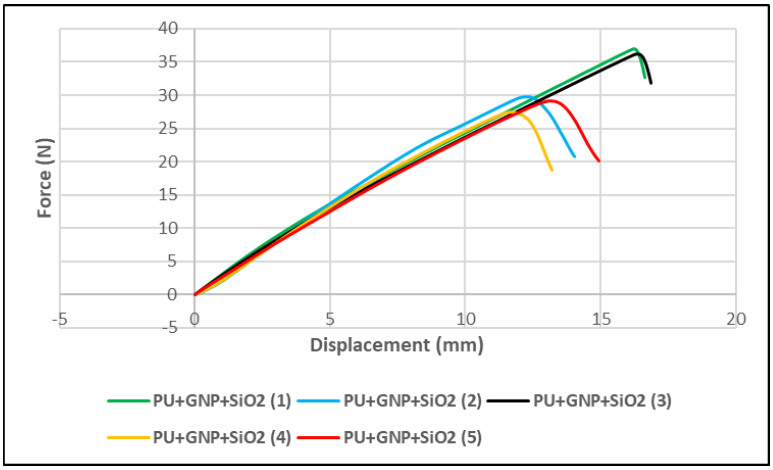

Figure 5.37. Load-displacement of PU+SiO_2+GNP specimens in tearing tests.

Table 5.12 summarises the results of tearing strength, elongation, tearing energy and hardness of PU+SiO_2+GNP at 0.3 wt.% loading. Compared to pure PU specimens, both the tearing strength and tearing energy increased by 28.2% and 21.8%, respectively, while both the elongation and hardness decreased by 9.3% and 19.8%, respectively.

The SEM images taken for PU+SiO_2+GNP fracture surface are shown in *Figure 5.38* demonstrate the presence of microcracking creating very rough surfaces with fragments of nanocomposite scattered across the whole fracture surface resulting in higher energy absorption.

Table 5.12. Key parameters for PU+SiO_2+GNP tearing tests.

Material	Tearing strength (N/mm)	EL%	Tearing energy (mJ)	Shore D Hardness
PU+SiO_2+GNP-1	15.1	33.3	337.3	18.0
PU+SiO_2+GNP-2	12.3	28.1	242.9	15.0
PU+SiO_2+GNP-3	14.9	33.8	335.8	16.5
PU+SiO_2+GNP-4	11.6	26.4	208.9	14.5
PU+SiO_2+GNP-5	12.4	29.9	253.7	17.0
Average	13.2±1.6	30.3±3.2	275.7±57.9	16.2±1.4

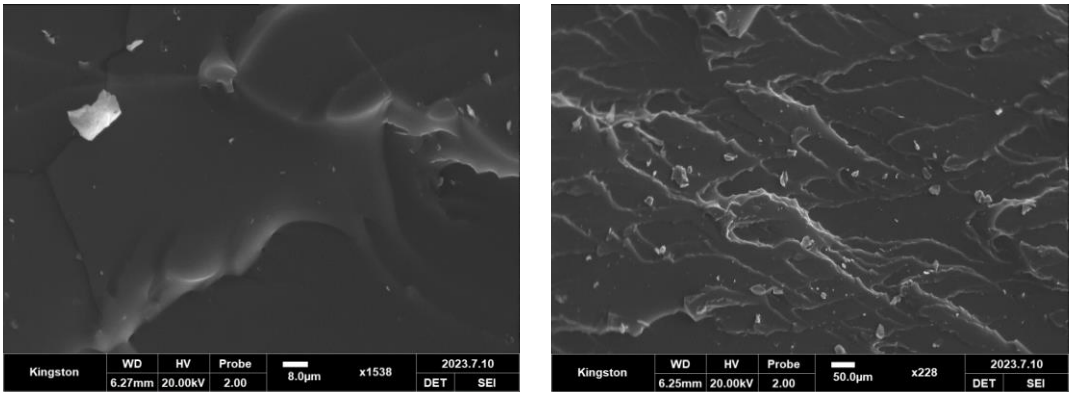

(a) (b)

Figure 5.38. SEM images for PU+SiO_2+GNP-1 at (a)8µm and (b)50µm

5.3.6 Tearing test results of PU+SiO2+CNT

Five specimens of PU+SiO_2+CNT with 0.15 wt.% of SiO_2 and 0.15 wt.% of CNT underwent the tearing test at a crosshead speed of 500 mm/min until specimen ruptured. The load-displacement results for PU+SiO_2+CNT specimens are illustrated in *Figure 5.39*. The results show that the tearing force initially increased linearly and then began to increase nonlinearly. The load has reached to its peak at an elongation between 17 mm to 21 mm, at which point crack propagation started from the sharp notch, causing the force to drop until the specimens ruptured.

Table 5.13 summarises the results of tearing strength, elongation, tearing energy and Shore D hardness of PU+SiO_2+CNT at 0.3 wt.% loading. Compared to pure PU specimens, tearing strength, elongation and tearing energy increased by 67%, 13.2% and 86.7%, respectively, while the hardness decreased by 16.8%.

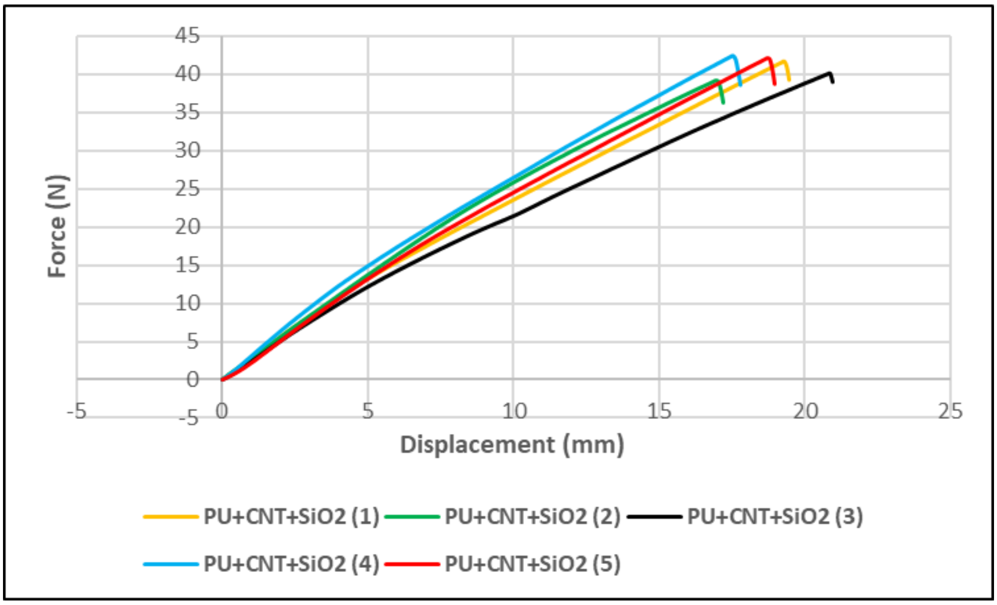

Figure 5.39. Load-displacement of PU+SiO_2+CNT specimens.

Table 5.13. Key parameters for all PU+SiO_2+CNT tearing tests.

Materials	Tearing strength (N/mm)	EL%	Tearing energy (mJ)	Shore D Hardness
PU+SiO_2+CNT-1	17.3	38.9	436.8	15.5
PU+SiO_2+CNT-2	16.5	34.4	372.9	17
PU+SiO_2+CNT-3	17.1	41.9	457.3	18
PU+SiO_2+CNT-4	17.5	35.6	415.2	17
PU+SiO_2+CNT-5	17.4	38.0	429.9	19
Average	17.2±0.4	37.8±2.9	422.4±31.6	17.3±1.3

An SEM image of the fractured surface of PU+SiO_2+CNT is shown in *Figure 5.40*. Microcracks, voids and crack branching are visible throughout the fracture surface. The presence of the microcracks, microvoids and crack branching on the fracture surface contributed to an increase in energy absorption in tearing. The EDX images taken for PU+SiO_2+CNT specimen are shown in *Figure 5.41*. The distribution of carbon, oxygen and fumed silica can be seen across the entire specimen.

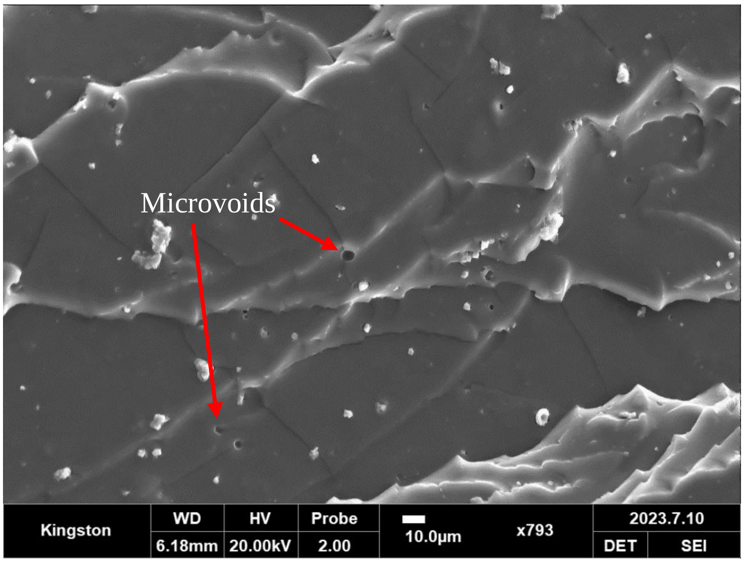

Figure 5.40. SEM images of fracture surface for PU+SiO_2+CNT.

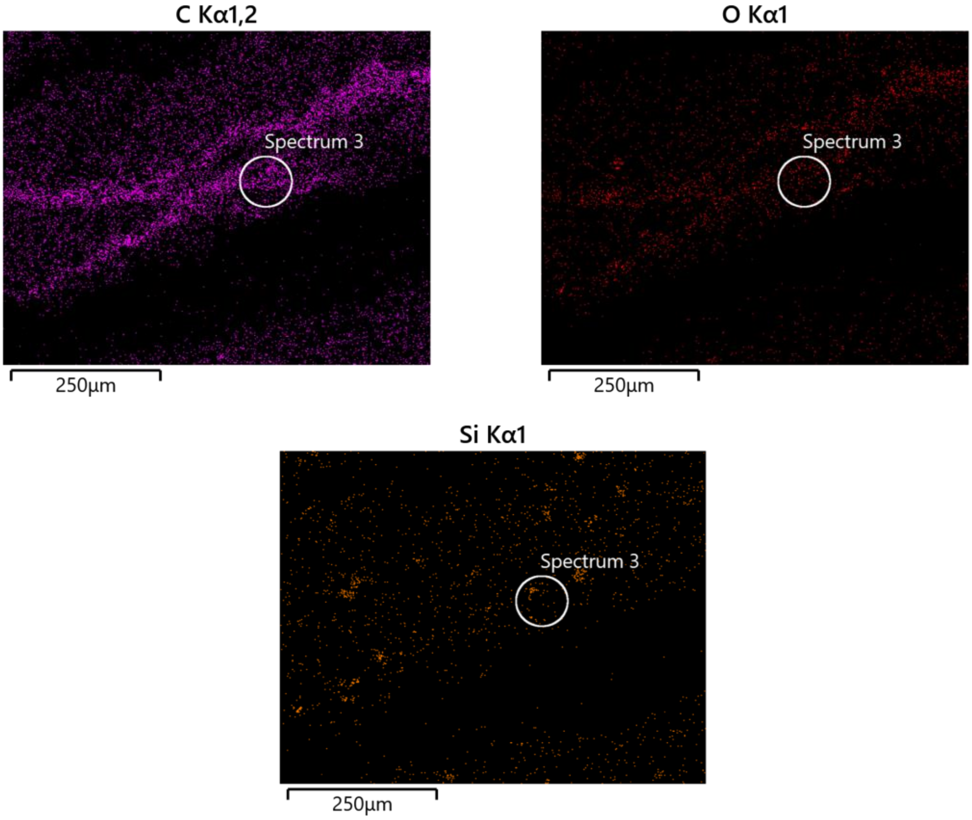

Figure 5.41. EDX images showing the surface composition of PU+SiO2+CNT.

Representative tear test results for PU and all PU-modified nanocomposites are plotted in *Figure 5.42*. The results indicate that PU+SiO_2+CNT absorbed the highest energy during tearing compared to the other specimens, requiring a tearing force exceeding 40 N to cause failure, along with significantly higher elongation. This suggests enhanced resistance to tearing even in the presence of a notch. In contrast, neat PU and PU+GNP+CNT specimens showed relatively poorer tearing performance. The inferior tearing performance of PU+GNP+CNT is likely due to GNP and/or CNT agglomeration and trapped air bubbles within the mixture.

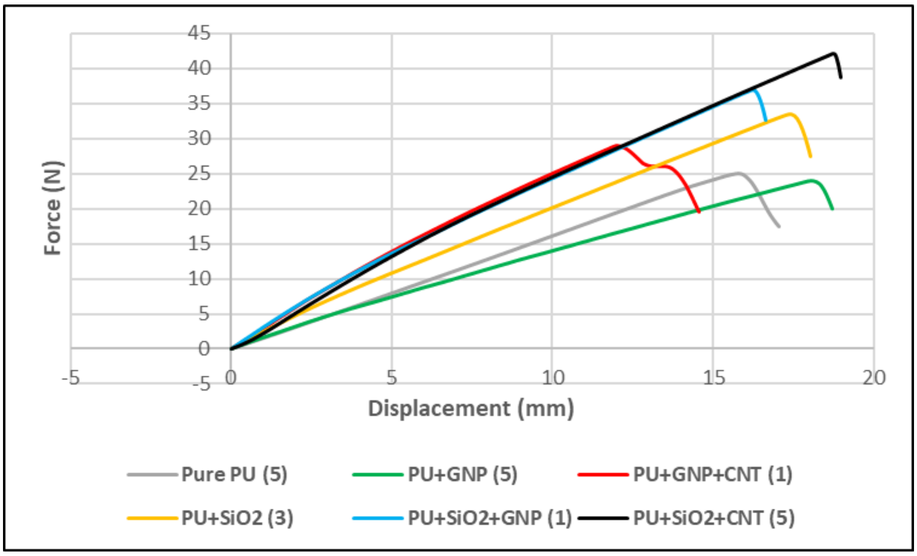

Figure 5.42. Load-displacement of tearing specimens for all nanocomposites.

5.4 Abrasive wear tests

Although the corrosion and wear of structures such as wind turbine blade exposed to harsh erosive-corrosive environments such as sandstorm cannot be thoroughly eliminated, protective coatings can be employed to improve the lifetime of these structures and prevent early and unpredicted failures.

Polyurethane (PU) elastomers have shown excellent resistance to corrosion, erosive and abrasive wear that make them suitable for a variety of applications [107, 108].

Figure 5.43 shows a schematic of the material removal from a ductile surface caused by cutting and plastic deformation in abrasive wear. One of the major types of abrasion is micro-cutting. Alongside with micro-cutting, the erodent materials may also plough the surface by a combined action of cutting and plastic deformation. The two wear modes of micro-cutting and ploughing are categorized as cutting mechanisms. The cracks formed from material defects will propagate by repeated loading-unloading, leading to reduced strength of surface and loss of material.

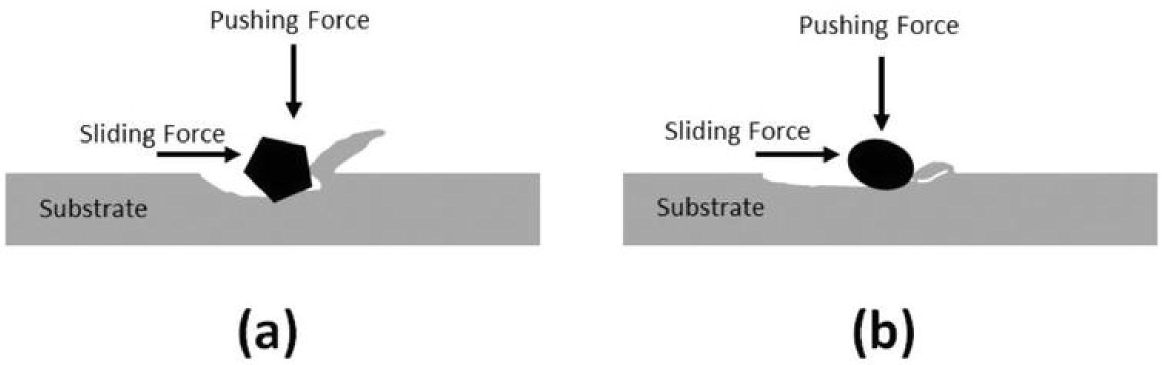

Figure 5.43. Abrasive wear of ductile substrates: (a) cutting mechanism and (b) plastic deformation together with fatigue mechanism [109].

Hill, et al. [110] conducted wear performance of PU according to the ASTM Standard G65 [111] and they reported that the wear rate profile can be separated into three regions A, B and C as shown in *Figure* 5.44. In region A, the wear rate decreases with increasing hardness (60A–75A); in region B, the wear rate is approximately independent of hardness (75A–95A); and in region C, the wear rate increases with increasing hardness (95A–65D). PU has the highest Shore D hardness of 20.2±1.6 and PU+SiO_2+GNP has the lowest Shore D hardness of 16.2±1.4. PU+SiO_2+CNT Shore D harness is 17.3±1.3. The expectation is pure PU has the highest abrasion rate.

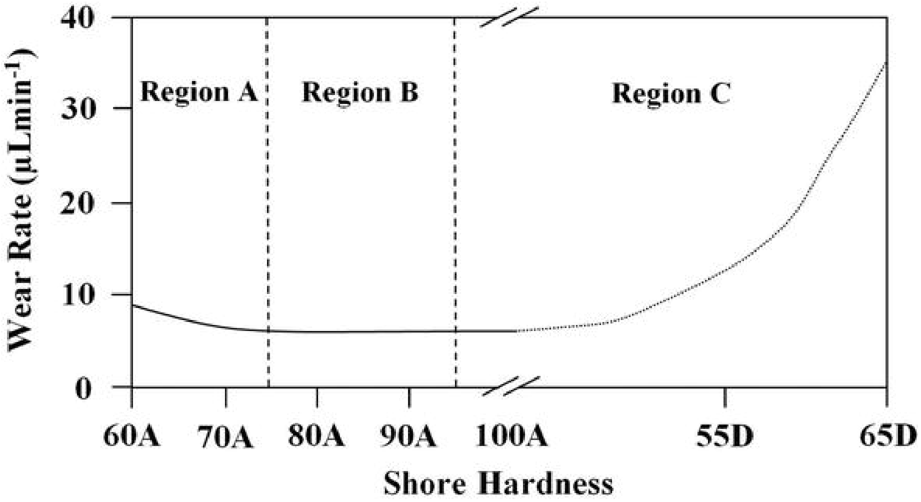

Figure 5.44. Approximate relationship between wear rate and hardness for polyurethane [110].

Standard wear testing procedures are commonly used to determine a material's resistance to abrasive and erosive wear. In most wear testing methods, the mass or volume loss over a specific time period is measured as an indicator of the material's wear resistance. The volume loss is typically determined by measuring the mass loss and then calculating the volume loss using $V = m/\rho$, where ρ is the density of the tested material.

In this project, the abrasion test method consisted of placing a cylindrical specimen in continuous contact with an abrasive surface mounted on a revolving wheel, subjected to a specified weight and speed.

Using a CNC machine, a mould for abrasion specimens was machined from an aluminium block, as shown in *Figure 5.45*. This mould was used to manufacture a series of cylindrical abrasion specimens, each with a diameter of 16 mm and a thickness of 6 mm, from the PU and five PU nanocomposites being investigated in this project (see *Figure 5.4c*).

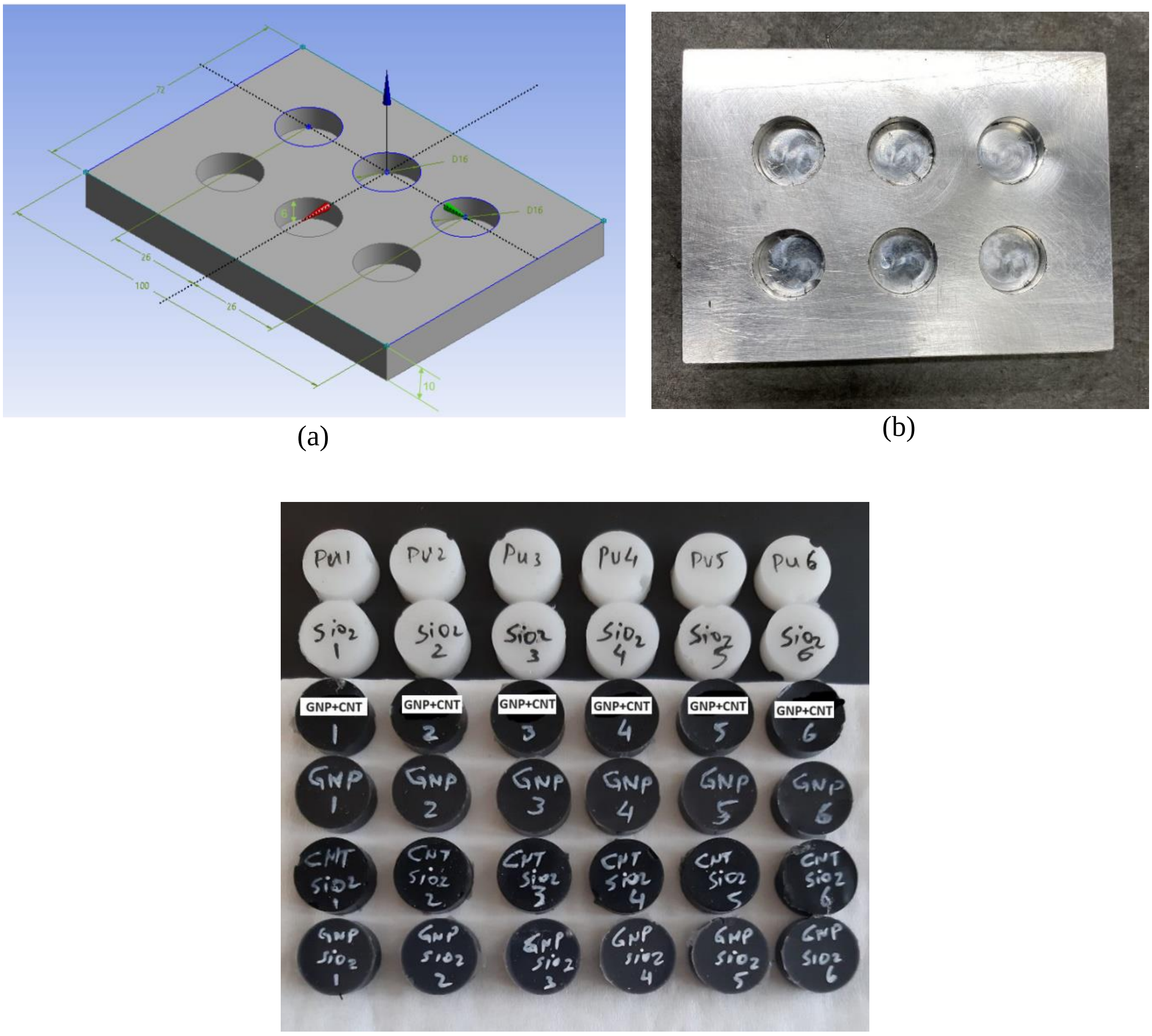

(a) (b)

(c)

Figure 5.45. (a) An abrasion mould modelled in ANSYS with dimensions assigned, (b) an aluminium abrasion mould made from CNC machining and (c) labelled abrasion specimens.

The abrasion tests was adhered to the standard ISO 4649:2010 in which the abrasion process occurred over one of the end surfaces of a cylindrical test piece. The test piece was pressed against a rotating cylindrical drum with an abrasive sheet attached to its surface (see *Figure 5.46*). The volume loss of each specimen was determined by obtaining the density of each material and measuring the mass loss of the specimen as a result of being subjected to wear, the calculated volume loss was validated and compared with the volume loss of a reference test piece under similar conditions. [112]

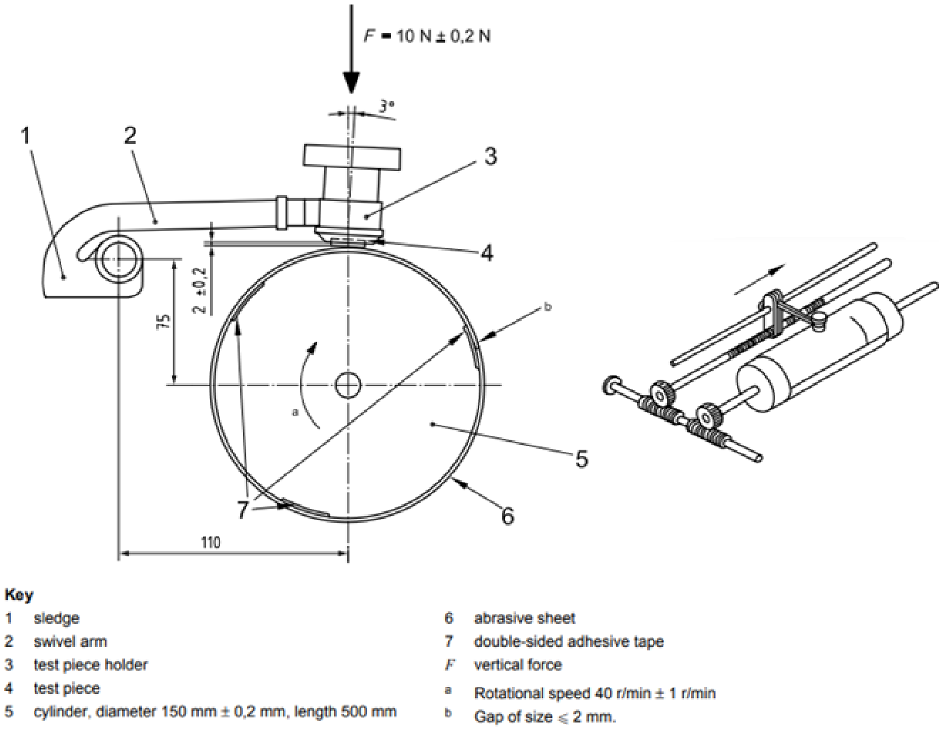

Figure 5.46. Illustration of rotary drum abrasion test apparatus.

The relative volume loss (ΔV_{rel}) of a specimen is calculated using the equation (5.6) [112].

$$\Delta V_{rel} = \frac{\Delta m_t \times \Delta m_{const}}{\rho_t \times \Delta m_r} \tag{5.6}$$

Where the variable Δm_t represents the mass loss of the tested specimen and has a unit of mg, Δm_{const} represents the defined mass loss value of a reference test specimen and has a unit of mg, ρ_t is the density of the tested specimen and has a unit of mg/mm^3, and the variable Δm_r is the mass loss of the reference test specimen which has a unit of mg. Note that reference compounds are necessary because these abrasion tests are comparative tests. The quality of the reference compounds significantly influences the repeatability and reproducibility of the tests.

After manufacturing the abrasion specimens, each was placed in an abrasion test machine and pressed against a rotating drum with a vertical force of 10 ± 0.2 N to assess their wear resistance. The drum rotated at a speed of 40 rpm. Six specimens were tested for each material. The results, which show the average abrasion of all six specimens for each material, along with their corresponding density are presented in *Figure 5.47* and *Figure 5.48*.

.

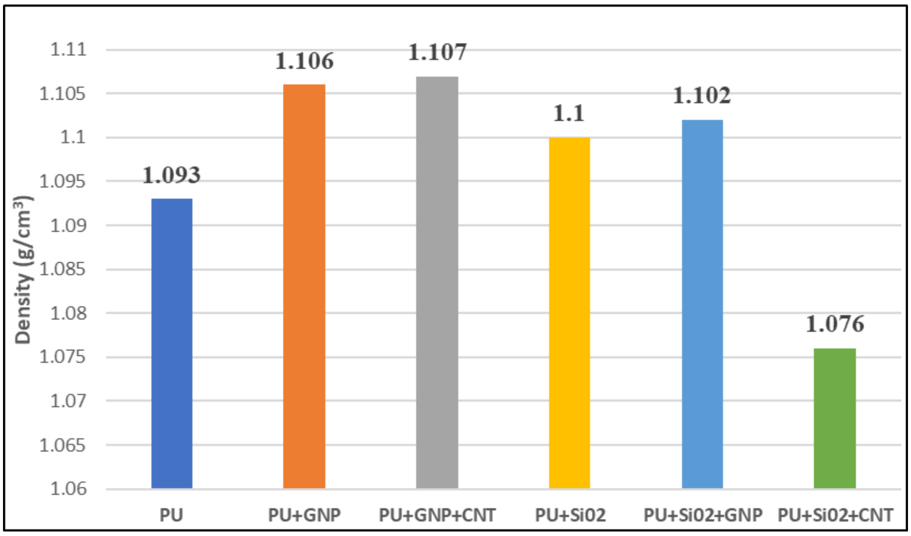

Figure 5.47. Density for each nanomaterial of the abrasion specimens

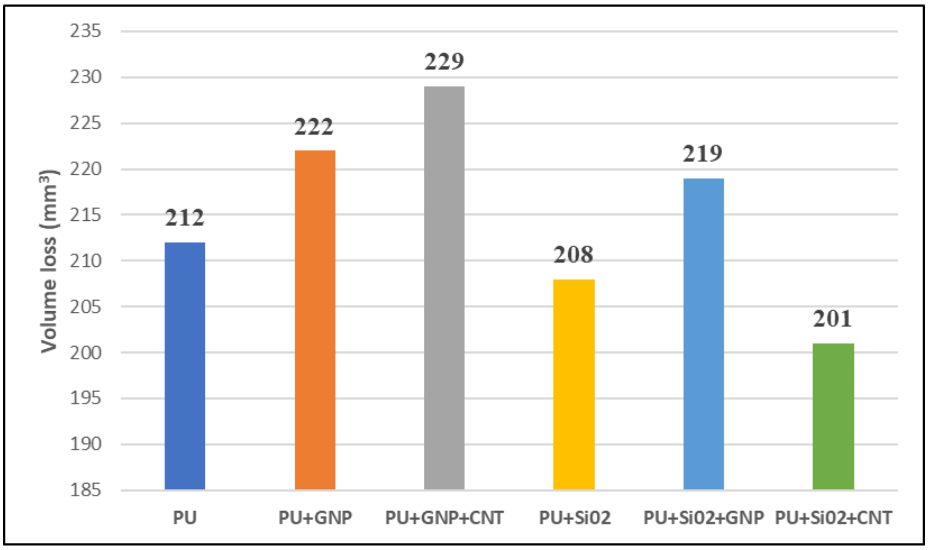

Figure 5.48. Averaged volume loss for each nanomaterial of all the abrasion specimens

Figure 5.48 shows that the PU+SiO_2+CNT material exhibited the least wear, with a 6.9% reduction in mass loss and a 5.2% reduction in volume loss compared to the other materials. This indicates that this PU nanocomposite has a greater ability to resist material loss due to repetitive friction or abrasion. Its high wear resistance makes PU+SiO_2+CNT more effective in applications subject to abrasive wear, such as sandstorms and airborne particles impacting wind turbine blades installed in deserts or near polluted industrial areas.

5.4.1 Effect of SiO_2 loading on abrasion of PU+CNT+SiO_2

After determining that PU+SiO_2+CNT had the highest wear resistance, a series of additional abrasion tests were carried out to study the effects of SiO_2 on wear resistance and mass loss. Three batch of PU+ SiO_2+CNT were manufactured with increasing the weight percentage of SiO_2 from 0.3, to 0.5 and 0.7wt.% while keeping CNT loading constant at 0.15 wt.%. The test conditions assigned were 22°C, 10N for the test force, 40m for the abrasion distance and the test piece cylinder diameter was as before at 16.2 mm. Six specimen were tested for each CNT loading. The mass losses due to wear for these three batches are reported in *Table 5.14*. The results of mass loss as a function of SiO_2 loading are shown in *Figure* 5.49. It is evident that increasing the SiO_2 loading from 0.3 wt.% to 0.7 wt.% within the PU+ SiO_2+CNT coating reduces abrasion mass loss by 7.6%. This suggests that optimising the SiO_2 loading is crucial for enhancing the wear resistance of the PU+ SiO_2+CNT coating material.

Table 5.14. Mass loss for all PU+SiO_2+CNT abrasion batch

CNT wt.%	SiO_2 wt.%	Mass loss (mg)
0.15	0.3	287.1
0.15	0.5	267.7
0.15	0.7	265.3

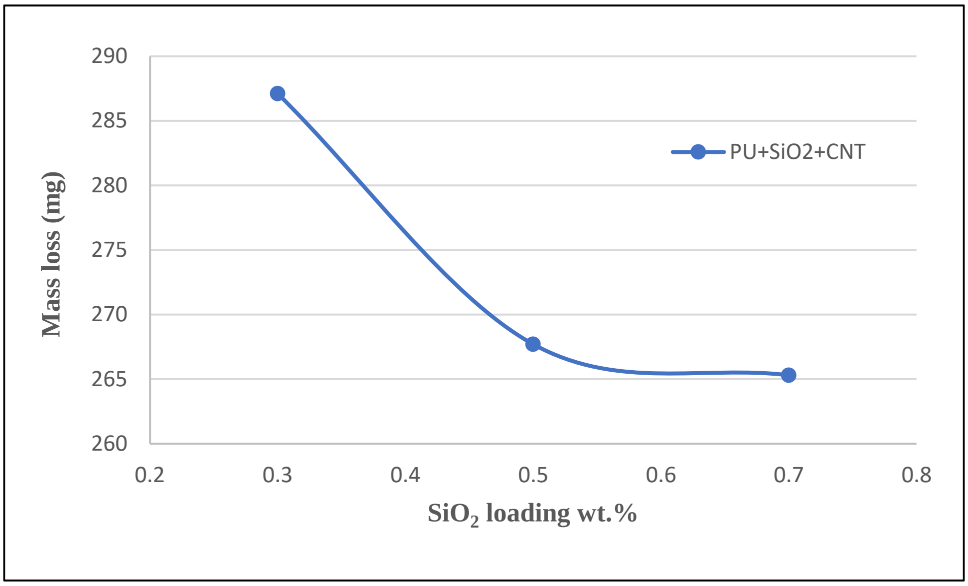

Figure 5.49. Effect of nanosilica loading on abrasion resistance of PU+SiO_2+CNT nanocomposite.

5.5 Conclusion

In this chapter, the results of tensile, tearing, and abrasion tests on various polyurethane nanocomposites in dry conditions are reported. The tensile and tearing tests were conducted at speeds of 30 mm/min and 500 mm/min, respectively. The mechanical properties of both pure PU and modified PU were obtained from the tensile tests. The results indicate that UTS, strain at rupture, and modulus of toughness for all nanomodified PUs have improved compared to pure PU. However, this is not the case for Young's modulus. PU+SiO_2 showed the highest UTS and modulus of toughness compared to the other specimens, along with the highest strain at rupture, second only to PU+SiO_2+GNP. The Young's modulus increased slightly with the addition of fumed nanosilica particles. Except for Young's modulus, the mechanical properties of the PU+SiO_2+GNP nanocomposite have improved considerably, while all mechanical properties of the PU+SiO_2+CNT nanocomposite, including Young’s modulus, have improved to varying degrees.

The tearing test results indicated that PU+SiO_2+CNT absorbed the highest energy during tearing compared to the other specimens, achieving a maximum tearing force exceeding 40 N to cause failure, along with significantly higher elongation, suggesting enhanced resistance to tearing even in the presence of a notch. In contrast, neat PU and PU+GNP+CNT specimens showed relatively poorer tearing performance. The inferior tearing performance of PU+GNP+CNT is likely due to GNP and/or CNT agglomeration and trapped air bubbles within the mixture.

Wear resistance tests were conducted for pure PU and the modified PU nanocomposites. The results indicated that PU+SiO_2+CNT has the highest wear resistance, demonstrating its ability to resist material loss from repeated exposure to friction. In addition, the SiO_2 loading was varied in the PU+SiO_2+CNT nanocomposite while keeping the CNT weight percentage unchanged at 0.15%. Increasing the SiO_2 loading from 0.3 wt.% to 0.7 wt.% in the PU+SiO_2+CNT formulation resulted in a 7.6% reduction in abrasion mass loss. This underscores the importance of optimizing SiO_2 loading to enhance the wear resistance of the PU+SiO_2+CNT coating material.

While the literature identifies fatigue as a potential mode of failure for coatings on wind turbine blades, conducting fatigue testing was ultimately not feasible within the timeframe of this study. These tests typically require subjecting samples to thousands or even millions of load cycles, which would have extended the testing timeline beyond the available project resources. Therefore, fatigue testing is recommended for future work to continue this project.

Chapter 6: Water absorption testing

6.1. Introduction

Polyurethane coatings are exposed to water in various applications, such as wind turbine blades and the leading edges of airplanes wings. Water diffusion in polyurethane coatings also plays an important role in other applications, including the packaging of food, pharmaceuticals, and polymeric multilayer films used for the encapsulation of flexible bioelectronic implants. The delamination of polyurethane coating from glass fibre reinforced polymer (GFRP) substrates in wind turbines blades and aluminium alloys substrates in aircraft, caused by water diffusion, is of a serious concern. Furthermore, understanding the kinetics of water diffusion and hence the distribution of water within a polymer coating is essential for predicting the long-term mechanical behaviour of the coatings. Water absorption is a key mechanism for degradation in polymer coatings. On one hand, water uptake can deteriorate the mechanical performance of the polymer coating, while on the other hand, the increased weight of the structure could affect its structural integrity.

In this chapter, the performance of developed coatings under water exposure was investigated. The water uptake of pure PU and various nanomodifed PU coatings was examined. In this regard, water uptake tests were conducted at three different temperatures of 22°C, 32°C and 45°C. The time-dependent concentration of water in the coatings was predicted using Fickian diffusion modelling approaches [113]. The Fickian diffusion law was applied to the experimental results to obtain the diffusion coefficients and permeabilities of PU and various nanomodified PU coatings. Tensile tests were performed on water-saturated pure PU and nanomodified PU coatings. The mechanical properties of water-saturated specimens were compared with those of the dry specimens with similar compositions. Finally, SEM studies were conducted on the fracture surface of water-saturated specimens and then were compared with the dry ones.

6.2. Accelerated water aging

For water absorption testing, an aluminium mould was designed according to ASTM standard D570 and it was made using CNC machining. Cylindrical water absorption specimens were made according to this standard with a diameter of 50.8 mm and a thickness of 3.2 mm. The CAD model of the mould with the required specifications is shown in *Figure* 6.1(a), and the manufactured mould from CNC machining of an aluminium plate is shown in *Figure* 6.1(b). The PU and modified PU materials were prepared in a vacuum chamber and then the polymer casted in this mould.

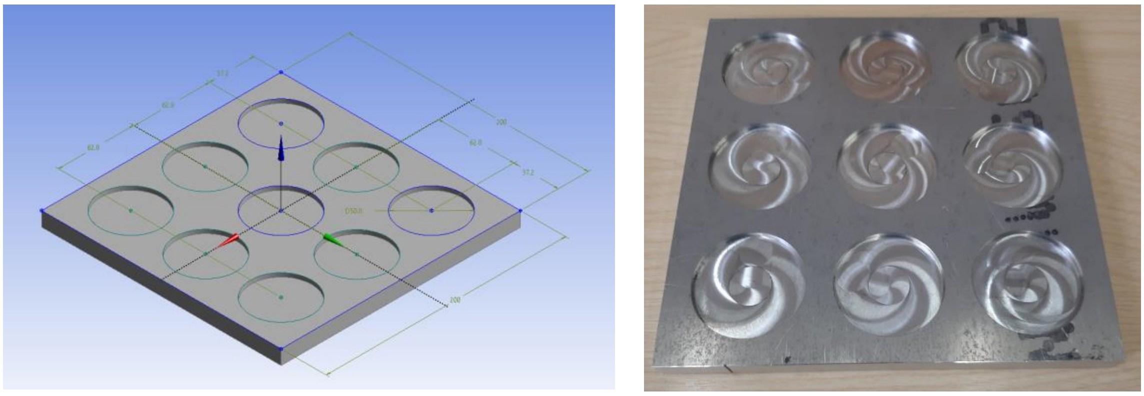

(a) (b)

Figure 6.1. (a) CAD model of water absorption mould, (b) Aluminium mould made from CNC machining.

Two sets of nine specimens were manufactured for each nanocomposite. One set of each coating material was mixed inside an industrial vacuum chamber while the other set was mixed in ambient atmosphere. Typical manufactured specimens are shown in *Figure 6.2(a)*. These two sets were made to study the effects on water uptakes when more air bubbles were present due to manufacturing in ambient environment. Once the specimens were manufactured and prior to starting the test, all specimens were conditioned by placing them inside a heating oven at 50°C for 24 hours and then they were put inside a desiccator shown in *Figure 6.2(b)* for 20-30 min to cool down to room temperature. Once all specimens were conditioned, their weights were measured using a digital scale. The weight recorded for each specimen at this point is the specimens' dry mass m_0.

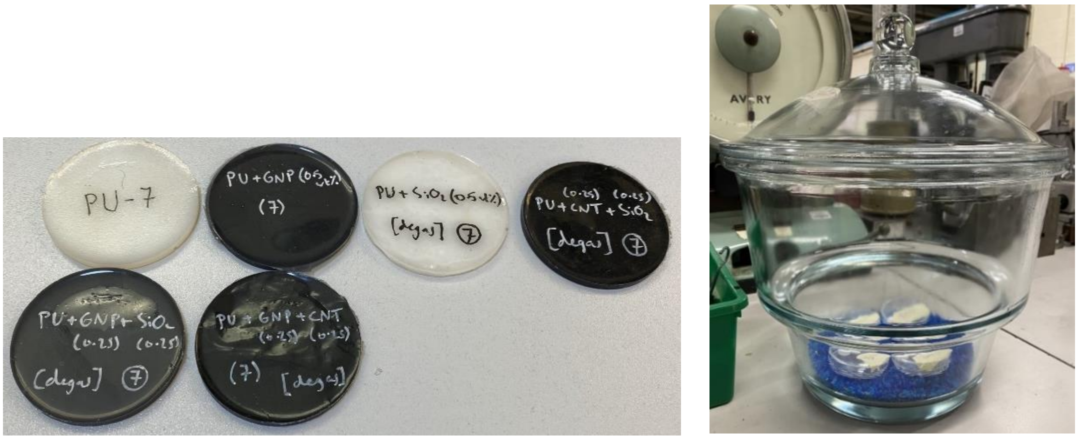

(a) (b)

Figure 6.2. (a) Samples of manufactured water absorption specimens, (b) A desiccator.

The water absorption testing was carried out within a span of a month and at three different temperatures of 22°C (RT), 32°C and 45°C.

At room temperature (RT), three degassed and three un-degassed specimens were submerged in a plastic container filled with water. The water's temperature was controlled by an aquarium heating device fitted with a temperature sensor that kept the temperature to the set temperature of 22°C (see *Figure 6.3*).

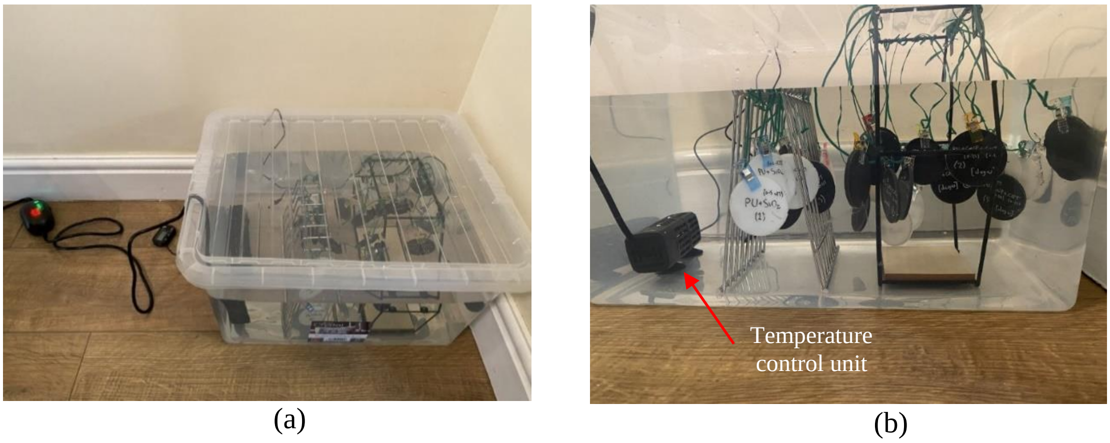

(a) (b)

Figure 6.3. (a) Specimens submerged in water at RT in a plastic container, (b) Close-up view showing the temperature control unit.

For tests at 32°C and 45°C, six specimens from each material (three degassed and three un-degassed except for the PU+GNP+SiO_2 and PU+CNT+SiO_2 specimens which only three degassed samples were made) were submerged in a glass bottle filled with water (see *Figure 6.4*), and the glass bottles were then placed inside an urn tank partially filled with water. The urn thermostat had the ability to control the water temperature between 20°C to 110°C. For safety reasons, in addition to the urn's thermostat, an additional external thermostat was used to cut-off the electricity to the urn when the temperature rose above the set temperature (see *Figure 6.5*).

Figure 6.4. The specimens inside glass bottles for the water absorption test at 32 ℃ and 45 ℃.

(a) (b)

Figure 6.5. (a) The stainless-steel urn tank with internal temperature controller and showing the external thermostat for cutting off electricity, (b) Glass bottles with the water submerged specimens inside the urn tank.

The water uptake of each specimen was measured at any time interval by taking the specimen out of the tank, then it was gently dried using a fabric cloth, after which the weight of the specimen was measured using a digital scale. From the weight measurements, the amount of water uptake per gram of each specimen was calculated.

6.3. Water diffusion in polyurethane

It is necessary to study water diffusion in polyurethane coatings when they are exposed to humid environment before using them in different applications. The diffusion of water in polymers has been widely studied and was mathematically described by Fick in 1855 [114] in which the driving force is the difference in water concentration when water only diffuses in the micro-pores of polymers. Fick used the heat conduction equations and developed the one-dimensional diffusion equation [115]:

$$\frac{\partial c(x,t)}{\partial t} = D\left(\frac{\partial^2 c(x,t)}{\partial x^2}\right) \tag{6.1}$$

where c is the water concentration, t is the immersion time and D is the diffusion coefficient expressed in unit of $m^2.s^{-1}$ or $mm^2.h^{-1}$. The water diffusion coefficient for thin film polyurethane is reported as [116, 117, 118]:

$$D = \begin{cases} 0.5 \times 10^{-11}\ m^2.s^{-1}\ (0.02\ mm^2h^{-1}) \text{ at } 23\ ℃ \\ 2.1 \times 10^{-11}\ m^2.s^{-1}\ (0.08\ mm^2h^{-1}) \text{ at } 60\ ℃ \end{cases}$$

For a polymer submerged at $t = 0$, the appropriate boundary conditions for $t \geq 0$ are as follows:

$$c(x,0) = 0;\ c(0,t) = c_s;\ and\ \frac{\partial c}{\partial t}(h,t) = 0 \tag{6.2}$$

Where $2h$ is the specimen thickness. The saturation moisture content c_s is calculated from:

$$c_s = \frac{m_\infty - m_0}{m_0} \tag{6.3}$$

Where m_0 is the mass of dry specimen, and m_∞ is the mass of saturated specimen.

The water uptake concentration at any time t is calculated from:

$$c(t) = \frac{m(t) - m_0}{m_0} \tag{6.4}$$

c_s and $c(t)$ is often expressed in percentage.

The solution of Eqs. (6.1) and (6.2) can be found in [113] for water concentration $c(x, t)$. The fractional mass $c(t)/c_s$ of water in the polymer is expressed as:

$$\frac{c(t)}{c_s} = 1 - \left[\frac{8}{\pi^2} \sum_{n=0}^{\infty} \frac{1}{(2n+1)^2} exp\left(\frac{-D(2n+1)^2 \pi^2 t}{h^2}\right)\right] \tag{6.5}$$

Where n is the concentration index, and generally, the results for $n = 10$ fit the experimental data but the specific value of n should be determined using an actual model with an acceptable range of error [113, 119]. In Eq. (6.5), D is the Fickian diffusion constant, h is the specimen thickness, $c(t)$ is the moisture content concentration at a time t and c_s is the moisture content at saturation. Saturation mass is the mass of the specimen when the difference in the weight gains from three successive measurements is less than 1%.

A simplified version of Eq. (6.5) was developed for two cases: short and long immersion times [120]. For short immersion times, when $c(t)/c_s < 0.6$ and for a dry sample at time $t = 0$ while ignoring the edge effects, the early stages of homogenous diffusion-controlled water uptake, when the diffusion occurs through micro-pores, can be predicted by plotting the fractional mass uptake $c(t)/c_s$ as a function of $4\sqrt{t}/h\sqrt{\pi}$ and the slope is proportional to $\sqrt{D}$.

$$\frac{c(t)}{c_s} = \sqrt{D} \frac{4\sqrt{t}}{h\sqrt{\pi}} \tag{6.6}$$

Therefore:

$$D = \frac{\pi h^2}{16} q^2 \tag{6.7}$$

Where q is the slope of linear section of the plot of the fractional mass uptake $c(t)/c_s$ versus $\sqrt{t}$ for $c(t)/c_s < 0.6$.

For the long immersion times, when $c(t)/c_s > 0.6$, the equation pertaining to absorption can be expressed as follows:

$$\frac{c(t)}{c_s} = 1 - exp\left[-7.3 \left(\frac{D.t}{h^2}\right)^{0.75}\right] \tag{6.8}$$

For Fickian diffusion, this plot is approximately linear until $c(t)$ approaches to $(0.5 \text{ to } 0.7) \times c_s$ [121]. Following this stage, the material approaches to saturation state and there will be no further water diffusion.

The sorption coefficient can be calculated using the following equation:

$$S = m_\infty / m_0 \tag{6.9}$$

where m_∞ is the water uptake mass at equilibrium and m_0 is the initial mass of the polymer.

The permeability coefficient can be expressed as in the following equation:

$$P = D.S \tag{6.10}$$

For polyurethane, Fick's diffusion equation is commonly used to describe water uptake with relatively good results. The above equations can be used for accelerated ageing tests, allowing determination of the Fickian diffusion constant for polyurethane in several months rather for a long-term aged state of several years or decades. Note that the ageing at higher temperature accompanies activation of other degradation mechanisms that will not occur at lower temperatures.

6.3.1. Water uptake test results of pure PU

Pure PU specimens were kept submerged inside the tank filled with water for a month at three set temperatures of 22°C (RT), 32°C and 45°C, and at different selected periods, the amount of water uptake for each specimen was measured. *Figure 6.6(a)* demonstrates the variation of the fractional water uptake $c(t)/c_s$ versus root time for the degassed pure PU specimen at three temperatures of 22°C (RT), 32°C and 45°C where the nominal specimens' thicknesses were $h = 3.2\ mm$.

Figure 6.6(a) shows the variation of the experimental fractional water uptake $c(t)/c_s$ versus $\sqrt{t}$ for the degassed pure PU specimen at 22°C (RT), 32°C, and 45°C, the theoretically predicted water content was calculated using the Fickian diffusion model. The experimental results are the average of the three specimens. The results show that the water uptake of the degassed pure PU specimens at 22°C increased continuously until it reached saturation point after approximately 120 hours of being submerged in water. The rate of water uptake into the degassed pure PU increased as the water temperature increased from 22°C to 32°C, and 45°C.

Figure 6.6(b) shows the water uptake for the undegassed specimens at 22°C and at 32°C. The specimens that were not degassed during material processing did not reach saturation point after one month. This is caused by the presence of multiple air bubbles within the specimens, as the material processing was not carried out in a vacuum chamber. Similar behaviour was observed for other undegassed nanocomposites, and their results will not be discussed any further. The diffusion coefficient for PU at 22°C, 32°C and 45°C were obtained from the slope of tangent line to the linear section of the curves in *Figure 6.6(a)* and the results are summarised in *Table* 6.1.

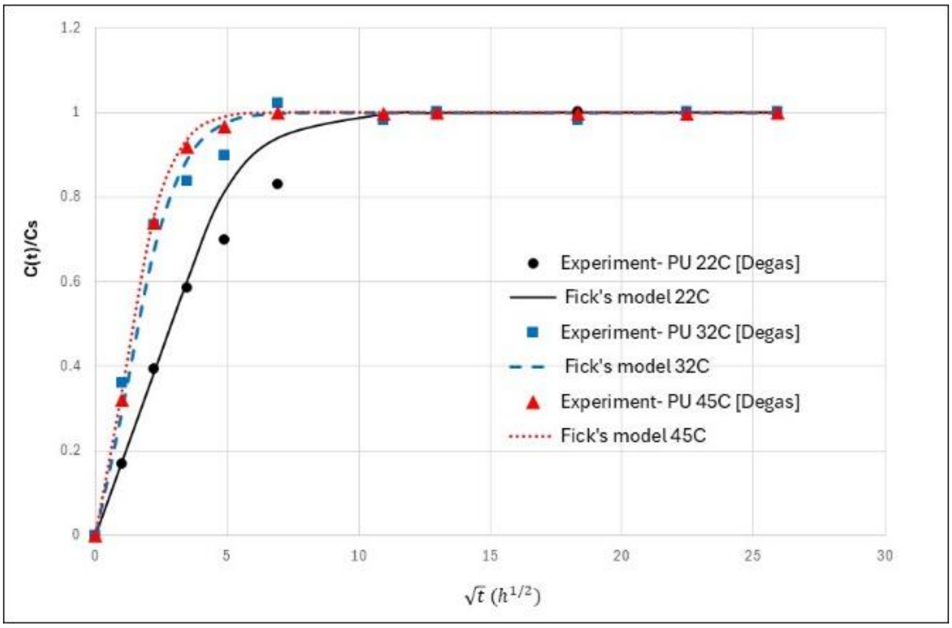

(a)

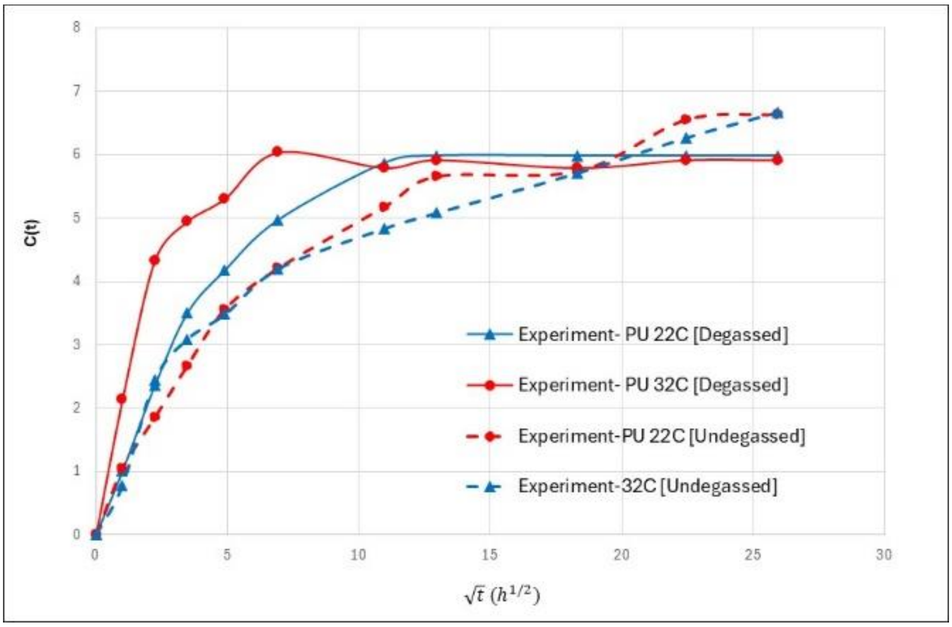

(b)

Figure 6.6. Water uptake for pure PU specimens (a) $c(t)/c_s$ *for degassed at 22°C, 32°C and 45°C, and (b)* $c(t)$ *for both degassed and undegassed at 22°C, and 32°C versus* $\sqrt{t}$ *.*

6.3.2. Water uptake test results of PU+GNP

PU+GNP specimens at 0.3 wt.% loading of GNP were kept submerged inside the tank filled with water for a month at the three set temperatures of 22°C (RT), 32°C and 45°C. At different selected periods, the amount of water uptake for each specimen was measured. *Figure 6.7* demonstrates the variation of the fractional water uptake $c(t)/c_s$ versus root time for the degassed PU+GNP specimens at three temperatures of 22°C (RT), 32°C and 45°C.

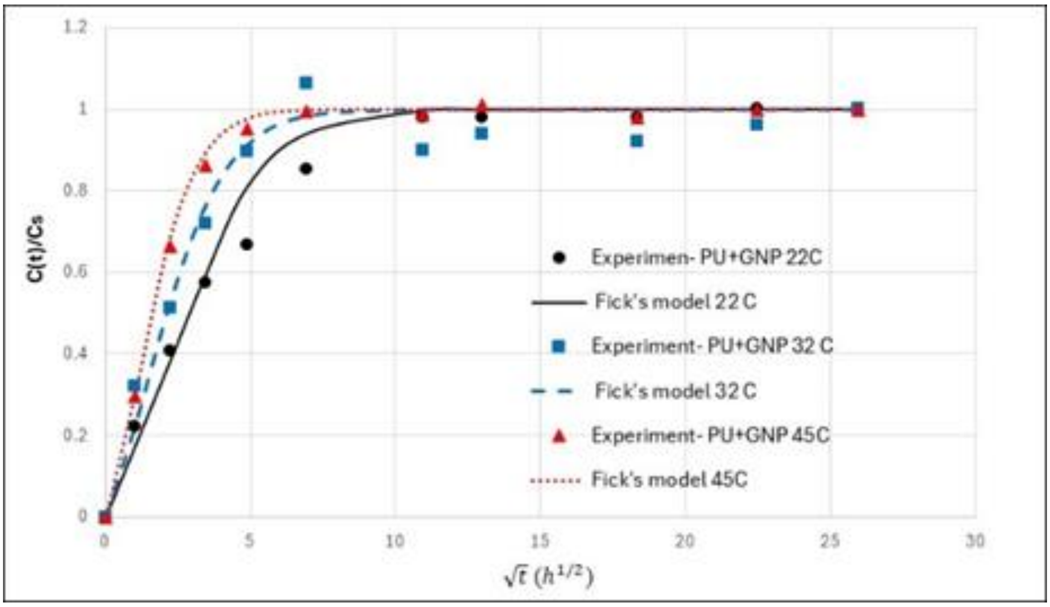

Figure 6.7. Water uptake for PU+GNP specimens; 3.2 mm thick at 22°C, 32°C and 45°C

The water uptake results in *Figure 6.7* show that the degassed PU+GNP specimens' water uptake at 22°C is increasing continuously up to around 120 hours of submerging in water when it has reached to saturation point. The rate of water uptake for the degassed specimens at 32°C is higher, and it overshoot the saturation water uptake level at 22°C before it settles down to almost the same level of water absorption at 22°C. In addition, it can be seen from *Figure 6.7* that the water uptake for the PU+GNP at 32°C and 45°C are faster than at 22°C, and higher temperature accelerate the water uptake. The diffusion coefficient for PU+GNP at 22°C, 32°C and 45°C were obtained from the slope of tangent line to the linear section of the curves in *Figure 6.7* and the results are summarised in *Table* 6.1.

6.3.3. Water uptake test results of PU+GNP+CNT

PU+GNP+CNT specimens at 0.15 wt.% loading of GNP and 0.15 wt.% loading of CNT were kept submerged inside the tank filled with water for a month at the three set temperatures of 22°C (RT), 32°C and 45°C. At different selected periods, the amount of water uptake for each specimen was measured. *Figure 6.8* demonstrates the variation of the fractional water uptake $c(t)/c_s$ versus root time for the degassed PU+GNP+CNT specimens at two temperatures of 22°C (RT), 32°C and 45°C where the nominal specimens' thicknesses were 3.2 mm.

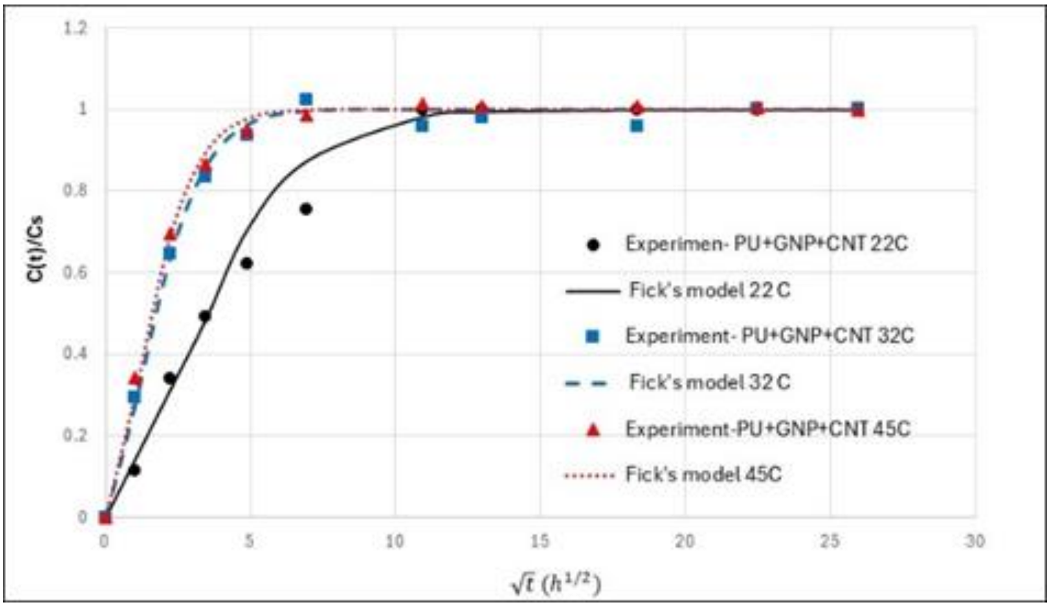

Figure 6.8. Water uptake for PU+GNP+CNT specimens; 3.2 mm thick at 22°C, 32°C and 45°C.

The water uptake results in *Figure 6.8* show that the degassed PU+GNP+CNT specimens' water uptake at 22°C is increasing continuously up to around 120 hours of submerging in water until it has reached to saturation point. It is to be noted that the environmental conditions during the testing remained nearly steady with no significant change occurring by observing the temperature of the water at a regular basis. In addition, it can be seen from *Figure 6.8* that the water uptake for the PU+GNP+CNT at 32°C and 45°C are higher than at 22°C and higher temperature accelerate the water uptake. The diffusion coefficient for PU+GNP+CNT at 22°C, 32°C and 45°C were obtained from the slope of tangent line to the linear section of the curves in *Figure 6.8* and the results are summarised in *Table* 6.1.

6.3.4. Water uptake test results of PU+SiO_2

PU+SiO_2 specimens at 0.3 wt.% loading of SiO_2 were kept submerged inside the tank filled with water for a month at three set temperatures of 22°C (RT), 32°C and 45°C and at different selected periods, the amount of water uptake for each specimen was measured. *Figure 6.9* demonstrates the variation of the fractional water uptake $c(t)/c_s$ versus root time for the degassed PU+SiO_2 specimens at three temperatures of 22°C (RT), 32°C and 45°C where the nominal specimens' thicknesses were 3.2 mm.

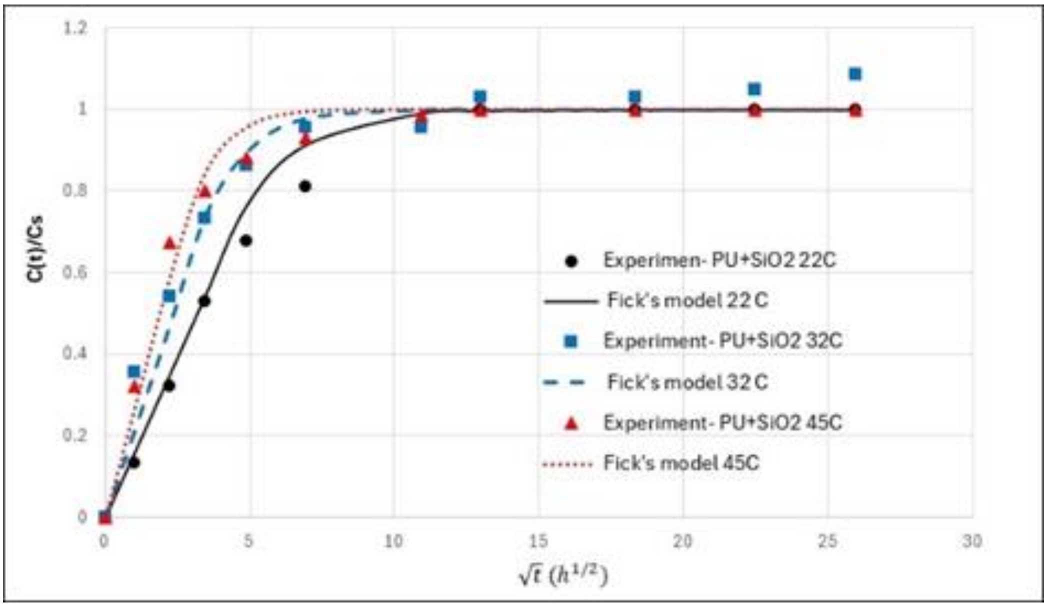

Figure 6.9. Water uptake for PU+SiO$_2$ specimens; 3.2 mm thick at 22°C, 32°C and 45°C.

The water uptake results in *Figure 6.9* show that the degassed PU+SiO$_2$ specimens' water uptake at 22°C is increasing continuously up to around 168 hours of submerging in water when it has reached to saturation point. In addition, it can be seen from *Figure 6.9* that the water uptake for the PU+SiO$_2$ at 32°C and 45°C are higher than at 22°C and higher temperature accelerate the water uptake. The diffusion coefficient for PU+SiO$_2$ at 22°C, 32°C and 45°C were obtained from the slope of tangent line to the linear section of the curves in *Figure 6.9* and the results are summarised in *Table* 6.1.

6.3.5. Water uptake test results of PU+SiO$_2$+GNP

PU+SiO$_2$+GNP specimens at 0.15 wt.% loading of SiO$_2$ and 0.15 wt.% loading of GNP were kept submerged inside the tank filled with water for a month at the two set temperatures of 22°C (RT), 32°C and 45°C. At different selected periods the amount of water uptake for each specimen was measured. *Figure 6.10* shows the variation of the fractional water uptake $c(t)/c_s$ versus root time for the degassed PU+SiO$_2$+GNP specimens at two temperatures of 22°C (RT), 32°C and 45°C where the nominal specimen's thicknesses were 3.2 mm.

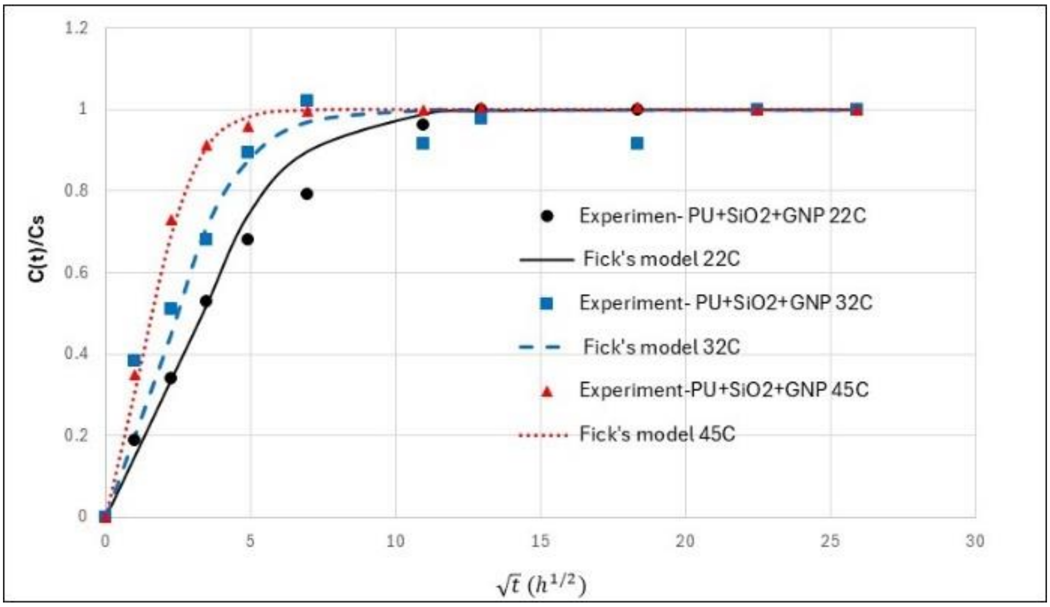

Figure 6.10. Water uptake for PU++SiO_2+GNP specimens; 3.2 mm thick at 22°C, 32°C and 45°C.

The water uptake results in *Figure 6.10* show that the degassed PU+SiO_2+GNP specimens' water uptake at 22°C is increasing continuously up to around 168 hours of submerging in water when it has reached to saturation point. The water uptake for the PU+SiO_2+GNP at 32°C and 45°C are higher than the rate at 22°C as higher temperature accelerate the water uptake. The diffusion coefficient for PU+SiO_2+GNP at 22°C, 32°C and 45°C were obtained from the slope of tangent line to the linear section of the curves in *Figure 6.10* and the results are summarised in *Table* 6.1.

6.3.6. Water uptake test results of PU+SiO_2+CNT

PU+SiO_2+CNT specimens at 0.15 wt.% loading of SiO_2 and 0.15 wt.% loading of CNT were kept submerged inside the tank filled with water for a month at the three set temperatures of 22°C (RT), 32°C and 45°C. At different selected periods the amount of water uptake for each specimen was measured. *Figure 6.11* shows the variation of the fractional water uptake $c(t)/c_s$ versus root time for the degassed PU+SiO_2+CNT specimens at two temperatures of 22°C (RT), 32°C and 45°C where the nominal specimen's thicknesses were 3.2 mm.

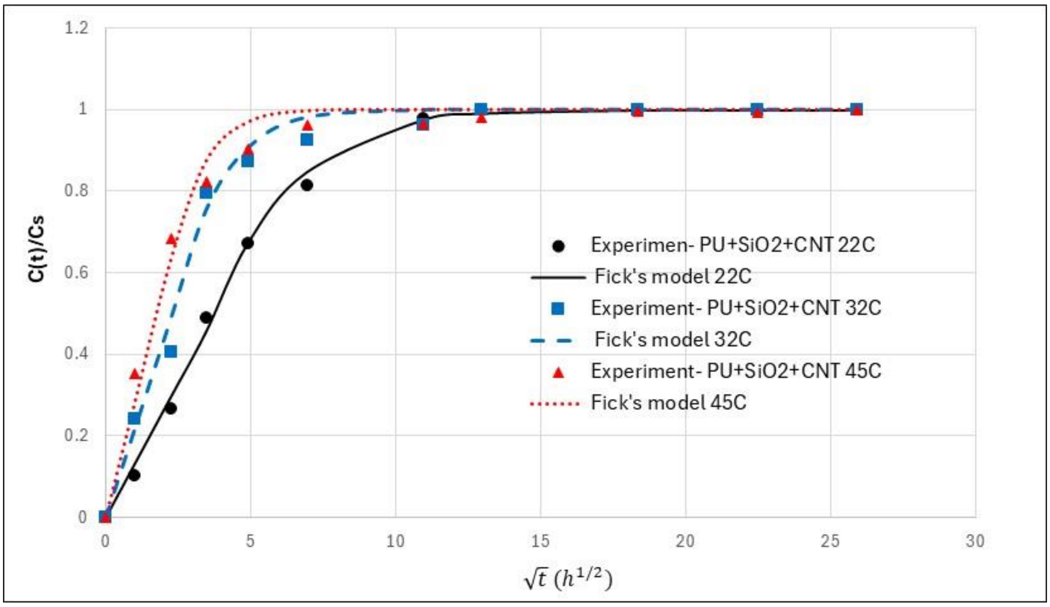

Figure 6.11. Water uptake for PU++SiO$_2$+CNT specimens; 3.2 mm thick at 22°C, 32°C and 45°C.

The water uptake results in *Figure 6.11* show that the degassed PU+SiO$_2$+CNT specimens' water uptake at 22°C is increasing continuously up to around 168 hours of submerging in water when it reached to saturation point. The water uptake for the PU+SiO$_2$+CNT at 32°C and 45°C are higher than the rate at 22°C as higher temperature accelerate the water uptake. The diffusion coefficient for PU+SiO$_2$+CNT at 22°C, 32°C and 45°C were obtained from the slope of tangent line to the linear section of the curves in *Figure 6.11* and the results are summarised in *Table* 6.1.

6.3.7. Summary of the water uptake results

The diffusion coefficients (D) for pure PU and all PU nanocomposite were computed by squaring the slope of the linear section of the graphs of the fractional mass uptake $c(t)/c_s$ versus root time and the results are summarised in *Table* 6.1. The last column shows the water contact angle previously discussed in Chapter 3.

The results show that pure PU had the highest permeability and water diffusion coefficient at both temperatures while its WCA was the least (i.e. it was relatively the most hydrophilic material). On the other hand, PU+SiO$_2$+GNP had the least permeability and water diffusion coefficient with WCA of 78.8° (2nd hydrophobic nanocomposite after PU+GNP+CNT and 16% higher than PU).

Having highest water diffusion coefficient along with the lowest WCA indicate that the pure PU is prone to water uptake when it is exposed to rain droplet as the droplets spread over the surface and because of a high water diffusivity, the water is absorbed inside PU. The opposite is true for PU+SiO$_2$+GNP due to its lowest diffusion coefficient and relatively higher WCA.

Table 6.1. Diffusion coefficient and permeability for pure PU and PU nanocomposites at 22°C, 32°C and 45°C, and their WCA.

Material	D (mm^2/h)			Water contact angle
	22°C	32°C	45°C	
Pure PU	0.06	0.17	0.23	67.9°
PU+GNP	0.06	0.10	0.18	77.6°
PU+GNP+CNT	0.04	0.15	0.18	91.6°
PU+SiO_2	0.05	0.09	0.14	70.6°
PU+SiO_2+GNP	0.045	0.08	0.19	78.8°
PU+SiO_2+CNT	0.035	0.1	0.16	74.3°

6.3.8. Kinetics of water absorption

The experimental data collected from the water absorption tests were utilised to determine the kinetic of diffusion mechanism by identifying exponent n in the Fick's equation, as represented in the following equations:

$$\frac{c_t}{c_s} = kt^n \tag{6.11}$$

$$log(\frac{c_t}{c_s}) = log\,k + n\,log\,t \tag{6.12}$$

The values of kinetic parameters n and k which indicate interaction between polyurethane and water are found from *Figure* 6.12. According to Sperling [122], Comyn [119] and Fehri et al. [123], diffusion behaviour can be categorised into three cases. Case I involves Fickian diffusion, characterised by $n = 0.5$, where the diffusion rate is significantly lower than the mobility of polymer segments. Case II pertains to polymer relaxation-controlled diffusion, observed when $n > 1$, indicating that the mobility of the penetrant surpasses the relaxation processes. Case III encompasses non-Fickian or anomalous diffusion, occurring within the range of $0.5 < n < 1$, where the mobility of the penetrant and the relaxation of the polymer segments are at the same speed. However, as reported by Sreekala et al. [124], Haddar et al. [125] and Tay & Rozman [126], diffusion mechanisms are classified as Fickian when the values of n are very close to 0.5 ($0.38 < n < 0.62$). From the results illustrated in *Figure* 6.12, it is evident that all values of the kinetic rate coefficient n fall within the range of $0.35 < n < 0.6$ at 22°C, and $0.26 < n < 0.43$ at 32°C and 45°C suggesting that all formulation of pure PU and all PU nanocomposites follow Fickian diffusion behaviour and the value of n reduces at higher temperature.

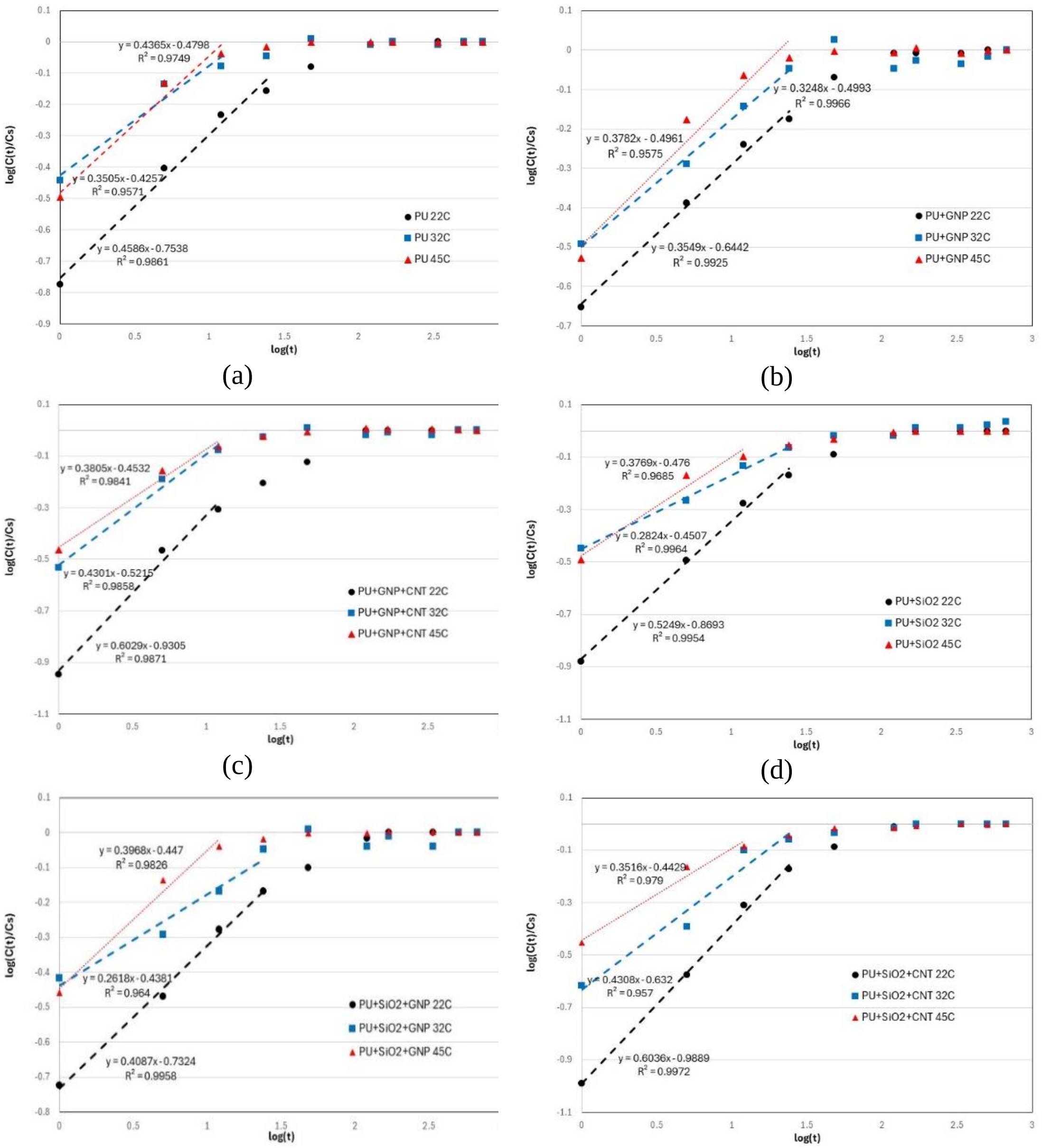

(a) (b)

(c) (d)

(e) (f)

Figure 6.12. Determining diffusion coefficient n by curve fitting of PU and various PU nanocomposite: (a) PU, (b) PU+GNP, (c) PU+GNP+CNT, (d) PU+SiO$_2$, (e) PU+SiO$_2$+GNP, and (f) PU+SiO$_2$+CNT

6.3.9. Scanning electron microscopy study

Scanning electron microscopy was utilised to examine the features on the fracture surfaces of dry and wet tensile specimens. These images are shown in *Figure 6.13*. Zhou, et al. reported that liquid water may disturb the formation of polyurethane chains into spherical particles [127]. Using FTIR, Wang et al. [128] found that the N-H and C=O groups of polyurethane were strongly affected by the water absorption process. The water molecule initially interacts with the free N-H and C=O groups, then with the hydrogen-bonded N-H and C=O groups in the PU chain segment. In addition, the water molecules interact sequentially with free carbonyl, hydrogen-bonded carbonyl group between hard and soft segments, and finally with the hydrogen-bonded carbonyl group in hard domains.

SEM images of the fracture surfaces of the dry and wet PU and PU-modified nanocomposites are shown in *Figure* 6.13. The dry PU surface showed a relatively smooth surface morphology, while the wet PU had a rugged surface with cavities. Dry PU+GNP had ridges on the fracture surface, while the wet PU+GNP surface was not smooth and contained many cavities. The SEM image of dry PU+SiO_2 showed the SiO_2 particles, and it contained a uniform distribution of cavities with diameters ranging from 1 to 5 μm. From the SEM image, the fracture surface of wet PU+SiO_2 was rough, and some cracks were visible on the fracture surface. The image of fracture surface for dry PU+GNP+CNT was wavy, showing crack deflection, while the wet PU+GNP+CNT surface contained many cracks, possibly formed from elongation of trapped air bubbles. The image for dry PU+SiO_2+GNP was also corrugated, showing crack deflection during crack propagation, contributing to higher modulus of toughness. On the wet surface of PU+SiO_2+GNP elongated holes were visible, indicating the presence of trapped air in the specimens. Finally, the SEM image of fracture surface for dry PU+ SiO_2+CNT showed that it was wavy, and the wet one was also rough, with some visible cracks on the fracture surface.

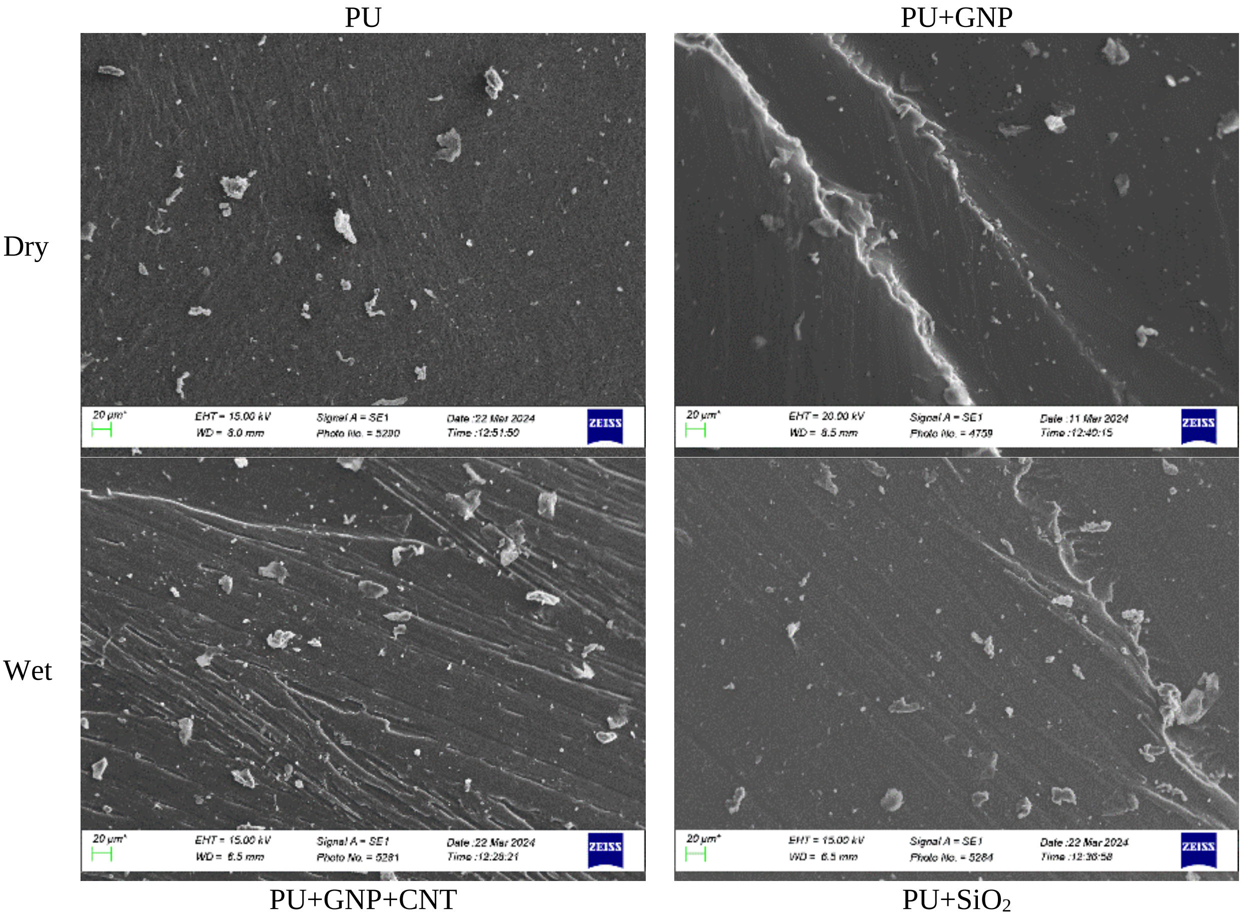

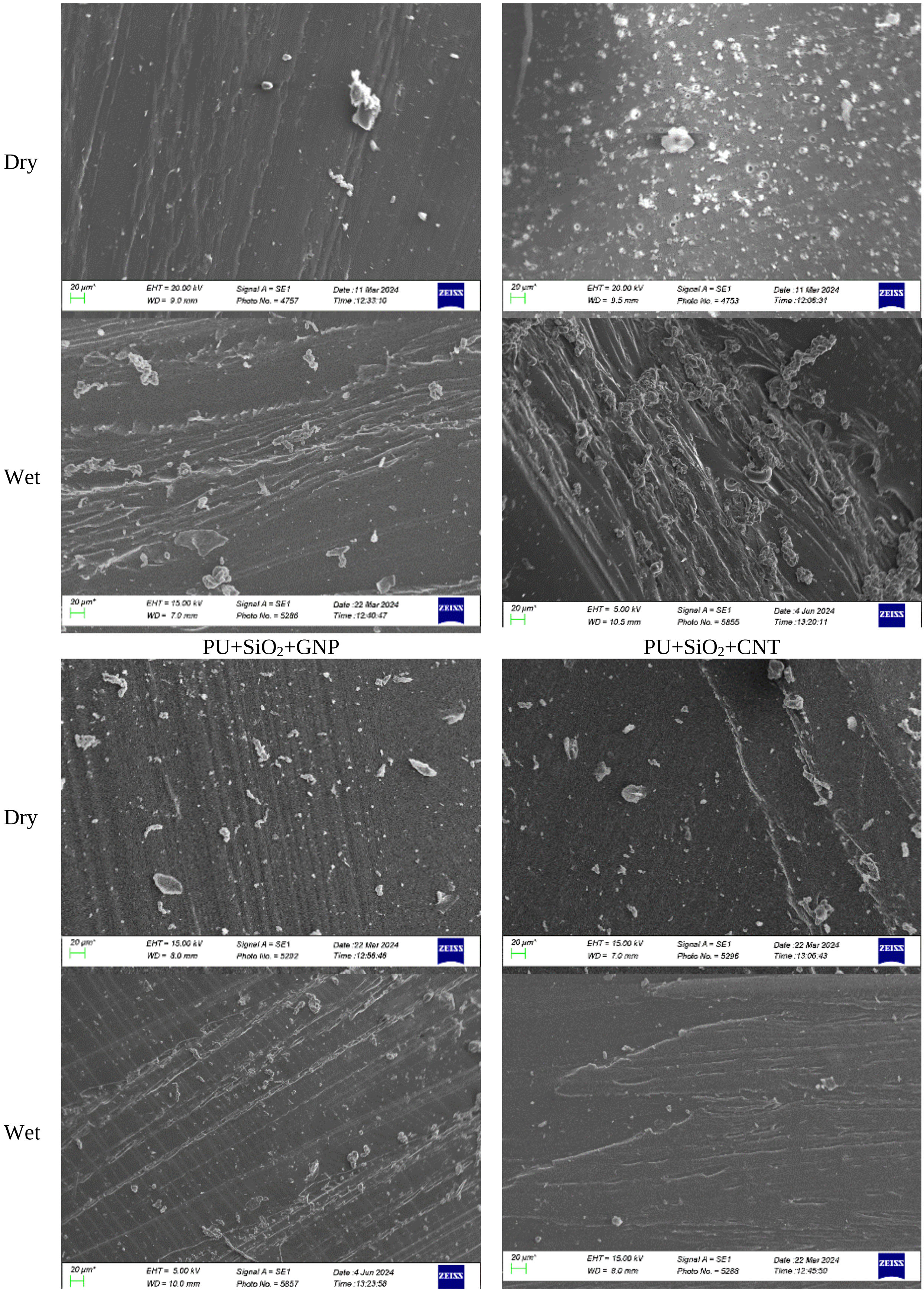

Figure 6.13. SEM images of fracture surfaces of dry and wet PU nanocomposites after rupture of tensile specimens.

6.4. Tensile test of water saturated specimens

In this section, the effect of water absorption on the mechanical properties of pure PU and all developed PU nanocomposites was investigated. For this purpose, new sets of tensile specimens for all materials were manufactured. These specimens were then submerged in water inside the glass bottles shown in *Figure 6.4*. The specimens were kept in the water for a month, so pure PU and all PU nanocomposite materials reached to their saturation state. Then, the specimens were taken out and gently dried using a cloth, and tensile tests were carried out and the true stress-strain and mechanical properties were obtained. These data were then compared to those of the dry specimens to understand the effects of water absorption on the stress-strain characteristic along with the effect on the mechanical properties of the different nanocomposites.

6.4.1. Tensile test results of wet pure PU

Specimens of water-exposed pure polyurethane (PU) were subjected to tensile tests using an HTE Hounsfield universal testing machine, equipped with a 0.5 kN load cell. The tests were conducted at a speed of 30 mm/min and continued until the specimens ruptured. The true stress-strain results for water saturated pure PU specimens (here after called “wet”) are shown in *Figure 6.14* together with a representative results of dry pure PU specimen (dashed line in *Figure 6.14*).

The results in *Figure 6.14* show that all pure PU specimens exhibit consistent stress-strain behaviour up to the point of failure. Compared to the dry PU specimens (dashed line), the stiffness of all wet specimens decreased due to moisture-induced softening, while the strain at failure increased. This increase can be attributed to water filling the microvoids in the PU, making it softer and more ductile. In effect, the absorbed water acted as a plasticizer, leading to a higher strain at failure.

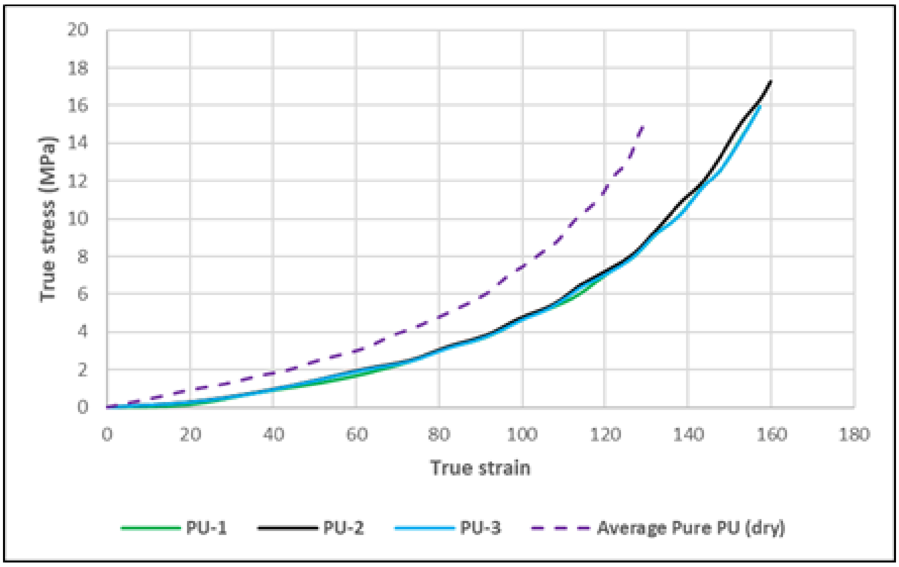

Figure 6.14. True stress-strain curves for water saturated pure PU specimens together with the results of a representative dry pure PU specimen.

The mechanical properties of dry and wet pure PU specimens are summarised in *Table* 6.2. The average Young's modulus of the wet pure PU specimens decreased by 29% compared to the dry specimens. In contrast, the ultimate tensile strength (UTS), strain at rupture, and modulus of toughness increased by 15.9%, 22.3%, and 22.2%, respectively. The decrease in Young's modulus indicates that the wet specimens exhibit lower stiffness, deforming to a greater extent under the same applied load compared to the dry specimens.

Table 6.2. Mechanical properties of wet pure PU obtained from tensile tests.

	Young's modulus (MPa)	UTS (MPa)	Strain at rupture	Modulus of toughness (J/mm^3)
Wet PU-1	2.94	15.9	157.4	671
Wet PU-2	2.91	17.2	160	745
Wet PU-3	3.10	17.1	161.3	745
Av- wet PU	2.98±0.1	16.8±0.7	159.6±2	720±43
Av- dry PU	4.2±0.2	14.5±0.7	130.5±0.9	589±16.4

6.4.2. Tensile test results of wet PU+GNP

Wet PU+GNP specimens with GNP loading of 0.3 wt.% underwent the tensile tests at a speed of 30 mm/min and the tests continued until the point of failure. The true stress-strain results for wet PU+GNP specimens are shown in *Figure* 6.15 together with the result of a representative dry PU+GNP specimen (dashed line).

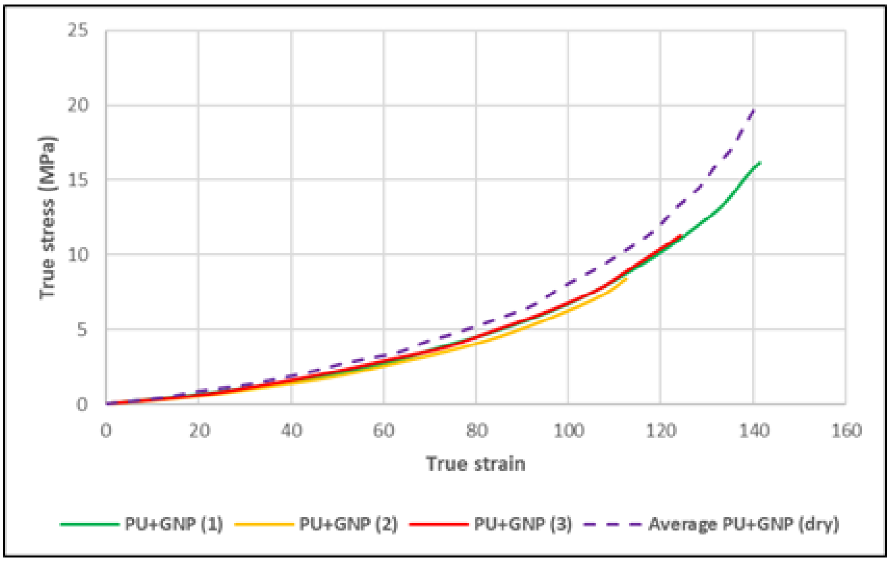

Figure 6.15. True stress-strain curves of wet PU+GNP specimens together with the results of a representative dry PU+GNP specimen.

The results in *Figure* 6.15 show that all wet PU+GNP specimens experience moisture-induced softening, resulting in lower stiffness compared to the dry specimens. However, the strain at failure for the wet specimens was inconsistent, likely due to variations in the number and distribution of entrapped air bubbles within the specimens. Compared to their dry counterparts (dashed line in *Figure* 6.15), the wet specimens displayed reduced stiffness and lower strain at failure.

Table 6.3. Mechanical properties of wet PU+GNP obtained from tensile tests.

	Young's modulus (MPa)	UTS (MPa)	Strain at rupture	Modulus of toughness (J/mm^3)
Wet PU+GNP-1	4.1	16.2	141.3	693
Wet PU+GNP-2	3.8	8.4	112.4	320
Wet PU+GNP-3	4.3	11.3	124.2	470
Av-wet PU+GNP	4.1±0.3	9.4±3.9	126±14.5	494±188
Av-dry PU+GNP	4.3±0.4	20.2±2	141.4±8	858±113.8

Table 6.3 shows that the average Young's modulus of the wet PU+GNP specimens had decreased by 4.7% compared to the dry ones. Also, the UTS, strain at rupture and modulus of toughness have decreased by 53.5%, 10.9% and 42.4%, respectively. The decrease in Young's modulus indicate that the wet specimens have lower stiffness, and they deform to a higher magnitude under the same applied loading than the dry one.

6.4.3. Tensile test results of wet PU+GNP+CNT

Wet PU+GNP+CNT specimens, with GNP and CNT loadings of 0.15 wt.% each, underwent tensile testing at a speed of 30 mm/min until failure. The true stress-strain results for wet PU+GNP+CNT specimens are shown in *Figure* 6.16.

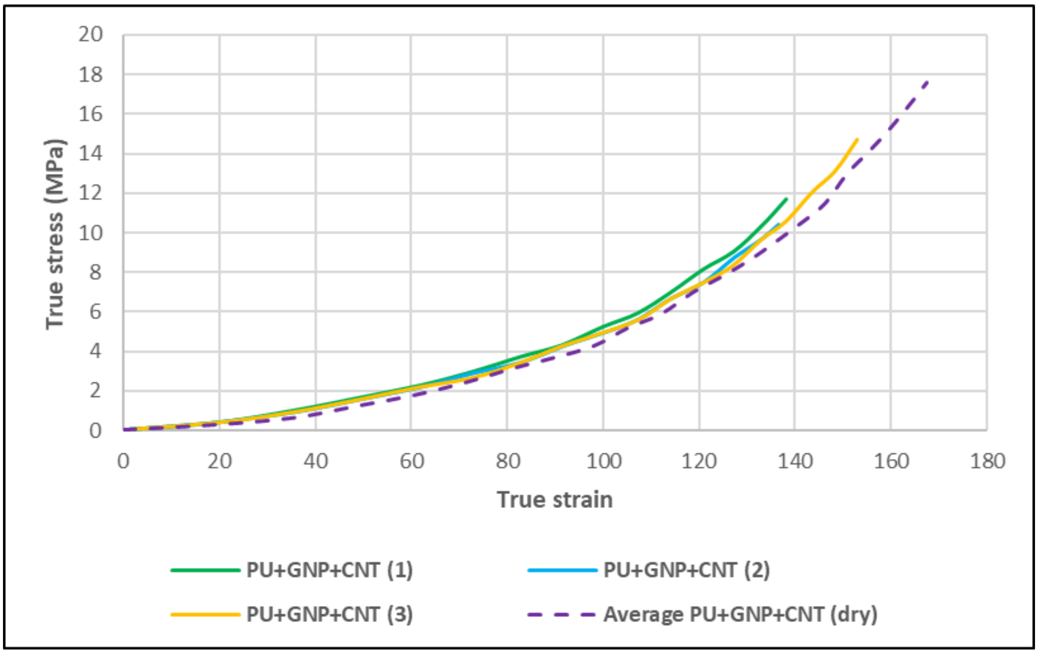

Figure 6.16.True stress-strain curves of wet PU+GNP+CNT specimens together with the results of a representative dry PU+GNP+CNT specimen.

The results show that all the wet PU+GNP+CNT specimens have consistent stress-strain behaviour with maximum strain at rupture of 153%. Compared to their dry counterparts (dashed line in *Figure* 6.16), all wet specimens exhibited similar stiffness, with no moisture softening observed in this nanocomposite. However, both the strain at rupture and tensile strength remained lower than the average for the dry specimens. This may be due to the entrapment of micro air bubbles during the mixing of polyol with isocyanates, GNP, and CNT nanoparticles, leading to high stress concentrations at various points within the specimens.

Table 6.4. Mechanical properties of wet PU+GNP+CNT obtained from tensile tests.

	Young's modulus (MPa)	UTS (MPa)	Strain at rupture	Modulus of toughness (J/mm^3)
Wet PU+GNP+CNT-1	2.49	11.7	138.1	496
Wet PU+GNP+CNT-2	2.72	10.4	136.5	453
Wet PU+GNP+CNT-3	2.71	14.7	153	651
Av-wet PU+GNP+CNT	2.64±0.13	12.3±2.2	142.6±9.1	533±104
Av-dry PU+GNP+CNT	2.4±0.3	19.1±4	172.2±8	885±158

The results in *Table* 6.4 show that, compared to the dry specimens, the average Young's modulus increased by 9.1%. However, the UTS, strain at rupture, and modulus of toughness decreased significantly by 35.6%, 17.2%, and 39.8%, respectively.

6.4.4. Tensile test results of wet PU+SiO_2

Wet PU+SiO_2 specimens, with SiO_2 loading of 0.3 wt.%, underwent tensile test at a speed of 30 mm/min until failure. The true stress-strain results for wet PU+SiO_2 specimens are shown in *Figure* 6.17 together with true stress-true strain curve of a representative dry PU+SiO_2 specimen (dashed line in *Figure* 6.17).

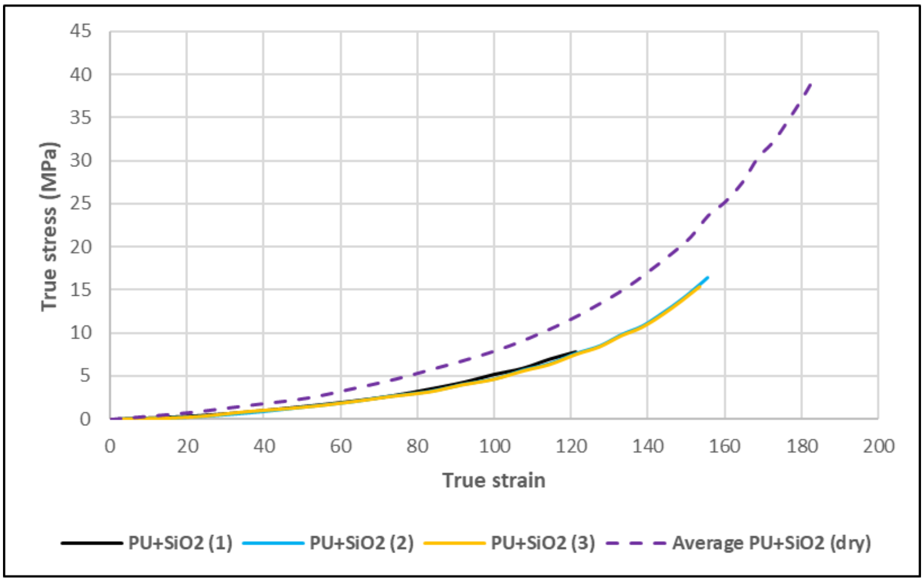

Figure 6.17.True stress-strain curves of wet PU+SiO_2 specimens together with the results of a representative dry PU+SiO_2 specimen.

The results show that all the wet PU+SiO_2 specimens have consistent stress-strain behaviour up to 156% strain at rupture. In contrast to their counterparts before water exposure (a representative dry specimen is shown *Figure* 6.17), the results indicate that all wet specimens experienced moisture softening, leading to reduced stiffness and lower strains at failure compared to the average dry specimen.

The deterioration of the wet silica modified PU was partly caused by the hydrophilic nature of silica nanoparticles. SiO_2 nanoparticles have high aspect ratio, high interface energy, and large surface area, hence they are easily intertwined together and aggregated, which leads to decreased performance [129].

Saliba et al. [130] reported that SiO_2 is hydrophilic and interacts strongly with water. Keskinen et al. [131] also observed that for nanosilica particles as small as 8 to 10 nm, a few (2 to 3) layers of adsorbed water formed under subsaturated conditions (50–90% RH) due to silica's hydrophilic nature, with these initial water layers binding to silanol groups on the particle surface. In addition, Alvarez et al. [132] reported that for the formation and stability of waterborne polyurethane films, it is advantageous for acrylate monomers with carbon–carbon double bonds (C=C) to be situated in different sections of the polymer structure, allowing for various chemical bonds, such as dangling chains, polyurethane pendant chains, and free polyurethane chains, to form. In this study, silica nanoparticles were used as received, without functionalization.

Table 6.5 shows that the average Young's modulus of the wet PU+SiO_2 specimens decreased by 58.7% compared to the dry specimens. In addition, the UTS, strain at rupture, and modulus of toughness decreased by 69.3%, 21.7%, and 73.4%, respectively. The reduction in Young's modulus indicates that moisture softening occurred in the wet specimens, leading to decreased stiffness.

Table 6.5. Mechanical properties of wet PU+SiO_2 obtained from tensile tests.

	Young's modulus (MPa)	UTS (MPa)	Strain at rupture	Modulus of toughness (J/mm^3)
Wet PU+SiO_2-1	1.8	12.8	144.2	552
Wet PU+SiO_2-2	1.3	16.5	155.7	690
Wet PU+SiO_2-3	2.4	15.4	153.7	649
Av-wet PU+SiO_2	1.9±0.6	14.9±1.9	151.2±6.2	630±71
Av-dry PU+SiO_2	4.6±0.4	48.6±15	193.1±16	2371±729

6.4.5. Tensile test results of wet PU+SiO_2+GNP

Wet PU+SiO_2+GNP specimens, with SiO_2 and GNP loadings of 0.15 wt.% each, underwent tensile testing at a speed of 30 mm/min until failure. The true stress-strain results for wet PU+SiO_2+GNP specimens are shown *Figure* 6.18.

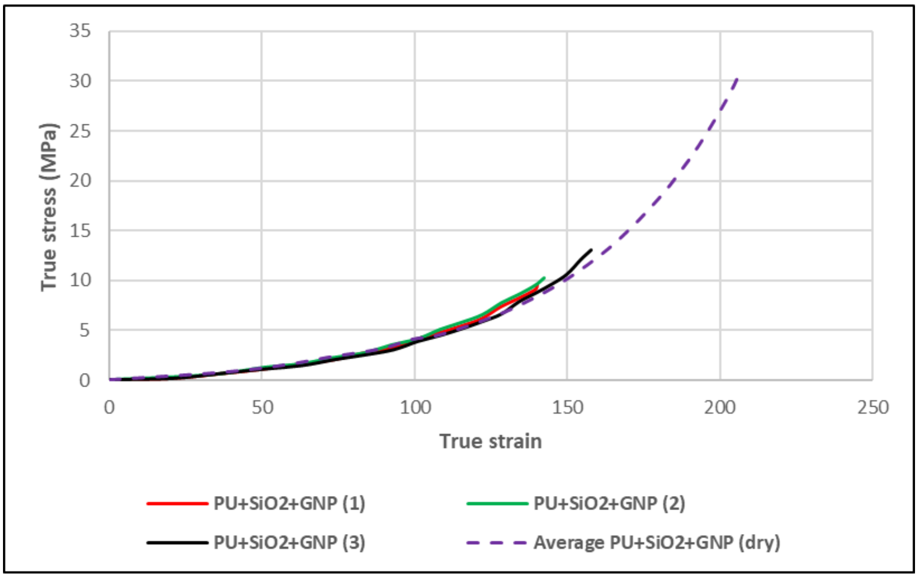

Figure 6.18. True stress-strain curves of wet PU+SiO_2+GNP specimens together with the results of a representative dry PU+SiO_2+GNP specimen.

The results show that the wet PU+SiO_2+GNP specimens exhibited consistent behaviour up to 158% strain at rupture. Compared to their dry counterparts (a representative dry specimen is shown in *Figure* 6.18), the stiffness of the wet specimens remained unchanged, while their strain at rupture and UTS decreased substantially.

Table 6.6. Mechanical properties of wet PU+SiO_2+GNP obtained from tensile tests.

	Young's modulus (MPa)	UTS (MPa)	Strain at rupture	Modulus of toughness (J/mm^3)
Wet PU+SiO_2+GNP-1	1.7	9.6	140.3	387
Wet PU+SiO_2+GNP-2	2.2	10.3	142.2	429
Wet PU+SiO_2+GNP-3	2.1	13.1	157.6	550
Av-wet PU+ SiO_2+GNP	2.0±0.3	11.0±1.9	146.7±9.5	455±85
Av-dry PU+SiO_2+GNP	2.8±0.6	28.1±8	192.3±35	1328±347

The results in *Table* 6.6 show that the average Young's modulus of the wet PU+SiO_2+GNP specimens decreased by 28.6% compared to the dry specimens. The UTS, strain at rupture, and modulus of toughness also decreased by 60.9%, 23.7% and 65.7%, respectively.

6.4.6. Tensile test results of wet PU+SiO_2+CNT

Wet PU+SiO_2+CNT specimens, with SiO_2 and CNT loadings of 0.15 wt.% each, underwent tensile testing at a speed of 30 mm/min until failure. The true stress-strain results for wet PU+SiO_2+CNT specimens are shown in *Figure 6.19***.**

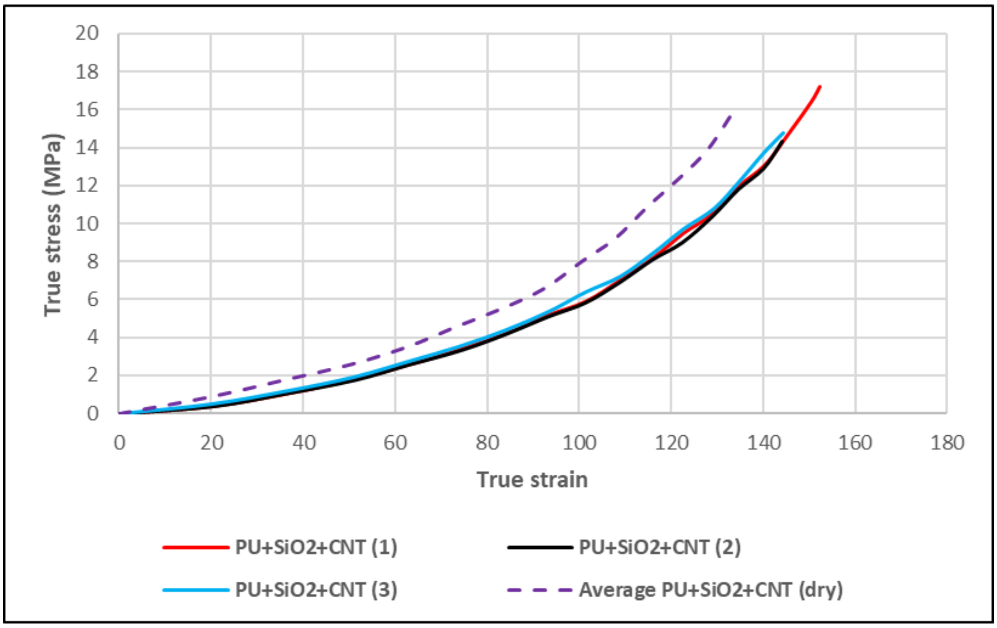

Figure 6.19. True stress-strain curves of wet PU+SiO_2+CNT specimens together with the results of a representative dry PU+SiO_2+CNT specimen.

The results of all the wet PU+SiO_2+CNT specimens showed consistent stress-strain behaviour up to 152% strain at rupture. Compared to their dry counterparts (a representative dry specimen is shown in *Figure 6.19*), the stiffness of the wet specimens decreased, while the strains at rupture and UTS increased for some of them. This behaviour was caused by moisture softening of the nanocomposite, as the increased water content within the PU+SiO_2+CNT structure made it softer and more ductile. The absorbed water acted as a plasticizer, leading to higher strain at rupture in some specimens, surpassing those of the dry specimens.

Table 6.7. Mechanical properties of wet PU+SiO_2+CNT obtained from tensile tests.

	Young's modulus (MPa)	UTS (MPa)	Strain at rupture	Modulus of toughness (J/mm^3)
Wet PU+SiO_2+CNT-1	2.58	17.2	152.5	763
Wet PU+SiO_2+CNT-2	2.56	14.3	144.1	624
Wet PU+SiO_2+CNT-3	3.06	14.8	144.3	667
Av-wet PU+SiO_2+CNT	2.73±0.3	15.4±1.6	147±4.7	685±71
Av-dry PU+SiO_2+CNT	4.8±0.3	17.5±0.7	135.2±1.5	776±31

Table 6.7 shows that the average Young's modulus of the wet PU+SiO_2+CNT specimens decreased by 43.1% compared to the dry specimens. In addition, the UTS and modulus of toughness also decreased by 12% and 11.7%, respectively, while the strain at rupture increased by 8%.

6.4.7. Comparison of tensile test results for dry and wet PU nanocomposites

The average Young's modulus, UTS, strain at rupture, and modulus of toughness for dry and wet pure PU and PU nanocomposites are compared in *Figure 6.20* to *Figure 6.23*.

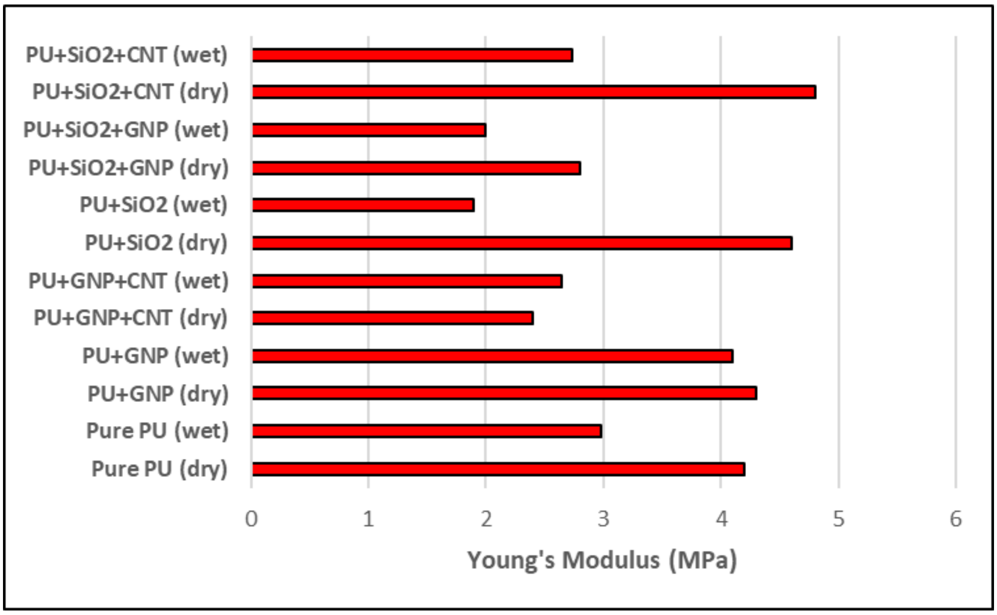

Figure 6.20. Comparison of average Young's modulus for dry and wet PU nanocomposites.

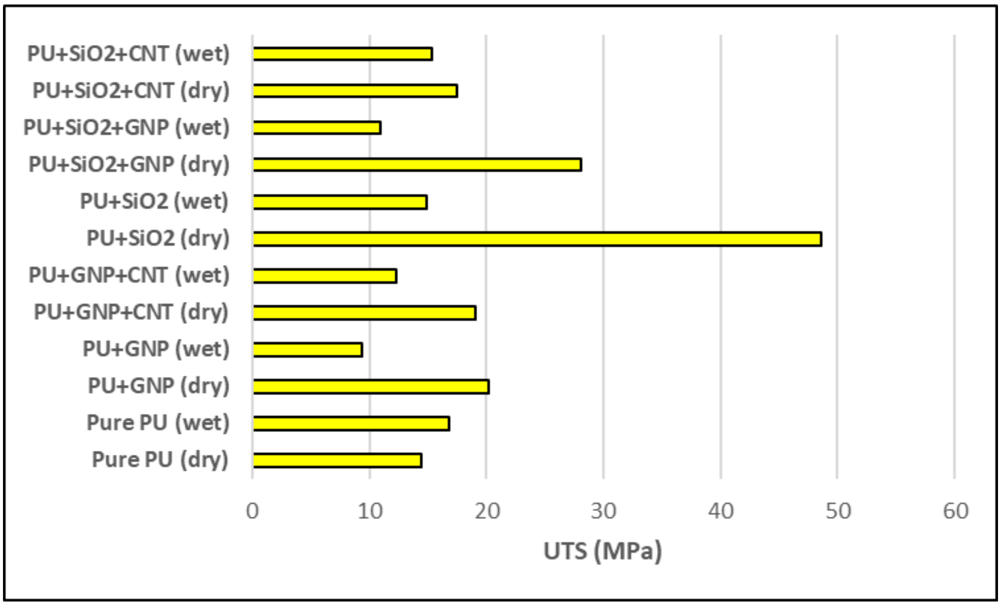

Figure 6.21. Comparison of average UTS for dry and wet PU nanocomposites.

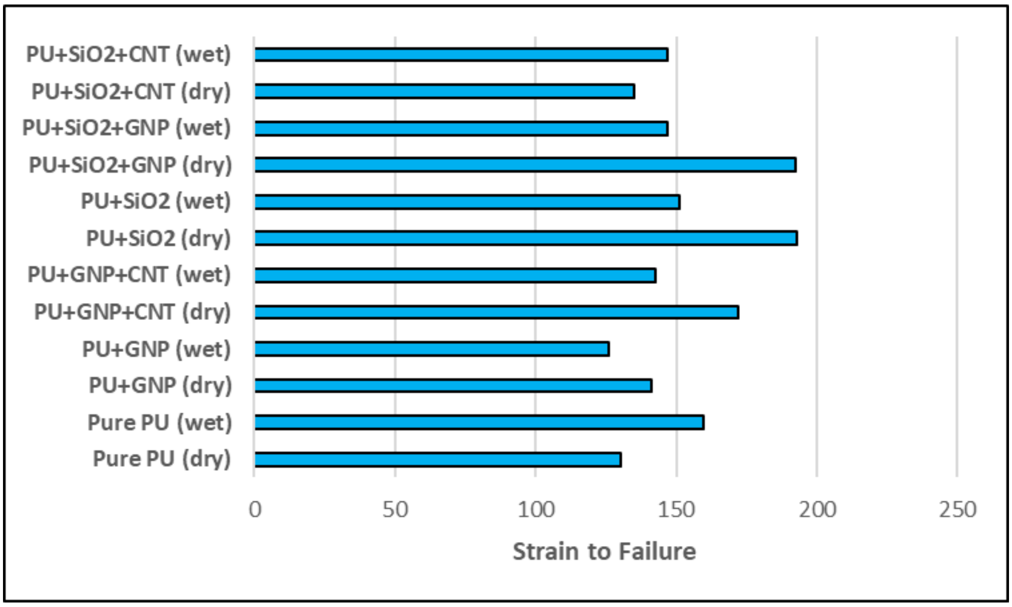

Figure 6.22. Comparison of average strain at rupture for dry and wet PU nanocomposites.

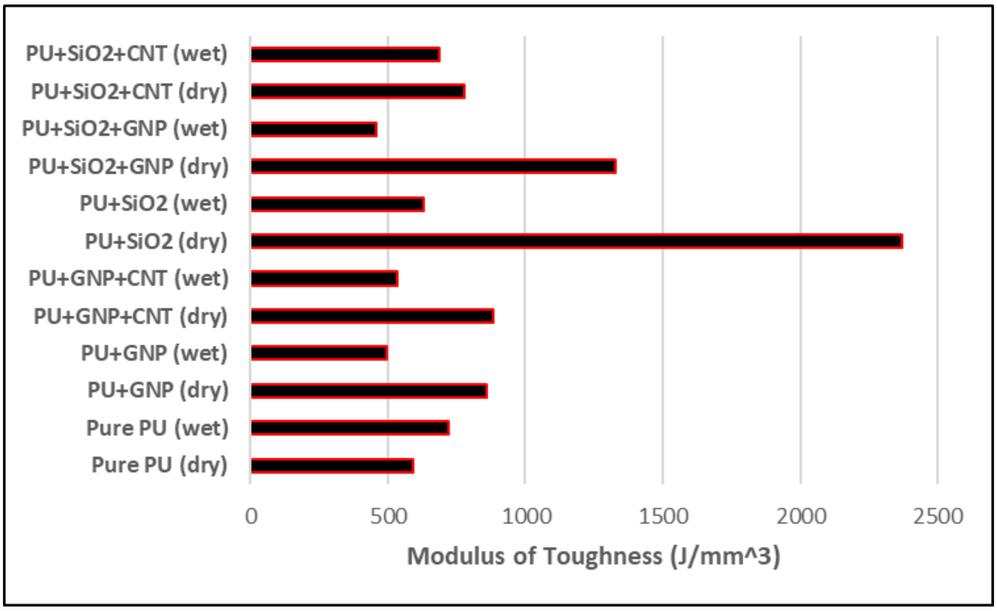

Figure 6.23. Comparison of average toughness modulus for dry and wet PU nanocomposites.

From the results shown in *Figure 6.20* to *Figure 6.23*, it can be concluded that the PU+SiO_2+CNT nanocomposite demonstrates overall superiority over all other nanocomposites in various mechanical properties, water diffusivity coefficient, and water contact angle. While PU+SiO_2 is also a strong candidate, its very low WCA causes water to spread on the coating surface, leading to substantial water uptake. Although PU+SiO2 has a low water diffusion coefficient, its Young's modulus decreases significantly when exposed to water, making it more prone to elastic deformation under load. These factors are particularly critical for coating applications in open environments, such as wind turbine blades and airplane wings.

Despite having the highest WCA among the nanocomposites, indicating a hydrophobic surface, the PU+GNP+CNT exhibited a high diffusion coefficient, allowing water molecules to penetrate its structure deeply and rapidly. This high diffusivity is most likely due to manufacturing inadequacies that resulted in trapped air bubbles, which can absorb water molecules.

6.5. Conclusion

In this chapter, water uptake tests were conducted at three different temperatures: 22°C, 32°C, and 45°C. The time-dependent concentration of water in pure PU and various PU nanocomposites was predicted using Fickian diffusion modelling. Fickian diffusion laws were applied to the experimental results, and the diffusion coefficients of both pure PU and nanomodified PU materials were identified.

Tensile tests were conducted on all water-saturated (wet) PU specimens, which had been immersed in water for a month, and their mechanical properties were obtained and compared with those of the dry specimens. Finally, SEM studies of the fracture surfaces of the wet specimens were compared with their dry counterparts.

The mechanical properties, water diffusivity, and water contact angles of pure PU and all PU nanocomposites were measured and compared. The results showed that the PU+SiO2+CNT nanocomposite exhibited superior mechanical performance, water diffusivity, and contact angle (a measure of the material’s hydrophobicity) compared to the other nanocomposites.

Chapter 7: Conclusions and recommendations

7.1 General conclusions

In this thesis, many aspects relating to leading-edge erosion protection of wind turbine blades have been investigated. Firstly, it has been shown that leading-edge erosion deteriorates the aerodynamics performance of the wind turbine blades, which can lower the annual energy production (AEP) by 20 to 25%. It has also been demonstrated that a two-dimensional blade model has sufficient accuracy for usage in a digital twin protection system, with high fidelity compared to a three-dimensional model that has 30 times higher computational cost. It is reported that tensile strength and Young's modulus are directly proportional to average erosion rates, while elongation at break has an inverse relationship [133]. Hence, further studies focused on developing new polyurethane nanocomposite coatings with enhanced mechanical properties compared to neat polyurethane. In addition, the water absorption of the developed PU nanocomposites was experimentally assessed to determine weight gain during exposure to rain. Finally, based on the cumulative test results, the high-performance novel PU nanocomposite was recommended for the protection of wind turbine blades.

7.2 Summary of characterisation of developed polyurethane nanocomposites

The mechanical performance of the developed PU nanocomposites has been characterised through tensile, tearing, and wear tests. In addition, various physicochemical tests, including Fourier-transform infrared spectroscopy (FTIR), differential scanning calorimetry (DSC), thermogravimetric analysis (TGA), and dynamic mechanical analysis (DMA) were used to understand their microstructure and correlate micro-level behaviour to the macro-level behaviour of these coatings. Water contact angle (WCA) measurements were carried out on all coatings to access the hydrophobicity of each one.

7.2.1 Physicochemical characterisation

FTIR tests showed no noticeable difference in spectra among pure PU and PU nanocomposites. The consistent behaviour across all nanocomposites was due to the high percentages of PU in the nanocomposite structures (99.7 wt%). This consistency also suggests effective incorporation and homogenous dispersion of nanofillers within the PU matrix. The identified characteristic peaks of key functional groups in PU and its modified nanocomposites were N-H stretch at 3312 cm^{-1}, C-H stretches at 2868-2969 cm^{-1}, and C=O stretches at 1703-1727 cm^{-1}.

The TGA results showed that the decomposition of the five PU nanocomposites followed a two-step degradation process: the soft segments degraded at lower temperatures, followed by the decomposition of the hard segments at higher temperatures. The soft segments in both pure PU and the five types of nanomodified PU predominantly consisted of polyether polyols. This uniformity in the soft segment structure among all nanomodified PUs contributes to the similarity in their degradation behaviour. The thermal stability of PU is determined by T_5 representing the temperature at which 5% of the mass is lost. It was shown that all PU nanocomposites exhibit thermal stability up to approximately 278°C, beyond which decomposition occurs. This characteristic makes PU a suitable candidate for coating wind turbine blades, as they are typically not exposed to temperatures exceeding 60°C under extreme weather conditions.

The DMA results for the polyurethane nanocomposites indicated that the onset of glass transition (Tg) based on the storage modulus (E′) occurred around -43°C, marked by a downward bend in the curves. Beyond this point, there was a rapid decrease in modulus due to significant softening. In contrast, the Tg identified from the tan δ peaks ranged from -22°C to -18°C, with this method preferred due to its greater accuracy over using the E′ tangent. The discrepancy between the two methods shows that glass transitions occur over a temperature range rather than a single point. In addition, peaks in the loss modulus (E″) at -43°C to -40°C corresponded to the onset of significant segmental motion in the polymer chains. The percentage improvements of the two best-performing nanocomposites relative to PU, based on DMA and TGA tests, are summarised in Table 7.1.

Table 7.1. Summary of DMA and TGA test results

Material	tan(δ) from DMA	% Imp.	T_{15} (°C) from TGA	% Imp.
PU	0.447	-	302	-
PU+SiO_2+GNP	0.475	**6.3**[*]	308	**2.0**
PU+SiO_2+CNT	0.478	**6.9**	318	**5.3**

---

[*] In Tables 7.1 to 7.5, green indicates enhancement, while red indicates deterioration.

7.2.2 Water contact angle

The water contact angle tests showed that the addition of hydrophobic silica, GNP, and CNT nanomaterials reduced the surface free energy of PU from 100.2 mJ/m^2 to 70.8 mJ/m^2 for the PU+GNP+CNT nanocomposite. All other modified PUs also exhibited lower surface free energies compared to pure PU. This decrease in surface free energy indicates an improvement in the water repellency of the PU-modified coatings, potentially enhancing the durability of structures exposed to rain.

7.2.3 Tensile tests

Tensile tests were conducted on both dry and water-saturated PU and PU nanocomposites to determine their mechanical properties under these conditions. The results for dry specimens showed that the modulus of toughness, UTS, and strain at rupture all improved for the nanomodified PUs compared to pure PU. However, this was not the case for Young's modulus. PU+SiO_2 exhibited the highest UTS and modulus of toughness among the nanocomposites, and it also had the highest strain at rupture, second only to PU+SiO_2+GNP. The Young's modulus increased slightly with the addition of fumed nanosilica particles. Except for Young's modulus, the mechanical properties of the PU+SiO_2+GNP nanocomposite improved significantly. For the PU+SiO_2+CNT nanocomposite, all mechanical properties, including Young's modulus, improved to varying degrees.

For water-saturated specimens, stiffness deteriorated for both PU and PU nanocomposites compared to the dry specimens. This deterioration is caused by moisture-induced softening of the nanocomposites. When the PU nanocomposites are immersed in water, the water penetrates into micropores within the PU structure. The absorbed water acts as a plasticizer, causing the nanocomposites to become softer and more ductile, which leads to a reduction in stiffness and a higher strain at failure, surpassing those of dry specimens.

The percentage improvements of the two best-performing nanocomposites relative to PU, based on tensile tests, are summarised in Table 7.2.

Table 7.2. Summary of dry tensile test results

Material	E (MPa)	% Imp.	UTS (MPa)	% Imp.	Strain at Rupture (%)	% Imp.	Modulus of Toughness (J/m^3)	% Imp.
PU	4.2	-	14.5	-	130.5	-	589	-
PU+GNP+SiO_2	2.8	**-33.3**	28.1	**93.8**	192.3	**47.4**	1328	**125**
PU+CNT+SiO_2	4.8	**14.3**	17.5	**20.7**	135.2	**3.6**	776	**31.7**

7.2.4 Tearing tests

Tearing tests were performed on the developed nanocomposites to measure elongation at break, tearing strength, and tearing energy. The results showed that PU+SiO_2+CNT nanocomposite exhibited the highest tearing energy compared to the others. For this nanocomposite, the tearing force exceeded 40N, with significantly higher elongation, indicating enhanced resistance to tearing, even in the presence of a notch. In contrast, neat PU and PU+GNP specimens showed relatively poorer tearing performance. The inferior tearing performance of PU+GNP is likely due to GNP agglomeration and/or trapped air bubbles within the nanocomposite.

The percentage improvements of the two best-performing nanocomposites relative to PU, based on tearing tests, are summarised in Table 7.3.

Table 7.3. Summary of tearing test results

Material	Tearing Strength (N/mm)	% Imp.	EL%	% Imp.	Tearing Energy (mJ)	% Imp.
PU	10.3	-	33.4	-	226	-
PU+GNP+SiO_2	13.2	**28.2**	30.3	**-9.3**	275.7	**21.8**
PU+CNT+SiO_2	17.2	**67**	37.8	**13.2**	422.4	**86.7**

7.2.5 Wear tests

The wear test results showed that PU+ SiO_2+CNT exhibited the highest wear resistance, demonstrating its ability to withstand material loss from repeated friction. In addition, the effect of SiO_2 loading in the PU+SiO_2+CNT nanocomposite on wear resistance was investigated. The results showed that increasing SiO_2 loading from 0.3 wt.% to 0.7 wt.% in the PU+ SiO_2+CNT nanocomposite led to a 7.6% reduction in abrasion mass loss. This highlights the importance of optimising SiO_2 loading to enhance the wear resistance of the PU+SiO_2+CNT coating

The percentage improvements of the two best-performing nanocomposites relative to PU, based on wear tests, are summarised in Table 7.4.

Table 7.4. Summary of abrasion test results

Material	Mass loss (mg)	% Imp.	Hardness (Shore D)	% Imp.
PU	232	-	20.2	-
PU+GNP+SiO_2	241	**-3.9**	16.2	**-19.8**
PU+CNT+SiO_2	216	**6.9**	17.3	**-16.8**

7.2.6 Water absorption tests

Wind turbine blades are exposed to rain droplets, particularly in offshore environments, where they encounter misty and humid conditions. As a result, understanding the performance of the developed coatings under water exposure and varying temperatures is crucial. Accelerated water uptake tests were conducted on PU and PU nanocomposites at temperatures of 22°C, 32°C, and 45°C. The time-dependent concentration of water in these coatings was predicted using Fickian diffusion law. The Fickian diffusion law was applied to the experimental data, and diffusion coefficients for PU and various nanomodified PUs were obtained.

Tensile tests were also performed on all water-saturated nanocomposites, which had been immersed in water for one month, and their mechanical properties were compared to those of the dry counterparts.

The percentage improvements of the two best-performing nanocomposites relative to PU, based on water absorption tests, are summarised in Table 7.5.

Table 7.5. Summary of water absorption test results

Material	D at 22°C (mm^2/h)	% Imp.	D at 32°C (mm^2/h)	% Imp.	D at 45°C (mm^2/h)	% Imp.	WCA	% Imp.
PU	0.06	-	0.17	-	0.23	-	67.9°	-
PU+GNP+SiO_2	0.045	**-25**	0.08	**-52.9**	0.19	**-17.4**	78.8°	**16.1**
PU+CNT+SiO_2	0.035	**-41.7**	0.1	**-41.2**	0.16	**-30.4**	74.3°	**9.4**

The mechanical properties, water diffusivity, and water contact angles of pure PU and PU nanocomposites were compared. It was concluded that the **PU+SiO_2+CNT** nanocomposite demonstrated overall superiority over pure PU and all other nanocomposites in terms of mechanical properties, water diffusivity coefficient, and water contact angle.

7.3 Key contributions

The key outcomes of this project are:

- The relationship between leading-edge erosion and the loss in annual energy production of wind turbines was quantified.
- It was proven that a two-dimensional CFD model of a wind turbine blade provided sufficient accuracy for a digital twin protection system, with high fidelity compared to a three-dimensional model, which requires 30 times more computational time.
- New polyurethane nanocomposite coatings were developed, showing enhanced mechanical performance relative to pure polyurethane.
- The water absorption of the developed PU nanocomposites was experimentally evaluated, and the water diffusivity coefficient for PU and all PU nanocomposites was determined.

7.4 Recommendations and future work

There are various areas for the continuation of this project. One of the most interesting emerging areas is the use of artificial intelligence (AI) for calibrating the quantity and type of additive materials in polymer nanocomposites.

In traditional methodologies, a huge amount of time and energy is spent finding high-performance nanocomposites due to the numerous combinations of particle loadings and types, making the process very time-consuming and expensive. An emerging alternative solution to this problem is the use of machine learning (ML) approach, where enormous amounts of data are used for training. This approach has been shown to be a very powerful predictive tool for data-driven multi-physical modelling, leading to unique insights and the exploration of properties beyond the capabilities of conventional computational and experimental analyses. Recent studies have demonstrated the effectiveness of this approach in relating materials’ structure to their properties and in accelerating the design of polymeric nanocomposites [134].

Machine learning (ML) models, including regression, classification, and deep learning, are versatile tools for predicting various properties of polymer nanocomposites, such as mechanical, thermal, optical, and electrical characteristics. The accuracy of predictions depends on the composition and structure of the material. With these models we can understand material behaviours and optimize formulations to achieve desired properties [134, 135]. Algorithms like Artificial Neural Networks (ANN), Adaptive Neuro-fuzzy Inference System (ANFIS), and Genetic Algorithms (GA) have been successfully used to map material features to nanocomposite properties, showing high correlation with experimental values.

For example, Sorour [136] discussed the use of ML for analysing the mechanical behaviour of fibre-reinforced polymers (FRP). Zakaulla et al. [137] predicted the mechanical properties of polyetheretherketone (PEEK) nanocomposites with graphene and titanium additives, with ANN models yielding accurate results for hardness, tensile strength, modulus of elasticity, and elongation. The optimal performance was achieved with 10 wt% graphene, with a correlation factor over 0.9. Ul Hassan et al. [138] used a data-driven approach to predict glass transition temperature using molecular descriptors and ML models. These studies demonstrate that ML offers superior accuracy, cost-effectiveness, and flexibility compared to traditional methods, requiring less expert analysis and allowing re-training for other applications [134].

Therefore, employing machine learning (ML) for smarter selection of nanomaterials loading and types, which can result in better erosion-resistant coatings, is an interesting area for exploration in future projects. There are few publications that have investigated using artificial neural network (ANN) for improving mechanical properties of polymers. For example, Najjar, et al. [139] reported on improving wear resistance of nanocomposites.

Other areas worthy of further investigation include:

- A deeper investigation of the functionalisation of CNT and SiO_2 nanoparticles for better dispersion and covalent bonding within the polyurethane matrix.
- Exploring other types of polyurethanes and elastomers, and using other additives such as chain extenders, are areas which needs further investigation.
- A novel testing method for evaluating the durability and performance of wind turbine blade coatings.
- Recommendations for industry standards and best practices for mitigating leading-edge erosion in wind turbines.
- Conducting rain and solid particles erosion tests for validating the improvement in the PU nanocomposite coatings relative to pure PU.

References

[1] I. Mora-Barrantes, A. Rodríguez, L. Ibarra, L. Gonzáleza and J. Valentín, “Overcoming the disadvantages of fumed silica as filler in elastomer composites,” *J. Mater. Chem.,* vol. 21, pp. 7381-7392, 2011.

[2] A. Sareen, C. Sapre and M. Selig, “Effects of leading edge erosion on wind turbine blade performance,” *Wind Energy,* vol. 17, no. 10, p. 1531–1542, 2014.

[3] H. Law and V. Vasileios Koutsos, “Leading edge erosion of wind turbines: Effect of solid airborne particles and rain on operational wind farms.,” *Wind Energy,* vol. 23, no. 10, p. 1955–1965, 2020.

[4] F. Zahle, A. Barlas, K. Lønbæk, P. Bortolotti, D. Zalkind, L. Wang, C. Labuschagne, L. Sethuraman and G. Barter, “Definition of the IEA Wind 22-Megawatt Offshore Reference Wind Turbine,” Technical University of Denmark, 2024.

[5] A. Dashtkar, H. Hadavinia, M. N. Sahinkaya, N. Williams, S. Vahid, F. Ismail and M. Turner, “Rain erosion-resistant coatings for wind turbine blades: a review,” *Polymers and Polymer Composites,* vol. 27, no. 8, pp. 443-475, 2019.

[6] L. Mishnaevsky Jr., A. Tempelis, N. Kuthe and P. Mahajan, “Recent developments in the protection of wind turbine blades against leading edge erosion: Materials solutions and predictive modelling,” *Renewable Energy,* vol. 215, p. 118966, 2023.

[7] D. Eisenberg, S. Laustsen and J. Stege, “Wind turbine blade coating leading edge rain erosion model: Development and validation,” *Wind energy,* vol. 21, no. 10, pp. 942-951, 2018.

[8] “The Leading Edge: April 2020 Wind Energy Newsletter,” the National Renewable Energy Laboratory (NREL), [Online]. Available: https://www.nrel.gov/wind/newsletter-202004.html. [Accessed July 2024].

[9] E. Cortes, F. Sanchez, A. O'Carroll, B. Madramany, M. Hardiman and T. Young, “On the Material Characterisation of Wind Turbine Blade Coatings: The Effect of Interphase Coating–Laminate Adhesion on Rain Erosion Performance,” *Materials,* vol. 10, no. 10, p. 1146, 2017.

[10] M. Liebreich, “London Summit 2017. Bloomberg New Energy Finance,” 19 September 2017. [Online]. Available: https://data.bloomberglp.com/professional/sites/24/2017/09/BNEF-Summit-London-2017-Michael-Liebreich-State-of-the-Industry.pdf. [Accessed 01 October 2024].

[11] Ö. S. Özçakmak, D. Bretos, B. Méndez and C. Bak, “Determination of annual energy production loss due to erosion on wind turbine blades,” *Journal of Physics: Conference Series, Aerodynamics, aeroleasticity, and aeroacustics,* vol. 2767, p. 022066 , 2024.

[12] L. Cappugi, A. Castorrini, A. Bonfiglioli, E. Minisci and M. S. Campobasso, “Machine learning-enabled prediction of wind turbine energy yield losses due to general blade leading edge erosion,” *Energy Conversion and Management,* vol. 245, p. 114567, 2021.

[13] G. Heyman, B. Jonkman, R. Murray, R. Damiani and J. Jonkman, “AERODYN: a time-domain wind and MHK turbine aerodynamics module,” NREL, [Online]. Available: https://nwtc.nrel.gov/AeroDyn. [Accessed 27 06 2024].

[14] B. J. Wilcox, E. B. White and D. C. Maniaci, "Roughness Sensitivity Comparisons of Wind Turbine Blade Sections.," Report No. SAND2017-11288. Sandia National Laboratories, California, CA, 2017.

[15] O. Pires, X. Munduate, K. Boorsma, O. Ceyhan, H. Madsen and W. Timmer, "Experimental investigation of surface roughness effects and transition on wind turbine performance," *Journal of Physics: Conference Series,* vol. 1037, p. 052018, 2018.

[16] B. Mendez and O. Pires, "Impact of high size distributed roughness elements on wind turbine performance," *Journal of Physics: Conference Series,* vol. 2265, p. 032027, 2022.

[17] E. Saenz, B. Mendez and A. Munoz, "A Effect of erosion morphology on wind turbine production losses.," *Journal of Physics: Conference Series,* vol. 2265, p. 032059, 2022.

[18] M. Keegan, D. Nash and M. Stack, "On erosion issues associated with the leading edge of wind turbine blades," *J Phys D Appl Phys,* vol. 46, no. 38, p. 383001, 2013.

[19] H. Law and V. Koutsos, "Leading Edge Erosion of Wind Turbines: Effect of Solid Airborne Particles and Rain on Operational Wind Farms," *Wind energy (Chichester, England),* vol. 23, no. 10, pp. 1955-1965, 2020.

[20] L. Bartolome and J. Teuwen, "Prospective challenges in the experimentation of the rain erosion on the leading edge of wind turbine blades," *Wind Energy,* vol. 22, no. 1, pp. 140-151, 2017.

[21] L. Mishnaevsky Jr. and K. Thomsen, "Costs of repair of wind turbine blades: influence of technology aspects,," *Wind Energy 23 (12) (2020) 2247–2255,* vol. 23, no. 12, p. 2247–2255, 2020.

[22] O. Gohardani, "Impact of erosion testing aspects on current and future flight conditions," *Prog. Aerosp. Sci.,* vol. 47, p. 280–303, 2011.

[23] S. S. Cook, "Erosion by Water-Hammer,," *Proceedings of the Royal Society A: Mathematical. Phys. Eng. Sci.,* 1928.

[24] J. Zahavi and S. Nadiv, "Indirect damage in composite materials due to raindrop impact," *Wear,* vol. 72, p. 305–313, 1981.

[25] L. Mishnaevsky Jr., C. Hasager, C. Bak, A.-M. Tilg, J. Bech and S. Doagou Rad, "Leading edge erosion of wind turbine blades: Understanding, prevention and protection," *Renewable Energy,* vol. 169, pp. 953-969., 2021.

[26] L. Mishnaevsky Jr, "Repair of wind turbine blades: Review of methods and related computational mechanics problems," *Renewable Energy,* vol. 140, pp. 828-839, 2019.

[27] A. Fraisse, J. Bech, K. Borum, V. Fedorov, N. Frost-Jensen, M. McGugan, L. Mishnaevsky Jr. and Y. Kusano, "Impact fatigue damage of coated glass fibre reinforced polymer laminate," *Renew. Energy,* vol. 126, pp. 1102-1112, 2018.

[28] I. Yilgor, E. Yilgor and G. L. Wilkes, "Critical parameters in designing segmented polyurethanes and their effect on morphology and properties: A comprehensive review," *Polymer* , vol. 58, pp. A1-A36, 2015.

[29] M. Bone and et al., "A novel approach to atomistic molecular dynamics simulation of phenolic resins using symthons," *Polymers* , vol. 12, p. 926, 2020.

[30] K. Jespersen, G. Monastyreckis and L. Mishnaevsky Jr, "On the potential of particle engineered anti-erosion coatings for leading edge protection of wind turbine blades: Computational studies," *IOP Conf. Ser.: Mater. Sci. Eng.,* vol. 942, p. 012027, 2020.

[31] G. V. Pham, D. L. Pham, T. D. Nguyen, H. H. Do, K. N. Hui, G. K. Pham and D. A. Dinh, “Solution blending preparation of polyurethane/graphene composite: Improving the mechanical and anti-corrosive properties of the coating on aluminum surface,” *Materials Letters,* vol. 359, p. 135905, 2024.

[32] M. Verma, S. S. Chauhan, S. Dhawan and V. Choudhary, “Graphene nanoplatelets/carbon nanotubes/polyurethane composites as efficient shield against electromagnetic polluting radiations,” *Composites Part B: Engineering,* vol. 120, pp. 118-127, 2017.

[33] C. Zhang, S. Huang, W. W. Tjiu, W. Fan and T. Liu, “Facile preparation of water-dispersible graphene sheets stabilized by acid-treated multi-walled carbon nanotubes and their poly(vinyl alcohol) composites,” *J Mater Chem,* vol. 22, no. 6, pp. 2427-2434, 2012.

[34] A. Navidfar and L. Trabzon, “Analytical modeling and experimentally optimizing synergistic effect on thermal conductivity enhancement of polyurethane nanocomposites with hybrid carbon nanofillers,” *Polymer Composites,* vol. 42, pp. 944-954, 2021.

[35] M. Pourmohammadi-Mahunaki, V. Haddadi-Asl, H. Roghani-Mamaqani, M. Koosha and M. Yazdi, “Preparation of polyurethane composites reinforced with halloysite and carbon nanotubes,” *Polymer Composites,* vol. 42, pp. 450-461, 2021.

[36] E. Legge and et al., “Determining the Level and Location of Functional Groups on Few-Layer Graphene and Their Effect on the Mechanical Properties of Nanocomposites,” *ACS Appl. Mater. Interfaces,* vol. 12, p. 13481−13493, 2020.

[37] P. Ma and Y. Zhang, “Perspectives of Carbon Nanotubes/polymer Nanocomposites for Wind Blade Materials,” *Renewable & Sustainable Energy Reviews,* vol. 30, pp. 651-660, 2014.

[38] D. Perry, “Aerodynamic Design and Structural Analysis Procedure for Small Horizontal-Axis Wind Turbine Rotor Blade,” California Polytechnic State University, San Luis Obispo, 2015.

[39] J. M. McDonough, “Lectures In Elementary Fluid Dynamics: Physics, Mathematics and Applications,” University of Kentucky, Lexington, KY 40506-0503, 2009.

[40] K. Gharali and D. Johnson, “Numerical modeling of an S809 airfoil under dynamic stall, erosion and high reduced frequencies,” *Applied Energy,* vol. 93, pp. 45-52, 2012.

[41] Y. Wang, X. Zheng, R. Hu and P. Wang, “Effects of Leading Edge Defect on the Aerodynamic and Flow Characteristics of an S809 Airfoil,” *PLoS ONE,* vol. 11, no. 9, p. e0163443, 2016.

[42] M. Gea, H. Zhang, Y. Wu and Y. Lia, “Effects of leading edge defects on aerodynamic performance of the S809 airfoil,” *Energy Conversion and Management,* vol. 195, pp. 466-479, 2019.

[43] W. Han, K. J. and B. Kim, “Effects of contamination and erosion at the leading edge of blade tip airfoils on the annual energy production of wind turbines,” *Renewable Energy,* vol. 115, pp. 817-823, 2018.

[44] I. R. A. H. Abbott, A. von Doenhoff and L. Stivers Jr., “Summary of Airfoil Data, Report No. 824, p. 195,” National Advisory Committee for Aeronautics, 1945.

[45] P. Kundu and I. Cohen, Fluid Mechanics, 4th ed.,, Burlington, MA,: Academic Press, 2008.

[46] J. M. Foale, “Simulating Extinction and Blow-off in Kerosene Swirl Spray Flames,” PhD thesis, Department of Engineering, University of Cambridge, UK, 2021.

[47] B. Sun, “Revisiting the Reynolds-averaged Navier–Stokes equations,” *Open Physics,* vol. 19, no. 1, pp. 853-862, 2021.

[48] S. Kubacki, “Turbulence Modelling (CFD Course),” 2016.

[49] S. Rodriguez, “LES and DNS Turbulence Modeling,” in *Applied Computational Fluid Dynamics and Turbulence Modeling*, Springer, Cham. https://doi.org/10.1007/978-3-030-28691-0_5, 2019.

[50] P. Sagaut, S. Deck and M. Terracol, Multiscale and multiresolution approaches in turbulence: LES, DES and hybrid RANS/LES methods: applications and guidelines, 2nd edn, p. 448. :, 2nd ed., London, UK: Imperial College Press, 2013.

[51] J. Anderson, Computational Fluid Dynamics, McGraw-Hill Education, 1995.

[52] D. C. Wilcox, Turbulence Modelling for CFD, 2nd ed., La Cañada, CA: DCW Industries, 1998.

[53] K. Oukassou, S. El Mouhsine, A. El Hajjaji and B. Kharbouch, “Comparison of the power, lift and drag coefficients of wind turbine blade from aerodynamics characteristics of Naca0012 and Naca2412,” *Procedia Manufacturing,* vol. 32, pp. 983-990, 2019.

[54] P. Spalart and S. S. Allmaras, “A One-Equation Turbulence Model for Aerodynamic Flows,” *AIAA,* vol. 439, pp. doi: 10.2514/6.1992-439., 1992.

[55] T. Javaherchi, “Review of the Spalart-Allmaras Turbulence Model and its Modification,” Tech. Rep., 2010.

[56] A. Rezaeiha, H. Montazeri and B. Blocken, “On the accuracy of turbulence models for CFD simulations of vertical axis wind turbines,” *Energy,* vol. 180, pp. 838-857, 2019.

[57] C. Suvanjumrat, “Comparison of Turbulence Models for Flow Past NACA0015 Airfoil Using OpenFOAM,” *Engineering Journal ,* vol. 21, no. 3, pp. 207-221, 2017.

[58] A. Fernandez, J. Oro, K. Diaz and S. Suarez, “Turbulence-Model Comparison for Aerodynamic-Performance Prediction of a Typical Vertical-Axis Wind-Turbine Airfoil,” *Energies,* vol. 12, no. 3, p. 488, 2019.

[59] S. Aftab, A. Mohd Rafie, N. Razak and K. Ahmad, “Turbulence Model Selection for Low Reynolds Number Flows,” *PLoS ONE,* vol. 11, no. 4, 2016.

[60] H. Rahimi, W. Medjroubi, B. Stoevesandt and J. Peinke, “2D Numerical Investigation of the Laminar and Turbulent Flow Over Different Airfoils Using OpenFOAM.,” *Journal of Physics Conference Series,* vol. 555, no. 1, 2014.

[61] M. Lin and H. Sarlak, “A Comparative Study on the Flow over an Airfoil using Transitional Turbulence Models,” *Aip Conference Proceedings,* vol. 1738, 2016.

[62] S. Cakmakcioglu, I. Sert, O. Tugluk and N. Sezer-Uzol, “2-D and 3-D CFD Investigation of NREL S826 Airfoil at Low Reynolds Numbers,” *Journal of Physics Conference Series,* vol. 524, no. 1, 2014.

[63] J. Yao, W. Yuan, J. Wang, J. Xie, H. Zhou, M. Peng and Y. Sun, “Numerical simulation of aerodynamic performance for two dimensional wind turbine airfoils,” *Procedia Engineering,* vol. 12, no. 21, pp. 80-86, 2012.

[64] D. Eleni, T. Athanasios and M. Dionissios, “Evaluation of the turbulence models for the simulation of the flow over a National Advisory Committee for Aeronautics (NACA) 0012 airfoil,” *Journal of Mechanical Engineering Research,* vol. 4, no. 3, pp. 100-111, 2012.

[65] F. Villalpando, M. Reggio and A. Ilinca, “Assessment of Turbulence Models for Flow Simulation around a Wind Turbine Airfoil,” *Modelling and Simulation in Engineering,* vol. 2011, pp. 1-8, 2011.

[66] W. Basha and W. Ghaly, “Drag Prediction in Transitional Flow over Airfoils,” *Journal of Aircraft,* vol. 44, no. 3, pp. 824-832, 2007.

[67] O. Badran and H. Bruun, “Two-Equation Turbulence Models for Turbulent Flow over a NACA 4412 Airfoil at Angle of Attack 15 Degree,” *ASME/JSME 2003 4th Joint Fluids Summer Engineering Conference,* pp. 137-141, 2003.

[68] M. Genc, “Numerical Simulation of Flow over a Thin Aerofoil at a High Reynolds Number Using a Transition Model,” *Proceedings of the Institution of Mechanical Engineers. Part C, Journal of mechanical engineering science,* vol. 224, no. 10, pp. 2155-2164, 2010.

[69] S. Deck, N. Renard, R. Laraufie and P. Weiss, “Large scale contribution to mean wall shear stress in high Reynolds number flat plate boundary layers up to Reθ = 13650,” *J. Fluid Mech.* , vol. 743, p. 202–248 http://doi:10.1017/jfm.2013.629 , 2014.

[70] “Turbulence Modeling Resource,” Langley Research Center, NASA, [Online]. Available: https://turbmodels.larc.nasa.gov/naca0012_val.html. [Accessed 29th January 2021].

[71] C. Rumsey, B. Smith and G. Huang, “Description of a Website Resource for Turbulence Modeling Verification and Validation,” in *40th Fluid Dynamics Conference and Exhibition*, Chicago, Illinois, 2012.

[72] M. Carraro, F. De Vanna, F. Zweiri, E. Benini, A. Heidari and H. Hadavinia, “CFD Modeling of Wind Turbine Blades with Eroded Leading Edge,” *Fluids,* vol. 302, no. 7, 2022.

[73] A. Dashtkar, N. F.-J. Johansen, L. Mishnaevsky Jr., N. Williams, S. Hasan, V. Wadi, A. Silvello and H. Hadavinia, “Graphene/sol–gel modified polyurethane coating for wind turbine blade leading edge protection: Properties and performance,” *Polymers and Polymer Composites,* vol. 30, 2022.

[74] H. Madhad, N. Mishra, S. Patel, S. Panchal and D. Vasava, “Graphene/graphene nanoplatelets reinforced polyamide nanocomposites: A review,” *High Performance Polymers,* vol. 33, no. 9, pp. 981-997, 2021.

[75] N. Domun, H. Hadavinia, T. Zhang, T. Sainsbury, G. Liaghat and S. Vahid, “Improving the fracture toughness and the strength of epoxy using nanomaterials – a review of the current status,” *Nanoscale,* vol. 7, no. 23, pp. 10294-10329, 2015.

[76] H. Chong, S. Hinder and A. Taylor, “Graphene nanoplatelet-modified epoxy: effect of aspect ratio and surface functionality on mechanical properties and toughening mechanisms,” *J Mater Sci,* vol. 51, pp. 8764-8790, 2016.

[77] J. Slonczewski and P. Weiss, “ Band structure of graphite Phys. Rev.,” vol. 109, pp. 272-279, 1958.

[78] H. Tetlow, J. Posthuma de Boer, I. Ford, D. Vvedensky, J. Coraux and L. Kantorovich, “Growth of epitaxial graphene: Theory and experiment,” *Physics Reports,* vol. 542, no. 3, pp. 195-295, 2014.

[79] A. Castro~Neto, F. Guinea and N. Peres, “Drawing conclusions from graphene,” *Phys. World,* vol. 19, p. 33, 2006.

[80] R. Sadri, G. Ahmadi , H. Togun, M. Dahari, S. Kazi, E. Sadeghinezhad and N. Zubir , “An experimental study on thermal conductivity and viscosity of nanofluids containing carbon nanotubes,” *Nanoscale Research Letters,* vol. 9, no. 1, p. 151, 2014.

[81] S. Berber, Y. Kwon and D. Tomanek, “Unusually high thermal conductivity of carbon nanotubes,” *Physical Review Letters,* vol. 84, no. 20, p. 4613–4616, 2000.

[82] C.-M. Tîlmaciu and M. C. Morris, “Carbon nanotube biosensors,” *Frontiers in Chemistry,* vol. 3, no. 63, 2015.

[83] F. Buyuknalcaci, Y. Polat, T. Negawo, E. Doner, M. Alam, T. Hamouda and A. Kilic, “Carbon nanotube-based nanocomposites for wind turbine applications,” *Woodhead Publishing Series in Composites Science and Engineering,* pp. 635-661, 2018.

[84] L.-B. Zhang, H.-X. Zhang, Z.-J. Liu and X.-Y. Jiang, “Nano-silica anti-icing coatings for protecting wind-power turbine fan blades,” *Journal of Colloid and Interface Science,* vol. 630, no. 22, 2022.

[85] V. Ganesan, Natrayan L, Y. S. Rao and P. Gaur, “Influence of Epoxy/Nanosilica on Mechanical Performance of Hemp/Kevlar Fiber Reinforced Hybrid Composite with an Ultrasonic Frequency,” *Adsorption Science & Technology,* vol. 2022, no. 2018, pp. 1-11, 2022.

[86] “Differential Scanning Calorimetry (DSC) Analysis,” Intertek Group plc, [Online]. Available: https://www.intertek.com/analysis/dsc/. [Accessed 21 November 2020].

[87] “Differential Scanning Calorimeters,” TA instruments, 2020. [Online]. Available: https://www.tainstruments.com/products/thermal-analysis/differential-scanning-calorimeters/. [Accessed 23 November 2020].

[88] “Thermogravimetric Analysis (TGA),” PhotoMetrics Inc, [Online]. Available: https://photometrics.net/thermogravimetric-analysis-tga/. [Accessed 24 November 2020].

[89] “Thermal Gravimetric Analysis (TGA),” LPD Lab Services Ltd, [Online]. Available: https://www.lpdlabservices.co.uk/analytical_techniques/chemical_analysis/thermal_gravimetric_analysis.php. [Accessed 24 November 2020].

[90] M. Wagner, Thermal Analysis in Practice- Collected applications, Mettler-Toledo, 2017.

[91] N. Rohman, T. Mohiuddin and M. S. Al-Ruqeishi, “Effect of Surface Polarity on Water Contact Angle and Interfacial Hydration Structure,” *Inorganic Chemistry Communications,* vol. 153, p. 110855, 2023.

[92] E. Marlina, A. Alhikami, M. Negara, S. Sahwahita and M. Basjir, “Characterization of Voltage Generation Obtained from Water Droplets on a Taro Leaf (Colocasia esculenta L) Surface,” *Journal of Earth Energy Engineering,* vol. 12, no. 2, pp. 50-57, 2023.

[93] N. Rohman, T. Mohiuddin and M. S. Al-Ruqeishi, “Surface free energy of graphene-based coatings and its component elements,” *Inorganic Chemistry Communications,* vol. 153, p. 110855, 2023.

[94] S. Roh, E. Choi, Y. Choi and C. Kim, “Characterization of the surface energies of functionalized multi-walled carbon nanotubes and their interfacial adhesion energies with various polymers,” *Polymer,* vol. 55, no. 6, pp. 1527-1536, 2014.

[95] H. Alloul, T. Roques-Carmes, T. Hamieh, A. Razafitianamaharavo, O. Barres, J. Toufaily and F. Villiéras, “Effect of chemical modification on surface free energy components of Aerosil silica powders determined with capillary rise technique,” *Powder Technology,* vol. 246, pp. 575-582, 2013.

[96] R. N. Wenzel, “Resistance of solid surfaces to wetting by water,” *Industrial and Engineering Chemistry,* vol. 28, pp. 988-994, 1936.

[97] A. B. D. Cassie and S. Baxter, “Wettability of porous surfaces,” *Transaction of the Faraday Society,* vol. 40, pp. 546-551, 1944.

[98] M. Karevan, R. Pucha, M. Bhuiyan and et. al, “Effect of interphase modulus and nanofiller agglomeration on the tensile modulus of graphite nanoplatelets and carbon nanotube reinforced polypropylene nanocomposites.,” *Carbon Letter,* vol. 11, no. 4, p. 325–331, 2010.

[99] D. De Cicco and F. Taheri, “Effect of functionalized graphene nanoplatelets on the delamination-buckling and delamination propagation resistance of 3D fiber-metal laminates under different loading rates,” *Nanomaterials (Basel),* vol. 9, no. 1482, p. 1482, 2019.

[100] M. Naebe, J. Wang, A. Amini and et al., “Mechanical property and structure of covalent functionalised graphene/epoxy nanocomposites,” *Sci Rep,* vol. 4, no. 1, p. 4375, 2014; .

[101] C. Peng and X. Zhang, “Chemical Functionalization of Graphene Nanoplatelets with Hydroxyl, Amino, and Carboxylic Terminal Groups,” *Chemistry,* vol. 3, pp. 873-888, 2021.

[102] S.-Y. Yang, W.-N. Lin, Y.-L. Huang, H.-W. Tien, J.-Y. Wang, C.-C. Ma and et al., “Synergetic effects of graphene platelets and carbon nanotubes on the mechanical and thermal properties of epoxy composites,” *Carbon,* , vol. 49, pp. 793-803, 2011.

[103] A. Pontefisso and L. Mishnaevsky Jr., “Nanomorphology of graphene and CNT reinforced polymer and its effect on damage: Micromechanical numerical study,” *Composites Part B: Engineering,* vol. 96, pp. 338-349, 2016.

[104] N. Frost-Jensen Johansen, L. J. Mishnaevsky, A. Dashtkar, N. Williams, S. Fæster, A. Silvello, I. Cano and H. Hadavinia, “Nanoengineered Graphene-Reinforced Coating for Leading Edge Protection of Wind Turbine Blades,” *Coatings,* vol. 11, no. 1104, 2021.

[105] M. Malaki, Y. Hashemzadeh and M. Karevan, “Effect of nano-silica on the mechanical properties of acrylic polyurethane coatings,” *Progress in Organic Coatings,* vol. 101, pp. 477-485, 2016.

[106] W. Han, S. Chen, J. Campbell, X. Zhang and Y. Tang, “Fracture toughness and wearproperties of nanosilica/epoxy composites under marine environment,” *Mater.Chem. Phys.*, vol. 177, no. 1, pp. 147-155, 2016.

[107] J. Li and I. M. Hutchings, “Resistance of castable polyurethane elastomers to solid particle erosion,” *Wear,* vol. 135, no. 2, p. 293−303, 1990.

[108] J. C. Arnold and I. M. Hutchings, “The mechanism of erosion of unfilled elastomers by solid particle impact,” *Wear,* vol. 138, pp. 33-46, 1990.

[109] H. Ashrafizadeh, A. McDonald and P. Mertiny, “Erosive and Abrasive Wear Resistance of Polyurethane Liners [Internet],” in *Aspects of Polyurethanes*, InTech, 2017.

[110] D. Hill, M. Kileen, J. O’Donnell, P. Pomery, D. St John and A. Whittaker, “Laboratory wear testing of polyurethane elastomers,” *Wear,* vol. 208, p. 155−160, 1997.

[111] “ASTM Standard G65, Standard Test Method for Measuring Abrasion Using the Dry Sand/Rubber Wheel Apparatus.,” West Conshohocken, USA, ASTM International, 2015.

[112] “Rubber, vulcanized or thermoplastic: Determination of abrasion resistance using a rotating cylindrical drum device,” ISO, Switzerland, 2010.

[113] J. Crank and G. Park, Diffusion in Polymer, London, UK: Academic Press, 1968.

[114] A. Fick, “Ueber Diffusion,” *annalen der physik,* vol. 170, no. 1, 1855.

[115] C. Shen and G. S. G S Springer, “Moisture Adsorption and Desorption of Composite Materials,,” *J. Composite Materials,* vol. 10, pp. 2-20, 1976.

[116] W. Possart and B. Zimmer, “Water in polyurethane networks: physical and chemical ageing effects and mechanical parameters,” *Continuum Mech. Thermodyn.* , pp. https://doi.org/10.1007/s00161-022-01082-y, 2022.

[117] E. Schwiderke and A. di Sarli, “A mathematical basis for calculating the water permeability of organic films supported by metal substrates.,” *Prog. Org. Coat.* , vol. 14, p. 297–308, 1986.

[118] M. Wind and H. Lenderink, “A capacitance study of pseudo-fickian diffusion in glassy polymer.,” *Prog. Org. Coat.,* vol. 28, p. 239–250, 1996.

[119] J. Comyn, Polymer Permeability, London: Elsevier Applied Science, 1985.

[120] C.-H. Shen and G. Springer, “Moisture Adsorption and Desorption of Composite Materials,” *J. Composite Materials,* vol. 10, no. 1, pp. 2-20, 1976.

[121] J. Seo and H. Han, “Water diffusion studies in polyimide thin films.,” *Journal of applied polymer science,* vol. 82, p. 731–737, 2001.

[122] L. Sperling, Introduction to Physical Polymer Science, 4th Ed., New Jersey: Wiley-Interscience Publications, 2006.

[123] M. Fehri, R. R. Ragueh, A. Vivet, F. Dammak and M. Haddar, “Improvement of Natural Fiber Composite Materials by Carbon Fibers,” *J. Renew. Mater.,* vol. 5, no. 1, pp. 38-47, 2017.

[124] M. S. Sreekala, M. G. Kumaran and S. S. Thomas, “Water sorption in oil palm fiber reinforced phenol formaldehyde composites,” *Compos. Part A: Appl. Sci. Manuf. ,* vol. 33, no. 6, p. 763, 2002.

[125] M. Haddar, Y. B. Slim and S. Koubaa, “Mechanical and water absorption behavior of thermoset matrices reinforced with natural fiber,” *Polymer Composites,* vol. 43, no. 6, p. 3481, 2022.

[126] G. S. Ray and H. D. Rozman, “Swelling properties of chemically modified oil palm empty fruit bunch based polyurethane composites,” *J. Appl. Polym. Sci.,* vol. 108, no. 2, p. 995, 2008.

[127] X. Zhou, C. Fang, W. Lei, J. Du, T. Huang, Y. Li and Y. Cheng, “Various nanoparticle morphologies and surface properties of waterborne polyurethane controlled by water,” *Scientific Reports,* vol. 6, p. 34574 , 2016.

[128] Y. Wang, J. Song, Q. Tian and et al., “Understanding water absorption effect on molecular dynamics, microstructures and relaxation behavior of segmented polyurethane elastomers,” *Polymer Degradation and Stability,* vol. 214, no. 110415, 2023.

[129] X. Ding, X. Wang, H. Zhang, T. Liu, C. Hong, Q. Ren and C. Zhou, “Preparation of waterborne polyurethane-silica nanocomposites by a click chemistry method,” *Materials Today Communications,* vol. 23, p. 100911, 2020.

[130] N. A. Saliba, H. Yang and B. J. Finlayson-Pitts, “Reaction of Gaseous Nitric Oxide with Nitric Acid on Silica Surfaces in the Presence of Water at Room Temperature,” *J. Phys. Chem. A,* vol. 105, p. 339–346, 2001.

[131] H. Keskinen, S. Romakkaniemi, A. Jaatinen and et al., “Characterization of Morphology and WaterAdsorption on Fumed Silica Nanoparticles,” *Aerosol Science and Technology,* vol. 45, p. 1441–1447, 2011.

[132] G. Alvarez, M. Fuensanta and V. H. Orozco, “Hybrid waterborne polyurethane/acrylate dispersion synthesized with bisphenol A-glicidylmethacrylate (Bis-GMA) grafting agent,” *Progress in Organic Coatings,* vol. 118, pp. 30-39, 2018.

[133] S. Pathaka, V. Kumara, V. Bonua, J. L. Mishnaevsky, R. Lakshmi, P. Bera and H. Barshiliaa, “Enhancing wind turbine blade protection: Solid particle erosion resistant ceramic oxides-reinforced epoxy coatings,” *Renewable Energy,* p. In Press, 2024.

[134] E. Champa-Bujaico, P. García-Díaz and A. Díez-Pascual, “Machine learning for property prediction and optimization of polymeric nanocomposites: a state-of-the-art,” *International Journal of Molecular Sciences.,* vol. 23, p. 10712, 2022.

[135] J. Zhu, Y. Shi, X. Feng, H. Wang and X. Lu, “Prediction on tribological properties of carbon fiber and TiO2 synergistic reinforced polytetrafluoroethylene composites with artificial neural networks,” *Mater. Eng.*, vol. 30, p. 1042–1049, 2009.

[136] S. Sorour, C. Abdelrahman and S. M. Shazly, “A review on machine learning implementation for predicting and optimizing the mechanical behaviour of laminated fiber-reinforced polymer composites,” *Heliyon*, vol. 10, no. 13, p. e33681, 2024.

[137] M. Zakaulla, Y. Pasha and S. Siddalingappa, “Prediction of mechanical properties for polyetheretherketone composite reinforced with graphene and titanium powder using artificial neural network.,” *Mater. Today Proc.*, vol. 49, p. 1268–1274, 2022.

[138] A. Ul Hassan, S. S. Ahmad Shah and Z. M. El-Bahy, “Polymer design using machine learning: A quest for high glass transition temperature,” *Synthetic Metals* , vol. 307, p. 117659, 2024.

[139] I. Najjar, A. Sadoun, M. Alam and A. Fathy, “Prediction of wear rates of Al-TiO2 nanocomposites using artificial neural network modified with particle swarm optimization algorithm,” *Materials Today*, vol. 35, p. 105743, 2023.